

**Titre:** Impact of Seismic Hazard on the Performance of an Earth Dike in  
Title: Eastern North America

**Auteur:** Jessica Huo-Kang  
Author:

**Date:** 2021

**Type:** Mémoire ou thèse / Dissertation or Thesis

**Référence:** Huo-Kang, J. (2021). Impact of Seismic Hazard on the Performance of an Earth  
Citation: Dike in Eastern North America [Mémoire de maîtrise, Polytechnique Montréal].  
PolyPublie. <https://publications.polymtl.ca/6297/>

 **Document en libre accès dans PolyPublie**  
Open Access document in PolyPublie

**URL de PolyPublie:** <https://publications.polymtl.ca/6297/>  
PolyPublie URL:

**Directeurs de  
recherche:** Samuel Yniesta  
Advisors:

**Programme:** Génie civil  
Program:

**POLYTECHNIQUE MONTRÉAL**

affiliée à l'Université de Montréal

**Impact of seismic hazard on the performance of an earth dike in Eastern  
North America**

**JESSICA HUO-KANG**

Département de génie civil, géotechnique et des mines

Mémoire

Présentée en vue de l'obtention du diplôme de *Maîtrise ès sciences appliquées*

Génie civil

Mai 2021

# **POLYTECHNIQUE MONTRÉAL**

affiliée à l'Université de Montréal

Ce mémoire intitulé :

## **Impact of seismic hazard on the performance of an earth dike in Eastern North America**

Présentée par **Jessica HUO-KANG**

en vue de l'obtention du diplôme de *Maîtrise ès sciences appliquées*

a été dûment acceptée par le jury d'examen constitué de :

**Carlos OVALLE**, président

**Samuel YNIESTA**, membre et directeur de recherche

**Pooneh MAGHOUL**, membre

## ACKNOWLEDGEMENTS

This study was made possible with the participation of several persons and organisms and I would like to take this opportunity to thank them.

First of all, I would like to thank my supervisor Mr. Samuel Yniesta for introducing me to this fascinating subject, but also for his constant guidance, for having generously shared his knowledge and for always being present despite his busy schedule. I also want to thank him for having trusted me at the start and to have given me this opportunity.

Also, I would want to express my gratitude to the *Fond de recherche Nature et Technologie* (FRQNT) for making this study possible by funding this research.

Thanks to the jury's members, Mr. Carlos Ovalle and Ms Pooneh Maghoul, for having taken their time to evaluate my thesis and for having provided me constructive comments.

Special thanks to my coworkers/friends with whom we shared the same office. Your good mood was contagious and has cheered me up especially when times were tough. The moments we shared together in the office and outside would stay forever in my mind.

Last but definitely not least, I am infinitely grateful to my family and friends, especially my parents, sister, brother-in-law and to my special someone. Thanks for your exceptional support and to have listened to me day after day.

## RÉSUMÉ

Des analyses non-linéaires peuvent être réalisées pour évaluer la stabilité des digues contre les séismes. Il est d'abord nécessaire de sélectionner des scénarios sismiques représentant l'aléa sismique de la région et après, il est possible de procéder à l'étape de la sélection des accélérogrammes d'entrée pour chacun des scénarios. Par conséquent, la sélection des scénarios est une étape importante, car elle influence directement la sélection des mouvements d'entrée et par le fait même les résultats du modèle. Ce mémoire étudie l'impact de l'aléa sismique sur les performances d'une digue en terre dans le Nord-Est de l'Amérique. Le 2<sup>e</sup> objectif principal s'agit d'identifier des intensités de mesure (*IM*) capable de prédire efficacement les dommages (*DM*) d'une digue en terre. Alors que la sélection des accélérogrammes est basée sur la forme du spectre, l'utilisation d'un critère additionnel basé sur un *IM* qui peut prédire adéquatement les dommages recherchés pourrait permettre de réduire l'incertitude des résultats.

Pour commencer, la déaggrégation de l'aléa sismique est d'abord analysée pour sélectionner les scénarios sismiques suivi des mouvements d'entrée. Pour les besoins du projet, une digue existante construite dans l'*ENA* dont la période fondamentale  $T_0$  est de 0.34 s, est modélisée dans *FLAC* pour observer l'impact de l'aléa au moyen d'analyses nonlinéaires. Pour la sélection de la coupe à modéliser, une étude de la variabilité des conditions de sols est réalisée et consiste en la simulation numérique 1D dans *DEEPSOIL* de plusieurs profils correspondant à différentes coupes afin d'identifier le profil retournant la réponse maximale au sommet. Puis, après la création du modèle 2D, la réponse du modèle est étudiée pour évaluer l'impact des scénarios. Finalement, une étude paramétrique simplifiée est réalisée pour identifier de potentiels *IM* pouvant prédire efficacement les *DM* de la digue.

Au total, 4 scénarios sont définis. Entre 0.01 et 0.2 s (courtes périodes), 2 scénarios sont définis et caractérisent l'aléa : T1-1 M5-6 et T0-20 km et T1-2 : M6-7 et R20-40 km. Dans les périodes modérées entre 0.2 et 1.0 s, l'aléa est dominé par un scénario, soit le T2-1 avec M6-7 et R20-40 km. À longues périodes entre 1.0 et 10 s, le scénario T3-1 domine : M7-7.5 et R40-60 km.

Les scénarios T1-1 et T1-2 devraient avoir un fort contenu en hautes fréquences, tandis que les scénarios T2-1 et T3-1 devraient respectivement englober des séismes avec un fort contenu en moyennes et longues périodes. Après sélection, traitement et mise à l'échelle, le scénario T1-2 contient les mouvements sismiques les plus intenses en termes d'amplitude, alors que les

accélérogrammes du scénario T3-1 ont l'intensité la plus faible, même si la durée est la plus longue avec  $D_{75} = 20.4$  s. Le scénario T1-1 contient des mouvements relativement courts avec un  $D_{75}$  moyen de 4.5 s et l'intensité de ses mouvements est plus faible que le scénario T1-2. En contrepartie, le T2-1 caractérise les périodes moyennes de l'aléa sismique, mais englobe aussi le  $T_0$  avec un contenu fréquentiel plus rapproché de  $T_0$ , ce qui pourrait supposer un potentiel d'amplification plus élevé. D'autre part, le scénario T1-2 a des spectres d'entrée significativement plus élevés que le spectre de conception au pic et à moyennes périodes, ce qui résultera en une réponse exagérée du modèle.

Les résultats des simulations nonlinéaires montrent que chacun des scénarios retournent des réponses différentes. En termes d'amplitudes des mouvements de sortie, le scénario T2-1 induit des réponses à la surface dans la moyenne par rapport aux autres scénarios. Les scénarios T1-1 et T1-2 retournent respectivement les amplitudes les plus faibles et les plus élevés, à cause de la courte durée de ses séismes pour T1-1 et d'un contenu fréquentiel trop élevé des séismes d'entrée de T1-2. Il est à noter toutefois que la plus faible amplification est observée avec T1-2, malgré une forte réponse à la surface. Le scénario T3-1 génère des résultats comparables aux autres scénarios et la plus forte amplification, malgré que son contenu fréquentiel ne corresponde pas au  $T_0$ ; l'amplification pourrait être causée par une plus faible dégradation par rapport aux autres scénarios.

Au niveau du potentiel de liquéfaction, les *CSR* sont concentrés le long des pentes de la digue et au pied, en particulier dans le côté aval de la digue. On note que les facteurs de sécurité obtenus en pied de pente aval sont similaires entre les scénarios, ce qui signifie que peu importe le scénario considéré, les conclusions liées au potentiel de liquéfaction en pied de pente aval demeurent identiques. De plus, les *CSR* obtenus avec *FLAC* sont différents de ceux obtenus avec la méthode simplifiée de Boulanger et Idriss (2008, 2014) qui retournent de grands facteurs de sécurité pour les scénarios T2-1 et T3-1 à cause d'un faible *PGA*. Puis, l'étude paramétrique montre que les intensités de mesure par intégration sont les plus efficaces pour prédire le *CSR* et, qu'au contraire, le spectre d'entrée est une intensité de mesure peu efficace pour prédire le potentiel de liquéfaction, ce qui devrait motiver l'utilisation de paramètres additionnels au spectre de réponse lors de la sélection des séismes.

Ce mémoire montre qu'il est pertinent de considérer plusieurs scénarios sismiques lors des analyses dynamiques afin de capturer l'influence d'évènements à courtes, moyennes et longues périodes.

En effet, les scénarios à courtes périodes génèrent respectivement les plus faibles et les plus fortes réponses à la surface, tandis que le scénario à longues périodes a montré le plus grand potentiel d'amplification. Le scénario à moyenne période montre également une forte amplification et une réponse dans la moyenne parmi les autres scénarios. Il est possible qu'avec une géométrie et des sols différents, les réponses des scénarios pourraient être différents.

## ABSTRACT

Nonlinear analyses can be performed to evaluate the stability of embankments against earthquakes. It first requires the selection of seismic scenarios that represent the seismic hazard of the region and the selection of input ground motions consistent with said seismic scenarios. Hence, the selection of seismic scenarios is an important step because it directly influences the selection of input ground motions and thus the results of the simulations. This thesis focuses on the impact of the seismic hazard scenarios on the performance of an earth dike in Eastern North America (*ENA*). The second main objective of this thesis is to find candidate alternative intensity measures (*IM*) capable of predicting damage measures (*DM*) of an earth dike. As the selection of input motions is in practice based on the shape of the spectrum, introducing an additional criteria based on an *IM* that showed good efficiency in the prediction of the sought *DM* should reduce the variability of the results.

To start, the deaggregation of seismic hazard is first analyzed to then select scenarios followed by input ground motions. For this thesis, an existing dike in *ENA*, with a natural period  $T_0$  of 0.34 s. is modeled in *FLAC* to study the impact of the seismic hazard with nonlinear analyses. First, the spatial variability of the dike is studied to select the critical cross section to use in modelling. Multiple 1D profiles corresponding to varying sections are modeled in the software DEEPSOIL and the critical profile resulting in the highest surface response is identified and the corresponding cross-section is chosen as the 2D model. Then, after modelling the model in 2D, its response is studied to evaluate the impact of the scenarios. Finally, a parametric study is performed to identify potential candidate *IM* capable of predicting efficiently *DM* of the dike.

In the first step, the deaggregation of seismic hazard is studied and 4 seismic scenarios dominating the hazard are then selected: between 0.01 and 0.2 s (short-period range), two scenarios characterize the seismic hazard: T1-1- M5-6 and R0-20 km and T1-2- M6-7 and R20-40 km; in the moderate period range ranging between 0.2 and 1.0 s, the seismic hazard is mostly characterized by one scenario: events of M6-7 and R20-40 km (T2-1); and at long-period range, one scenario captures the seismic hazard: M7-7.5 and R40-60 km (T3-1). Therefore, scenarios T1-1 and T1-2 should be rich in high frequency content while scenarios T2-1 and T3-1 should respectively be rich in medium and low frequency content. After selection, processing and scaling, the scenario T1-2 contains the strongest motions in terms of amplitude while the T3-1 contains the weakest motions

although it has the longest significant duration (average  $D_{75} = 20.4$  s). T1-1 contains relatively short motions (average  $D_{75} = 4.5$  s) and its intensity of shaking is lower than T1-2. The scenario T2-1 characterizes the medium period range and also the dike's  $T_0$  with frequency content closer to  $T_0$ , which might result in higher amplification. In addition, the average response spectrum of T1-2 is higher than the target spectrum at the peak and at medium periods which will further lead to an exaggerated response of the model.

The results of nonlinear simulations show that each scenario returned a different response of the model. In terms of amplitude, the medium-period scenario T2-1 generates fairly average results at the surface among scenarios. Meanwhile the weakest and highest resulting amplitudes are generated respectively by T1-1 and T1-2 because of short motions of T1-1 and an exceedingly high frequency content of input motions of T1-2. It is worth mentioning that the weakest amplification is observed under T1-2 despite high response computed at the surface. The long-period scenario T3-1 leads to surface results comparable to other scenarios and the highest amplification despite its frequency content being far from  $T_0$ ; the amplification might result from a lower level of soils degradation.

The distribution of *CSR* in the model is concentrated along the sloping faces and the toes, especially in the downstream side of the model. Factors of safety against liquefaction below the downstream toe are relatively similar between scenarios meaning that the same conclusion regarding the triggering of liquefaction could be made regardless of the scenario used. In addition, the *CSR* obtained using *FLAC* and from the simplified method proposed by Boulanger and Idriss (2008, 2014) are significantly different from each other in which the latter returned higher factors of safety against liquefaction under T2-1 and T3-1 due to weaker *PGA*. Finally, the parametric study has shown that integration-based *IM* are the most efficient in the prediction of liquefaction (i.e. *CSR*), meanwhile the input spectrum is a poor *IM* in the prediction of *CSR*. Hence, engineers should not rely solely on the shape of the input spectrum during the selection of input motions but should also consider other *IM* that showed adequate efficiency in the prediction of the sought damage measures.

Therefore, when assessing the potential of earthquake damage on an earth dike, it is important to consider multiple scenarios to capture the influence of seismic events rich in short, medium and long periods. This thesis shows that short-periods scenarios led to the weakest and also the

maximum response at the surface while the long-periods scenario returned the highest amplification. The medium-period scenario has also shown high amplification and a response in the same order among other scenarios. It should be mentioned that with a different geometry, level of seismicity, and soil conditions, the response under each scenario may be different.

## TABLE OF CONTENTS

|  |               |
|--|---------------|
| <b>ACKNOWLEDGEMENTS .....</b>                  | <b>iii</b>    |
| <b>RÉSUMÉ.....</b>                             | <b>iv</b>     |
| <b>ABSTRACT.....</b>                           | <b>vii</b>    |
| <b>TABLE OF CONTENTS.....</b>                  | <b>x</b>      |
| <b>LIST OF TABLES .....</b>                    | <b>xv</b>     |
| <b>LIST OF FIGURES.....</b>                    | <b>xvii</b>   |
| <b>LIST OF SYMBOLS AND ABBREVIATIONS .....</b> | <b>xxviii</b> |
| <b>LIST OF APPENDICES .....</b>                | <b>xxxii</b>  |
| <b>Chapter 1 INTRODUCTION.....</b>             | <b>1</b>      |
| <b>1.1 Context.....</b>                        | <b>1</b>      |
| <b>1.2 Objectives of this thesis.....</b>      | <b>2</b>      |
| <b>1.3 Methodology .....</b>                   | <b>3</b>      |
| <b>1.4 Content of the thesis .....</b>         | <b>3</b>      |
| <b>Chapter 2 LITERATURE REVIEW .....</b>       | <b>5</b>      |
| <b>2.1 Review of basic soil behavior .....</b> | <b>5</b>      |
| 2.1.1 Mohr-Coulomb model.....                  | 5             |
| 2.1.2 Stiffness parameters .....               | 6             |
| <b>2.2 Dynamic behavior of soil .....</b>      | <b>8</b>      |
| 2.2.1 Hysteretic behavior .....                | 8             |
| 2.2.2 Masing rules .....                       | 10            |
| 2.2.3 Modulus reduction and damping.....       | 11            |
| 2.2.4 Liquefaction.....                        | 14            |
| 2.2.5 Seismic site classification .....        | 15            |
| 2.2.6 Natural modes.....                       | 17            |
| <b>2.3 Ground motion characteristics.....</b>  | <b>18</b>     |
| 2.3.1 Seismic waves.....                       | 18            |

|                  |  |           |
|------------------|--|-----------|
| 2.3.2            | Ground motion characterization.....  | 18        |
| 2.3.3            | Quality metrics .....  | 31        |
| <b>2.4</b>       | <b>Site effects .....</b>  | <b>33</b> |
| 2.4.1            | Effect of the nature and the inclination of incident waves and material damping.....         | 34        |
| 2.4.2            | Effect of the motion frequency content.....  | 35        |
| 2.4.3            | Effect of soil stratigraphy .....  | 35        |
| <b>2.5</b>       | <b>Seismic design of embankments in practice .....</b>                                       | <b>37</b> |
| 2.5.1            | Static analysis .....  | 37        |
| 2.5.2            | Dynamic analysis .....   | 37        |
| <b>Chapter 3</b> | <b>SELECTION OF GROUND MOTIONS.....</b>  | <b>39</b> |
| <b>3.1</b>       | <b>Introduction.....</b>   | <b>39</b> |
| <b>3.2</b>       | <b>Period range and response spectrum .....</b>  | <b>40</b> |
| 3.2.1            | Uniform hazard spectrum $UHS$ and design spectrum $S(T)$ .....                               | 40        |
| 3.2.2            | Period range $T_R$ .....   | 42        |
| 3.2.3            | Target response spectrum $S_T(T)$ .....  | 42        |
| <b>3.3</b>       | <b>Selection of seismic scenarios based on the seismic hazard deaggregation.....</b>         | <b>43</b> |
| 3.3.1            | Short-period scenarios .....   | 44        |
| 3.3.2            | Medium-period scenarios .....  | 46        |
| 3.3.3            | Long-period scenarios .....  | 47        |
| <b>3.4</b>       | <b>Databases of historical ground motions .....</b>  | <b>48</b> |
| <b>3.5</b>       | <b>Selection criteria .....</b>  | <b>49</b> |
| <b>3.6</b>       | <b>Scaling of ground motions .....</b>   | <b>50</b> |
| <b>3.7</b>       | <b>Selection of ground motions .....</b>   | <b>51</b> |
| 3.7.1            | Compatibility issues .....   | 55        |
| 3.7.2            | Ground motions intensity measures (IM) and number of equivalent number of stress cycles..... | 56        |
| <b>Chapter 4</b> | <b>GROUND MOTIONS PROCESSING.....</b>  | <b>60</b> |
| <b>4.1</b>       | <b>Introduction.....</b>   | <b>60</b> |
| <b>4.2</b>       | <b>Filtering procedure.....</b>  | <b>60</b> |
| 4.2.1            | Tapers and zero-pads .....   | 62        |
| 4.2.2            | Low-cut and high-cut frequencies.....  | 64        |

|                  |  |           |
|------------------|--|-----------|
| <b>Chapter 5</b> | <b>DESCRIPTION OF THE WATER-RETAINING DIKE STUDIED</b> | <b>68</b> |
| 5.1              | Introduction   | 68        |
| 5.2              | Geometry of the embankment                             | 69        |
| 5.3              | Geotechnical properties                                | 70        |
| 5.3.1            | Embankment   | 71        |
| 5.3.2            | Foundation, bedrock and water level                    | 73        |
| 5.4              | Dynamic properties                                     | 76        |
| 5.4.1            | Minimum Damping ratio $D_{min}$                        | 76        |
| 5.4.2            | Modulus reduction and damping curves                   | 76        |
| 5.5              | Liquefaction potential                                 | 81        |
| 5.6              | Foundation soils spatial variability                   | 85        |
| 5.6.1            | Cross-sections A, B and C                              | 85        |
| 5.6.2            | Non-linear 1D simulations                              | 88        |
| 5.6.3            | Results  | 89        |
| <b>Chapter 6</b> | <b>NUMERICAL MODELING</b>                              | <b>91</b> |
| 6.1              | Introduction   | 91        |
| 6.2              | Summary of the simulations                             | 93        |
| 6.3              | Numerical software <i>FLAC</i>                         | 94        |
| 6.4              | Construction of the model                              | 94        |
| 6.4.1            | Geometry and discretization                            | 94        |
| 6.4.2            | Dynamic boundary conditions                            | 96        |
| 6.4.3            | Damping  | 98        |
| 6.4.4            | Input parameters and soil models                       | 98        |
| 6.4.5            | Presentation of the model                              | 99        |
| 6.4.6            | Natural modes  | 100       |
| 6.5              | Static simulations                                     | 102       |
| 6.5.1            | Static equilibrium                                     | 103       |
| 6.5.2            | Initialization of the reservoir                        | 104       |
| 6.5.3            | Static slope stability                                 | 108       |
| 6.6              | Dynamic linear damped simulations                      | 110       |

|                  |  |            |
|------------------|--|------------|
| 6.6.1            | Validation of the model.....   | 110        |
| <b>6.7</b>       | <b>Calibration of the hysteretic model.....</b>  | <b>113</b> |
| <b>6.8</b>       | <b>Factors affecting the timestep .....</b>  | <b>116</b> |
| 6.8.1            | Materials stiffness .....  | 116        |
| 6.8.2            | Center frequency $f_c$ of Rayleigh damping.....  | 116        |
| 6.8.3            | Damping ratio of Rayleigh damping .....  | 117        |
| <b>Chapter 7</b> | <b>RESULTS.....</b>  | <b>119</b> |
| <b>7.1</b>       | <b>Introduction.....</b>   | <b>119</b> |
| <b>7.2</b>       | <b>Summary of the results .....</b>  | <b>119</b> |
| <b>7.3</b>       | <b>Tracked variables and history points .....</b>  | <b>121</b> |
| <b>7.4</b>       | <b>Scenario-specific study of the seismic behavior of the dike .....</b>   | <b>123</b> |
| 7.4.1            | Spectral response and spectral amplification .....   | 123        |
| 7.4.2            | Soils nonlinearity .....   | 128        |
| 7.4.3            | Amplification of intensity measures $IM$ .....   | 134        |
| <b>7.5</b>       | <b>Cyclic stress ratio (<math>CSR</math>).....</b>   | <b>140</b> |
| 7.5.1            | Distribution of $CSR$ .....  | 140        |
| 7.5.2            | Evaluation of the potential of liquefaction .....  | 146        |
| 7.5.3            | Comparison of liquefaction triggering using the simplified method .....  | 148        |
| <b>7.6</b>       | <b>Topographic effects.....</b>  | <b>150</b> |
| <b>7.7</b>       | <b>Impact of seismic hazard in the short-period range .....</b>  | <b>153</b> |
| 7.7.1            | Input ground motions .....   | 153        |
| 7.7.2            | Impact on the seismic response.....  | 155        |
| <b>7.8</b>       | <b>Parametric study: Ground motions intensity measures <math>IM</math> to evaluate damage measures <math>DM</math></b> | <b>160</b> |
| 7.8.1            | Damage measures $DM$ and candidate intensity measures $IM$ .....   | 161        |
| 7.8.2            | Efficiency of candidate input motions $IM$ in the prediction of damage measures $DM$ .....                             | 162        |
| <b>Chapter 8</b> | <b>CONCLUSION.....</b>   | <b>166</b> |
| <b>8.1</b>       | <b>Summary and conclusion.....</b>   | <b>166</b> |
| 8.1.1            | Seismic hazard and selection and scaling of input motions.....   | 167        |

8.1.2 Results of nonlinear simulations and parametric study ..... 168  
8.1.3 Scope of research ..... 169

**REFERENCES ..... 171**

**APPENDICES 215**

## LIST OF TABLES

|  |     |
|--|-----|
| Table 2.1 Ranges of $(K_2)_{max}$ .....  | 7   |
| Table 2.2 Soil classification suggested by <i>NBCC 2015</i> (NEHRP, 1994) .....  | 16  |
| Table 2.3 Period-dependent site factors $F(T)$ (Finn and Wightman, 2003), retrieved from Humar (2015) .....                    | 17  |
| Table 3.1 Values of $UHS$ and $S(T)$ over the entire period range $T_R$ .....  | 41  |
| Table 3.2 Seismic scenarios based on the deaggregation of the city of Montreal .....   | 44  |
| Table 3.3 Second scaling factors $F_2$ to adjust the match of $S_g$ with $S_T(T)$ .....  | 51  |
| Table 3.4 Presentation of selected and scaled input ground motions – Scenarios T1-1 and T1-2.....                              | 52  |
| Table 3.5 Presentation of selected and scaled input ground motions – scenarios T2-1 and T3-1 .....                             | 53  |
| Table 4.1 $LC$ and $HC$ of selected input ground motions, taken from the Flatfile .....  | 67  |
| Table 5.1 Geotechnical properties of the embankment.....   | 72  |
| Table 5.2 Geotechnical properties of foundation soils and bedrock .....  | 75  |
| Table 5.3 Materials damping ratio $D_{min}$ obtained from Darendeli (2001).....  | 76  |
| Table 5.4 Parameters used to compute the $MRD$ curves of Darendeli.....  | 80  |
| Table 6.1 Input motions used in the simulations for each scenario. ....  | 93  |
| Table 6.2 Materials input parameters in <i>FLAC</i> .....  | 99  |
| Table 6.3 Natural frequencies of the <i>FLAC</i> model, obtained using a linear dynamic simulation.....                        | 101 |
| Table 6.4 Estimated theoretical natural frequencies of a 1D column of soil based on the $V_{sI}$ and the $H$ of the model..... | 102 |
| Table 7.1 Average values of maximum $CSR$ and of $CSR$ below the downstream toe .....  | 145 |
| Table 7.2 Standard deviation of resulting intensity measures $IM$ at the surface of the model for scenarios T1-1 and T1-2..... | 158 |
| Table 7.3 Damage measures $DM$ and locations considered in the parametric study .....  | 161 |
| Table 7.4 Candidate input motions intensity measures $IM$ in the parametric study .....  | 162 |

|   |     |
|---|-----|
| Table C.1 Details of the calculation of the liquefaction potential based on the <i>SPT</i> -method for soil class D and $M = 6$ ..... | 224 |
| Table C.2 Details of the calculation of the liquefaction potential based on the $V_s$ -method for soil class D .....                  | 225 |

## LIST OF FIGURES

|   |    |
|---|----|
| Figure 2.1 Mohr-Coulomb failure criterion .....   | 5  |
| Figure 2.2 Correlations of $\phi$ based on $(N_1)_{60}$ retrieved from NCHRP (2010).....  | 6  |
| Figure 2.3 Illustration of a typical backbone curve.....  | 8  |
| Figure 2.4 Damping ratio obtained from a loading loop, retrieved from Yniesta et al. (2017) .....   | 9  |
| Figure 2.5 Illustration of a typical modulus reduction and damping curve (those presented are<br>calculated with Darendeli (2001) for the core of the dike) .....       | 9  |
| Figure 2.6 Extended Masing rules (Vucetic, 1990), retrieved from Kammerer et al. (2018).....  | 10 |
| Figure 2.7 Example of viscous Rayleigh damping with $f_{min} = 4.8$ Hz .....  | 12 |
| Figure 2.8 Illustration of typical a) modulus curves and b) damping curves for clayey soils<br>developed by Darendeli. Retrieved from Darendeli (2001).....             | 13 |
| Figure 2.9 Illustration of a typical Fourier amplitude spectrum processed using a $LC$ of 0.7 Hz and<br>$HC$ of 20 Hz (earthquake Friuli, Italy – 03 – RSN3553H1) ..... | 20 |
| Figure 2.10 Illustration of a typical response spectrum (earthquake Coalinga – 02 – RSN381H1)<br>.....  | 20 |
| Figure 2.11 Illustration of $PGA$ obtained from $a(t)$ .....  | 22 |
| Figure 2.12 Illustration of $PGV$ obtained from $v(t)$ .....  | 23 |
| Figure 2.13 Illustration of $PGD$ obtained from $d(t)$ .....  | 24 |
| Figure 2.14 Illustration of $S_a(T_0)$ obtained from a response spectrum .....  | 25 |
| Figure 2.15 Illustration of $S_a(1.5T_0)$ obtained from a response spectrum .....   | 25 |
| Figure 2.16 Calculation of $CAV$ and $CAV_{STD}$ , retrieved from Campbell and Bozorgnia (2011) ...   | 28 |
| Figure 2.17 Efficiency of candidate $IM$ for the prediction of $DM$ .....   | 31 |
| Figure 2.18 $PGA$ on soft soil sites, retrieved from Idriss (1990) .....  | 36 |
| Figure 3.1 Illustration of the $UHS$ at the site.....   | 41 |
| Figure 3.2 Illustration of $S(T)$ and $UHS$ at the site.....  | 42 |

|  |    |
|--|----|
| Figure 3.3 Definition of $S_T(T)$ and illustration of an example of $mean S_g$ scaled to the $S_T(T)$ over the $T_{RS}$ .....                    | 43 |
| Figure 3.4 Deaggregation of the seismic hazard of the site at periods a) 0.01 s, b) 0.05 s, c) 0.1 s and d) 0.2s .....                           | 45 |
| Figure 3.5 Deaggregation of the seismic hazard at the site for periods a) 0.2 s, b) 0.3 s, c) 0.5 s and d) 1.0 s.....                            | 46 |
| Figure 3.6 Deaggregation of the seismic hazard at the site for periods a) 1.0 s, b) 2.0 s, c) 5.0 s and d) 10.0 s.....                           | 47 |
| Figure 3.7 Illustration of $mean S_g$ matched to the $S_T(T)$ over $T_{RS}$ for scenarios a) T1-1, b) T1-2, c) T2-1 and d) T3-1 .....            | 54 |
| Figure 3.8 Incompatibility of the shape of $mean S_g$ of scenarios T1-1 and T1-2 a) before scaling and b) after scaling .....                    | 55 |
| Figure 3.9 Input ground motions $IM$ and average $IM$ for all scenarios.....   | 57 |
| Figure 3.10 Number of equivalent stress cycles at $0.65\tau_{max}$ .....   | 58 |
| Figure 4.1 Input ground motions processing procedure (inspired by PEER NGA post-processing procedure).....                                       | 61 |
| Figure 4.2 Zero-pads and tapers at the extremity of the ground motion.....   | 63 |
| Figure 4.3 Minimal length of the zero-pads (Converse and Brady, 1992).....   | 63 |
| Figure 4.4 Illustration of a typical Butterworth a) $LC$ filter and b) $HC$ filter with a $f_c$ of 0.7 Hz and a $n$ of 4.....                    | 64 |
| Figure 4.5 Illustration of the effects of motion processing on RSN381H1 with $LC$ of 0.7 Hz, $HC$ of 30 Hz and $n$ of 4.....                     | 65 |
| Figure 4.6 Illustration of the effects of motion processing of RSN381H1 on the a) acceleration, b) velocity and c) displacement time series..... | 66 |
| Figure 5.1 Section of the embankment and its surrounding areas .....   | 69 |
| Figure 5.2 Location of the boreholes and the $MASW$ test .....   | 70 |
| Figure 5.3 Detailed section of the embankment with identified types of soils .....   | 71 |

|  |     |
|--|-----|
| Figure 5.4 a) $(N_1)_{60}$ profile of foundation soils for BH-1 to BH-3 and b) $V_{sI}$ profile at BH-2 .....  | 73  |
| Figure 5.5 Illustration of the cross-section of the dike including the thickness of each layer of the foundation soils and the piezometric line.....                             | 75  |
| Figure 5.6 Separation of the core into 2 sublayers with confining pressures of 24.4 kPa and 58.7 kPa.....  | 77  |
| Figure 5.7 Comparison of <i>MRD</i> curves between the top and base sublayers of the core .....  | 78  |
| Figure 5.8 Separation of the loose silt layer into 3 sublayers with varying confining pressure ....  | 79  |
| Figure 5.9 Comparison of <i>MRD</i> curves between the top, middle and base sublayers of the loose silt deposit .....  | 79  |
| Figure 5.10 a) Modulus reduction curves and b) damping curves for the embankment and foundation soils .....  | 80  |
| Figure 5.11 a) $(N_1)_{60}$ and b) $V_{sI}$ of the loose silt under the vicinity of the dike .....   | 81  |
| Figure 5.12 Factor of safety against liquefaction evaluated for the saturated silt underneath the embankment based on the a) <i>N</i> -based method and b) $V_{sI}$ -method..... | 82  |
| Figure 5.13 Curves of <i>CRR</i> for a) <i>N</i> -based method and b) $V_{sI}$ -based method for the prediction of liquefaction.....   | 83  |
| Figure 5.14 Soil column of cross-sections A, B and C of the dike .....   | 86  |
| Figure 5.15 $V_s$ profiles of sections A, B and C.....   | 87  |
| Figure 5.16 One-dimensional horizontally layered deposit shaken at the base, retrieved from Hashash and Park (2001).....   | 88  |
| Figure 5.17 Crest response spectra of sections A, B and C .....  | 90  |
| Figure 6.1 Geometry of the model on <i>FLAC</i> with coordinates of each point (meter) .....   | 95  |
| Figure 6.2 Meshing of the model on <i>FLAC</i> with 240 x 54 quadrilateral zones .....   | 96  |
| Figure 6.3 Dynamic boundaries of the model on <i>FLAC</i> .....  | 97  |
| Figure 6.4 Illustration of the model in <i>FLAC</i> including materials, dynamic boundary conditions and the input stress .....  | 100 |

|   |     |
|---|-----|
| Figure 6.5 Transfer function of the <i>FLAC</i> model.....  | 101 |
| Figure 6.6 Initial state of shear stress $\tau$ including the weight of the embankment in static state using<br>a) method 1 and b) method 2.....  | 103 |
| Figure 6.7 Initial state of total vertical stress $\sigma_v$ including the weight of the embankment in static<br>state with a) method 1 and b) method 2 .....   | 104 |
| Figure 6.8 Hydraulic input conditions for the initialization of pore pressure while rising the<br>reservoir in static state.....  | 105 |
| Figure 6.9 Pore pressure distribution in the model with the reservoir at full pool in static state.   | 106 |
| Figure 6.10 Mechanical input condition for the initialization of the state of stress with the reservoir<br>at full pool in static state .....   | 106 |
| Figure 6.11 Distribution of shear stress and total vertical stress with the reservoir at full pool in<br>static state .....   | 107 |
| Figure 6.12 Horizontal and vertical displacement with the reservoir at full pool in static state..  | 108 |
| Figure 6.13 Factor of safety of 2.66 for a potential slope failure at the downstream face of the model<br>– Static slope stability analysis.....  | 109 |
| Figure 6.14 Maximum level of shear strain of the preliminary analysis performed using RSN598H2<br>of scenario T2-1 .....  | 111 |
| Figure 6.15 Comparison of recorded motion at the base and input motion in terms of a) $v(t)$ and b)<br>$S_g$ .....  | 112 |
| Figure 6.16 Calibration of the hysteretic sig 4 model for a) the rockfill and sand and gravel, b) the<br>clay, c) the top core sublayer and d) the base core sublayer .....   | 114 |
| Figure 6.17 Calibration of the hysteretic sig 4 model for the foundation soils: a) compact silt and<br>b) loose silt .....  | 115 |
| Figure 6.18 Comparison of the response spectrum between approach 1 (accurate values of materials<br>damping ratio) and approach 2 (uniform damping value of 0.2 %) at the a) middle crest, b)<br>upstream toe, c) downstream toe, d) upstream free-field, e) downstream free-field, f) in the<br>dike and g) in the foundation soils (loose silt) ..... | 118 |

|  |     |
|--|-----|
| Figure 7.1 Location of history points in the 2D <i>FLAC</i> model .....  | 122 |
| Figure 7.2 Average spectral response calculated at the crest and compared to the input spectrum of scenarios a) T1-1, b) T1-2, c) T2-1 and d) T3-1 .....   | 123 |
| Figure 7.3 Average spectral response calculated at the crest for each scenario.....  | 124 |
| Figure 7.4 Amplification ratios calculated between the average spectral response at the crest and the input average spectral response.....   | 124 |
| Figure 7.5 Average spectral response calculated at the crest and compared to the free-field and the applied input spectrum of scenarios a) T1-1, b) T1-2, c) T2-1 and d) T3-1 .....  | 126 |
| Figure 7.6 Average spectral response calculated at the free-field.....   | 126 |
| Figure 7.7 Amplification ratios calculated between the average spectral response at the free-field and the applied input spectrum at the base.....   | 127 |
| Figure 7.8 Amplification ratios calculated between the <i>mean S<sub>g</sub></i> of the crest and the free-field.  | 128 |
| Figure 7.9 Degradation of the natural modes of scenarios a) T1-1, b) T1-2, c) T2-1 and d) T3-1 .....   | 129 |
| Figure 7.10 Average spectral response calculated at the crest using elastic and nonlinear properties for scenarios a) T1-1, b) T1-2, c) T2-1 and d) T3-1.....  | 130 |
| Figure 7.11 Influence of nonlinearity evaluated at the crest as the ratio between the <i>mean S<sub>g</sub></i> obtained from elastic and nonlinear simulations.....   | 131 |
| Figure 7.12 Profile of <i>T<sub>m</sub></i> in the centerline .....  | 132 |
| Figure 7.13 Average spectral response in the centerline at several depths of scenarios a) T1-1, b) T1-2, c) T2-1 and d) T3-1 .....   | 133 |
| Figure 7.14 Amplitude-based <i>IM</i> at the surface of the model including a) <i>PGA</i> and b) <i>PGV</i> .....  | 134 |
| Figure 7.15 Amplification ratios of amplitude-based <i>IM</i> at the surface of the model including a) <i>PGA</i> and b) <i>PGV</i> .....  | 134 |
| Figure 7.16 Integration-based <i>IM</i> at the surface of the model including a) <i>I<sub>a</sub></i> , b) <i>CAV</i> , c) <i>CAV<sub>5</sub></i> , d) <i>CAV<sub>std</sub></i> , e) <i>ASI</i> , f) <i>SI</i> , g) <i>SIR<sub>75</sub></i> and h) <i>SIR<sub>95</sub></i> ..... | 136 |

|  |     |
|--|-----|
| Figure 7.17 Amplification ratios of the integration-based <i>IM</i> at the surface a) $I_a$ , b) <i>CAV</i> , c) $CAV_5$ ,<br>d) $CAV_{std}$ , e) <i>ASI</i> , f) <i>SI</i> , g) $SIR_{75}$ and h) $SIR_{95}$ .....              | 136 |
| Figure 7.18 Spectral-based <i>IM</i> at the surface of the model including a) $S_a(T_0)$ , b) $S_a(1.5T_0)$ , c)<br>$S_a(0.1)$ , d) $S_a(1.0)$ and e) $S_a(10)$ .....  | 138 |
| Figure 7.19 Amplification ratios of spectral-based <i>IM</i> at the surface of the model including a)<br>$S_a(T_0)$ , b) $S_a(1.5T_0)$ , c) $S_a(0.1)$ , d) $S_a(1.0)$ and e) $S_a(10)$ .....                                    | 138 |
| Figure 7.20 Frequency-based <i>IM</i> at the surface of the model with values of a) $T_m$ and b)<br>amplification ratios of $T_m$ .....  | 139 |
| Figure 7.21 Average spectral response calculated at mid-slopes and compared to the crest of<br>scenarios a) T1-1, b) T1-2, c) T2-1 and d) T3-1 .....   | 140 |
| Figure 7.22 Distribution of CSR of each simulation of scenario T1-1 .....  | 141 |
| Figure 7.23 Distribution of CSR of each simulation of scenario T1-2 .....  | 142 |
| Figure 7.24 Distribution of CSR of each simulation of scenario T2-1 .....  | 143 |
| Figure 7.25 Distribution of CSR of each simulation of scenario T3-1 .....  | 144 |
| Figure 7.26 Number of equivalent stress cycles at $0.65\tau_{max}$ at critical locations for liquefaction<br>triggering .....  | 146 |
| Figure 7.27 Profile of CSR at the downstream toe obtained with <i>FLAC</i> and <i>CRR</i> calculated using<br>the method based on <i>SPT</i> and $V_s$ results .....   | 147 |
| Figure 7.28 Factors of safety against liquefaction by comparing the <i>CRR</i> using the method based<br>on <i>SPT</i> and $V_s$ results and the CSR obtained with <i>FLAC</i> .....   | 147 |
| Figure 7.29 CSR profiles calculated with the simplified method at the a) the crest, b) downstream<br>toe and the c) near the bottom of the downstream slope.....   | 149 |
| Figure 7.30 Factors of safety against liquefaction triggering at the downstream toe using CSR<br>calculated with the simplified method and considering the <i>CRR</i> by <i>SPT</i> results and the <i>CRR</i><br>by $V_s$ ..... | 150 |
| Figure 7.31 Amplification ratios of <i>IM</i> calculated between the crest and the free-field.....   | 151 |

|  |     |
|--|-----|
| Figure 7.32 Average spectral response at the crest, the mid-slopes, the toes and the free-field for a) T1-1, b) T1-2, c) T2-1 and d) T3-1 .....  | 152 |
| Figure 7.33 Input motions intensity measures $IM$ of T1-1 and T1-2 .....   | 154 |
| Figure 7.34 Shape of input motions $mean S_g$ of T1-1 and T1-2 and $S_T(T)$ .....  | 155 |
| Figure 7.35 Comparison of amplitude, frequency and duration-based $IM$ at the surface of the model between T1-1 and T1-2, including a) $PGA$ , b) $PGV$ , c) $I_a$ , d) $CAV$ , e) $CAV_5$ , f) $CAV_{std}$ , g) $S_a(T_0)$ , h) $S_a(1.5T_0)$ , i) $S_a(0.1)$ , j) $S_a(1.0)$ , k) $T_m$ , l) $ASI$ , m) $SI$ , n) $SIR_{75}$ and o) $SIR_{95}$ ..... | 157 |
| Figure 7.36 Response spectrum calculated at the crest with T1-1 and T1-2 .....   | 159 |
| Figure 7.37 Efficiency of candidate input motion $IM$ for the prediction of a) $PGA$ , $S_a(T_0)$ and $S_a(1.5T_0)$ and b) $S_a(0.1)$ , $S_a(1.0)$ and $S_a(10.0)$ at the crest, both mid-slopes and the toes and the free-field .....   | 163 |
| Figure 7.38 Efficiency of candidate $IM$ for the prediction of the maximum $CSR$ and the $CSR$ at the downstream toe .....   | 164 |
| Figure A.1 Acceleration, velocity and displacement time series of the event Coalinga – 02 (RSN381H1).....  | 177 |
| Figure A.2 Response spectrum of the event Coalinga – 02 (RSN381H1).....  | 178 |
| Figure A.3 Fourier amplitude spectrum of the event Coalinga – 02 (RSN381H1) .....  | 178 |
| Figure A.4 Arias intensity of the event Coalinga – 02 (RSN381H1) .....   | 178 |
| Figure A.5 Acceleration, velocity and displacement time series of the event Gilroy (RSN2019H2) .....   | 179 |
| Figure A.6 Response spectrum of the event Coalinga – 02 (RSN381H1).....  | 179 |
| Figure A.7 Fourier amplitude spectrum of the event Gilroy (RSN2019H2) .....  | 180 |
| Figure A.8 Arias intensity of the event Gilroy (RSN2019H2) .....   | 180 |
| Figure A.9 Acceleration, velocity and displacement time series of the event Friuli, Italy – 03 (RSN3553H1).....  | 181 |
| Figure A.10 Response spectrum of the event Friuli, Italy – 03 (RSN3553H1).....   | 181 |

|  |     |
|--|-----|
| Figure A.11 Fourier amplitude spectrum of the event Friuli, Italy – 03 (RSN3553H1).....  | 182 |
| Figure A.12 Arias intensity of the event Friuli, Italy – 03 (RSN3553H1).....   | 182 |
| Figure A.13 Acceleration, velocity and displacement time series of the event Umbria Marche<br>(Aftershock 8), Italy (RSN4377H1)..... | 183 |
| Figure A.14 Response spectrum of the event Umbria Marche (Aftershock 8), Italy (RSN4377H1)<br>.....                                  | 183 |
| Figure A.15 Fourier amplitude spectrum of the event Umbria Marche (Aftershock 8), Italy<br>(RSN4377H1).....                          | 184 |
| Figure A.16 Arias intensity of the event Umbria Marche (Aftershock 8), Italy (RSN4377H1)..   | 184 |
| Figure A.17 Acceleration, velocity and displacement time series of the event Mineral 2011-08-23<br>(RSN8571H2).....                  | 185 |
| Figure A.18 Response spectrum of the event Mineral 2011-08-23 (RSN8571H2).....   | 185 |
| Figure A.19 Fourier amplitude spectrum of the event Mineral 2011-08-23 (RSN8571H2).....  | 186 |
| Figure A.20 Arias intensity of the event Mineral 2011-08-23 (RSN8571H2).....   | 186 |
| Figure A.21 Acceleration, velocity and displacement time series of the event San Fernando<br>(RSN72H1).....                          | 187 |
| Figure A.22 Response spectrum of the event San Fernando (RSN72H1) .....  | 187 |
| Figure A.23 Response spectrum of the event San Fernando (RSN72H1) .....  | 188 |
| Figure A.24 Arias intensity of the event San Fernando (RSN72H1).....   | 188 |
| Figure A.25 Acceleration, velocity and displacement time series of the event San Fernando<br>(RSN72H2).....                          | 189 |
| Figure A.26 Response spectrum of the event San Fernando (RSN72H2) .....  | 189 |
| Figure A.27 Fourier amplitude spectrum of the event San Fernando (RSN72H2).....  | 190 |
| Figure A.28 Arias intensity of the event San Fernando (RSN72H2).....   | 190 |
| Figure A.29 Acceleration, velocity and displacement time series of the event San Fernando<br>(RSN87H2).....                          | 191 |

|  |     |
|--|-----|
| Figure A.30 Response spectrum of the event San Fernando (RSN87H2) .....  | 191 |
| Figure A.31 Fourier amplitude spectrum of the event San Fernando (RSN87H2).....                                      | 192 |
| Figure A.32 Arias intensity of the event San Fernando (RSN87H2).....   | 192 |
| Figure A.33 Acceleration, velocity and displacement of the event Whittier Narrow – 01<br>(RSN598H2).....             | 193 |
| Figure A.34 Response spectrum of the event Whittier Narrow – 01 (RSN598H2).....                                      | 193 |
| Figure A.35 Fourier amplitude spectrum of the event Whittier Narrow – 01 (RSN598H2) .....                            | 194 |
| Figure A.36 Arias intensity of the event Whittier Narrow – 01 (RSN598H2) .....                                       | 194 |
| Figure A.37 Acceleration, velocity and displacement time series of the event Big Bear – 01<br>(RSN935H1).....        | 195 |
| Figure A.38 Response spectrum of the event Big Bear – 01 (RSN935H1).....   | 195 |
| Figure A.39 Fourier amplitude spectrum of the event Big Bear – 01 (RSN935H1).....                                    | 196 |
| Figure A.40 Arias intensity of the event Big Bear – 01 (RSN935H1).....   | 196 |
| Figure A.41 Acceleration, velocity and displacement time series of the event Whittier Narrow – 01<br>(RSN671H1)..... | 197 |
| Figure A.42 Response spectrum of the event Whittier Narrow – 01 (RSN671H1).....                                      | 197 |
| Figure A.43 Fourier amplitude spectrum of the event Whittier Narrow – 01 (RSN671H1) .....                            | 198 |
| Figure A.44 Arias intensity of the event Whittier Narrow – 01 (RSN671H1) .....                                       | 198 |
| Figure A.45 Acceleration, velocity and displacement time series of the record San Fernando<br>(RSN72H2).....         | 199 |
| Figure A.46 Response spectrum of the record San Fernando (RSN72H2).....  | 199 |
| Figure A.47 Fourier amplitude spectrum of the record San Fernando (RSN72H2) .....                                    | 200 |
| Figure A.48 Arias intensity of the record San Fernando (RSN72H2) .....   | 200 |
| Figure A.49 Acceleration, velocity and displacement time series of the record North Palm Springs<br>(RSN511H1).....  | 201 |

|   |     |
|---|-----|
| Figure A.50 Response spectrum of the record North Palm Springs (RSN511H1).....  | 201 |
| Figure A.51 Fourier amplitude spectrum of the record North Palm Springs (RSN511H1).....                               | 202 |
| Figure A.52 Arias intensity of the record North Palm Springs (RSN511H1).....  | 202 |
| Figure A.53 Acceleration, velocity and displacement time series of the event Whittier Narrows –<br>01 (RSN598H2)..... | 203 |
| Figure A.54 Response spectrum of the event Whittier Narrows – 01 (RSN598H2) .....                                     | 203 |
| Figure A.55 Fourier amplitude spectrum of the event Whittier Narrows – 01 (RSN598H2).....                             | 204 |
| Figure A.56 Arias intensity of the event Whittier Narrows – 01 (RSN598H2).....  | 204 |
| Figure A.57 Acceleration, velocity and displacement time series of the event Northridge<br>(RSN954H1).....            | 205 |
| Figure A.58 Response spectrum of the event Northridge (RSN954H1).....   | 205 |
| Figure A.59 Fourier amplitude spectrum of the event Northridge (RSN954H1) .....                                       | 206 |
| Figure A.60 Arias intensity of the event Northridge (RSN954H1) .....  | 206 |
| Figure A.61 Acceleration, velocity and displacement time series of the event San Simeon<br>(RSN4016H1).....           | 207 |
| Figure A.62 Response spectrum of the event San Simeon (RSN4016H1) .....   | 207 |
| Figure A.63 Fourier amplitude spectrum of the event San Simeon (RSN4016H1).....                                       | 208 |
| Figure A.64 Arias intensity of the event San Simeon (RSN4016H1).....  | 208 |
| Figure A.65 Acceleration, velocity and displacement time series of the event Irpinia, Italy<br>(RSN293H2).....        | 209 |
| Figure A.66 Response spectrum of the event Irpinia, Italy (RSN293H2) .....  | 209 |
| Figure A.67 Fourier amplitude spectrum of the event Irpinia, Italy (RSN293H2).....                                    | 210 |
| Figure A.68 Arias intensity of the event Irpinia, Italy (RSN293H2).....   | 210 |
| Figure A.69 Acceleration, velocity and displacement time series of the event Irpinia, Italy<br>(RSN294H2).....        | 211 |

|   |     |
|---|-----|
| Figure A.70 Response spectrum of the event Irpinia, Italy (RSN294H2) .....  | 211 |
| Figure A.71 Fourier amplitude spectrum of the event Irpinia, Italy (RSN294H2).....                                  | 212 |
| Figure A.72 Arias intensity of the event Irpinia, Italy (RSN294H2).....   | 212 |
| Figure A.73 Acceleration, velocity and displacement time series of the event Taiwan, SMART1<br>(45) (RSN572H2)..... | 213 |
| Figure.A.74 Response spectrum of the event Taiwan, SMART1 (45) (RSN572H2).....                                      | 213 |
| Figure A.75 Fourier amplitude spectrum of the event Taiwan, SMART1 (45) (RSN572H2) ....                             | 214 |
| Figure A.76 Arias intensity of the event Taiwan, SMART1 (45) (RSN572H2) .....                                       | 214 |
| Figure B.1 Boreholes reports a) BH-1, b) BH-2 and c) BH-3 .....   | 223 |

## LIST OF SYMBOLS AND ABBREVIATIONS

### List of symbols

|               |  |
|---------------|--|
| $\phi$        | Friction angle   |
| $\phi'$       | Effective friction angle                                 |
| $\phi_i$      | Regression coefficients in the Darendeli's formulation   |
| $\rho$        | Density  |
| $\tau$        | Shear stress   |
| $\sigma$      | Normal (total) stress                                    |
| $\sigma'_m$   | Mean effective stress                                    |
| $\sigma_v$    | Vertical total stress                                    |
| $\mu$         | Poisson ratio  |
| $\alpha$      | Damping coefficient for the [M]                          |
| $\beta$       | Damping coefficient for the [K]                          |
| $\omega$      | Angular frequency  |
| $\gamma$      | Shear strain   |
| $\gamma_r$    | Pseudo-reference strain                                  |
| $\varepsilon$ | Residual   |
| $\theta$      | Angle of incidence of waves                              |
| $\lambda$     | Wavelength   |
| $\Delta L$    | Size of an element                                       |
| $a(t)$        | Acceleration time series                                 |
| [C]           | Damping matrix   |
| C             | Fourier amplitude coefficients                           |
| D             | Duration   |
| $D_{\min}$    | Damping ratio  |
| $D_i$         | Critical damping ratio                                   |
| $d_i$         | Thickness of a layer                                     |
| $d(t)$        | Displacement time series                                 |
| $D_{5-75}$    | Significant duration corresponding to 5 to 75 % of $I_a$ |

|                 |  |
|-----------------|--|
| $D_{5-95}$      | Significant duration corresponding to 5 to 95 % of $I_a$ |
| E               | Young's modulus  |
| f               | Frequency  |
| $f_{\max}$      | Highest frequency component of the input wave            |
| $F_1$           | Motion scaling factor                                    |
| $F_2$           | Second scaling factor                                    |
| $f_c$           | Motion center frequency                                  |
| $f_{\min}$      | Center frequency of Rayleigh damping                     |
| F(T)            | Period-dependent site factors                            |
| G               | Secant shear modulus                                     |
| $G_{\max}$      | Stiffness  |
| H               | Horizontal direction of the motion                       |
| $H_m$           | Height of the model                                      |
| $I_a$           | Arias intensity  |
| k               | Hydraulic conductivity                                   |
| K               | Bulk modulus   |
| $K_1$           | Adjustment factor for the input stress                   |
| [K]             | Stiffness damping matrix                                 |
| $(K_2)_{\max}$  | Maximum soil modulus coefficient                         |
| M               | Magnitude  |
| [M]             | Mass damping matrix                                      |
| n               | Porosity   |
| N               | N indices of SPT test                                    |
| $(N_1)_{60}$    | N indices of SPT test corrected for an energy of 60 %    |
| $N_{\text{eq}}$ | Equivalent number of stress cycles                       |
| $P_a$           | Atmospheric pressure                                     |
| R               | Site-to-source distance                                  |
| $r_u$           | Excess pore pressure                                     |
| $S_a$           | Spectral acceleration value                              |
| $S_a(T_0)$      | Spectral acceleration at fundamental period              |
| $S_a(1.5T_0)$   | Spectral acceleration at the degraded fundamental period |

|                     |  |
|---------------------|--|
| SF                  | Factor of safety against liquefaction                              |
| $S_g$               | Motion response spectrum   |
| SIR <sub>5-75</sub> | Shaking intensity rate between 5 to 75 % of $I_a$                  |
| SIR <sub>5-95</sub> | Shaking intensity rate between 5 to 75 % of $I_a$                  |
| S(T)                | Design spectrum  |
| $S_T(T)$            | Target design spectrum   |
| $S_{Ti}$            | Scenario-specific target spectrum                                  |
| $S_u$               | Cohesion   |
| t                   | Time   |
| $T_m$               | Mean period  |
| $T_0$               | Fundamental period   |
| $T_R$               | Period range   |
| $T_{RS}$            | Scenario-specific period range                                     |
| $V_s$               | Shear wave speed   |
| $V_{s1}$            | Normalized $V_s$ for 100 kPa                                       |
| $V_{s30}$           | Shear wave speed in the uppermost 30 m of soils                    |
| $V_{a1\_eq}$        | Equivalent and normalized to 100 kPa shear wave speed of the layer |
| v(t)                | Velocity time series   |

### List of abbreviations

|                    |  |
|--------------------|--|
| CAV                | Cumulative absolute velocity   |
| CAV <sub>5</sub>   | Cumulative absolute velocity with 5 cm/s <sup>2</sup> threshold acceleration |
| CAV <sub>std</sub> | Standardized cumulative absolute velocity                                    |
| CSR                | Cyclic stress ratio  |
| CRR                | Cyclic resistance ratio  |
| DM                 | Damage measure   |
| ENA                | Eastern North America  |
| FAS                | Fourier amplitude spectrum   |
| GMM                | Ground motion model  |
| HC                 | High-cut frequency corner  |

|       |  |
|-------|--|
| LC    | Low-cut frequency corner                     |
| IM    | Intensity measure                            |
| MASW  | Multichannel analysis surface wave           |
| MASWW | Modal analysis surface wave                  |
| MKZ   | Pressure-dependent hyperbolic model          |
| MRD   | Modulus reduction and damping                |
| NBCC  | National Building Code of Canada             |
| NEHRP | National earthquake hazard reduction program |
| OCR   | Overconsolidated ratio                       |
| PGA   | Peak ground acceleration                     |
| PSA   | Pseudo-spectral acceleration                 |
| PGD   | Peak ground displacement                     |
| PSD   | Pseudo-spectral displacement                 |
| PGV   | Peak ground velocity                         |
| PSV   | Pseudo-spectral velocity                     |
| PI    | Plasticity index                             |
| RMSA  | Root mean square acceleration                |
| RSN   | Record sequence number                       |
| RQD   | Rock quality designation                     |
| SDOF  | Single-degree-of-freedom                     |
| SI    | Spectrum intensity                           |
| SPT   | Standard penetration test                    |
| SSI   | Soil-structure interaction                   |
| TF    | Transfer function                            |
| UHS   | Uniform hazard spectrum                      |
| USCS  | Unified soil classification system           |

**LIST OF APPENDICES**

|            |   |     |
|------------|---|-----|
| Appendix A | Details of the selected, processed and scaled input ground motions.....   | 177 |
| Appendix B | Borehole reports.....   | 215 |
| Appendix C | Details of the calculation for the evaluation of the liquefaction potential of the foundation soils using simplified methods..... | 224 |

## CHAPTER 1 INTRODUCTION

### 1.1 Context

Earth dikes are water retention structures of usually short height. Dikes are generally built as a protection against flooding. Most embankments are not built directly on the rock, but often on a soft soil deposit, sometimes of weak consistency and, as a result, dikes might be more vulnerable to instability especially caused by cyclic loading. The failure of a dike may lead to important damages to infrastructures and the environment. Despite the extensive damage they may cause, little emphasis in research has been given to the seismic stability of water retaining earth dikes in the past, especially in the *ENA*. Therefore, this project will focus on the performance of an earth dike in *ENA* against seismic loading.

In practice, the seismic design of a dike can be based on multiple types of analysis of different levels of complexity, from the simpler ones, such as the pseudo-static analysis, to more complex ones such as nonlinear deformation analyses. The latter require the selection of seismic scenarios representative of the seismicity of the region, i.e. the seismic hazard, for a given period range of interest, based on a deaggregation analysis. Then, for each selected scenario, a minimum number of ground motions are to be selected to run dynamic simulations. Thus, the selection of seismic scenarios is a crucial step, because it directly influences the selection of input ground motions and the results of simulations, but it is often overlooked. Hence, this thesis will focus on the impact of seismic hazard on the performance of an earth dike in the *ENA*, and will aim at assessing the influence of each selected scenario on the results of numerical simulations.

A secondary aspect of the study is the use of alternative intensity measures to characterize seismic hazard. In practice, the selection of input motions is solely based on the correspondence between the shape of a motion spectrum with the target spectrum, within the period range considered. However, the response spectrum does not capture the effects of many intensity measures (*IM*), such as duration and cumulative effects. Some *IM* might be more efficient in predicting damage measures (*DM*) than the response spectrum. Considering them during the selection process may reduce the variability of the input motions and thus reduce the uncertainty associated with the results obtained. In this way, this thesis also focuses on the ability of predicting *DM* based on *IM*

with the objective to offer insight on which *IM* may be more efficient to serve as a basis during the selection of input motions.

## 1.2 Objectives of this thesis

The main objectives of this thesis are 1- to evaluate the impact of seismic scenarios on the response of an earth dike using nonlinear 2D dynamic simulations and 2- to find candidate *IM* capable of predicting *DM* to reduce the uncertainty associated to the selection of input motions. That may be summarized into the following questions:

- What would be the difference in terms of seismic response of the dike between scenarios?
- Are there potential candidate *IM* capable of predicting the *DM* of an earth dike ?

To meet the main objectives of the project, below is a list of secondary objectives:

- Define seismic scenarios over the entire spectrum (0.01 to 10 s) based on the seismic hazard deaggregation analysis of Montreal and select associated input motions.
- Assess the differences between the selected motions between each scenario. Evaluate the differences in terms of *IM*.
- Study the seismic response of the model between scenarios based on nonlinear dynamic 2D analyses:
  - Compare the *IM* on the surface of the model;
  - Compare the level of amplification due to soil conditions and topographic effects in terms of *IM* characterizing the amplitude, duration and/or frequency content of response motions;
  - Compare the level of soils degradation in the model
  - Compare the potential of liquefaction
- Assess the efficiency of candidate *IM* in the prediction of *DM* with a parametric study.

## 1.3 Methodology

Below is a summary of the main steps followed to meet the objectives of the thesis and how they fit within the organization of said thesis:

- Chapter 3: Define the seismic scenarios characterizing the seismic hazard over the entire spectrum defined by the NBCC 2015 (0.01 to 10 s) based on the deaggregation of Montreal.
- Chapters 3 and 4: For each scenario, select input ground motions that match the target spectrum inside the scenario-specific period range. Process and scale selected input motions to enhance the match with the target spectrum.
- Chapter 5: Define the geotechnical parameters and geometry of the earth dike based on geotechnical studies. To account for spatial variability of existing soil conditions:
  - Select multiple cross-sections of varying soil conditions and;
  - Perform 1D nonlinear simulations on DEEPSOIL to identify the cross-section returning the highest crest acceleration. This cross-section is then used in 2D analyses.
- Chapter 6: Build the numerical model in FLAC.
- Chapter 6: Validate the behavior of the model using linear damped dynamic simulations in terms of the level of strains and the location of the boundaries.
- Chapters 6 and 7: Run fully nonlinear dynamic analyses.
- Chapter 7: Compare the response of the model between scenarios.
- Chapter 7: Perform a parametric study to evaluate the efficiency of candidate *IM* in the prediction of *DM*.

## 1.4 Content of the thesis

This thesis is separated into 8 chapters including the introduction and conclusion.

- Chapter 2: presents a literature review of the soil models used, the concept of nonlinearity, the parameters used to characterize motions and the topographic effects.

- Chapter 3: presents the target response spectrum, the selection of seismic scenarios and input ground motions based on selection criteria followed by the scaling method. Compatibility issues of selected input motions with the hazard spectrum are also discussed, before presenting the *IM* characterizing the input motions.
- Chapter 4: presents the method of ground motion processing and parameters used in filtering.
- Chapter 5: focuses on the embankment and presents the geometry of the dike, the selection of geotechnical parameters as well as the dynamic modulus reduction and damping curves (*MRD*). The liquefaction potential of the subsoil is also evaluated. Then, the steps leading to the selection of a cross-section of the embankment are presented.
- Chapter 6: presents the construction of the 2D numerical model. The initial state of stress is presented following by the static slope stability and the validation of the model using linear damped dynamic simulations.
- Chapter 7: presents and discusses the results of 2D nonlinear simulations
- Chapter 8: presents the conclusion.

## CHAPTER 2 LITERATURE REVIEW

### 2.1 Review of basic soil behavior

#### 2.1.1 Mohr-Coulomb model

The Mohr-Coulomb failure criterion is a linear strength envelope as shown in figure 2.1, separating the plastic and linear domain, and used to model the soil behavior. The envelope is constructed by drawing a line tangent to Mohr circles at failure, showing shear stresses ( $\tau$ ) against normal stresses ( $\sigma$ ), obtained from laboratory test results.

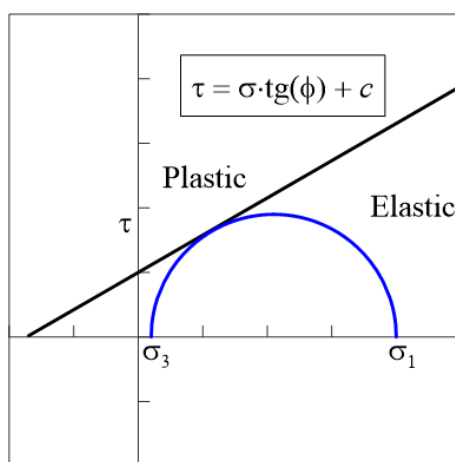
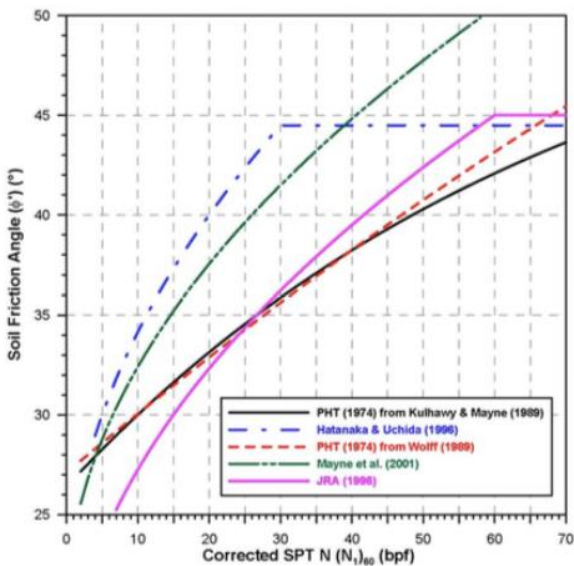


Figure 2.1 Mohr-Coulomb failure criterion

The failure criterion can be calculated with equation 2.1 where  $\phi$  is the friction angle and  $c$  the cohesion.

$$\tau = \sigma \cdot \operatorname{tg}(\phi) + c \quad \text{Eq. 2.1}$$

The friction angle ( $\phi$ ) is directly correlated with the density of the soil and, in the absence of laboratory tests, can be computed from the results of field tests, such as a standard penetration test (*SPT*), using empirical relationships. The  $N$  indices measured during *SPT* tests are corrected for the energy ratio, overburden pressure, and the equipment used. Several correlations exist to obtain the  $\phi$  based on the corrected indices  $(N_1)_{60}$  and some are illustrated in figure 2.2. The cohesion  $c$  is 0 for non-plastic soils, and can be obtained using a vane shear test on the field for plastic soils. For purely cohesive soils, the term undrained shear strength  $S_u$  is commonly used instead of cohesion.



| Equation   | Reference  |
|--|--|
| $\phi' = 54^\circ - 27.6034 \cdot \exp(-0.014(N_1)_{60})$                                  | Peck, Hanson, & Thorton (1974) from Kulhawy & Mayne (1990) |
| $\phi' = [20 \cdot (N_1)_{60}]^{0.5} + 20^\circ$<br>for $3.5 \leq (N_1)_{60} \leq 30$      | Hatanaka & Uchida (1996)                                   |
| $\phi' = 27.1^\circ + 0.3 \cdot (N_1)_{60} - 0.00054(N_1)_{60}^2$                          | Peck, Hanson, & Thorton (1974) from Wolff (1989)           |
| $\phi' = [15.4(N_1)_{60}]^{0.5} + 20^\circ$  | Mayne et al. (2001) based on Hatanaka & Uchida (1996)      |
| $\phi' = [15(N_1)_{60}]^{0.5} + 15^\circ$<br>for $(N_1)_{60} > 5$ and $\phi \leq 45^\circ$ | JRA (1996)   |

Figure 2.2 Correlations of  $\phi$  based on  $(N_1)_{60}$  retrieved from NCHRP (2010)

The correlation developed by Wolff (1989) based on the work by Peck et al. (1974) is used in this project (equation 2.2.).

$$\phi' = 27.1 + 0.3(N_1)_{60} - 0.00054(N_1)_{60}^2 \quad \text{Eq. 2.2}$$

### 2.1.2 Stiffness parameters

The shear-wave velocity ( $V_s$ ) is a key parameter for the dynamic analysis of soil deposits. It is representative of the stiffness of the medium, and is related to the stiffness ( $G_{max}$ ), with equation 2.3 where  $\rho$  is the soil density.

$$G_{max} = \rho V_s^2 \quad \text{Eq. 2.3}$$

$V_s$  might be obtained using either:

- field tests such as multichannel analysis surface wave (*MASW*), or the modal analysis surface wave (*MMASW*) (Karray, 2010)
- Laboratory tests equipped with shear wave velocity measurement devices such as bender elements,

- Or correlations based on other tests such as *SPT* tests.

The  $G_{max}$  for cohesionless soils can be calculated based on  $N$  indices with equation 2.4 **Error! Reference source not found.** suggested by Seed and Idriss (1970).  $\sigma'_m$  is the mean effective stress in kPa and the  $(K_2)_{max}$  is the maximum soil modulus coefficient. The  $(K_2)_{max}$  is mainly affected by the density of the soil and the grain size of soil particles (Seed et al., 1986). Equation 2.5 can be used to calculate  $(K_2)_{max}$  for sands. The  $G_{max}$  obtained is in kPa.

$$G_{max} = 4570(K_2)_{max}(\sigma'_m)^{1/2} \quad \text{Eq. 2.4}$$

$$(K_2)_{max} \cong 20(N_1)_{60}^{1/3} \quad \text{Eq. 2.5}$$

Ranges of  $(K_2)_{max}$  suggested by Seed et al. (1986) are provided in table 2.1 for sandy and gravelly soils.

Table 2.1 Ranges of  $(K_2)_{max}$

| Materials                      | $(K_2)_{max}$ |
|--------------------------------|---------------|
| Very loose to very dense sands | 30 – 75       |
| Dense to very dense gravels    | 80 – 180      |

The bulk modulus ( $K$ ) describes the stiffness of the soil against isotropic compression.  $K$  can be calculated with equation 2.6 where  $\mu$  is the Poisson ratio and  $E$  is the Young's modulus. The latter is calculated with equation 2.7.

$$K = \frac{E}{3(1 - 2\mu)} \quad \text{Eq. 2.6}$$

$$E = 2G_{max}(1 + \mu) \quad \text{Eq. 2.7}$$

Upon cyclic loading, the shear modulus of the soil can degrade, and the relationship between the degradation of the secant shear modulus  $G$  and the shear strain is described by a modulus reduction curve. Soils nonlinearity are further described in section 2.2.

## 2.2 Dynamic behavior of soil

Soils are highly nonlinear when subjected to cyclic loading and might exhibit a reduction in stiffness. In this section, a review of the nonlinear and hysteretic behavior of the soil is provided, and a discussion on the modeling of such phenomena is presented. After that, the modulus reduction and damping curves developed by Darendeli (2001) are described.

### 2.2.1 Hysteretic behavior

The dynamic behavior of soils is highly nonlinear even at small strains (Hashash et al., 2010). Nonlinearity may result in soil degradation leading to a reduction in  $G$  and an increase in soil damping. The  $G$  represents the secant shear modulus, of the shear stress ( $\tau$ ) and the shear strain ( $\gamma$ ) curve as shown in figure 2.3. This curve is also referred to as the backbone curve. The  $G_{max}$  is the initial shear stiffness of the soil at  $\gamma = 0\%$ .

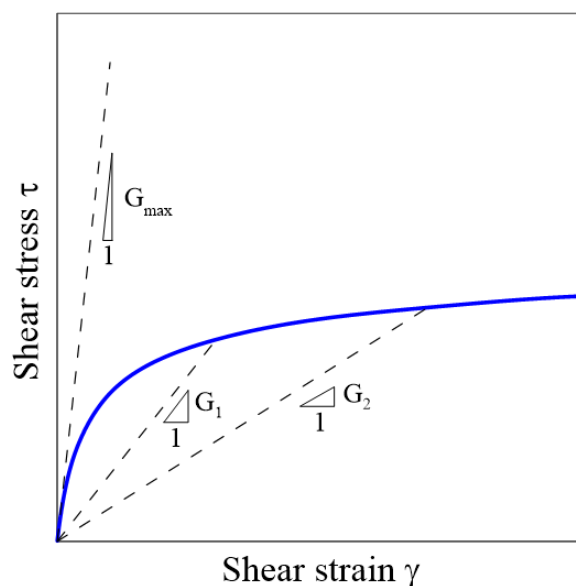


Figure 2.3 Illustration of a typical backbone curve

The modulus reduction curve  $G/G_{max}$  can be obtained from the backbone curve and the hysteretic damping curve is obtained based on computing the area of an unloading-reloading loop at a given strain level. The damping ratio is proportional to the area of a loading loop as illustrated in figure 2.4. An example of  $G/G_{max}$  and damping ratio curves are presented in figure 2.5.

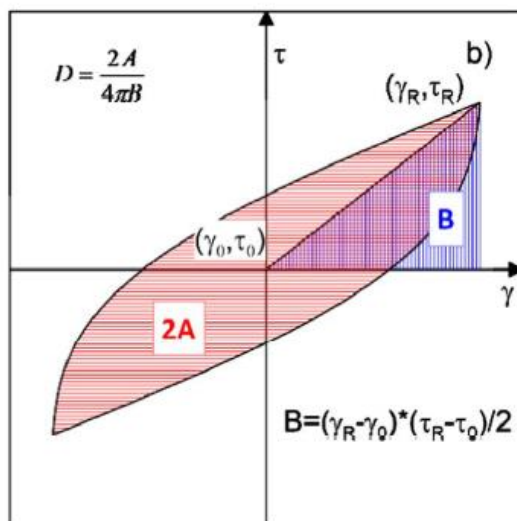


Figure 2.4 Damping ratio obtained from a loading loop, retrieved from Yniesta et al. (2017)

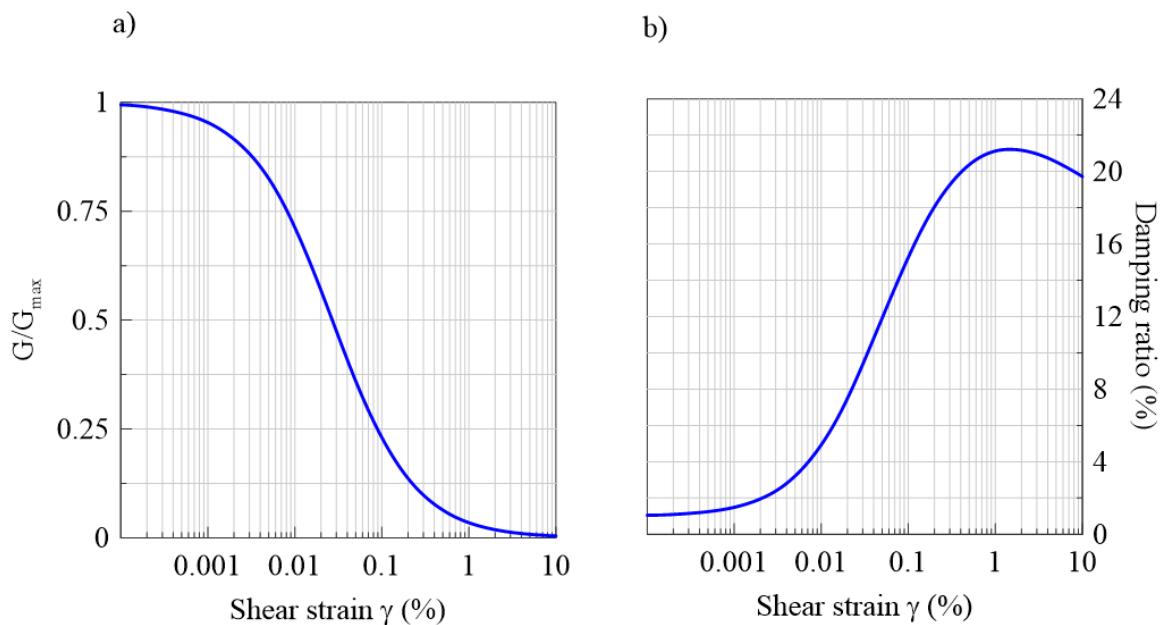


Figure 2.5 Illustration of a typical modulus reduction and damping curve (those presented are calculated with Darendeli (2001) for the core of the dike)

## 2.2.2 Masing rules

Masing (1926) proposed a simplified hysteretic model commonly called “Masing rules” to define the stress-strain soil behavior upon cyclic loading. Vucetic (1990) has proposed the extended Masing rules adding 2 rules (3 and 4) to the existing Masing rules. The extended Masing rules are listed below and illustrated in figure 2.6.

- 1- During initial loading, the stress-strain curve follows the backbone curve;
- 2- The reloading curve starts with a shape identical to the shape of the positive initial loading backbone curve enlarged by a factor of 2. The same applies to the unloading curve.
- 3- If the unloading or reloading curve exceeds the maximum past strain and intersects the backbone curve, it follows the backbone curve until the next stress reversal;
- 4- If the unloading or reloading curve crosses an unloading or reloading curve from a previous cycle, it follows the curve of that previous cycle.

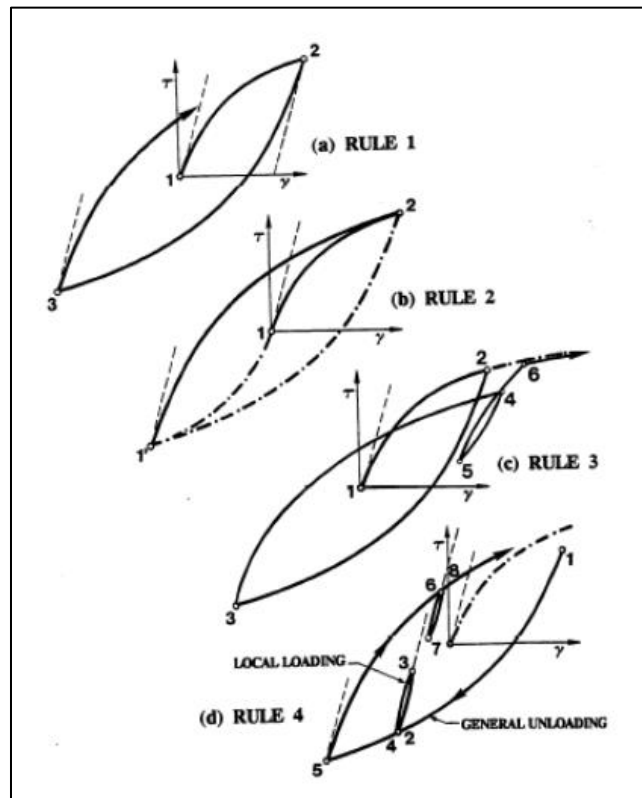


Figure 2.6 Extended Masing rules (Vucetic, 1990), retrieved from Kammerer et al. (2018)

The extended Masing rules have essentially 2 shortcomings:

- 1- although the Masing-type of unloading and reloading adequately captures the hysteretic behavior of soils at moderate strains, it overestimates the hysteretic damping at large strains as the hysteretic loops are too large (Kwok et al., 2007);
- 2- the damping at small strains is 0 because the backbone curve is linear; the zero damping condition is incompatible with the laboratory tests results at small strains (e.g. Lanzo et al., 1997; Vucetic et al., 1998). Many models have been proposed to overcome these limitations, but they typically build upon the framework introduced by Masing.

## 2.2.3 Modulus reduction and damping

Soil degradation upon cyclic loading can be described by a reduction of  $G$  and an increase in damping. In soil and rock, damping is mainly hysteretic, thus independent of the frequency, and nonlinear even at small strains (Hashash et al., 2010). However, for numerical purposes, small strain damping is often modelled using frequency-dependent Rayleigh damping (Itasca, 2016). In this project, modulus reduction and damping curves ( $MRD$ ) computed from the formulation developed by Darendeli (2001) are used. In addition, viscous damping is added to the model to introduce damping at small strains. Both viscous and hysteretic damping formulation are presented below.

### 2.2.3.1 Viscous damping

*FLAC* uses the original expression proposed by Rayleigh and Lindsay (1945), in which, the damping matrix results from the addition of 2 matrices; one is proportional to the mass matrix and the other one is proportional to the stiffness matrix as resumed in equation 2.8.

$$[C] = \alpha[M] + \beta[K] \quad \text{Eq. 2.8}$$

where  $[C]$  is the damping matrix,  $[M]$  the mass damping matrix,  $[K]$  the stiffness damping matrix and  $\alpha$  and  $\beta$  are the associated coefficients.

Rayleigh damping as a function of frequency is shown in figure 2.7. As observed, the system is overdamped by the formulation at high and low frequencies; the damping is correct only at the center frequency ( $f_{min}$ ) where  $D_i/D_{min} = 1$ . Also, on either side of the  $f_{min}$ , a plateau of frequencies is observed where it might be said that the damping is frequency-independent.

Hence, the  $f_{min}$  is chosen such that the frequencies of interest are located inside the plateau to avoid overdamping. Usually, the  $f_{min}$  is chosen equal to the natural frequency of the model, the input motion center frequency ( $f_c$ ) or a combination of both.

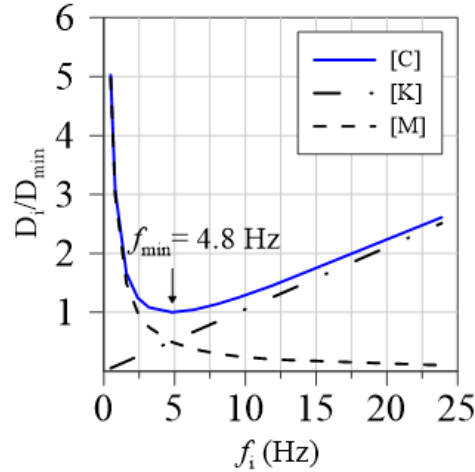


Figure 2.7 Example of viscous Rayleigh damping with  $f_{min} = 4.8$  Hz

In this project, the input motion center frequency is chosen as the  $f_{min}$  and is calculated with the equation 2.9 where  $T_m$  is the mean period defined by Rathje et al. (1998, 2004).

$$f_{min} = \frac{1}{T_m} \quad \text{Eq. 2.9}$$

The damping ratio ( $D_{min}$ ) must be defined by the user and the value depends on the type of soil. The user might select literature values to define  $D_{min}$ . The critical damping ratio ( $D_i$ ) is calculated with equation 2.10.

$$D_i = \frac{1}{2} \left( \frac{\alpha}{\omega_i} + \beta \omega_i \right) \quad \text{Eq. 2.10}$$

where  $\omega_i$  is the angular frequency and

$$\alpha = D_{min} \omega_{min} \quad \text{Eq. 2.11}$$

$$\beta = \frac{D_{min}}{\omega_{min}} \quad \text{Eq. 2.12}$$

$$\omega_{min} = 2\pi \cdot f \quad \text{Eq. 2.13}$$

### 2.2.3.2 Modulus Reduction and Damping Ratio Curves

Modulus reduction and damping curves plot  $G/G_{max}$  and  $D_i$  against the shear strain  $\gamma$ . The *MRD* curves used in this project follow the empirical relationships developed by Darendeli (2001). Darendeli defines the backbone curve based on the hyperbolic model developed by Hardin and Drnevich (1972), computes Masing damping, and adds a correction to the damping at small and large strains to enhance compatibility with the results from laboratories.

Figure 2.8 presents typical *MRD* curves of Darendeli.

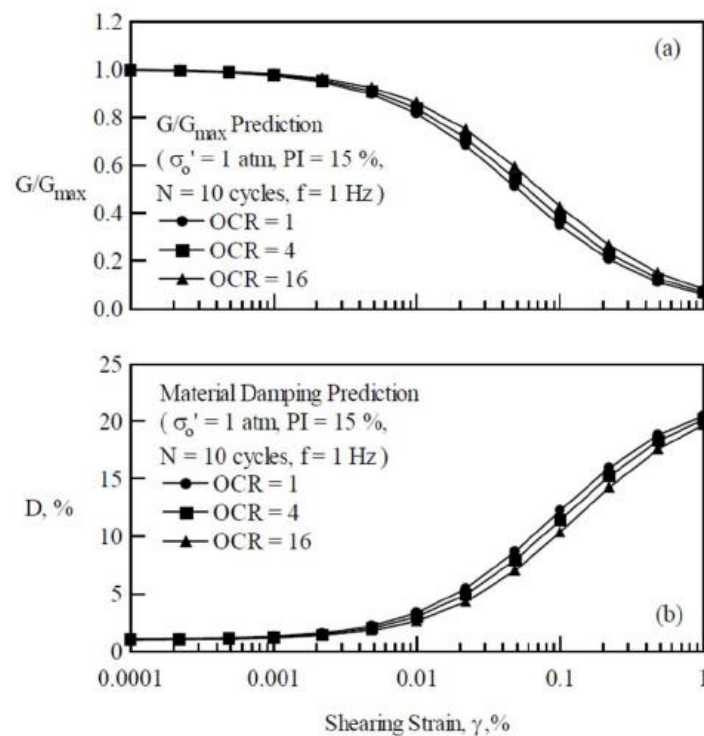


Figure 2.8 Illustration of typical a) modulus curves and b) damping curves for clayey soils developed by Darendeli. Retrieved from Darendeli (2001)

However, as the model is based on empirical data, the dataset is limited for strains ranging from 0.00001 % to less than 1 % and thus is not intended to be used for high strains.

## 2.2.4 Liquefaction

Liquefaction is defined as a loss of strength of a granular soil resulting from a change of state from a solid to a liquefied state as a consequence of an increased pore-water pressure which consequently reduces the effective stress. Three (3) conditions must be met to satisfy susceptibility to liquefaction:

- Full or nearly full saturation
- Contractive soil
- Rapid loading

A soil with poor drainage increases its susceptibility to liquefaction because the high rate of cyclic loading does not allow for drainage. Consequently, the pore pressure will increase in the soil matrix followed by the reduction of the effective stress. When the effective stresses of the soil reach 0, the soil liquefies.

During liquefaction, soils will soften leading to large cyclic deformations. Liquefaction is most likely to occur in a loose to moderately compact granular soil rather than in a dense soil. Post liquefaction, loose soils will tend to compact while moderately compact materials would tend to loosen. This is called reconsolidation.

The factor of safety against liquefaction may be calculated with equation 2.14 that compares the resistance to liquefaction to forces triggering liquefaction.

$$FS = \frac{CRR}{CSR} \quad \text{Eq. 2.14}$$

where *CRR* is the cyclic resistance ratio and *CSR* the cyclic stress ratio. The *CRR* and *CSR* may be calculated based on the procedure described in Boulanger and Idriss (2014).

The *CRR* may be evaluated based on empirical curves. Those curves are developed based on liquefied and non-liquefied case histories. On the other hand, the *CSR* is based on hazard analysis and hence is directly correlated with the seismic demand. In fact, the *CSR* is the ratio between the shear stress representative of the earthquake and the effective overburden stress.

### 2.2.5 Seismic site classification

Soil conditions have an important effect on the amplitude of seismic waves arriving at the surface. Simplified site response characterization relies on the definition of seismic classes and the application of class-specific amplification factors. Hence, the *NBCC 2015* has specified 5 different soil classes based on soil conditions: A, B, C, D and E. An additional soil class F represents soils vulnerable to potential failure such as liquefiable soils, which require site-specific geotechnical investigations and dynamic site response analyses. The classification is based on the soil conditions in the uppermost 30 m represented by either the average  $V_s$ ,  $(N_I)_{60}$  or the  $S_u$ . The soil conditions may be evaluated with equation 2.15 as follows:

$$X = \frac{30}{\sum_i^n d_i / X_i} \quad \text{Eq. 2.15}$$

where  $n$  is the total number of layers,  $d_i$  the thickness of the layer, and  $X$  the soil property ( $V_s$ ,  $(N_I)_{60}$  or  $S_u$ ) representing that layer. The definition of site classes is provided in table 2.2 and was initially adopted by NERHP (1994).

The soil class C is generally considered as the reference soil condition as the spectral acceleration values ( $S_a$ ) provided by the *NBCC 2015* are given for this soil class. Spectral acceleration values for other soil classes must be modified with period-dependent site factors  $F(T)$  provided by Finn and Wightman (2003) for *NBCC 2015*. The  $F(T)$  are presented in table 2.3.

Table 2.2 Soil classification suggested by *NBCC 2015* (NEHRP, 1994)

| Soil classes | Soil class name              | Soil conditions in the top 30 m   |                              |                        |
|--------------|------------------------------|---|------------------------------|------------------------|
|              |                              | $V_s$   | $(N_1)_{60}$                 | $S_u$                  |
| A            | Hard rock                    | $V_s > 1500$  | N.A.                         | N.A.                   |
| B            | Rock                         | $760 < V_s \leq 1500$   | N.A.                         | N.A.                   |
| C            | Very dense soil or soft rock | $360 < V_s \leq 760$  | $(N_1)_{60} > 50$            | $S_u > 100$            |
| D            | Stiff soil                   | $180 < V_s \leq 360$  | $15 \leq (N_1)_{60} \leq 50$ | $50 \leq S_u \leq 100$ |
| E            | Soil profile with soft clay  | $V_s < 180$   | $(N_1)_{60} < 15$            | $S_u < 50$             |
|              |                              | Soil profile of minimum 3 m thickness with all the following characteristics: <ul style="list-style-type: none"> <li>- <math>V_s &lt; 180</math> m/s</li> <li>- Plasticity index <math>&gt; 20</math></li> <li>- Water content <math>&gt; 40</math> %</li> <li>- <math>S_u &lt; 25</math> kPa</li> </ul>  |                              |                        |
| F            | Other                        | Site-specific geotechnical investigations and dynamic site response analyses required for: <ul style="list-style-type: none"> <li>- Soils vulnerable to potential failure or collapse under seismic loading (liquefiable soils, quick and highly sensitive clays, collapsible weakly cemented soils, etc.)</li> <li>- Peats and/or highly organic clays (more than 3 m thickness of peat)</li> <li>- Very high plasticity clays (more than 8 m thickness with plasticity index <math>&gt; 75</math>)</li> <li>- Very thick soft to medium-stiff clays (more than 36 m thickness)</li> </ul> |                              |                        |

Table 2.3 Period-dependent site factors  $F(T)$  (Finn and Wightman, 2003), retrieved from Humar (2015)

|                     | Site Class | $PGA_{ref} \leq 0.1$ | $PGA_{ref} = 0.20$ | $PGA_{ref} = 0.30$ | $PGA_{ref} = 0.40$ | $PGA_{ref} \geq 0.50$ |
|---------------------|------------|----------------------|--------------------|--------------------|--------------------|-----------------------|
| Values of $F(0.2)$  | A          | 0.69                 | 0.69               | 0.69               | 0.69               | 0.69                  |
|                     | B          | 0.77                 | 0.77               | 0.77               | 0.77               | 0.77                  |
|                     | C          | 1.00                 | 1.00               | 1.00               | 1.00               | 1.00                  |
|                     | D          | 1.24                 | 1.09               | 1.00               | 0.94               | 0.90                  |
|                     | E          | 1.64                 | 1.24               | 1.05               | 0.93               | 0.85                  |
| Values of $F(0.5)$  | A          | 0.57                 | 0.57               | 0.57               | 0.57               | 0.57                  |
|                     | B          | 0.65                 | 0.65               | 0.65               | 0.65               | 0.65                  |
|                     | C          | 1.00                 | 1.00               | 1.00               | 1.00               | 1.00                  |
|                     | D          | 1.47                 | 1.30               | 1.20               | 1.14               | 1.10                  |
|                     | E          | 2.47                 | 1.80               | 1.48               | 1.30               | 1.17                  |
| Values of $F(1.0)$  | A          | 0.57                 | 0.57               | 0.57               | 0.57               | 0.57                  |
|                     | B          | 0.63                 | 0.63               | 0.63               | 0.63               | 0.63                  |
|                     | C          | 1.00                 | 1.00               | 1.00               | 1.00               | 1.00                  |
|                     | D          | 1.55                 | 1.39               | 1.31               | 1.25               | 1.21                  |
|                     | E          | 2.81                 | 2.08               | 1.74               | 1.53               | 1.39                  |
| Values of $F(2.0)$  | A          | 0.58                 | 0.58               | 0.58               | 0.58               | 0.58                  |
|                     | B          | 0.63                 | 0.63               | 0.63               | 0.63               | 0.63                  |
|                     | C          | 1.00                 | 1.00               | 1.00               | 1.00               | 1.00                  |
|                     | D          | 1.57                 | 1.44               | 1.36               | 1.31               | 1.27                  |
|                     | E          | 2.90                 | 2.24               | 1.92               | 1.72               | 1.58                  |
| Values of $F(5.0)$  | A          | 0.61                 | 0.61               | 0.61               | 0.61               | 0.61                  |
|                     | B          | 0.64                 | 0.64               | 0.64               | 0.64               | 0.64                  |
|                     | C          | 1.00                 | 1.00               | 1.00               | 1.00               | 1.00                  |
|                     | D          | 1.58                 | 1.48               | 1.41               | 1.37               | 1.34                  |
|                     | E          | 2.93                 | 2.40               | 2.14               | 1.96               | 1.84                  |
| Values of $F(10.0)$ | A          | 0.67                 | 0.67               | 0.67               | 0.67               | 0.67                  |
|                     | B          | 0.69                 | 0.69               | 0.69               | 0.69               | 0.69                  |
|                     | C          | 1.00                 | 1.00               | 1.00               | 1.00               | 1.00                  |
|                     | D          | 1.49                 | 1.41               | 1.37               | 1.34               | 1.31                  |
|                     | E          | 2.52                 | 2.18               | 2.00               | 1.88               | 1.79                  |

## 2.2.6 Natural modes

Natural modes are important in seismic engineering because when the natural periods of a structure match the predominant frequency of an earthquake, resonance may happen, and the structure may experience heavier damage. The first mode, also called the fundamental period  $T_0$  corresponds to the period at which the system tends to oscillate. It is also called the natural period and it corresponds to the 1<sup>st</sup> mode of vibration of the system.

## 2.3 Ground motion characteristics

### 2.3.1 Seismic waves

There are essentially two types of seismic waves: 1- body waves and 2- surface waves. Both types of waves propagate differently. Body waves propagate through a media such as soils and rock while surface waves propagate along the surface of a media or an interface of different medias. Body waves are of higher frequency than surface waves.

Body waves are of 2 types: 1- primary waves (P-waves) and 2- secondary waves (S-wave, also called shear-waves). P-waves are also called compressional waves and are the fastest waves. P-waves can propagate through soils, liquids and gases. They are generally the first type of waves to be recorded during an earthquake. S-waves are the second type of waves to arrive at a seismic recording station. Unlike the P-waves, S-waves cannot travel through liquids and gases. S-waves shake the media in 2 directions: out-of-plane (SH-waves) and in-plane (SV-waves). When SV-waves hit an interface such as the surface or the interface between 2 contrasting medias, diffraction occurs and as a result, SV-waves generate additional wave type: the surface waves. Surface waves are of 2 types: 1- Love-waves and 2- Rayleigh-waves. Most of the damage caused during an earthquake are caused by surface waves (Michigan Technological University, 2020).

### 2.3.2 Ground motion characterization

Ground motion parameters studied in this project are presented in this section. For seismic engineering, the most important characteristics of a strong motion are 1- the frequency content, 2- the amplitude and 3- the duration of the motion (Kramer, 1996). These characteristics have a significant influence on earthquake damage. Therefore, to describe a ground motion, parameters are defined to measure the 3 characteristics. Each parameter describes the amplitude, the frequency content, the duration or describes a combination of multiple characteristics.

Finally, a section is dedicated to quality metrics. Earthquake intensity measures *IM* are key parameters in the prediction of earthquake damage. Knowledge and use of an optimum *IM* during the selection and scaling of ground motions will help reduce uncertainties and as a result will allow to use a reduced number of motions in an analysis for the same level of confidence.

### 2.3.2.1 Frequency content parameters

The frequency content is an important topic in seismic engineering because it has an important influence on the seismic response. A structure submitted to an earthquake motion with a frequency content that matches its natural periods would sustain an amplified response. Thus it is important to characterize a ground motion with consideration of its frequency content. A ground motion can be defined in the frequency domain by decomposing the motion into a sum of sinusoidal functions using a Fourier transform. The frequency content of ground motions can be described through the use of different spectra such as the Fourier spectrum and the response spectrum.

It may also be useful to characterize motions frequency content using a single parameter. Several parameters were proposed throughout the years and for this project, the  $T_0$  and the mean period  $T_m$  will be used and described in this section. Although the predominant period ( $T_p$ ) is a widely used parameter because it is easy to obtain (period associated with the maximum  $S_a$ ), its use has been discouraged and hence not used in this project. This parameter is unstable and does not adequately characterize the motion frequency content (Rathje et al., 1998).

#### 2.3.2.1.1 Fourier series and spectrum

A ground motion can be defined in the frequency domain by expressing the motion as the Fourier series. The Fourier series is the sum of sinusoidal harmonic series as presented in equation 2.16.

$$x(t) = c_0 + \sum_{n=1}^{\infty} c_n \sin(\omega_n t + \phi_n) \quad \text{Eq. 2.16}$$

where  $n$  is the  $n$ th harmonic of the Fourier series,  $\omega$  is the angular frequency,  $c$  is the Fourier amplitude and  $\phi$  the phase angle. Both amplitude and phase can be plotted against frequency. The ground motion in the temporal domain can be recovered by the inverse Fourier transform. The Fourier amplitude spectrum is generally called the Fourier spectrum and is a plot of  $c$  against frequency or period, generally plotted using a logarithmic scale. This spectrum clearly shows the frequency content of a ground motion thus making the process of its characterization easier. An example of a Fourier amplitude spectrum is shown in figure 2.9 where a motion is processed and high and low frequencies are filtered out. The motion was processed with a low cut frequency corner ( $LC$ ) of 0.7 Hz and a high-cut frequency corner ( $HC$ ) of 20 Hz. Thus, the motion is defined

accurately in the moderate frequency range between 0.7 and 20 Hz and the Fourier spectrum clearly shows the frequency content.

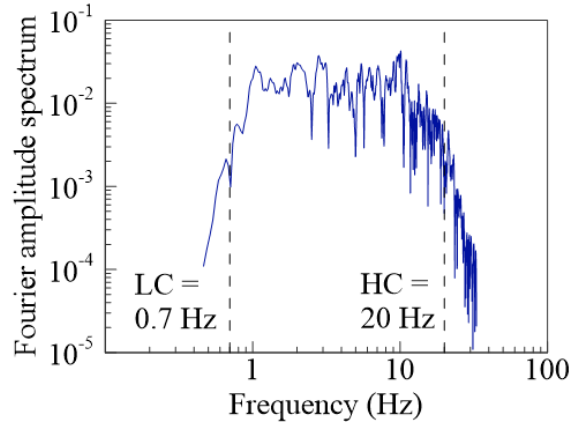


Figure 2.9 Illustration of a typical Fourier amplitude spectrum processed using a *LC* of 0.7 Hz and *HC* of 20 Hz (earthquake Friuli, Italy – 03 – RSN3553H1)

#### 2.3.2.1.2 Response spectrum

The response spectrum is used extensively in seismic engineering. It describes the maximum response of a single-degree-of-freedom (*SDOF*) oscillator to a particular motion. The response spectrum reflects the influence of the ground motion on structures of different natural periods. Response spectra can be expressed as acceleration ( $S_a$ ), velocity ( $S_v$ ) and displacement ( $S_d$ ) response spectra. The spectral values are plotted against the period as illustrated in figure 2.10.

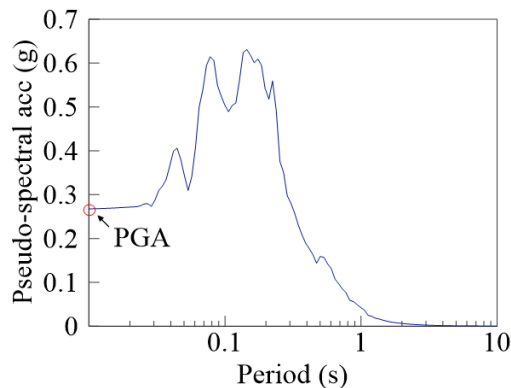


Figure 2.10 Illustration of a typical response spectrum (earthquake Coalinga – 02 – RSN381H1)

### 2.3.2.1.3 Mean period ( $T_m$ )

The mean period ( $T_m$ ) is the most robust parameter to characterize motions frequency content (Rathje et al., 1998). It averages periods weighted by the Fourier amplitudes in the Fourier spectrum (Rathje et al., 2004). The  $T_m$  can be calculated with equation 2.17.

$$T_m = \frac{\sum_i C_i^2 (1/f_i)}{\sum_i C_i^2} \quad \text{Eq. 2.17}$$

where  $C_i$  are the Fourier amplitude coefficients,  $f_i$  is the discrete Fourier transform frequencies between 0.25 and 20 Hz. The equation is valid for a frequency interval of sampling of a maximum of 0.05 Hz. The authors recommend adding sampling points of zero value at the beginning and/or at the end of the series to reach the minimum frequency interval of sampling.

Soft soils subjected to dynamic loadings may change the recorded motion frequency content and increase  $T_m$  (period elongation) due to soil degradation such as observed during the Kocaeli earthquake in 1999 (Rathje et al., 2001).

### 2.3.2.1.4 Center frequency ( $f_c$ )

The center frequency  $f_c$  of a signal is where most of its frequency content is concentrated. In this project, the  $f_c$  is taken as the inverse of the  $T_m$ .

## 2.3.2.2 Amplitude parameters

Ground motions are commonly expressed in time histories such as acceleration  $a(t)$ , velocity  $v(t)$ , and displacement  $d(t)$ . The  $v(t)$  and  $d(t)$  are obtained by integration and double-integration of  $a(t)$  in the time domain as presented in equations 2.18 and 2.19. In this project, all parameters are associated with the horizontal components as the vertical component is less interesting in seismic engineering since structures are generally more resistant to vertical accelerations.

$$v(t) = \int_0^t a(t) dt \quad \text{Eq. 2.18}$$

$$d(t) = \iint_0^t a(t) dt \quad \text{Eq. 2.19}$$

Here is the list of amplitude parameters presented:

- Peak ground acceleration  $PGA$ ;
- Peak ground velocity  $PGV$ ;
- Peak ground displacement  $PGD$ ;
- Spectral acceleration at fundamental period  $S_a(T_0)$ ;
- Spectral acceleration at degraded fundamental period  $S_a(1.5T_0)$ ;

#### 2.3.2.2.1 Peak ground acceleration $PGA$

The peak ground acceleration is calculated with equation 2.20.

$$PGA = \max |a(t)| \quad \text{Eq. 2.201}$$

The  $PGA$  is the absolute value of the maximum acceleration of  $a(t)$  as illustrated in figure 2.11.

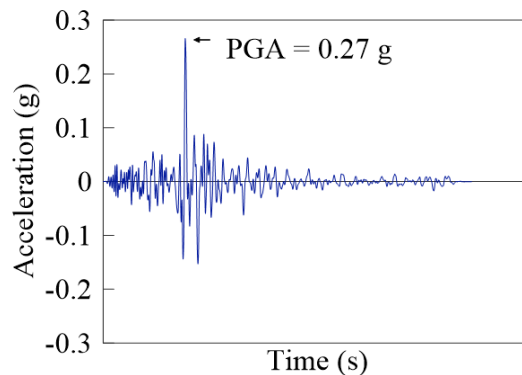


Figure 2.11 Illustration of  $PGA$  obtained from  $a(t)$

This parameter is commonly used as a measure of the amplitude of a particular ground motion as it can be easily obtained. Several relationships were developed to correlate the  $PGA$  with other parameters. However, correlations suffer from lack of precision as the  $PGA$  is heavily influenced by high spikes in  $a(t)$ , high frequency content and by processing. Observations and studies have shown in the past that the  $PGA$  alone is not a good parameter to characterize the intensity of ground motions (e.g. Cloud, 1967; Krawinkler and Rahnama, 1992), yet is commonly used in design such as in the evaluation of potential for liquefaction triggering.

Consequently, ground motions should not be represented only by its *PGA* since it corresponds to the peak value of  $a(t)$  that occurs in a very short period of time. Characterizing the results with extreme peaks may lead to an important scatter of the results. Nevertheless, the *PGA* remains a widely used and easy to obtain parameter.

#### 2.3.2.2.2 Peak ground velocity *PGV*

The peak ground velocity is calculated with equation 2.21.

$$PGV = \max|v(t)| = \max \left| \int_0^t a(t) dt \right| \quad \text{Eq. 2.21}$$

The *PGV* is the maximum velocity in the  $v(t)$  as illustrated in figure 2.12.

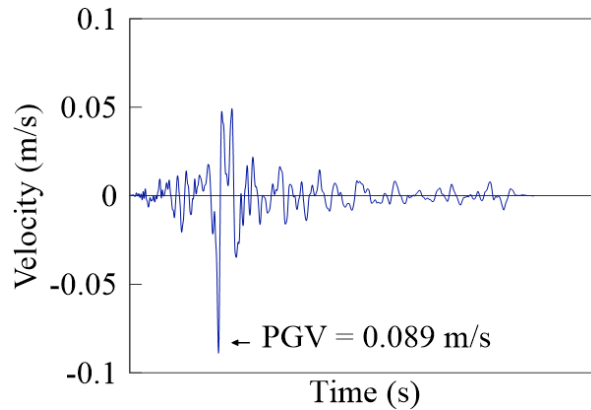


Figure 2.12 Illustration of *PGV* obtained from  $v(t)$

The *PGV* is a commonly used parameter to characterize the ground motions amplitude. The *PGV* is more accurate in intermediate frequencies than the *PGA* as the *PGV* is less sensitive to high-frequency content. The velocity time series is obtained by integration of  $a(t)$  and the process of integration filters out a certain amount of high-frequency content (Kramer, 1996).

Hence, the *PGV* has been proven to show better correlation with *DM* than the *PGA* (Bradley, 2012b) such as the prediction of liquefaction (Kostadinov and Towhata, 2002) and the peak displacement of piles embedded in both liquefiable and non-liquefiable soils (Bradley et al., 2008).

#### 2.3.2.2.3 Peak ground displacement *PGD*

The peak ground displacement is calculated with equation 2.22.

$$PGD = \max|d(t)| = \max \left| \iint_0^t a(t) dt \right| \quad \text{Eq. 2.22}$$

The  $PGD$  is the absolute maximum displacement of  $d(t)$  as illustrated in figure 2.13.

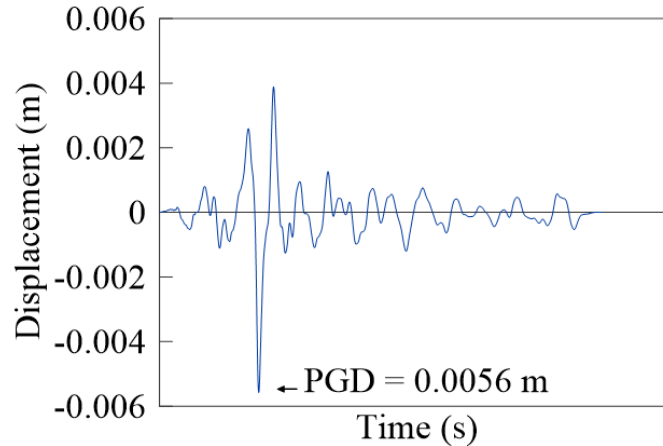


Figure 2.13 Illustration of  $PGD$  obtained from  $d(t)$

The  $d(t)$  is commonly calculated and presented along with  $a(t)$  and  $v(t)$ . However, the  $PGD$  is less frequently used because it is difficult to determine accurately. Long-period noise tends to be magnified by double integration of  $a(t)$ . Furthermore, the  $d(t)$  is significantly influenced by the arbitrary choice of high-pass filter cut-off ( $LC$ ) used in record processing (Joyner and Boore, 1988), and as a result  $PGD$  is seldomly used in earthquake engineering. The  $PGD$  is generally associated with the lower frequency component of ground motions (Kramer, 1996), as higher frequencies tend to be filtered out during double integration of  $a(t)$ .

#### 2.3.2.2.4 Spectral acceleration at the fundamental period $S_a(T_0)$

The  $S_a(T_0)$  illustrated in figure 2.14 is the spectral acceleration at the  $T_0$ .

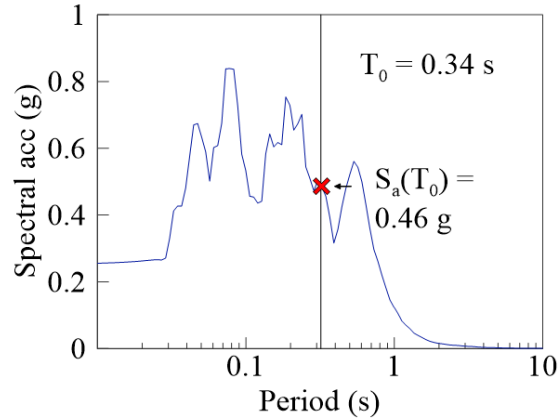


Figure 2.14 Illustration of  $S_a(T_0)$  obtained from a response spectrum

The  $S_a(T_0)$  is a widely used parameter to characterize the  $DM$  at the site's  $T_0$ . The seismic response of the system might be enhanced when the motion's frequency content matches  $T_0$ .

#### 2.3.2.2.5 Spectral acceleration at the degraded fundamental period $S_a(1.5T_0)$

The  $S_a(1.5T_0)$  illustrated in figure 2.15 is the spectral acceleration at the degraded  $T_0$  of the site.

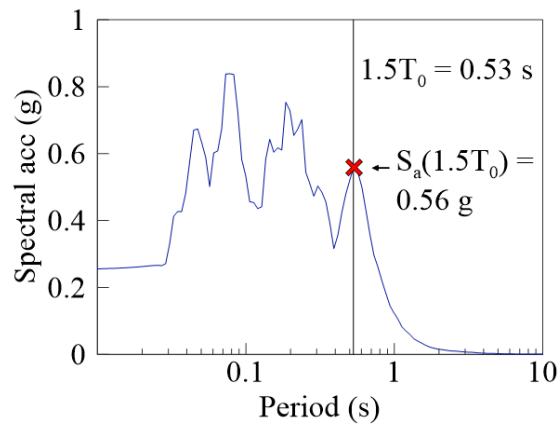


Figure 2.15 Illustration of  $S_a(1.5T_0)$  obtained from a response spectrum

Soils nonlinearity may result in the lengthening of the  $T_0$  of the model (i.e. degraded  $T_0$ ). This parameter seems promising in the prediction of crest displacements as shown by Bray and Travasarou (2007). The authors have suggested a simplified procedure to estimate crest permanent displacements using a dataset of more than 600 ground motions and have validated their model with 16 case studies. The results of their study showed that the  $S_a(1.5T_0)$  of the sliding block was the most efficient and sufficient  $IM$  in the prediction of permanent deformation of an earth dam, earth fill, etc.

### 2.3.2.3 Integration-based parameters

Parameters presented in this section reflect more than one characteristic of ground motions and as such, they are useful in characterizing earthquake ground motions. All of the parameters presented in this section use integration in the time domain or the frequency domain. Also, when integration is used, the parameters are less influenced by high-frequency accelerations which often occur over a very short period of time (Kramer, 1996). The parameters considered are:

- Arias intensity  $I_a$ ;
- cumulative absolute velocity  $CAV$ ;
- cumulative absolute velocity with a  $5\text{cm/s}^2$  threshold acceleration  $CAV_5$ ;
- Housner intensity  $HI$ ;
- acceleration spectrum intensity  $ASI$ ;
- shaking intensity rate  $SIR_{5-75}$ ;
- shaking intensity rate  $SIR_{5-95}$ ;

#### 2.3.2.3.1 Arias intensity $I_a$

The Arias intensity can be computed with equation 2.23 (Arias, 1970):

$$I_a = \frac{\pi}{2g} \int_0^t (a(t))^2 dt \quad \text{Eq. 2.23}$$

The Arias intensity is expressed in units of velocity (m/s) and it characterizes the intensity and duration of the earthquake ground motion. The square acceleration time series is integrated over the entire duration of the earthquake. Its formula is closely related to the root mean square acceleration ( $RMS$ ). As the latter is sensitive to the definition of the duration of the earthquake (McCaan and Shah, 1979), the  $I_a$  is independent of the method used to define the duration.

#### 2.3.2.3.2 Cumulative absolute velocity $CAV$

The cumulative absolute velocity can be calculated with equation 2.24.

$$CAV = \int_0^t |a(t)| dt \quad \text{Eq. 2.24}$$

The *CAV* is expressed in units of velocity (m/s). The *CAV* was initially developed and proposed by Reed and Kassawara (1988) to provide a threshold criterion for assessing the damage potential of an earthquake on a nuclear power plant. It computes the area under the absolute accelerogram over the entire duration of the earthquake.

The *CAV* is found to correlate well with several amplitude parameters of high frequencies such as the *PGA* and *ASI* and of moderate frequencies such as the *PGV* and *SI* (Bradley, 2012a). The results of Bradley et al. (2008) have shown a good correlation between the peak displacement of piles embedded in liquefiable soils and the *PGV*.

However, long-duration earthquakes often contain a significant portion of small amplitude (non-damaging) accelerations that contribute significantly to the *CAV* (O'Hara and Jacobson, 1991), thus, several definitions of *CAV* were introduced over the years to reduce or eliminate the contribution of non-damaging portions of records such as the *CAV<sub>STD</sub>* and *CAV<sub>5</sub>* defined below.

#### 2.3.2.3.3 Standardized cumulative absolute velocity *CAV<sub>STD</sub>*

The *CAV<sub>STD</sub>* is a modified version of the original *CAV* and can be calculated with equation 2.25.

$$CAV_{STD} = \sum_{i=1}^N \int_i^{i+1} \langle \chi \rangle |a(t)| dt \quad \text{Eq. 2.25}$$

$$\text{where } \chi = \begin{cases} 1 & \text{for } \max|a(t)| \geq 0.025 g \\ 0 & \text{for } \max|a(t)| < 0.025 g \end{cases}$$

where *N* is the total number of 1-s time-intervals and *i* is the *i*th time-interval of 1-second.

The *CAV<sub>STD</sub>* is expressed in units of velocity (m/s). The *CAV<sub>STD</sub>* was introduced by O'Hara and Jacobson (1991) to reduce the contribution of small-amplitude acceleration to the cumulative absolute velocity. It partitions the records into discrete 1-second time-interval. The increment of *CAV* of each time-interval is included in the calculation only when the absolute value of acceleration exceeds the threshold value of 0.025 g at least once during the time interval. Figure 2.16 shows the difference between *CAV* and *CAV<sub>STD</sub>*.

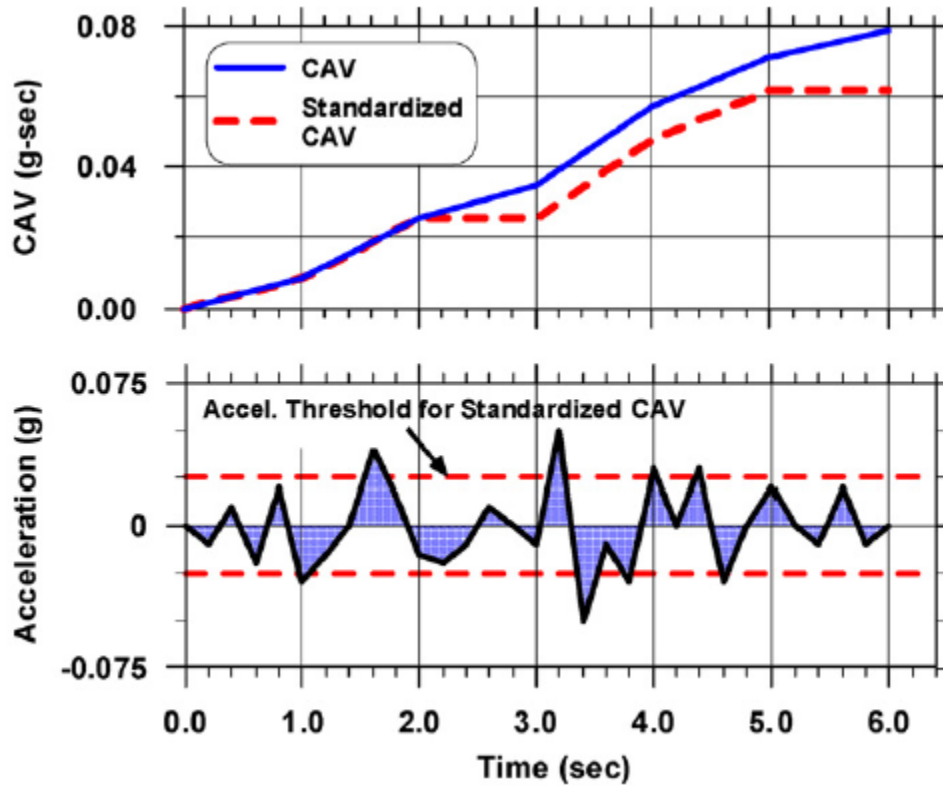


Figure 2.16 Calculation of CAV and  $CAV_{STD}$ , retrieved from Campbell and Bozorgnia (2011)

#### 2.3.2.3.4 Cumulative absolute velocity with $5 \text{ cm/s}^2$ threshold acceleration $CAV_5$

The  $CAV_5$  can be calculated with equation 2.26.

$$CAV_5 = \int_0^t \langle \chi \rangle |a(t)| dt \quad \text{where } \chi = \begin{cases} 1 & \text{for } |a(t)| \geq 5 \text{ cm/s}^2 \\ 0 & \text{for } |a(t)| < 5 \text{ cm/s}^2 \end{cases} \quad \text{Eq. 2.26}$$

The  $CAV_5$  is expressed in units of velocity (m/s) and it computes the area under the absolute accelerogram when the acceleration is higher than  $5 \text{ cm/s}^2$  over the entire duration of the earthquake. This parameter was introduced by Kramer and Mitchell (2006) to neglect the contribution of acceleration that has little effect on the pore pressure generation. The authors have shown that it is closely related to excess pore pressure generation ( $r_u$ ) for liquefaction prediction.

#### 2.3.2.3.5 Spectrum intensity $SI$

The spectrum intensity is calculated with equation 2.27.

$$SI = \int_{0.1}^{2.5} PSV(T) dT \quad \text{Eq. 2.27}$$

The spectrum intensity  $SI$  is expressed in units of distance (m). It computes the area under the pseudo-velocity response spectrum  $PSV$  between periods 0.1 and 2.5 s. The  $SI$  was introduced by Housner (1959) and indicates the potential response of structures whose  $T_0$  ranges between 0.1 and 2.5 s. As earth dams and rockfill dams generally have their  $T_0$  between 0.6 and 2.0 s (Makdisi and Seed, 1978), the  $SI$  should be useful for evaluating their response.

The  $SI$  has been proven to be an efficient and sufficient  $IM$  to predict the seismic response of pile foundations embedded on both liquefiable and non-liquefiable soils (Bradley et al., 2008).

#### 2.3.2.3.6 Acceleration spectrum intensity $ASI$ :

The  $ASI$  is calculated with equation 2.28.

$$ASI = \int_{0.1}^{0.5} S_a(T, D = 5\%) dT \quad \text{Eq. 2.28}$$

The  $ASI$  is expressed in units of velocity (m/s). It computes the area under the acceleration response spectrum of 5 % damping between periods 0.1 and 0.5 s. The  $ASI$  was introduced by Von Thun et al. (1988) to characterize the response of concrete dams, which generally have fundamental periods  $T_0$  between 0.1 and 0.5 s. Since the  $T_0$  of the numerical model in FLAC is 0.34 s, this parameter should be of interest for this project.

#### 2.3.2.3.7 Shaking intensity rate $SIR_{5-75}$ :

The  $SIR_{5-75}$  essentially corresponds to the slope of the  $I_a$  during the strongest shaking of the ground motion and it is calculated with equation 2.29.

$$SIR = \frac{I_{a5-75}}{D_{5-75}} \quad \text{Eq. 2.29}$$

where  $I_{a5-75}$  is the change of  $I_a$  from 5 to 75 % from its total value and  $D_{5-75}$  is its corresponding duration.

The  $SIR$  is introduced by Dashti et al. (2010). The authors found that the liquefaction-induced-settlements follow the rate of ground shaking intensity which can be captured by the  $SIR$ . This parameter reflects the influence of motion intensity, frequency content, and duration.

#### 2.3.2.3.8 Shaking intensity rate $SIR_{5-95}$ :

The  $SIR_{5-95}$  is based on the  $SIR_{5-75}$  defined above. The bracket used for  $SIR_{5-95}$  is enlarged and includes the change of  $I_a$  from 5 to 95 % instead of 75 %. The  $SIR_{5-95}$  is calculated with equation 2.30

$$SIR = \frac{I_{a5-95}}{D_{5-95}} \quad \text{Eq. 2.30}$$

where  $I_{a5-95}$  is the change of  $I_a$  from 5 to 95 % from its total value and  $D_{5-95}$  is its corresponding duration.

#### 2.3.2.4 Duration parameters

The duration of an earthquake can substantially impact the damage potential on soils and structures. The longer the earthquake the more damage it might cause. An earthquake with high amplitude but a short duration will most likely produce less damage than an earthquake with moderate amplitude combined with a long duration (Kramer, 1996). For example, as observed by Cloud (1967), the earthquake in Parkfield, California in 1966 had strong pulses of acceleration up to 0.5 g recorded in certain areas but no severe damage was observed in the surrounding structures due to the short duration of the earthquake.

In seismic engineering, since only the strong motion portion is of interest, significant duration may be used to define the duration in which potential damage might take place. In this project, the significant duration used are:

- $D_{5-75}$ ;
- $D_{5-95}$ ;

The significant duration  $D_{5-75}$  and  $D_{5-95}$  correspond to the duration needed to go from 5 to 75 % and 5 to 95 % of the total  $I_a$  recorded respectively.

### 2.3.3 Quality metrics

Intensity measures ( $IM$ ) are parameters that characterize the intensity of motions in terms of amplitude, frequency content and/or duration. Damage measures ( $DM$ ) are measures of damage such as crest displacement, crest  $PGA$  and  $r_u$ .

Quality metrics of  $IM$  may be described in terms of efficiency. The notion of efficiency was introduced by Shome and Cornell (1999). There exists several other quality metrics in the literature such as the sufficiency and predictability that are not discussed in this thesis as because they were not used in this project.

Indeed, a sufficient  $IM$  must predict a  $DM$  unbiased by the earthquake magnitude and distance. Using scaling factors to match the input ground motions to the design spectrum impacted the compatibility of motions to their corresponding magnitude and distance. Besides, the predictability of an  $IM$  might be evaluated if there exist correlations to predict the  $DM$  such as ground motion models ( $GMM$ ). However, the  $GMM$  developed for eastern America are heavily based on numerical simulations instead of on historical cases, which results in a significant uncertainty with  $GMM$ .

#### 2.3.3.1 Efficiency

The efficiency is a measure of the dispersion of residuals in the prediction of  $DM$  based on  $IM$ . An efficient  $IM$  should show a good correlation with the  $DM$ . The efficiency of an  $IM$  is defined as the standard deviation of the natural logarithmic residuals ( $\varepsilon_{DM|IM}$ ) of the regression between the  $IM$  and the  $DM$ . An example of a regression between the candidate  $IM$  for the prediction of the  $DM$  is illustrated in figure 2.17.

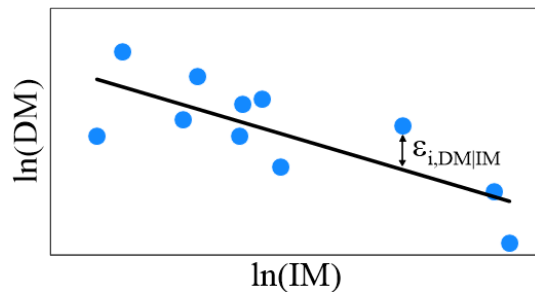


Figure 2.17 Efficiency of candidate  $IM$  for the prediction of  $DM$

Herein, the equation of efficiency using the notation of Bullock et al. (2019) is presented in equation 2.31.

$$\ln(DM) = a_0 + a_1 \ln(IM) + \varepsilon_{DM|IM} \quad \text{Eq. 2.31}$$

The efficiency corresponds to the standard deviation of  $\varepsilon_{DM|IM}$ . A smaller value of efficiency means less uncertainty in the prediction of the  $DM$ .

### 2.3.3.2 Short literature review of the efficiency of candidate $IM$ in the prediction of damage measures in dams

This section discusses the main candidate  $IM$  that predict  $DM$  for tall embankments as no study is available yet for small embankments. For stiff embankment dams in which significant strength reduction is not expected, it is found that the  $S_a(T_0)$  correlates well with the embankment deformations. Bray and Travararou (2007) used an extensive set of ground motions and a nonlinear Newmark sliding block model and found that the  $IM$  that correlates best with dam deformations is the  $S_a(1.5T_0)$ .

Armstrong (2018) perform over 700 nonlinear simulations on a tall earth dam and found that  $I_a$  correlates best with embankment deformations followed by  $PGA$  and  $S_a$  at short periods. However, its model can accurately propagate motion frequency of up to 10 Hz, which mean that  $S_a$  below 0.1 s may not be reliable.

For embankment dams founded on liquefiable ground, Beaty and Perla (2012) performed nonlinear simulations with 20 input motions using a combination of Mohr Coulomb and UBCSAND models and found that  $I_a$ ,  $CAV$  and  $(I_a \times D_{95})^{1/2}$  are the most efficient  $IM$  to predict crest settlements.

## 2.4 Site effects

It has often been reported that earthquakes cause more severe damage to buildings and infrastructures located on a hill, as noted after the San Fernando earthquake in 1971 (Nason, 1971), Friuli earthquake in Italy in 1976 (Géli et al., 1988) and Whittier Narrows earthquake in 1987 (Kawase and Aki, 1990). Recorded ground motions on tops of hills have also shown significant amplification as observed by Nechstchein et al. (1995), Trifunac and Hudson (1971) and Vahdani and Wikstrom (2002) who noted very high values of *PGA* at the crest of dams. Amplification due to topographic irregularities is known as topographic effects.

Topographic effects are highly frequency-dependent (Ohtsuki and Harumi, 1983; Nguyen and Gatmiri, 2007), but it is generally accepted that the response at the crest is always amplified. The amplification or attenuation of the response at the toes depend on the motion frequency content (Nguyen and Gatmiri, 2007). The toes are amplified with low frequency content, but is sometimes attenuated if the motion frequency content is high. Sloping faces undergo a rather complex pattern of amplification and attenuation, especially in the upper part of the sloping faces (Géli et al., 1988).

The level of topographic effects depends on:

- The selection of input ground motion
- The nature of incident waves (see section 2.4.1.)
- The direction of incident waves (see section 2.4.1.)
- The slope inclination (see section 2.4.1.)
- The motion frequency content (see section 2.4.2.)
- The soil stratigraphy (see section 2.4.3.)
- The material damping (see section 2.4.1.)

## **2.4.1 Effect of the nature and the inclination of incident waves and material damping**

### **2.4.1.1 Nature of incident waves**

The amplification at the crest is higher for SV waves than for SH waves because SV waves generate additional wave types during diffraction: P-waves and Rayleigh-waves. Rayleigh-waves produced at the toe propagate upward along the slope to the horizontal surface of the edge causing superposition of waves leading to the amplification felt at the crest and behind it (Ohtsuki and Harumi, 1983).

### **2.4.1.2 Direction of incident waves**

The direction of incident waves also affects the level of amplification due to topographic effects. Ashford and Sitar (1997) found that waves travelling into a slope tend to produce amplification at the crest in comparison to waves travelling away from a slope. However, the more inclined the waves, the more the *PGA* at the crest decreases. Hence, due to this incoherence, the authors suggest to neglect wave inclination. Also, it can be generally assumed that shear waves (SV-wave) are almost perfectly vertical for sites near the ground surface because the angle of incidence of SV-waves decreases as waves propagate upward in the soil profile with decreasing  $V_s$  (Vahdani and Wikstrom, 2002).

### **2.4.1.3 Slope inclination**

There seems to be consensus by several researchers that a steeper slope results in a greater amplification at the crest (Bard, 1999). Moreover, for steeper slopes, displacements at the crest are amplified and attenuated at the toes (Nguyen and Gatmiri, 2007). Seismic waves arriving at the surface are reflected into the model because the sloping faces cause the incident waves to be reflected in such a way that the waves may accumulate at the crest or along the slopes, in contrast with a 1D soil column where the waves are reflected vertically.

### **2.4.1.4 Material damping**

Besides, increased damping will generally reduce the amplitude of the seismic response. Ashford and Sitar (1997) showed that increased damping significantly reduces the response at the free-field

behind the crest and at the toes. However, they compared the amplification at the crest against the free-field and found that the damping ratio had little to no effect on the amplification at the crest.

### **2.4.2 Effect of the motion frequency content**

Based on numerous studies, it is evident that the amplification effects due to topographic irregularities are strongly dependent on the motion frequency content. The maximum amplification effects take place for motion frequency content close to the natural frequency of the topographic irregularity (Géli et al., 1988; Brennan and Madabhushi, 2009; Ohtsuki and Harumi, 1983) and, in contrast, for very low frequency content, topographic effects are negligible (Ashford et al., 1997; Nguyen and Gatmiri, 2007) as the topographic irregularity can be regarded as a small obstacle and thus its effects can be neglected.

Topographic effects led by high frequency energy are more likely to be observed in *ENA* since its motions are rich in high frequency content. Nguyen and Gatmiri (2007) have studied the effect of the motion frequency content on the amplification/attenuation of a topographic irregularity. The results of their study showed that high frequencies tend to produce amplification at the crest and at the toes and moreover, amplification tend to linearly increase with the increase of frequency content. With the increase of the frequency content, the maximum attenuation is no longer located at the toes but shifts closer to the crest, along the slope. Furthermore, high frequency content results in stronger and more complex topographic effects and also leads to a wider region influenced by the presence of the topographic irregularity. In general, lower frequency content tends to attenuate seismic waves while the response at the toes are attenuated with low frequency motions.

### **2.4.3 Effect of soil stratigraphy**

It is well known that soft soil tends to contribute to significant amplification of seismic waves. The amplification resulting from soft soils was extensively studied by several authors (e.g. Idriss, 1991; Krawinkler and Rahnama, 1992; Rathje et al., 2001).

Impedance contrast may lead to wave amplification. Body waves (P and S-waves) travel up and down in the soft layer and surface waves (L-wave and Rayleigh waves) are generated at the interface of impedance contrast. The interference of trapped waves will further lead to resonance in the soft layer. Furthermore, soft soils may amplify the intensity of the motion and change its frequency content (Rathje et al., 2001). Athanopoulos-Zekkos and Seed (2013) have computed

the response of 3 earth levees of different soil conditions and found that the dike with the greatest soil rigidity contrast shows the greatest amplification.

Idriss (1990) studied the amplification of bedrock motions on soft soil sites and plotted the resulting *PGA* on soft soil sites against the *PGA* on the bedrock as presented in figure 2.18. The author found that motions with *PGA* lower than 0.4 g would produce amplification of the *PGA* in soft soil sites. High amplification ratios, in the range of 1.5 – 4.0, are associated with *PGA* below 0.1 g, where the soil is nearly elastic. Increase of nonlinearity due to higher level of *PGA* are associated with lower amplification because of the increase of hysteretic damping and the decrease of the shear modulus  $G$ .

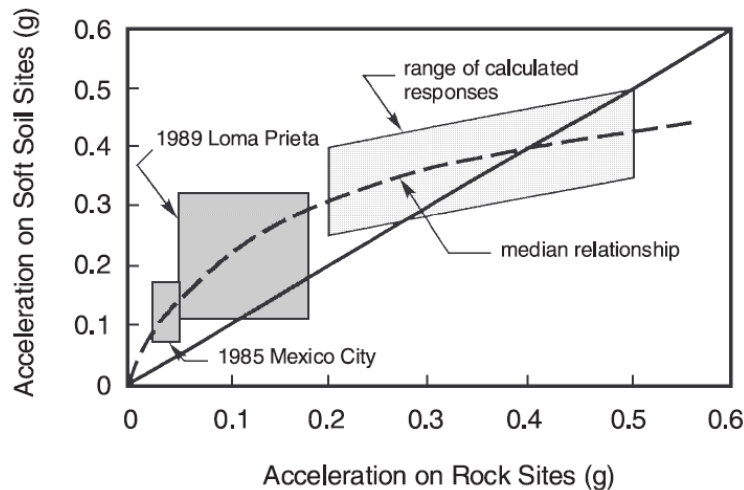


Figure 2.18 *PGA* on soft soil sites, retrieved from Idriss (1990)

## **2.5 Seismic design of embankments in practice**

Both static and dynamic stability of an embankment must be evaluated. Both types of analyses usually focus on the slope stability because it is the principal mode of failure of an earthen dike. Failure by internal instability such as erosion of materials is not considered in this project.

### **2.5.1 Static analysis**

An earthen dike must withstand the weight of the reservoir and have stable slopes under static conditions. Furthermore, the foundation soils must have an adequate bearing capacity. A static analysis performed in FLAC will assess the stability of the model against the weight of the reservoir and it will determine if excessive deformations may occur under the embankment that indicates an insufficient bearing capacity of the foundation soils. A factor of safety for the stability of the slopes in static state may be evaluated with FLAC. It uses the strength reduction technique to compute the factor of safety for slope stability.

### **2.5.2 Dynamic analysis**

Earthquakes generate horizontal forces and may cause the failure of the soil mass. Moreover, cyclic forces may cause degradation of the soil, which leads to the reduction of the  $G$  of the material of the dike and its foundation soils. A soil susceptible to liquefaction coupled with favorable conditions to liquefaction may result in liquefaction. A dynamic analysis must be performed to assess the resistance of the embankment against earthquakes.

Usually, it is accepted to start with simplified dynamic analyses and, if there are risks of liquefaction or failure of the embankment (factor of safety  $< 1$ ), move on to more complex analyses. Below is a list of usually performed analyses and a short description of the analyses performed in this project:

- 1- Preliminary evaluation of the seismic stability
- 2- Pseudo-static analysis
- 3- Pseudo-dynamic or permanent deformations analysis
- 4- Linear or equivalent-linear analysis:

This analysis is performed in the temporal or frequency domain and it uses the acceleration time series in the simulation. A factor of safety may be obtained against slope instability and deformations may be monitored throughout the model. This type of analysis better represents the real behavior of soils because frequency, duration and amplitudes of ground motions are all considered. However, the true hysteretic behavior of soils is not considered.

#### 5- Nonlinear analysis :

If there is a risk of liquefaction or the previous analyses show a risk of failure of the dike caused by seismic forces, nonlinear analyses should be carried out. This type of analysis is performed in the time domain with a finite-element or finite-difference software and it considers the hysteretic behavior of soils. Good knowledge of soil properties is required because several parameters are needed to calibrate the constitutive model.

In this project, the analysis of the impact of seismic hazard is performed using both linear and nonlinear analyses.

For the analysis of the resistance of earthen embankments against liquefaction, some authors have found that liquefaction should be evaluated in the vicinity of the structure. As such, Athanasopoulos-Zekkos and Seed (2013) have studied 3 earthen dikes by performing 2D dynamic analyses and found that the maximum *CSR* is computed at the upstream toe of the levees, thus suggesting that the triggering of liquefaction should be evaluated at the upstream toe and not only at the crest. The authors suggested that this may be caused by soil-structure-interaction (SSI) effects from the embankments. This is consistent with findings from several authors who have studied SSI effects on buildings and have found that the highest *CSR* is observed not below the buildings but just outside the building's footprint.

## CHAPTER 3 SELECTION OF GROUND MOTIONS

### 3.1 Introduction

Dynamic nonlinear analyses require input ground motions to be applied at the boundaries of the model. In practice, they are selected and scaled to match the seismic hazard of the site of interest which can be represented by the target response spectrum  $S_T(T)$ . In the *NBCC 2015*, the  $S_T(T)$  corresponds to the uniform hazard spectrum (*UHS*) for a probability of recurrence of 2 % in 50 years, modified to take into account the seismic class of the site (class A). In the current study, the target spectrum is defined as the *UHS* provided by the *NBCC 2015* for a site in Montreal. The relative contribution of earthquakes sources to seismic hazard in terms of magnitudes  $M$  and site-to-source distance  $R$  is analyzed first to define the seismic scenarios controlling the hazard, and to select motions that are consistent with said scenarios. Recent studies have shown that the selection of input ground motions is one of the most important parameters in dynamic analyses since it has a major influence on the dynamic response of an embankment (Bray, 2007; Athanasopoulos-Zekkos, 2010).

In practice and research, two (2) scenarios are typically selected in *ENA* to represent the seismic hazard, decomposed in a short period scenario controlled by low  $M$  earthquake occurring at a short  $R$  from the site, and the other scenario controls the long period range, and is associated with a high  $M$  event situated far from the site. However, the deaggregation showed that more than 2 scenarios in *ENA* might make sense, since contributions from other pairs of  $M$  and  $R$  are non-negligible.

For a better representation of the seismic hazard in the region of Montreal, four (4) scenarios are defined and separated into 3 period ranges: short, medium and long periods. In the short periods range, there is an important contribution of low  $M$  and low site-to-source  $R$ . Moderate  $M$  and  $R$  also have a significant contribution in the short periods which increases gradually with the period. In the long periods, the relative contribution of hazard is shifted to higher  $M$  and longer  $R$ . To sum it up, in the short periods ranging between 0.01 and 0.2 s, there are 2 scenarios: T1-1 with M5-6 and R0-20 km (average contribution of 23 %) and T1-2 with M6-7 and R20-40 km (average contribution of 22 %). In the medium periods between 0.2 and 1.0 s, the scenario T2-1 with M6-7 and R20-40 km (average contribution of 24 %) dominates the hazard and in the long periods

between 1.0 and 10 s, the scenario T3-1 with M7-7.5 and R40-60 km is defined (average contribution of 10 %).

Most of the ground motion recordings are selected from the NGAWest-2 database since NGA-East database lacks motions of interest. The selection of ground motions is performed based on predefined selection criteria. The frequency content of the motions has to roughly match the  $S_T(T)$  in the target period range  $T_R$  and the  $M$  and  $R$  of motions should match those of the scenario.

In short periods, the selection is particularly difficult; the shape of motions generally does not match the  $S_T(T)$  as the peak is shifted to higher periods. This can be attributed to a difference in frequency content of events occurring on the West coast compared to the *ENA*. Motions are then scaled to match the  $S_T(T)$ , using the *Sia* scaling method (Michaud and Léger, 2014).

Intensity measures (*IM*) are calculated for selected and scaled ground motions. One scenario in short-period contains the strongest intensity motions while the long-period scenario contains the weakest but longest-duration motions.

## 3.2 Period range and response spectrum

### 3.2.1 Uniform hazard spectrum *UHS* and design spectrum $S(T)$

The uniform hazard spectrum (*UHS*) is obtained from a probabilistic seismic hazard analysis (*PSHA*) and is provided by the *NBCC 2015* for soils of class C. The *UHS* is composed of the highest spectral values ( $S_a$ ) at all periods, and as a result is overly conservative since no design earthquake would trigger the maximum response at all periods (Baker, 2011). However, the *UHS* is still used nowadays to define the design spectrum  $S(T)$ .

The *UHS* used in this study corresponds to Montreal's hazard for a probability of exceedance of 2 % in 50 years as suggested by the *NBCC 2015*. The  $S_a$  of the *UHS* is defined for periods 0.01 s, 0.05 s, 0.1 s, 0.2 s, 0.3 s, 0.5 s, 1 s, 2 s, 5 s and 10 s and are provided by the Geological Survey of Canada (<https://earthquakescanada.nrcan.gc.ca/index-en.php>). The *UHS* at the site is illustrated in Figure 3.1.

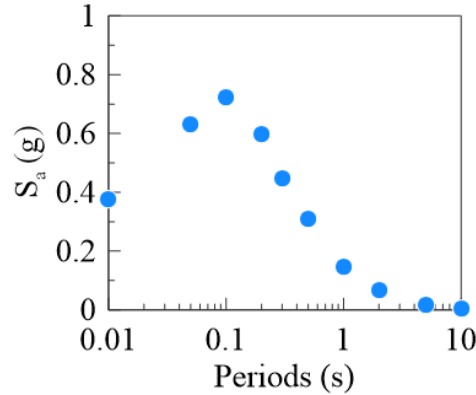


Figure 3.1 Illustration of the *UHS* at the site

The design spectrum ( $S(T)$ ) is specified by the *NBCC 2015* and it corresponds to the *UHS* modified for the corresponding seismic class. Linear interpolation between defined values of  $F(T)S_a$  must be performed to obtain the  $S(T)$ . Note that  $F(T)$  is the period-dependent site coefficients provided by *NBCC 2015* based on the study of Finn and Wightman (2003).

In this project, a seismic class A is considered since ground motions are applied at the top of the bedrock (see chapter 3 for the description of the bedrock). The  $S(T)$  is then obtained by modifying the *UHS* to class A.

Table 3.1 presents the spectral acceleration  $S_a$  of the *UHS* and of the  $S(T)$  at the periods specified by the Geological Survey of Canada. The coefficients  $F(T)$  used for the modification are also available in the table. Figure 3.2 illustrates the  $S(T)$  and the *UHS* at the site.

Table 3.1 Values of *UHS* and  $S(T)$  over the entire period range  $T_R$

| <b>T<br/>(s)</b> | <b>F(T)</b> | <b>UHS<br/>(Class C)<br/><math>S_a</math><br/>(g)</b> | <b>S(T)<br/>(Class A)<br/><math>F(T)S_a</math><br/>(g)</b> |
|------------------|-------------|---|--|
| 0.01             | 0.69        | 0.378   | 0.261  |
| 0.05             | 0.69        | 0.632   | 0.436  |
| 0.1              | 0.69        | 0.723   | 0.499  |
| 0.2              | 0.69        | 0.596   | 0.411  |
| 0.3              | 0.57        | 0.447   | 0.255  |
| 0.5              | 0.57        | 0.311   | 0.177  |
| 1                | 0.57        | 0.148   | 0.084  |
| 2                | 0.58        | 0.0680  | 0.039  |
| 5                | 0.61        | 0.0180  | 0.011  |
| 10               | 0.67        | 0.00610   | 0.00409  |

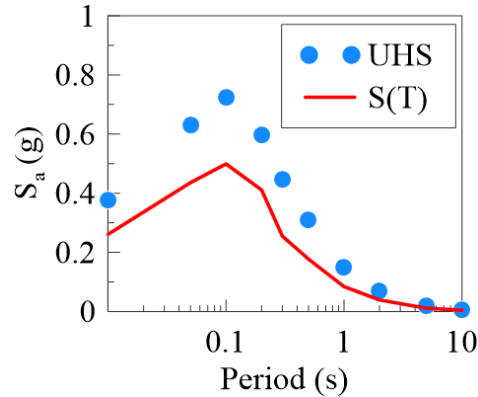


Figure 3.2 Illustration of  $S(T)$  and  $UHS$  at the site

### 3.2.2 Period range $T_R$

In a classic seismic design approach, the period range ( $T_R$ ) is usually defined as the range of periods in which the majority of inelastic deformations take place. However, as the main objective of this project is to analyze the impact of seismic hazard and seismic scenarios on the response of an embankment, the  $T_R$  is considered to span between the defined values of  $S_a$  by the *NBCC 2015*; the lower bound of  $T_R$  is taken as 0.01 and the upper bound of  $T_R$  as 10.0 s.

### 3.2.3 Target response spectrum $S_T(T)$

The target response spectrum  $S_T(T)$  can be defined with the definition proposed by the *NBCC 2015*; the  $S_T(T)$  corresponds to the design spectrum  $S(T)$  over the entire period range  $T_R$ . To define the seismic hazard over the entire  $T_R$ , dominating scenarios contributing to the seismic hazard must be established in terms of pair  $M-R$  within its scenario-specific period range ( $T_{RS}$ ). Ground motions are then selected for each individual scenario. Figure 3.3 presents an example which shows an average response spectrum (*mean*  $S_g$ ) scaled over the  $T_{RS}$  to match the  $S_T(T)$ . Scenarios, selection and scaling criteria and selected ground motions are presented in the next sections of this chapter.

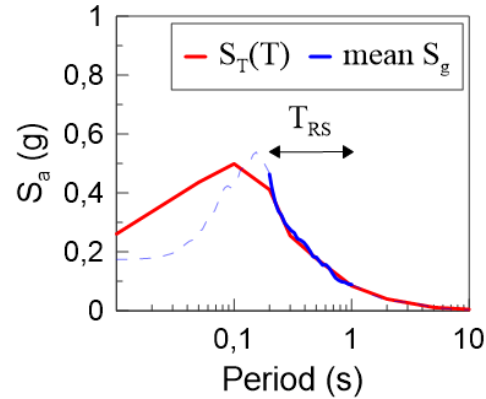


Figure 3.3 Definition of  $S_T(T)$  and illustration of an example of  $mean S_g$  scaled to the  $S_T(T)$  over the  $T_{RS}$

### 3.3 Selection of seismic scenarios based on the seismic hazard deaggregation

The deaggregation represents graphically the relative contribution of the earthquake sources in terms of  $M$  and  $R$  to the seismic hazard (Bazzurro and Cornell, 1999; Halchuk et al., 2019). The deaggregation of Montreal is provided by the Geological Survey of Canada and is available for periods 0.01 s, 0.05 s, 0.10 s, 0.20 s, 0.30 s, 0.50 s, 1.0 s, 2.0 s, 5.0 s and 10 s such as presented in Figure 3.4.

In *ENA*, it is widely accepted that the seismic hazard is dominated by events of low  $M$  and short  $R$  at short periods and of high  $M$  and long  $R$  at long periods (Atkinson, 2009). As a result it is common to use 2 scenarios to represent the seismic hazard in *ENA*: 1-  $M6$  with  $R$  between 10 and 30 km matching the short-period end of the  $S_T(T)$  and 2-  $M7$  with  $R$  between 15 to 100 km for the long-period range. However, based on the deaggregation of Montreal, the relative contribution to the seismic hazard might be separated in more scenarios to better capture the seismic hazard.

The deaggregation shows in the next sections that the hazard might be represented by 3 period ranges over which scenarios are established:

1. Short period range corresponding between 0.01 and 0.2 s
2. Medium period range corresponding between 0.2 and 1.0 s
3. Long period range corresponding between 1.0 and 10 s

A total of 4 seismic scenarios are defined to characterize the seismic hazard between 0.01 and 10 s for the city of Montreal and are summarized in Table 3.2.

Table 3.2 Seismic scenarios based on the deaggregation of the city of Montreal

| <b>Scenarios</b> | <b>Periods<br/>(s)</b> | <b>Magnitude<br/>M</b> | <b>Distance<br/>R<br/>(km)</b> |
|------------------|------------------------|------------------------|--------------------------------|
| T1-1             | 0.01 – 0.2             | 5 – 6                  | 0 – 20                         |
| T1-2             | 0.01 – 0.2             | 6 – 7                  | 20 – 40                        |
| T2-1             | 0.2 – 1.0              | 6 – 7                  | 20 – 40                        |
| T3-1             | 1.0 – 10               | 7 – 7.5                | 40 – 60                        |

### 3.3.1 Short-period scenarios

Figure 3.4 represents the deaggregation at the site between 0.01 and 0.2 s.

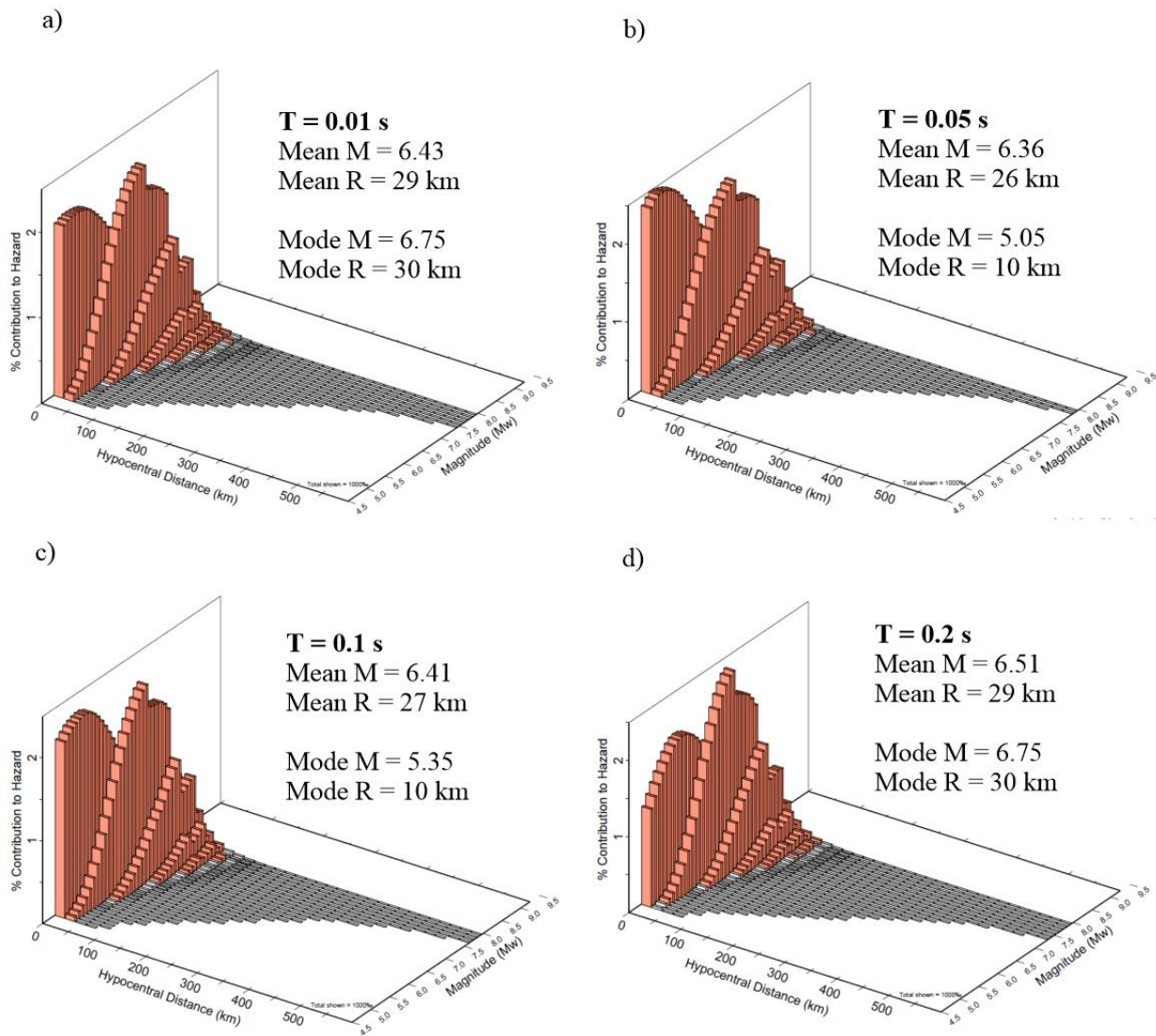


Figure 3.4 Deaggregation of the seismic hazard of the site at periods a) 0.01 s, b) 0.05 s, c) 0.1 s and d) 0.2s

The deaggregation clearly shows that the contribution to the hazard mainly comes from 2 events. Indeed, two (2) peaks are observed. Based on both peaks, 2 scenarios are established and they correspond to:

- **T1-1:**  $M_{5-6}$  and  $R_{0-20}$  km (average contribution of  $\pm 23$  %) and;
- **T1-2:**  $M_{6-7}$  and  $R_{20-40}$  km (average contribution of  $\pm 22$  %)

The contribution of higher  $M$  and longer  $R$  gradually increases with the periods. Motions in both scenarios are expected to have higher frequency content since shorter  $R$  generally results in higher frequency content (Trifunac and Hudson, 1971).

### 3.3.2 Medium-period scenarios

Figure 3.5 illustrates the deaggregation at the site between 0.2 and 1.0 s.

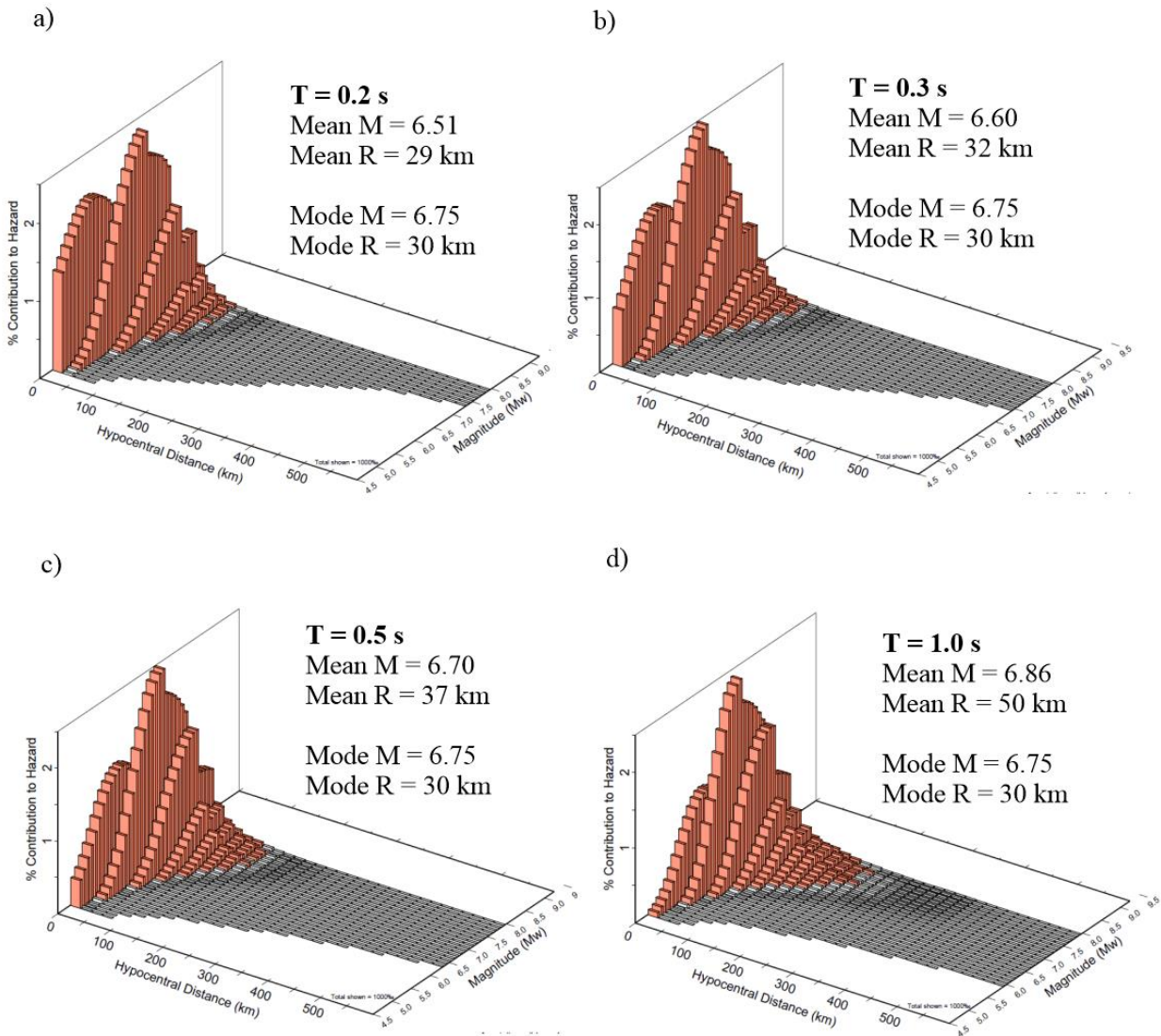


Figure 3.5 Deaggregation of the seismic hazard at the site for periods a) 0.2 s, b) 0.3 s, c) 0.5 s and d) 1.0 s

The hazard is shifted towards higher  $M$  and  $R$  as contribution from earthquakes of small  $M$  and short  $R$  has dropped significantly compared to scenarios T1-1 and T1-2. Hence, one scenario has been established to represent the main contribution to the hazard between 0.2 and 1.0 s:

- **T2-1:**  $M6-7$  and  $R20-40$  km (average contribution of  $\pm 24$  %)

### 3.3.3 Long-period scenarios

Figure 3.6 shows the deaggregation at the site between periods 1.0 and 10 s.

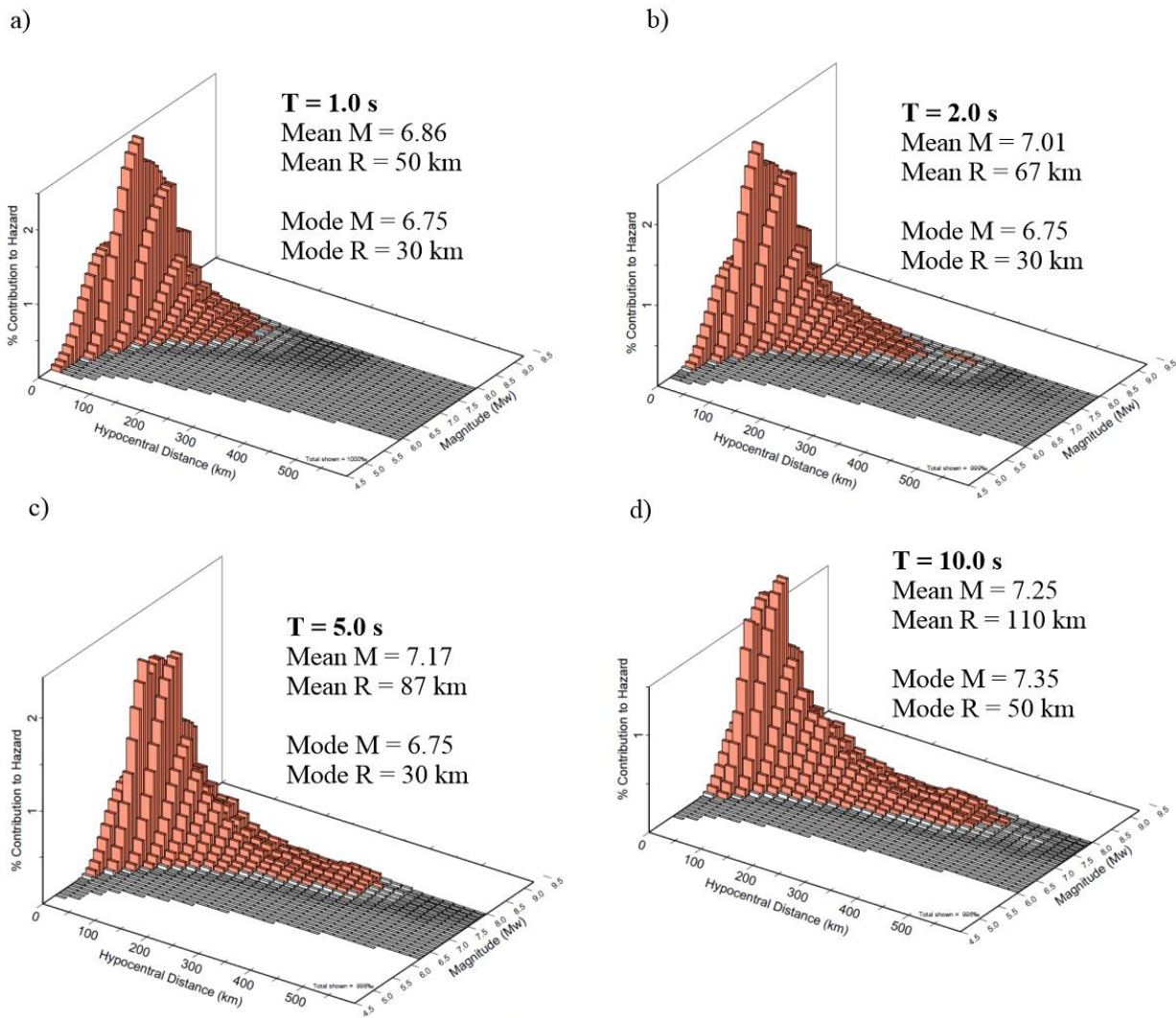


Figure 3.6 Deaggregation of the seismic hazard at the site for periods a) 1.0 s, b) 2.0 s, c) 5.0 s and d) 10.0 s

In this range, the seismic hazard is dominated by strong earthquakes with magnitude  $M$  higher than 6.5. Furthermore, the hazard is also shifted towards events farther to the epicenter. The major contribution to the hazard comes from events of high  $M$  and medium  $R$  although contributions from smaller and longer  $R$  events are also non-negligible. However, since the embankment has a relatively short fundamental period  $T_0$  (refer to chapter 6 - section 6.4.6), scenarios representing long periods may not have a major damage potential compared to lower periods scenarios. As such, to reduce the number of simulations, only one scenario is chosen to represent periods between 1.0 and 10 s:

- **T3-1:** M7-7.5 and R40-60 km (average contribution of  $\pm 10\%$ )

### 3.4 Databases of historical ground motions

Recorded ground motions are used as seismic excitation in numerical models. Recording instruments usually measure the acceleration time series of the ground motions, and ground motion is recorded in 3 directions, with 2 horizontal components and 1 vertical.

A few databases have compiled response spectra of historical ground motions to be used in dynamic analysis. This study uses two databases compiled by the Pacific Earthquake Engineering Research Center (*PEER*): the NGA-West-2 and the NGA-East accessible to the public via the website: <https://ngawest2.berkeley.edu/>.

NGA-East contains ground motions recorded in Central and Eastern North America (*CENA*) (Goulet et al., 2018) which should be of great interest for projects in the East considering that the soil and rock conditions are similar. Motions in the East tend to have higher frequency content since the rock is of better quality than in the West. However, NGA-East lacks records in the range of  $M$  and  $R$  of interest. For this project, only one ground motion, the Mineral 2011 of  $M = 5.7$  that struck in Virginia in the American East Coast, is selected from NGA-East that matches the short period range of the  $S_T(T)$  of Montreal.

NGA-West-2 is a database that contains recorded ground motions of shallow crustal earthquakes in active tectonic regimes (Ancheta et al., 2012). Meta-data are also included in the database such as  $R$ ,  $M$  and the type of recording instrument. All selected ground motions records in this project are taken from NGA-West 2 except for the one mentioned above.

The data contained in the databases are unscaled and as-recorded which means that they may contain a certain amount of noise and may need to be corrected. Ground motion processing must be performed and is detailed in Chapter 5.

The database also compiles the response spectra of all motions. In theory, both horizontal components of a seismic motion are used to compute the horizontal response spectrum, using either the geometric mean, or the RotD50 of the motion (Boore, 2010). For this project, ground motions are represented by only one horizontal component, i.e. the response spectra of each component are not combined.

### 3.5 Selection criteria

Selection criteria are inspired by the *NBCC 2015* Commentary J Guidelines. It is important to note that since the *NBCC 2015* does not focus on the construction of small embankments, not all recommendations from the Commentary J Guidelines are considered. Records are selected based on  $M$  and  $R$  and selection criteria are the following:

- 1- Scaling factor ( $F_1$ ) between 0.5 and 2.0
- 2- Shape of spectrum ( $S_g$ ) matches the  $S_T(T)$  over the  $T_{RS}$
- 3- Shape of  $S_g$  outside the  $T_{RS}$  falls below the  $S_T(T)$  but never below 75 % of  $S_T(T)$
- 4- No more than 2 records from the same earthquake per scenario
- 5- Site conditions of the recording site should be similar to the site analyzed in this project in terms of  $V_{s30}$
- 6- Average scaled spectrum (mean  $S_g$ ) does not fall below 90 % of the  $S_T(T)$  in the  $T_{RS}$ . A second scaling factor ( $F_2$ ) will adjust the average spectrum  $S_g$ .

The scaling method and the  $F_1$  are defined in the next section. In preference,  $F_1$  should be kept as close to 1 as possible (Krinitzsky and Chang, 1978). Limits of 0.5 to 2.0 to  $F_1$  are appropriate when selection is based on  $M$ ,  $R$  and site conditions as considered in this project (Watson-Lamprey and Abrahamson, 2005).

The ground motions should fall below the  $S_T(T)$  outside of  $T_{RS}$  because otherwise the response of the dike would be overestimated, and it would limit the interest of using different seismic scenarios.

The databases provide information on the  $V_{s30}$  of the subsoil of the recording instrument. The base of the model consists of rock of seismic class A of which the  $V_s > 1500$  m/s. However, considering the very limited amount of historical ground motions recorded in such subsoil conditions, the criterion of minimum  $V_s$  is loosened to  $V_s > 470$  m/s. Such soil condition represents a soil of seismic class C which is a very dense soil or soft rock.

### 3.6 Scaling of ground motions

Ground motions are scaled to match the  $S_T(T)$  over the  $T_{RS}$ . Several scaling methods exist in the literature and some of them may introduce bias in the results or alter the spectral shape of the motions. Michaud and Léger (2014) studied the response of a four-story steel structure located in *ENA* and compared its response under motions scaled with different scaling methods. They showed that the *SIA* scaling method provides reliable results with small standard deviation of motions *PGA*, root mean square of accelerations (*RMSA*),  $I_a$  and *CAV*. Obtained values are consistent with other scaling methods.

The *SIA* scaling method applies a  $F_1$  to the ground motion's response spectrum so that the area under the latter should be equal to the area under  $S_T(T)$  within  $T_{RS}$ . The  $F_1$  is calculated by Eq. 3.1:

$$F_1 = \frac{\int_{T_1}^{T_2} S_T(T)}{\int_{T_1}^{T_2} S_g} \quad \text{Eq. 3.1}$$

where  $T_1$  and  $T_2$  are the beginning and end of  $T_{RS}$  respectively.

The selection criteria # 6 states that the mean  $S_g$  should be at least 90 % of the  $S_T(T)$  anywhere over the  $T_{RS}$ . If not,  $F_2$  must be applied to the scaled ground motions over the entire spectrum. Factor  $F_2$  is computed with Eq. 3.2.

$$F_2 = \frac{0.9 \cdot S_T(T)}{\text{mean } S_g} \quad \text{Eq. 3.2}$$

Table 3.3 presents the  $F_2$  to adjust the mean  $S_g$  so that it is never less than 90 % of the  $S_T(T)$  within  $T_{RS}$ . The factor is applied to motions of scenarios T1-1, T1-2 and T3-1, while mean  $S_g$  of T2-1 is adequate within its  $T_{RS}$ .

Table 3.3 Second scaling factors  $F_2$  to adjust the match of  $S_g$  with  $S_T(T)$ 

| Scenario | Second scaling factor ( $F_2$ ) |
|----------|---------------------------------|
| T1-1     | 1.08                            |
| T1-2     | 1.16                            |
| T2-1     | 1.00                            |
| T3-1     | 1.09                            |

### 3.7 Selection of ground motions

Ground motions are selected for each scenario based on the aforementioned selection criteria. As mentioned, only one (1) horizontal component of motion is selected to represent the associated earthquake. Particular attention is given to the selection step because the input ground motion is one of the parameters that have the most impact on the response of small embankments (Bray, 2007, p.327-353; Athanasopoulos-Zekkos, 2010; Athanasopoulos-Zekkos and Seed, 2013).

In general, it is suggested that 11 ground motions per scenario are to be selected and used in simulations. Nevertheless, it is still acceptable to use 5 ground motions per scenario if the number of scenarios is superior to 2 (Tremblay et al., 2015). Hence, the number of records per scenario was reduced to 5 for scenarios T1-1, T1-2 and T2-1. Fewer motions (3) are chosen for T3-1 to reduce the computation time. Since, it represents motions scaled at long periods (1 to 10 s) and thus far from the natural period of the site, this scenario is not expected to produce high response. A total of 19 records is selected.

Tables 3.4 and 4.5 present the selected and scaled ground motions of scenarios T1-1, T1-2, T2-1 and T3-1 and their principal characteristics are presented, including the corresponding earthquake event, the year that the earthquake struck, the record sequence number (*RSN*) in the database, the horizontal component as numbered in the Flatfile by *PEER*,  $F_1$ , the mean period ( $T_m$ ), the moment magnitude  $M_w$ , the distance  $R$ , the duration of the record ( $D$ ), the  $V_{s30}$  and the *PGA*. Parameters are calculated after scaling by  $F_1$  and  $F_2$ .

The mean  $S_g$  per scenario including the scaled input motions are presented in Figure 3.7. Acceleration, velocity and displacement time series and Fourier amplitude spectrums of all input ground motions are presented in Annex A.

Table 3.4 Presentation of selected and scaled input ground motions – Scenarios T1-1 and T1-2

| <b>Event</b>                           | <b>Station</b>               | <b>Year</b> | <b>RSN</b> | <b>H</b> | <b>F<sub>1</sub></b> | <b>T<sub>m</sub><br/>(s)</b> | <b>M<sub>w</sub></b> | <b>R<br/>(km)</b> | <b>D<br/>(s)</b> | <b>V<sub>s30</sub><br/>(m/s)</b> | <b>PGA<br/>(g)</b> |
|--|------------------------------|-------------|------------|----------|----------------------|------------------------------|----------------------|-------------------|------------------|----------------------------------|--------------------|
| T1-1: 0.01 – 0.2 s [M5-6; R0-20 km]    |                              |             |            |          |                      |                              |                      |                   |                  |                                  |                    |
| Coalinga – 02                          | Oil Fields Fire Station      | 1983        | 381        | 1        | 1.06                 | 0.21                         | 5.1                  | 0.0               | 10.3             | 474                              | 0.268              |
| Gilroy                                 | Gilroy – Gavilan Coll.       | 2002        | 2019       | 2        | 0.92                 | 0.12                         | 4.9                  | 2.2               | 33.0             | 830                              | 0.251              |
| Fruili, Italy – 03                     | Tarcento                     | 1976        | 3553       | 1        | 1.16                 | 0.22                         | 5.5                  | 3.8               | 16.8             | 629                              | 0.248              |
| Umbria Marche<br>(Aftershock 8), Italy | Borgo – Cerreto Torre        | 1997        | 4377       | 1        | 1.10                 | 0.14                         | 5.2                  | 8.8               | 19.6             | 519                              | 0.205              |
| Mineral 2011-08-23                     | SE.NANPP                     | 2011        | 8571       | 2        | 1.11                 | 0.36                         | 5.7                  | 18.5              | 17.4             | 554                              | 0.313              |
| <i>Average</i>                         | Oil Fields Fire Station      | -           | -          | -        | <i>1.07</i>          | <i>0.21</i>                  | <i>5.3</i>           | <i>6.7</i>        | <i>19.4</i>      | <i>581</i>                       | <i>0.257</i>       |
| T1-2: 0.01 – 0.2 s [M6-7; R20-40 km]   |                              |             |            |          |                      |                              |                      |                   |                  |                                  |                    |
| San Fernando                           | Lake Hughes #4               | 1971        | 72         | 1        | 1.15                 | 0.21                         | 6.6                  | 19.4              | 35.0             | 600                              | 0.264              |
| San Fernando                           | Santa Anita Dam              | 1971        | 87         | 2        | 1.02                 | 0.18                         | 6.6                  | 30.7              | 29.7             | 667                              | 0.264              |
| Whittier Narrow – 01                   | Big Tujunga_Angeles<br>Nat F | 1987        | 598        | 2        | 1.29                 | 0.20                         | 6.0                  | 22.5              | 30.9             | 550                              | 0.312              |
| San Fernando                           | Lake Hughes #4               | 1971        | 72         | 2        | 1.38                 | 0.28                         | 6.6                  | 19.4              | 35.0             | 600                              | 0.253              |
| Big Bear – 01                          | Snow Creek                   | 1992        | 935        | 1        | 1.24                 | 0.17                         | 6.5                  | 37.0              | 60.0             | 524                              | 0.242              |
| Whittier Narrow – 01                   | Pacoima Kagel Canyon         | 1987        | 671        | 1        | 1.82                 | 0.38                         | 6.0                  | 31.6              | 40.0             | 508                              | 0.338              |
| <i>Average</i>                         |                              | -           | -          | -        | <i>1.30</i>          | <i>0.23</i>                  | <i>6.3</i>           | <i>28.3</i>       | <i>39.1</i>      | <i>570</i>                       | <i>0.284</i>       |

Table 3.5 Presentation of selected and scaled input ground motions – scenarios T2-1 and T3-1

| <b>Event</b>                         | <b>Station</b>            | <b>Yr</b> | <b>RSN</b> | <b>H</b> | <b>F<sub>1</sub></b> | <b>T<sub>m</sub><br/>(s)</b> | <b>M<sub>w</sub></b> | <b>R<br/>(km)</b> | <b>D<br/>(s)</b> | <b>V<sub>s30</sub><br/>(m/s)</b> | <b>PGA<br/>(g)</b> |
|--------------------------------------|---------------------------|-----------|------------|----------|----------------------|------------------------------|----------------------|-------------------|------------------|----------------------------------|--------------------|
| T2-1: 0.2 – 1.0 s [M6-7; R20-40 km]  |                           |           |            |          |                      |                              |                      |                   |                  |                                  |                    |
| San Fernando                         | Lake Hughes #4            | 1971      | 72         | 2        | 1.00                 | 0.28                         | 6.6                  | 19.4              | 35.0             | 600                              | 0.156              |
| North Palm Springs                   | Anza – Red Mountain       | 1986      | 511        | 1        | 1.56                 | 0.22                         | 6.1                  | 38.2              | 11.0             | 680                              | 0.151              |
| Whittier Narrows – 01                | Big Tujunga_Angeles Nat F | 1987      | 598        | 2        | 1.20                 | 0.20                         | 6.0                  | 22.5              | 30.9             | 550                              | 0.248              |
| Northridge – 01                      | Big Tujunga_Angeles Nat F | 1994      | 954        | 1        | 0.75                 | 0.24                         | 6.7                  | 19.1              | 30.0             | 550                              | 0.127              |
| San Simeon, California               | San Luis Obispo           | 2003      | 4016       | 1        | 1.14                 | 0.47                         | 6.5                  | 31.3              | 77.0             | 494                              | 0.188              |
| <i>Average</i>                       |                           | -         | -          | -        | <i>1.13</i>          | <i>0.28</i>                  | <i>6.4</i>           | <i>26.1</i>       | <i>36.8</i>      | <i>575</i>                       | <i>0.174</i>       |
| T3-1: 1.0 – 10 s [M7-7.5; R40-60 km] |                           |           |            |          |                      |                              |                      |                   |                  |                                  |                    |
| Irpinia, Italy – 01                  | Irpinia_Italy-01          | 1980      | 293        | 2        | 1.10                 | 0.69                         | 6.9                  | 59.6              | 52.8             | 593                              | 0.048              |
| Irpinia, Italy – 01                  | Irpinia_Italy-01          | 1980      | 294        | 2        | 0.96                 | 0.90                         | 6.9                  | 51.7              | 31.9             | 496                              | 0.035              |
| Taiwan, SMART1 (45)                  | Taiwan SMART1(45)         | 1986      | 572        | 2        | 0.79                 | 0.46                         | 7.3                  | 51.3              | 33.0             | 672                              | 0.117              |
| <i>Average</i>                       |                           | -         | -          | -        | <i>0.95</i>          | <i>0.68</i>                  | <i>7.0</i>           | <i>54.2</i>       | <i>39.2</i>      | <i>587</i>                       | <i>0.067</i>       |

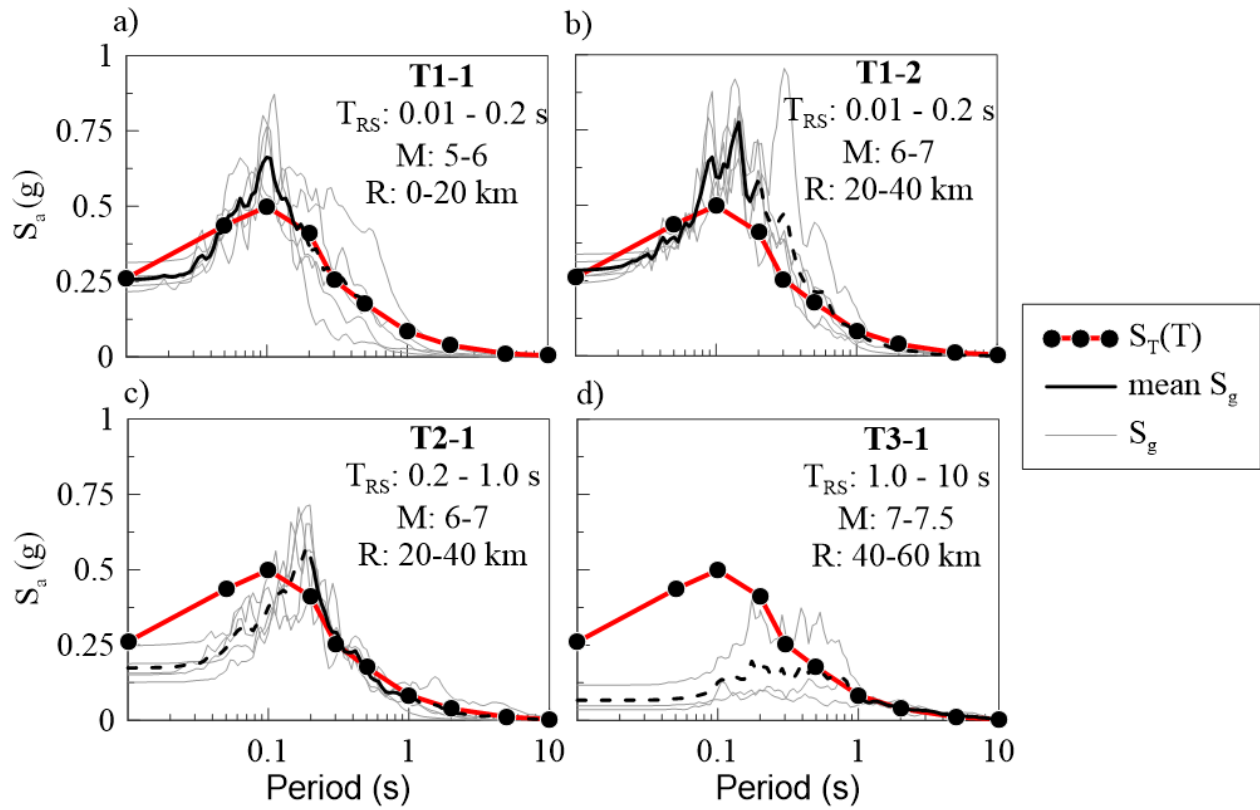


Figure 3.7 Illustration of mean  $S_g$  matched to the  $S_T(T)$  over  $T_{RS}$  for scenarios a) T1-1, b) T1-2, c) T2-1 and d) T3-1

### 3.7.1 Compatibility issues

#### Scenarios T1-1 and T1-2

The shape of  $S_g$  within the  $T_{RS}$  was the most limiting criterion for scenarios T1-1 and T1-2. Figure 3.8 shows the shape of  $mean S_g$  of T1-1 and T1-2 before and after scaling. Before scaling, the  $mean S_g$  is well below the  $S_T(T)$  and thus needs to be adjusted upwards. However, after scaling, the  $mean S_g$  exceeds significantly  $S_T(T)$  between 0.05 to 10 s, especially for T1-2 which represents stronger events. Hence, scenarios T1-1 and T1-2 do not respect the criteria # 3 due to the exceedance of  $S_g$  outside of  $T_{RS}$ . This leads to an acceptable  $F_I$  but a poor match between  $S_g$  and  $S_T(T)$ , which was unavoidable.

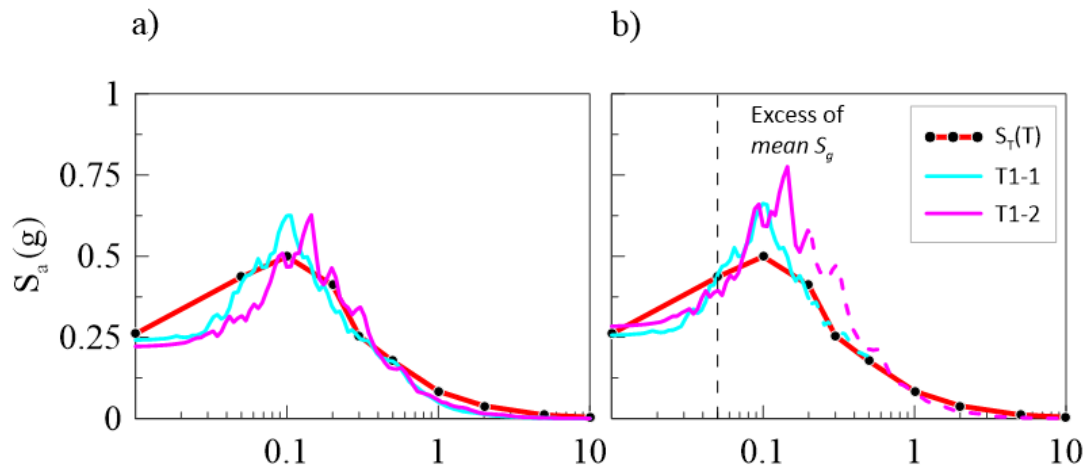


Figure 3.8 Incompatibility of the shape of mean  $S_g$  of scenarios T1-1 and T1-2 a) before scaling and b) after scaling

It is important to mention that, having considered a period range  $T_R$  that spans from both extremity of the range defined by the *NBCC 2015* (0.01 to 10 s) has significantly increased the difficulty in matching the  $S_g$  with the  $S_T(T)$ . Indeed, available motions with  $M-R$  of interest are generally taken from NGA-West 2 and thus medium to long-period energy are dominating their frequency content since rock conditions in the West are generally poorer than in the East. Hence, the shape of  $S_g$  of the available motions is usually lower in short periods and higher in medium to long periods which is the opposite than the spectrum of the site. Thus, a higher scaling factor  $F_I$  is needed to adjust the shape of  $S_g$  so that it matches the  $S_T(T)$  in short periods. However, by doing so, the  $S_g$  far exceeds the shape of  $S_T(T)$  in medium to long periods hence potentially leading to an exaggerated response of the dike during simulations.

If this project has considered a  $T_R$  which spans on either side of the natural period of the site and not the entire  $T_R$ , the match between the  $S_g$  and  $S_T(T)$  might be enhanced. Besides, for short periods structures such as short buildings, selection and scaling of motions might be difficult to perform due to this compatibility issue.

### **Scenarios T2-1 and T3-1**

Motions of scenario T3-1 matched adequately the  $S_T(T)$  within its  $T_{RS}$  but violated the selection criterion #3 with  $S_g$  above 75 % of the  $S_T(T)$  outside its  $T_{RS}$ . Few to no candidate ground motions respect this criterion in scenario T3-1, and as a result the  $PGA$  of the scenario T3-1 is much lower than the design values. For scenario T2-1, besides that the peak of  $S_g$  slightly exceeds the  $S_T(T)$ , the shape of  $S_g$  matches adequately the  $S_T(T)$  in the medium period range.

### **3.7.2 Ground motions intensity measures (IM) and number of equivalent number of stress cycles**

Ground motions may be characterized in terms of amplitudes, frequency content and duration. Each  $IM$  measure one or several characteristics. The definition of each  $IMs$  is provided in chapter 2: Literature review. Figure 3.9 shows the  $IM$  and average  $IM$  for each scenario.

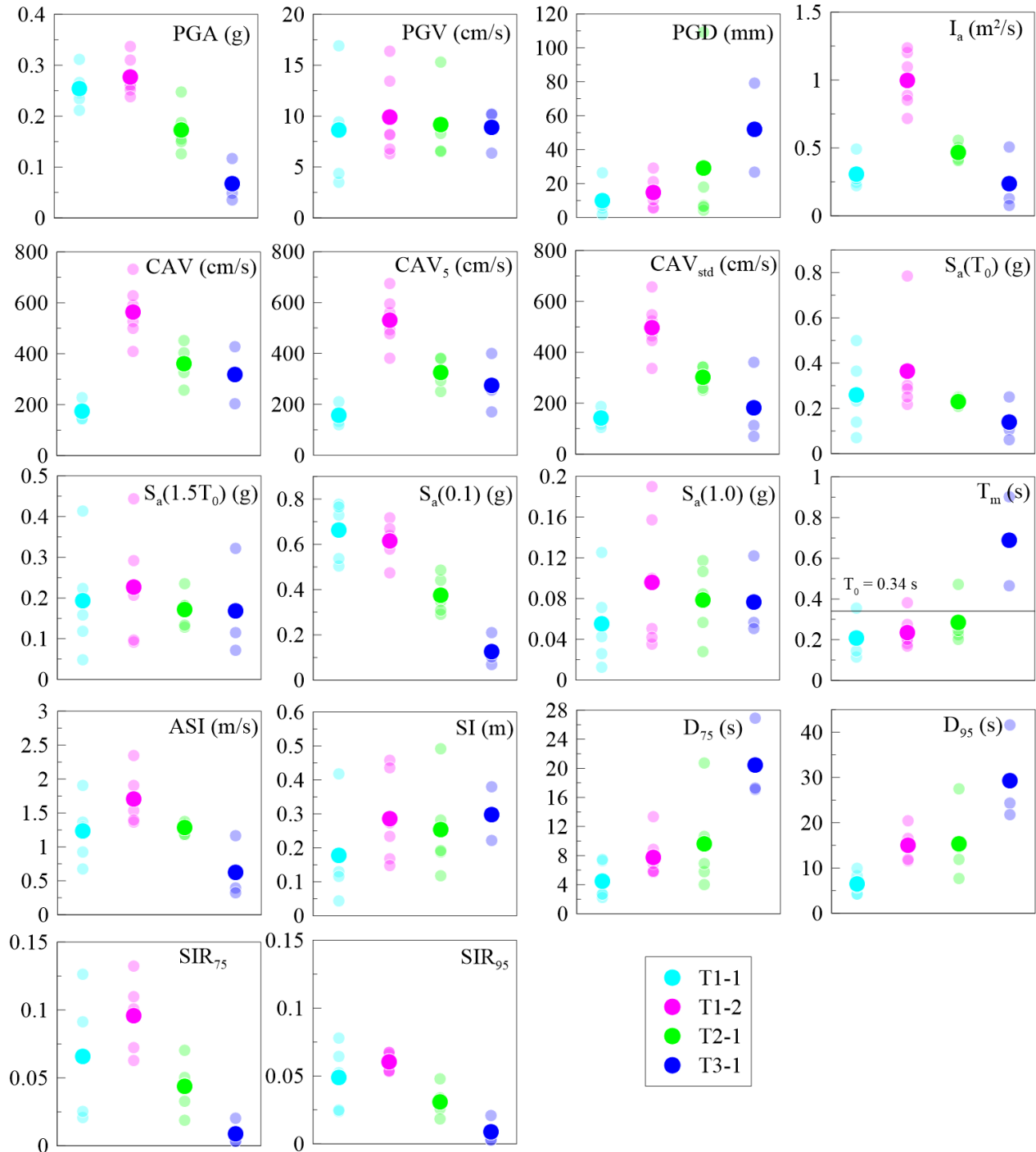


Figure 3.9 Input ground motions  $IM$  and average  $IM$  for all scenarios

Based on Figure 3.9, scenario T1-2 is the scenario that may produce the strongest response in the model with frequency content relatively close to  $T_0$ , high amplitude acceleration, with the highest  $PGA$  and  $S_a(T_0)$  and moderate duration with  $D_{75}$  of 7.8 s. Parameters measuring both intensity and duration such as  $I_a$ , cumulative absolute velocities and shaking-intensity rates all showed that T1-

2 contains the strongest motions. Parameters that indicate the potential response of structures most likely to resonate in the mid-periods, such as concrete and earth dams (*ASI* and *SI*) also showed that T1-2 scored the highest values.

Scenario T1-1 shows strong amplitude with *PGA* and  $S_a(T_0)$  of 0.25 g and 0.21 g respectively and frequency content relatively close to  $T_0$  with 0.26 s compared to 0.34 s. However, T1-1 mostly contains short-duration motions and as a result, the amplitude-based *IM* such as  $I_a$  and cumulative absolute velocities have lower values. Weaker response induced by T1-1 compared to T1-2 is expected.

Although scenario T2-1 showed moderate intensity and duration, its frequency content is the closest to  $T_0$  thus an amplified response within the model is to be expected. For scenario T3-1, although its motions have the longest-duration with  $D_{75}$  of 20.4 s, its peak accelerations are weak and its motions frequency content is far from  $T_0$ . As a result, the response of the model is expected to be low.

In addition, the number of equivalent stress cycles of each motion might be calculated to evaluate the potential for liquefaction of each scenario. The number of equivalent stress cycles is computed at a reference level of  $0.65\tau_{\max}$ , defined based on the recommendations of Seed et al. (1975). The Figure 3.10 presents number of equivalent cycles a function of the moment magnitude, along with the commonly used Idriss (1999) relationship.

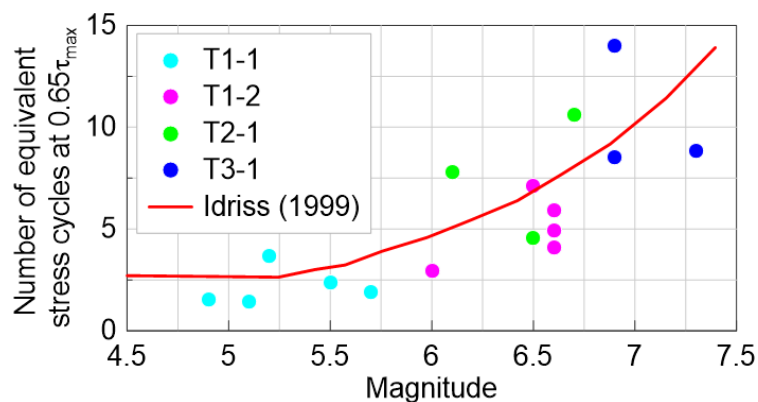


Figure 3.10 Number of equivalent stress cycles at  $0.65\tau_{\max}$

Contrary to the observations made above based on the input motions *IM*, the scenario T3-1 appears to be the scenario most likely to trigger liquefaction with input motions equivalent to 8 to 12 cycles

at an average stress of  $0.65\tau_{\max}$ . This is due to the much longer duration of its input motions with an average  $D_{75}$  of  $\pm 20$  s.

## CHAPTER 4 GROUND MOTIONS PROCESSING

### 4.1 Introduction

Recording instruments can induce noise and error in ground motion records. Thus processing of the selected ground motions must be performed to correct the records so that they can be used as input motions. This section describes step-by-step the ground motion processing procedure.

### 4.2 Filtering procedure

Figure 4.1 presents the steps followed for record processing. The steps are mainly inspired by the PEER NGA post-processing procedure. The main correction is the application of an acausal Butterworth filter applied in the frequency domain. To achieve zero-phase shift in the records, zero-pads are added at both ends. Additionally, tapers are added between the pads and the records to avoid ringing caused by abrupt jumps.

However, zero pads are stripped from the motions after filtering and scaling to avoid longer computational time in *FLAC*. Padstripping may result in a baseline drift in the displacement and velocity time series, thus resulting in an incompatibility between the acceleration and the integrated time series. To avoid drift in the baseline, initial values of the velocity and displacement padded time series are put back in the padstripped velocity and displacement time series (Boore et al., 2012).

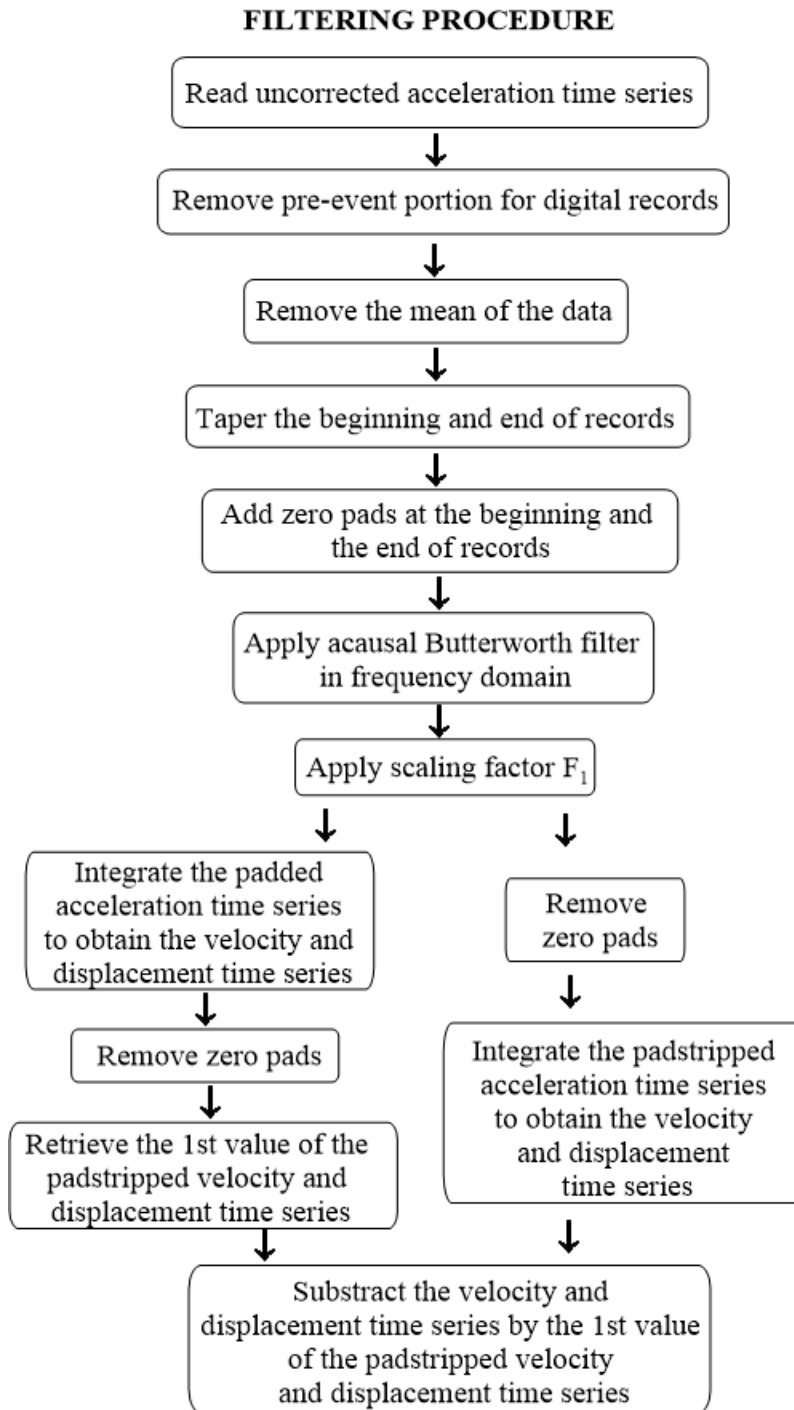


Figure 4.1 Input ground motions processing procedure (inspired by PEER NGA post-processing procedure)

As digital instruments are continuously recording (does not start to record when triggering value is reached), pre-event portions of the earthquake are sometimes found in the records and must be removed. After that, the mean of the acceleration time series is subtracted.

As mentioned above, records were zero-padded. To avoid discontinuity between the end values of the records and the zero-pads, a taper function is added between the zero-pads and the records. Details on the application of tapers and zero pads are presented in the next section. Then, the acausal filter (Butterworth) is applied to the ground motion in the frequency domain.

The padstripping process is performed in 2 steps; (1) the initial conditions of the velocity and displacement time series obtained from integration of the padded motion are recovered and (2) in parallel, the zero-pads are removed from the acceleration time series, and the velocity and displacement time series are obtained by integration of the padstripped acceleration. Then, the initial conditions are applied to the velocity and displacement time series obtained by integration of the padstripped acceleration.

#### **4.2.1 Tapers and zero-pads**

Tapers and zero-pads and the way they are introduced in the records are illustrated in Figure 4.2 by zooming in at the end of a ground motion. Tapers are added before the beginning of the motion and at the end of it. It is important to add the tapers as failure to do so will result in spurious high-frequency spikes during the filtering process (Converse and Brady, 1992). The tapers correspond to a cosine half-bell curve to smooth the discontinuity between the zero-pads and the acceleration time series. The end values of the unpadded acceleration time series will be multiplied by the taper function and the zero value of the taper will be multiplied by the last zero of the leading pad and by the first zero of the trailing pad. In this project, the tapers have a total length of 0.2 second per record, as the taper after the leading pad and before the trailing pad has a length of 0.1 second each.

The zero-pads should have sufficient length to provide stability during the filtering process. The length of the paddings depends on the order of the filter ( $n$ ) and the filter corner frequency ( $f_c$ ) which corresponds to the low-cut frequency. The minimal length of the zero pads is suggested by Converse and Brady (1992) as presented in Figure 4.3. and is added at both ends of records.

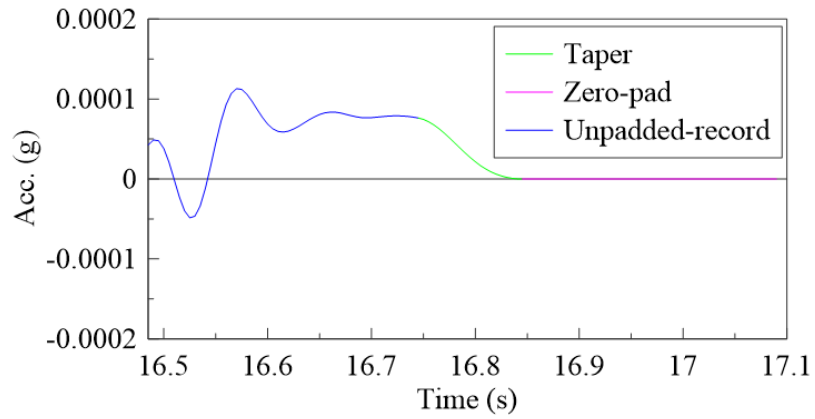


Figure 4.2 Zero-pads and tapers at the extremity of the ground motion

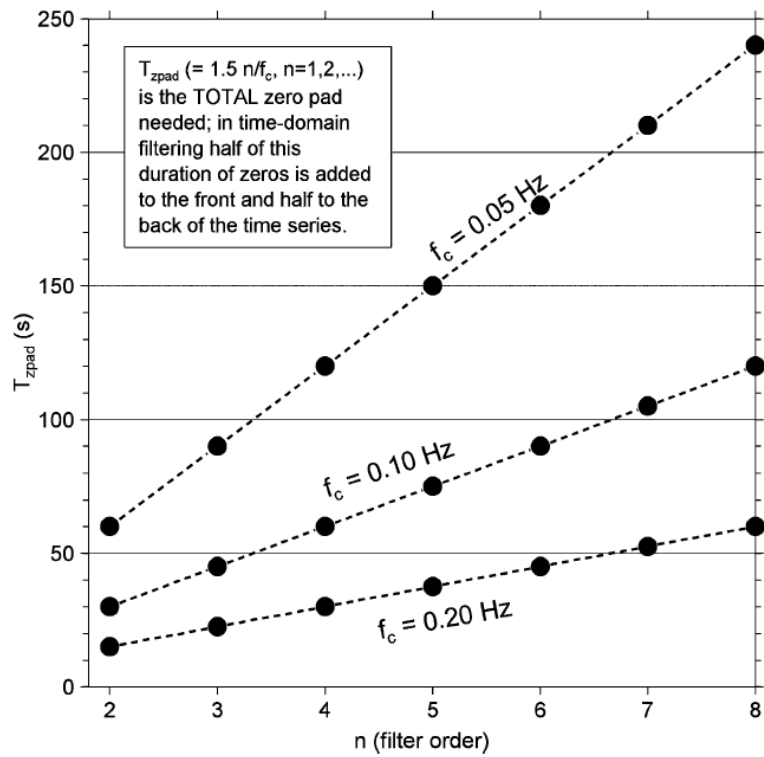


Figure 4.3 Minimal length of the zero-pads (Converse and Brady, 1992)

## 4.2.2 Low-cut and high-cut frequencies

Low and high-frequency noise is removed during filtering by using a high-pass and low-pass butterworth filter defined by a low-cut ( $LC$ ) and high-cut ( $HC$ ) frequency corners. The  $HC$  corresponds to the frequency above which noise is present and the  $LC$  the frequency below which there is noise. For example, Figure 4.4 shows the form of a  $LC$  filter, defined by a  $f_c$  of 0.7 Hz and a  $n$  of 4. It filters out the motion below the  $LC$  while acting as a ramp with the desired motion to avoid abrupt jump in the record. The higher the  $n$ , the more rapid the roll-off of the filter is.

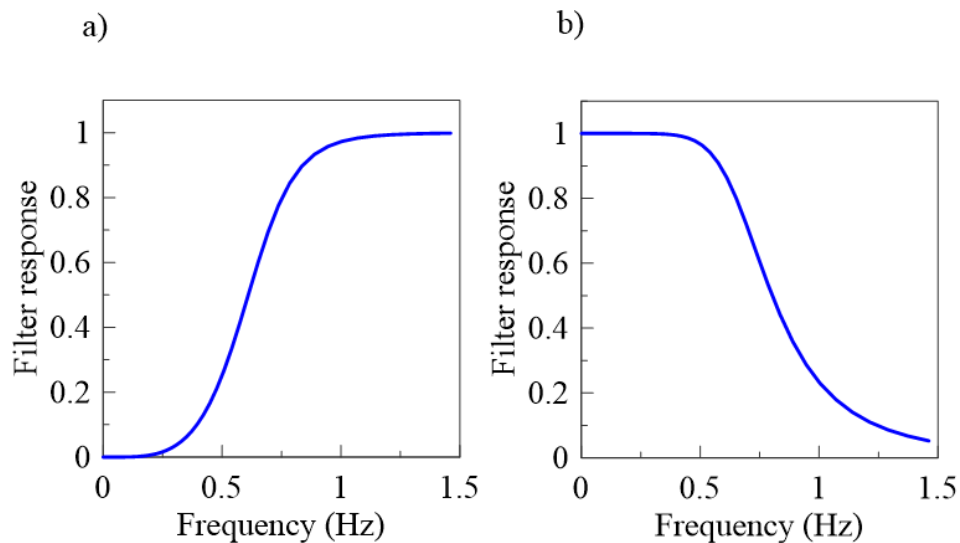


Figure 4.4 Illustration of a typical Butterworth a)  $LC$  filter and b)  $HC$  filter with a  $f_c$  of 0.7 Hz and a  $n$  of 4

Figure 4.5. shows an example of filtering at low and high frequency using the record RSN381H1 where high and low frequencies are filtered out. The Figure 4.6 shows the effect of filtering on the time series. Even though hard to observe with naked eyes, high spikes in the acceleration time series are reduced and it is reflected in the displacement time series which generally magnifies the effects of processing due to two times of integration.

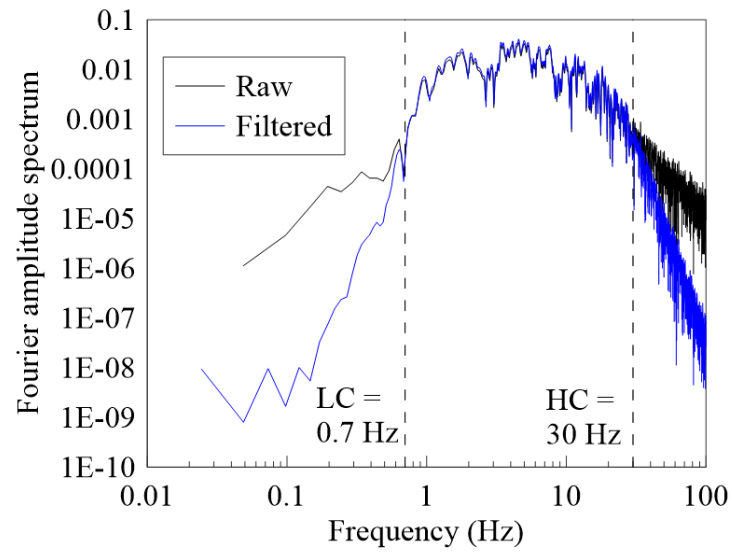


Figure 4.5 Illustration of the effects of motion processing on RSN381H1 with  $LC$  of 0.7 Hz,  $HC$  of 30 Hz and  $n$  of 4

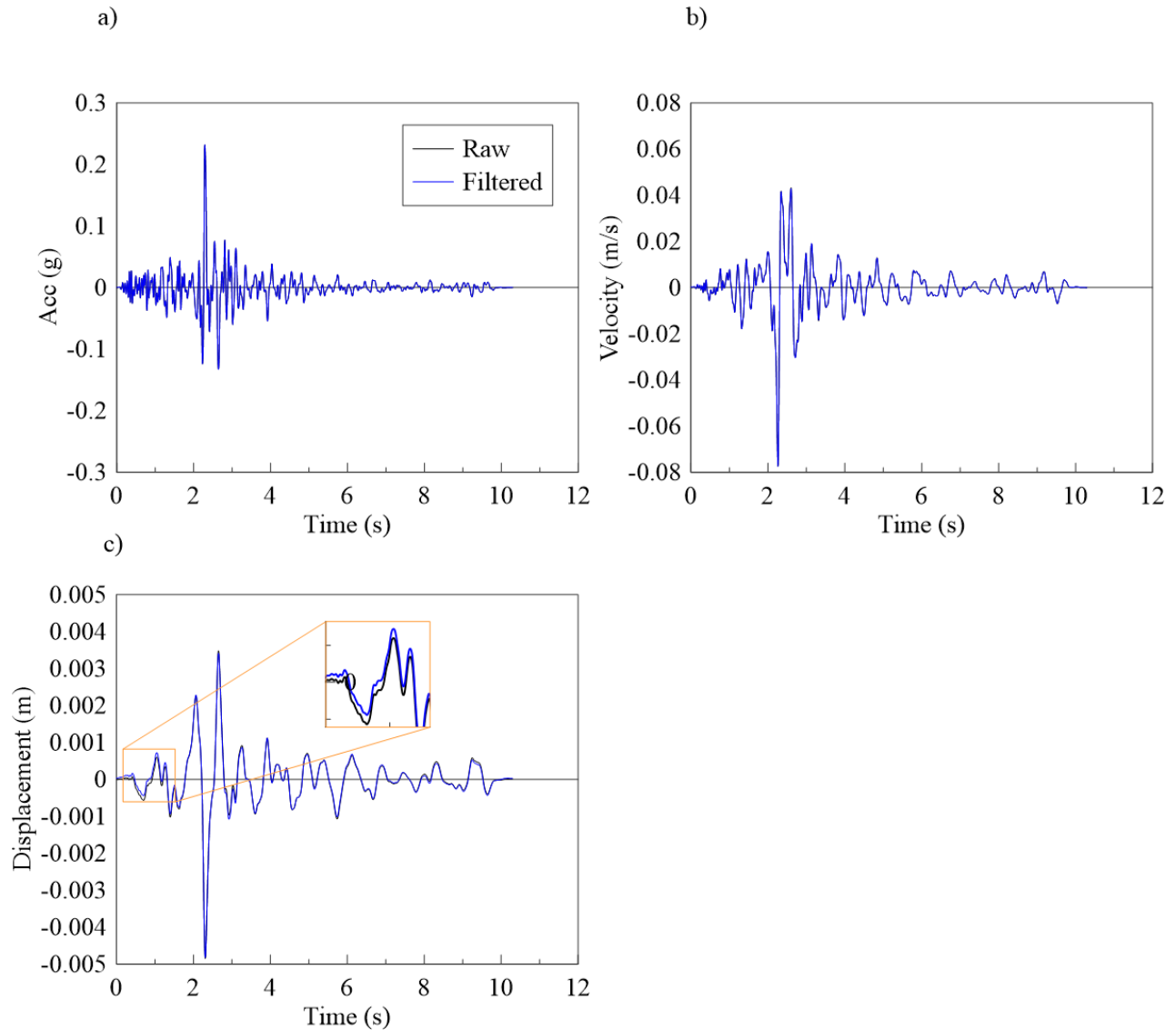


Figure 4.6 Illustration of the effects of motion processing of RSN381H1 on the a) acceleration, b) velocity and c) displacement time series

For most ground motions from the NGA-West 2 database, the *LC* and *HC* are given in the Flatfile available at the Pacific Earthquake Engineering Research Center (*PEER*) website (Ancheta et al., 2013). Those parameters are missing for certain motions and they are defined by trial-and-error by checking the Fourier Amplitude Spectrum (*FAS*). The *LC* and *HC* of the record from the NGA-East database are taken directly from the database (Goulet et al., 2018). The *LC* and *HC* for each motion are presented in table 4.1.

Table 4.1 *LC* and *HC* of selected input ground motions, taken from the Flatfile

| <b>Scenario</b> | <b>Event</b>                        | <b>RSN</b> | <b>H</b> | <b>LC<br/>(Hz)</b> | <b>HC<br/>(Hz)</b> |
|-----------------|-------------------------------------|------------|----------|--------------------|--------------------|
| T1-1            | Coalinga – 02                       | 381        | 1        | 0.7                | 30                 |
|                 | Gilroy                              | 2019       | 2        | 0.3                | 40                 |
|                 | Fruili, Italy – 03                  | 3553       | 1        | 0.7                | 20                 |
|                 | Umbria Marche (Aftershock 8), Italy | 4377       | 1        | 0.2                | 60                 |
|                 | Mineral 2011-08-23                  | 8571       | 2        | 0.229              | 25                 |
| T1-2            | San Fernando                        | 72         | 1        | 0.2                | 35                 |
|                 | San Fernando                        | 72         | 2        | 0.1                | 35                 |
|                 | San Fernando                        | 87         | 2        | 0.3                | 35                 |
|                 | Whittier Narrow – 01                | 598        | 2        | 0.1                | 30                 |
|                 | Big Bear – 01                       | 935        | 1        | 0.24               | 46                 |
|                 | Whittier Narrow – 01                | 671        | 1        | 0.13               | 23                 |
| T2-1            | San Fernando                        | 72         | 2        | 0.1                | 35                 |
|                 | North Palm Springs                  | 511        | 1        | 0.23               | 40                 |
|                 | Whittier Narrows – 01               | 598        | 2        | 1                  | 30                 |
|                 | Northridge – 01                     | 954        | 1        | 0.33               | 30                 |
|                 | San Simeon, California              | 4016       | 1        | 0.001              | 40                 |
| T3-1            | Irpinia, Italy – 01                 | 293        | 2        | 0.08               | 22                 |
|                 | Irpinia, Italy – 01                 | 294        | 2        | 0.12               | 23                 |
|                 | Taiwan, SMART1 (45)                 | 572        | 2        | 0.08               | 23                 |

## CHAPTER 5      DESCRIPTION OF THE WATER-RETAINING DIKE STUDIED

### 5.1 Introduction

This project investigates the response of an existing water retaining earth dike to different earthquake input ground motions using the software *FLAC*. The height of the dike is  $\pm 8.1$  m and its length is  $\pm 600$  m. The dike is made of a fine-grained non-plastic core. It sits on a natural deposit of silt of medium density becoming loose at depth following by the bedrock. As the embankment is a man-made structure, its conditions are relatively uniform along the dike, except for the depth of the bedrock which can vary as much as  $\pm 13.1$  m. Given that the thickness of the soil has an important impact on the predicted response, different cross sections of varying subsoils thicknesses are defined and their seismic responses are compared using the software *DEEPSOIL*. One-dimensional dynamic analyses are conducted on each cross-section and the section returning the highest amplification at its crest is selected based on the results. Using *FLAC*, the fundamental period  $T_0$  of the selected cross-section is found to be 0.34 s. The liquefaction potential is also evaluated using simplified liquefaction triggering analysis methods.

## 5.2 Geometry of the embankment

The earth-fill dike is a  $\pm 8.1$  m-high zoned embankment with a crest width of 8.2 m built on a relatively flat ground. Its core was built with compacted non-plastic silt and a layer of clay was placed on the upstream face of the embankment to lower the water level. Both upstream and downstream faces are protected with a thick layer of granular soils as well as the crest. The dike is founded on fine-grained non-cohesive soils. Figure 5.1. presents the geometry of the embankment.

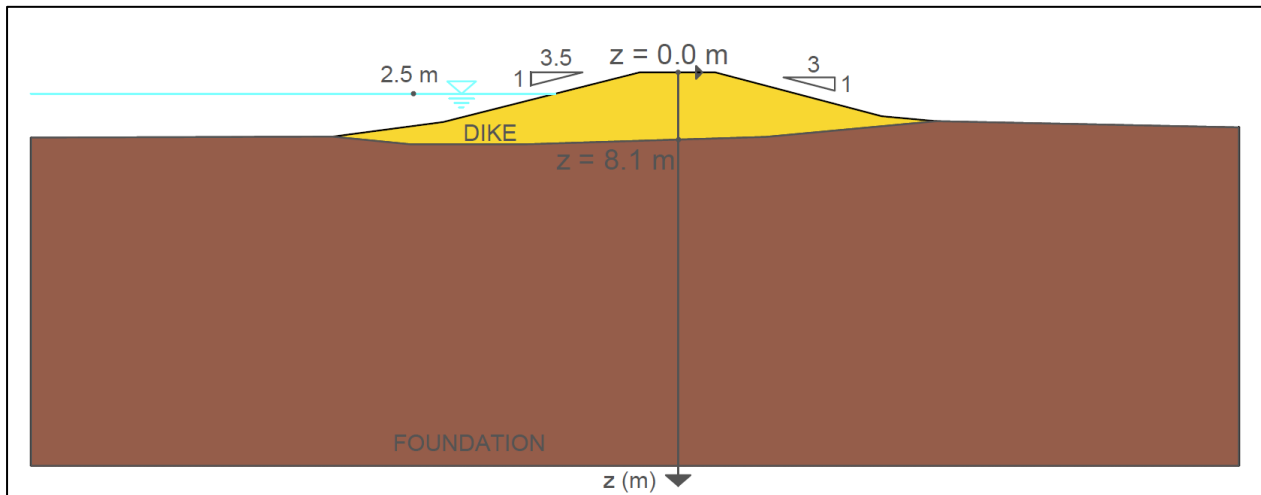


Figure 5.1 Section of the embankment and its surrounding areas

### 5.3 Geotechnical properties

The nature and the geotechnical properties of the embankment and subsoils are presented herein. All conclusions and interpretations are based on technical reports presenting results of *SPT* and *MASW* tests. Three (3) *SPT* are performed on the dike (BH-1), at the landside toe (BH-2) and at the far-field (BH-3). The location of the boreholes is illustrated in Figure 5.2.

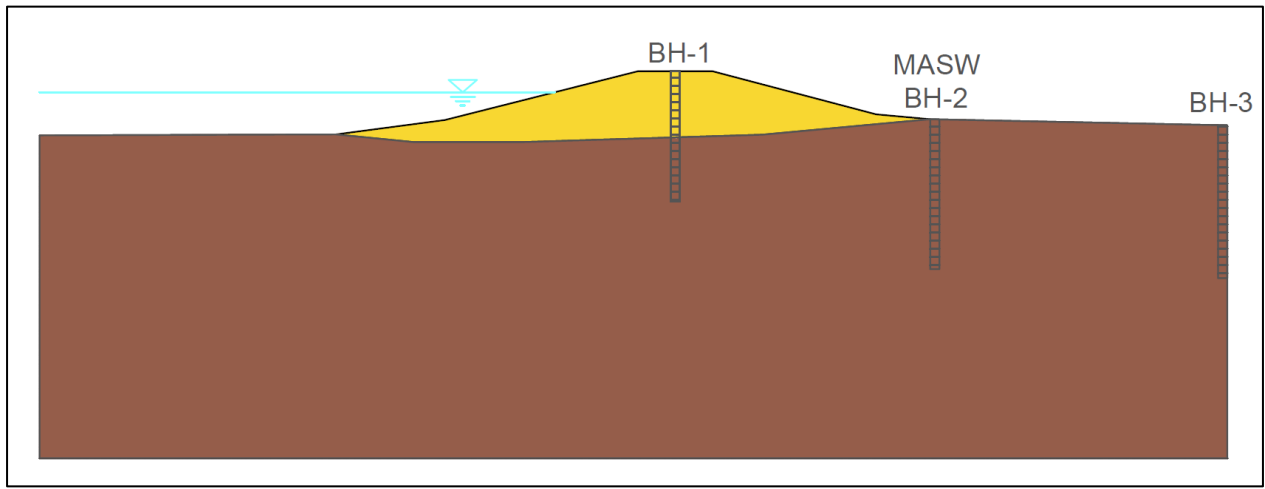


Figure 5.2 Location of the boreholes and the *MASW* test

The boreholes reports are presented in Annex B and the results are interpreted in the sections below as well as the results of the *MASW* test.

### 5.3.1 Embankment

The cross-section of the dike is illustrated in Figure 5.3. Its core is built with a compacted fine non-cohesive material of ML to SM type based on the unified soil classification system (*USCS*). A 90 cm-thick upstream clay face is placed over the core to reduce seepage in the dike. Then, a rockfill riprap covers the upstream face to protect the integrity of the dike against waves. A berm made of gravel and sand extends to the downstream toe. The downstream shoulder and the crest are also built with gravel and sand that acts as a coarse filter between the riprap and the clay face.

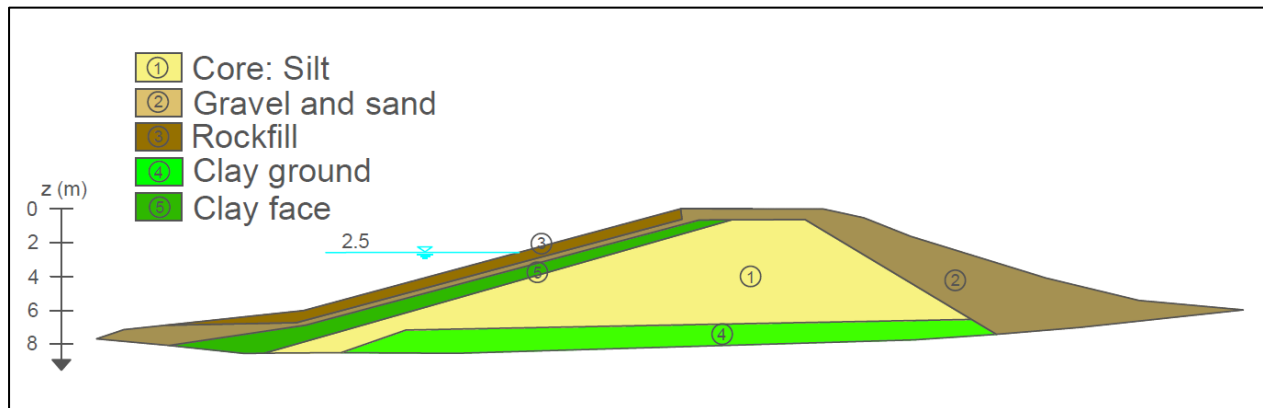


Figure 5.3 Detailed section of the embankment with identified types of soils

Spatial variability within the embankment is deemed negligible. Materials were all compacted during construction with heavy machines, therefore, materials may be considered dense to very dense.

Geotechnical parameters are estimated based on literature values, as explained subsequently or calculated based on the results of SPT and are presented in Table 5.1. Geotechnical parameters include the density ( $\rho$ ), normalized shear-wave-velocity ( $V_{s1}$ ), friction angle ( $\phi$ ), cohesion ( $c$ ), plasticity index ( $PI$ ), overconsolidation ratio ( $OCR$ ), Poisson's ratio ( $\mu$ ), bulk modulus ( $K$ ) and shear modulus ( $G$ ).

Table 5.1 Geotechnical properties of the embankment

| <b>Materials</b> | $\rho$<br>(kg/m <sup>3</sup> ) | $V_{sI}$<br>(m/s) | $\phi$<br>( $^{\circ}$ ) | $c$<br>(kPa) | $PI$ | $OCR$ | $\mu$ | $K$<br>(MPa) | $G$<br>(MPa) |
|------------------|--------------------------------|-------------------|--------------------------|--------------|------|-------|-------|--------------|--------------|
| Core: Silt       | 2039                           | 266               | 41                       | 0            | 0    | -     | 0.3   | 312          | 144          |
| Gravel and sand  | 1937                           | 340               | 45                       | 0            | 0    | -     | 0.3   | 482          | 222          |
| Rockfill         | 2141                           | 500               | 50                       | 0            | 0    | -     | 0.3   | 1160         | 535          |
| Clay ground      | 1937                           | 300               | 26                       | 7            | 30   | 2.5   | 0.3   | 378          | 174          |
| Clay face        | 1937                           | 200               | 26                       | 7            | 30   | 2.5   | 0.3   | 168          | 78           |

For the core, geotechnical parameters except for  $\mu$  are calculated based on  $N$  indices. As described in chapter 2: literature review, the  $V_{sI}$  is calculated with the relation proposed by Seed and Idriss (1970) and the  $K$  and  $G$  are based on  $\mu$  which was assigned a common value of 0.3 (Bowles, 1997, p. 123).

For other materials than the core, since no  $N$  indices were available, literature values were assigned to the  $\rho$  and  $V_{sI}$  considering that the soils were compacted to 95 % of Proctor during construction.

For clayey materials, parameters were defined considering drained conditions (long term). The  $\phi$  and  $c$  were assigned common values of  $26^{\circ}$  and 7 kPa respectively. Literature values are assigned to  $PI$  and  $OCR$ . A plasticity Index of 30 is a typical value of clays in Quebec (Leroueil and Tavenas, 1983) and the  $OCR$  of 2.5 reflects their slight overconsolidated state since materials are compacted and with the weight of the embankment over the years.

### 5.3.2 Foundation, bedrock and water level

Based on the information obtained from the boreholes, at the centerline of the dike, the water level was measured  $\pm 7.9$  m underneath the crest, hence, in the solid ground clay (BH-1). Then, at the downstream toe, the piezometric line drops at a depth of 4.9 m from the surface (BH-2) and continues dropping to 7.7 m in the landside (BH-3).

The boreholes reveal a deposit of non-plastic silt underneath the embankment, which is characterized as ML type based on *USCS*. The proportion of silt varies in the deposit between approximately 55 to 95 % with an average of 73 % and the proportion of sand varies between 5 to 40 % with an average of 20 %. The average thickness of the deposit is about 13.8 m, and the proportion of sand increases with depth.

Figures 5.4a and 5.4b respectively present the  $(N_1)_{60}$  indices corrected for the overburden pressure and energy ratio and the  $V_{s1}$  profile of the deposit of silt based on the results of *MASW* performed at the right of BH-2.

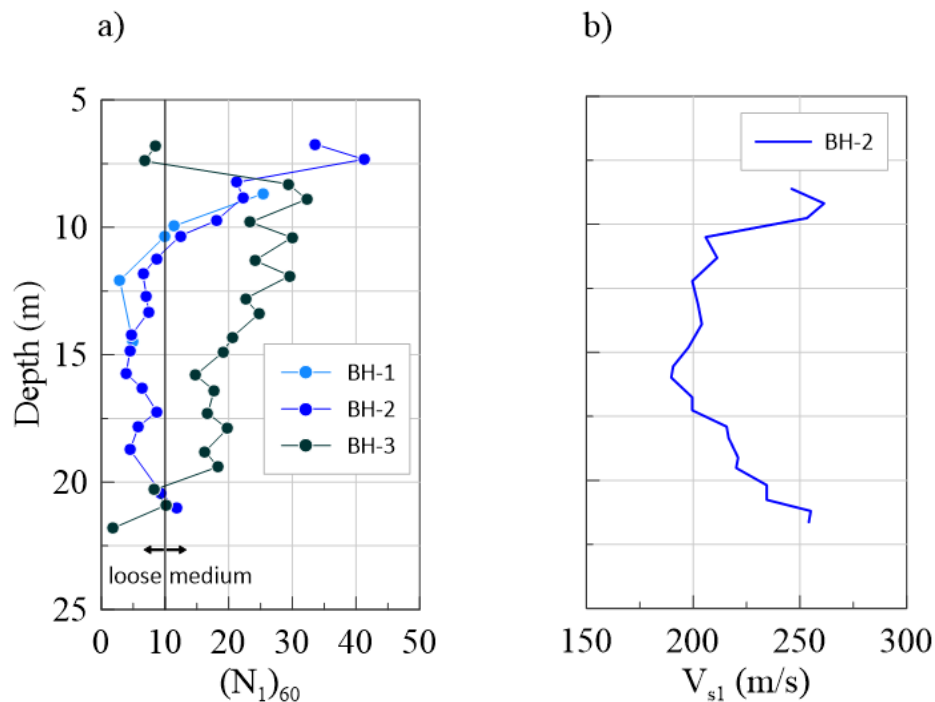


Figure 5.4 a)  $(N_1)_{60}$  profile of foundation soils for BH-1 to BH-3 and b)  $V_{s1}$  profile at BH-2

The  $(N_I)_{60}$  indices indicate a variation of density within the foundation soils. The soils underneath the dike (BH-1) and its toe (BH-2) are of medium density becoming loose starting at depths of 11.2 and 10.8 m respectively. At the free-field (BH-3), the medium silt becomes loose at 19.9 m.

Based on the variation of density observed with the  $(N_I)_{60}$  indices and the values of  $V_{sI}$ , it is considered that the  $\pm 3$  m-thick upper layer of the foundation soils is of medium density with an average  $V_{sI}$  of 225 m/s, and the lower layer is of loose density, with an average  $V_{sI}$  of 210 m/s at the right of the centerline of the dike. Increased  $V_{sI}$  are noted at the base of the deposit, possibly due to the soil being more sandy than silty (Yang and Liu, 2016; Goudarzy et al., 2016).

The bedrock is composed of an amphibole with a hardness generally comprised between 5 and 6. The rock is stiff and of excellent quality with rock quality designation ( $RQD$ ) indices greater than 90. Based on the depth of the  $MASW$  test, the bedrock might be located at a depth of 22 m at the right of the centerline of the dike. Based on local knowledge of geology, the rock might be considered as hard rock, corresponding to a  $NEHRP$  class A (Finn and Wightman, 2003;  $NEHRP$ , 1994).

Table 5.2 presents the geotechnical parameters of the foundation soils and the bedrock:  $\rho$ ,  $V_{sI}$ ,  $\phi$ ,  $c$ ,  $\mu$ ,  $K$  and  $G$ . For the foundation soils, the  $\rho$  and  $\phi$  are calculated based on the  $N$  indices and adjusted based on literature values (e.g. University of Mississippi, 2015) while  $K$  and  $G$  are calculated based on the  $V_{sI}$ . A common value of 0.3 is assigned to the Poisson ratio  $\mu$  (Bowles, 1997, p. 123).

The bedrock is modeled as an elastic rock and literature values are assigned considering an excellent quality of the rock.

Table 5.2 Geotechnical properties of foundation soils and bedrock

| Materials   | $\rho$<br>(kg/m <sup>3</sup> ) | $V_{s1}$<br>(m/s) | $\Phi$<br>( $^{\circ}$ ) | $c$<br>(kPa) | $\mu$ | $K$<br>(MPa) | $G$<br>(MPa) |
|-------------|--------------------------------|-------------------|--------------------------|--------------|-------|--------------|--------------|
| Medium silt | 2039                           | 225               | 34                       | 0            | 0.3   | 224          | 103          |
| Loose silt  | 1988                           | 210               | 29                       | 0            | 0.3   | 197          | 91           |
| Bedrock     | 2701                           | 1500              | 50                       | 0            | 0.3   | 13 169       | 6 078        |

The Figure 5.5 presents an illustration of the cross-section of the dike including the thickness of each layer of the foundation soils and the piezometric line.

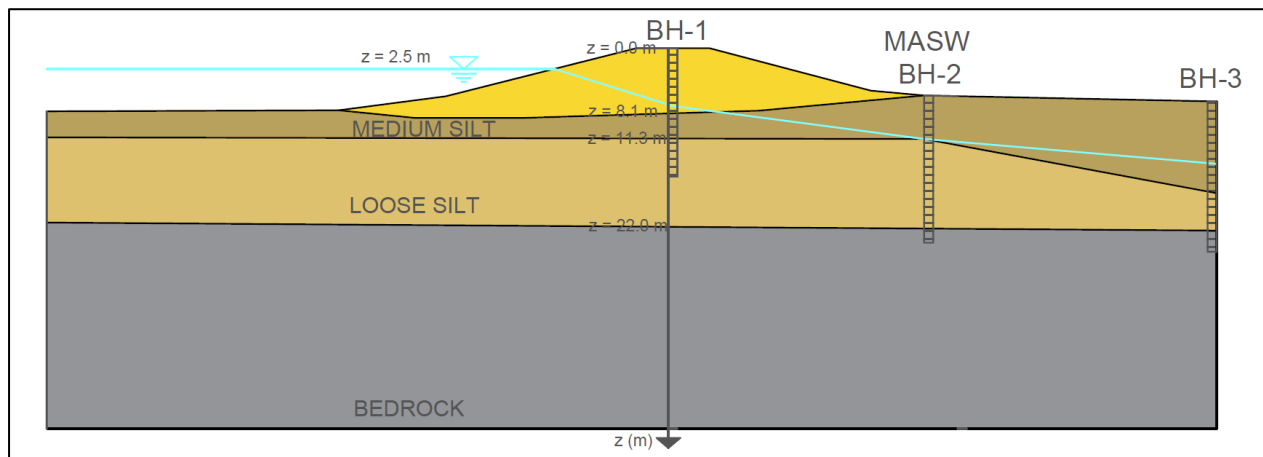


Figure 5.5 Illustration of the cross-section of the dike including the thickness of each layer of the foundation soils and the piezometric line

## 5.4 Dynamic properties

This section presents material dynamic properties such as the *MRD* curves.

### 5.4.1 Minimum Damping ratio $D_{min}$

The  $D_{min}$  is obtained from Darendeli (2001) and computed as a function of the mean effective stress  $\sigma'_m$ ,  $PI$ ,  $OCR$ , the frequency  $f$  and several coefficients  $\phi_i$  (Eq. 5.1).

$$D_{min} = (\phi_6 + \phi_7 \cdot PI \cdot OCR^{\phi_8}) \left( \frac{\sigma'_m}{P} \right)^{\phi_9} (1 + \phi_{10} \cdot \ln(f)) \quad \text{Eq. 5.1}$$

Because the variations within each layer are deemed small, an average value is attributed to each material. Table 5.3 presents the values of  $D_{min}$ , note that a value of 0.2 % is arbitrarily assigned to the bedrock based on literature values.

Table 5.3 Materials damping ratio  $D_{min}$  obtained from Darendeli (2001)

|                   | Materials       | $D_{min}$ (%) |
|-------------------|-----------------|---------------|
| <b>Embankment</b> | Core: silt      | 1.0           |
|                   | Gravel and sand | 1.9           |
|                   | Rockfill        | 1.9           |
|                   | Clay ground     | 1.5           |
|                   | Clay face       | 1.5           |
| <b>Foundation</b> | Medium silt     | 0.7           |
|                   | Loose silt      | 0.7           |
| <b>Bedrock</b>    | Bedrock         | 0.2           |

### 5.4.2 Modulus reduction and damping curves

In this project, the nonlinear behavior of soils is represented by the *MRD* curves developed by Darendeli (2001), while the bedrock is considered to behave like an elastic material.

#### 5.4.2.1 Variation of modulus reduction and damping curves with confining pressure

The *MRD* curves must be generated for each type of soil. Those are primarily influenced by the void ratio  $e$  and confining pressure (Hardin and Drnevich, 1972). The core and the loose silt layer which are relatively thick with a thickness of 6.8 and 10.7 m respectively, were separated into

multiple sublayers to take into account the effect of the confining pressure on the *MRD* curves without having to compute a different curve for every element.

### Core

The core has been separated equally into 2 sublayers: the top and base sublayers with mean effective stress ( $\sigma'_m$ ) of 24.4 and 58.7 kPa respectively and *PI* of 0 and *OCR* of 1. The Figure 5.6 illustrates both sub-layers.

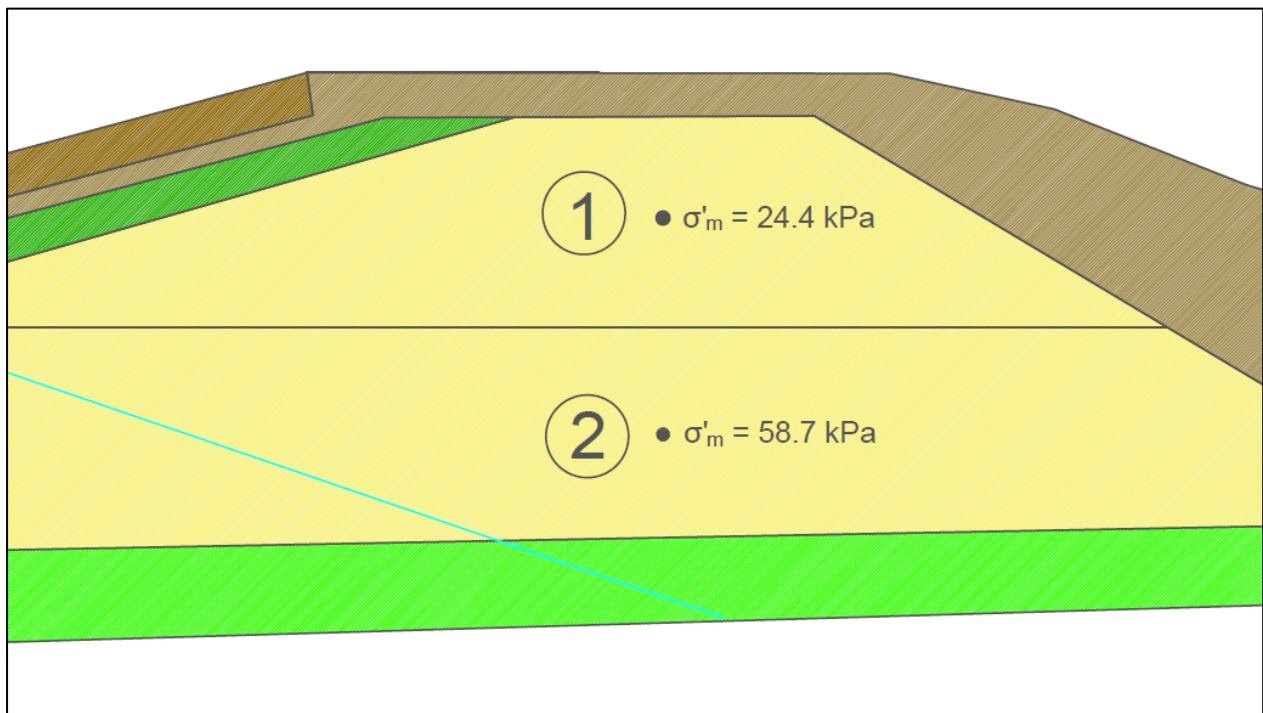


Figure 5.6 Separation of the core into 2 sublayers with confining pressures of 24.4 kPa and 58.7 kPa

The Figure 5.7 presents the *MRD* curves computed for the top and base sublayers of the core.

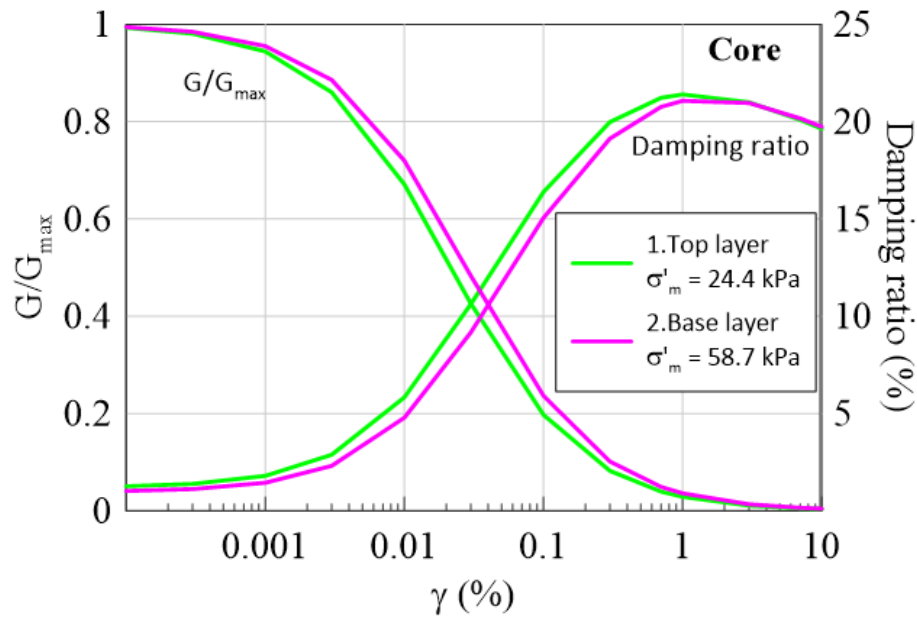


Figure 5.7 Comparison of *MRD* curves between the top and base sublayers of the core

The MRD curves in the core are relatively different between the top and base sublayer. For example, at  $\gamma = 0.1$  %, there is nearly 5 % of difference in the ratio  $G/G_{max}$ . The soil degradation and level of damping of the top sublayer is superior to the base sublayer.

### Loose silt

The loose silt has been separated into 3 sublayers: the top, the middle and the base sublayer with mean effective stress  $\sigma'_m$  of 138.01 kPa, 162.6 kPa and 187.25 kPa respectively and *PI* of 0, and *OCR* of 1. The Figure 5.8 illustrates the 3 sublayers.

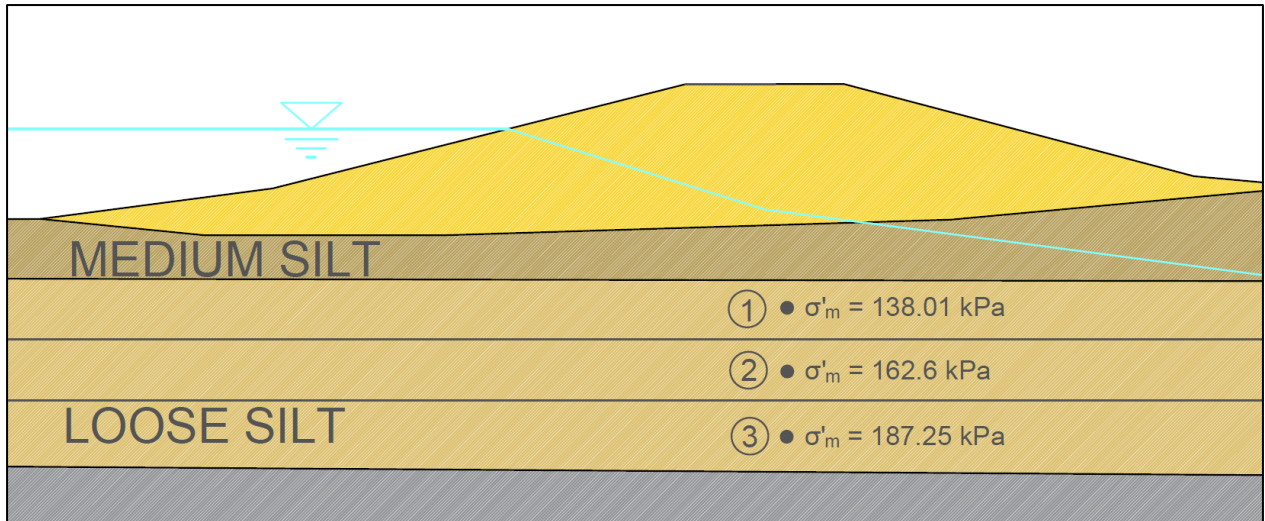


Figure 5.8 Separation of the loose silt layer into 3 sublayers with varying confining pressure

The Figure 5.9 presents the *MRD* curves computes for each sublayer of the loose silt.

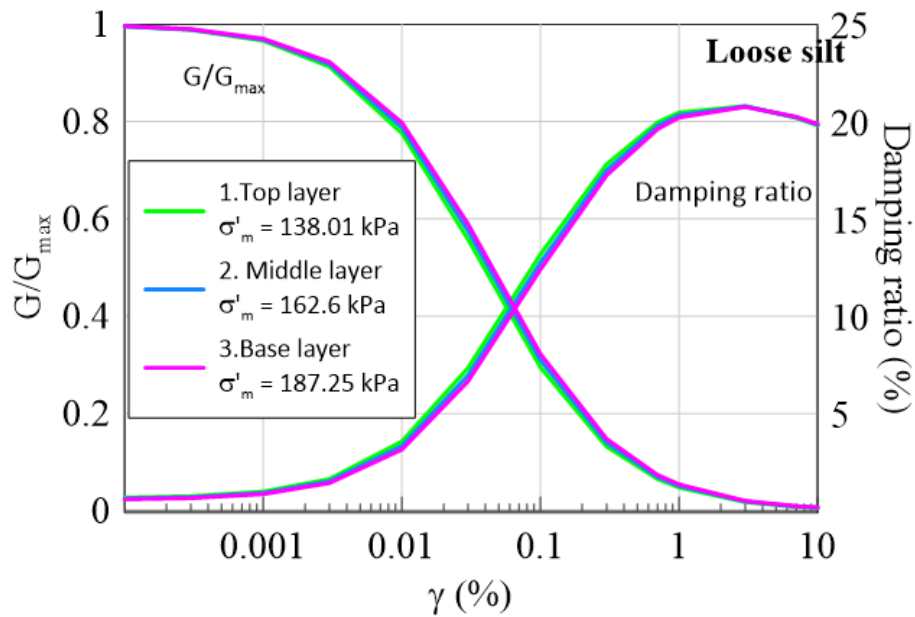


Figure 5.9 Comparison of *MRD* curves between the top, middle and base sublayers of the loose silt deposit

Despite the difference of  $\sigma'_m$ , the *MRD* curves in the loose silt are relatively constant with depth. Therefore, to simplify the problem, an average curve is considered for the loose silt layer.

### 5.4.2.2 Parameters and presentation of the modulus reduction and damping curves

Table 5.5 presents the parameters used to generate the Darendeli's *MRD* curves for 10 loading cycles. Those parameters include the *PI*, the *OCR* and the mean effective stress  $\sigma_m'$ .

Table 5.4 Parameters used to compute the *MRD* curves of Darendeli

|                   | Materials                      | PI | OCR | $\sigma_m'$<br>(kPa) |
|-------------------|--------------------------------|----|-----|----------------------|
| <b>Embankment</b> | Rockfill and [gravel and sand] | 0  | 1   | 3.2                  |
|                   | Clay ground and clay face      | 30 | 2.5 | 83.7                 |
|                   | Top-half core                  | 0  | 1   | 24.4                 |
|                   | Base-half core                 | 0  | 1   | 58.7                 |
| <b>Foundation</b> | Medium silt                    | 0  | 1   | 106.3                |
|                   | Loose silt                     | 0  | 1   | 162.6                |

Figure 5.10 presents the materials' *MRD* curves.

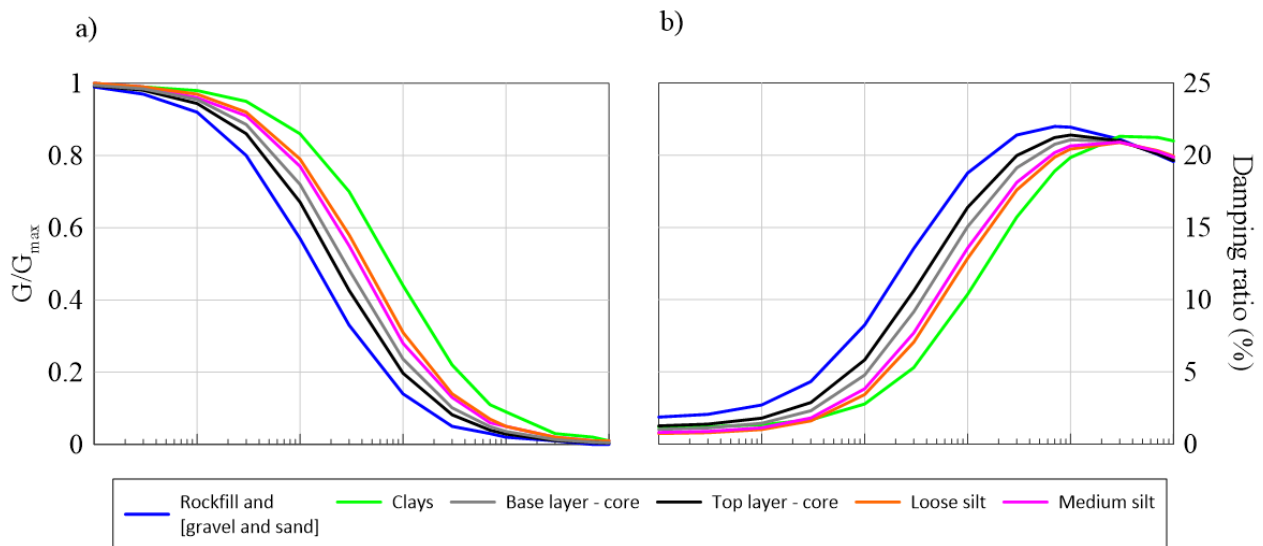


Figure 5.10 a) Modulus reduction curves and b) damping curves for the embankment and foundation soils

## 5.5 Liquefaction potential

Although liquefaction is not considered in the 2D dynamic analyses, the potential of liquefaction of the soil deposits is evaluated based on in situ  $(N_1)_{60}$  indices and  $V_{s1}$ , and a comparison can be made between the results obtained from both simplified methods:

1. Boulanger and Idriss (2014) with  $N$  indices
2. Kayen et al. (2013) with  $V_{s1}$ .

The simplified liquefaction triggering analysis method based on  $N$  indices was first proposed by Seed and Idriss (1971) and is based on liquefied cases. The method has since been updated by different researchers (e.g. Youd et al. (2001); Boulanger and Idriss (2014)). The  $V_{s1}$ -based method is first introduced by Andrus and Stokoe (2000) and it is based on the formulation of the  $SPT$ -based method, and a more recent model was developed by Kayen et al. (2013).

The soils deemed susceptible to liquefaction are the loose silt underneath the embankment dike; the deposit is saturated and loose. The Figure 5.11 presents the  $N$  indices and  $V_{s1}$  of the saturated loose silt under the vicinity of the dike.

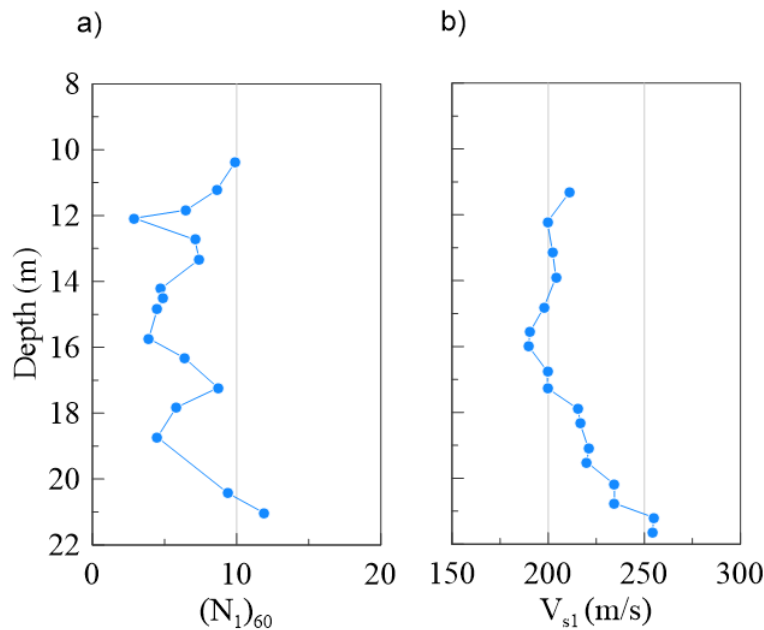


Figure 5.11 a)  $(N_1)_{60}$  and b)  $V_{s1}$  of the loose silt under the vicinity of the dike

With  $V_{s1}$  between 180 and 360 m/s on the uppermost 30 m soil layer, the subsoil is considered stiff corresponding to a soil class D. The design scenario considered in this study is based on the hazard

in Montreal associated with a probability of 2 % in 50 years (i.e. a 2475-year return period) as defined by the NBCC 2015. For this probability, the NBCC 2015 returns a surface *PGA* of 0.378 g for a soil class C. A coefficient of 0.95 (refer to chapter 2, section 2.2.5) is applied to the *PGA* class C to obtain the surface *PGA* class D corresponding to 0.360 g.

For this hazard the factors of safety against liquefaction (*FS*) are computed as  $CRR/CSR$  and are presented in Figure 5.12. Details of computation are presented in Annex C.

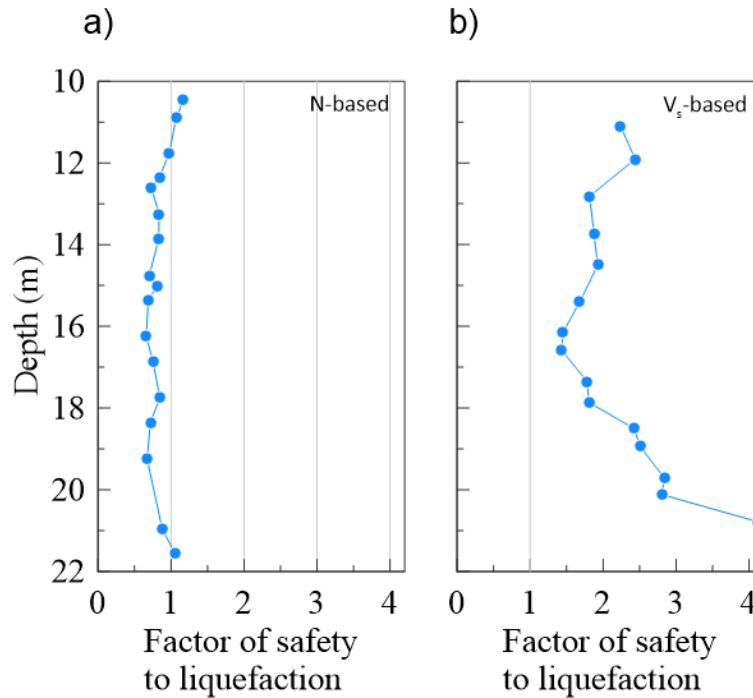
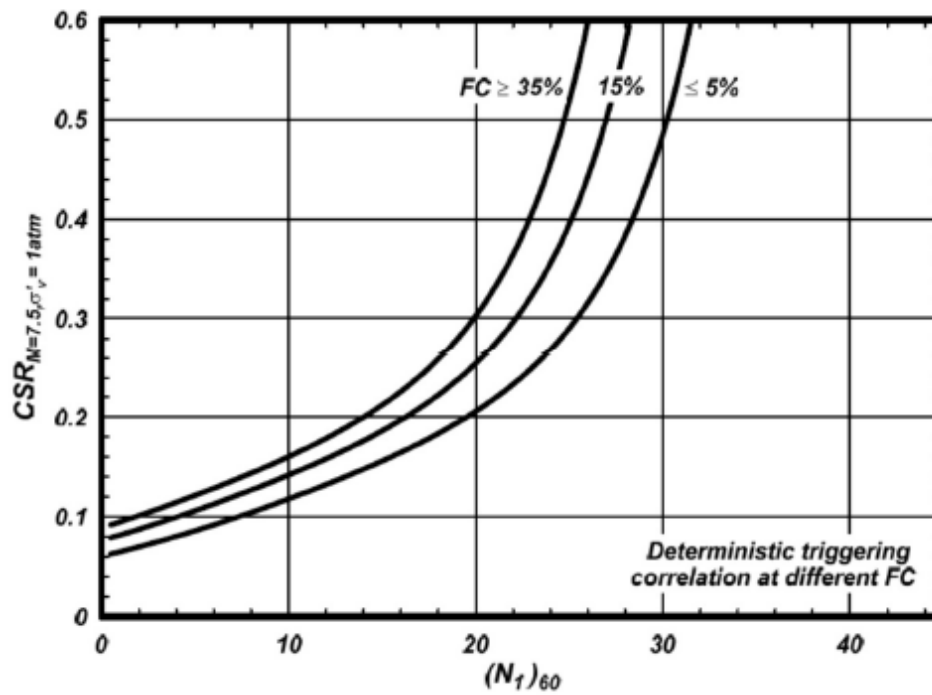


Figure 5.12 Factor of safety against liquefaction evaluated for the saturated silt underneath the embankment based on the a) *N*-based method and b)  $V_{sI}$ -method

The Figure 5.12 shows that both methods predict contradictory results. Indeed, *FS* values are mostly inferior to 1 based on the *N*-based method, predicting liquefaction, while the  $V_{sI}$ -based method does not predict liquefaction with *FS* superior to 1. The difference in the prediction between both methods lies in the values of *CRR* which vary significantly. Figure 5.13 present typical curves of *CRR* for both methods.

a)



b)

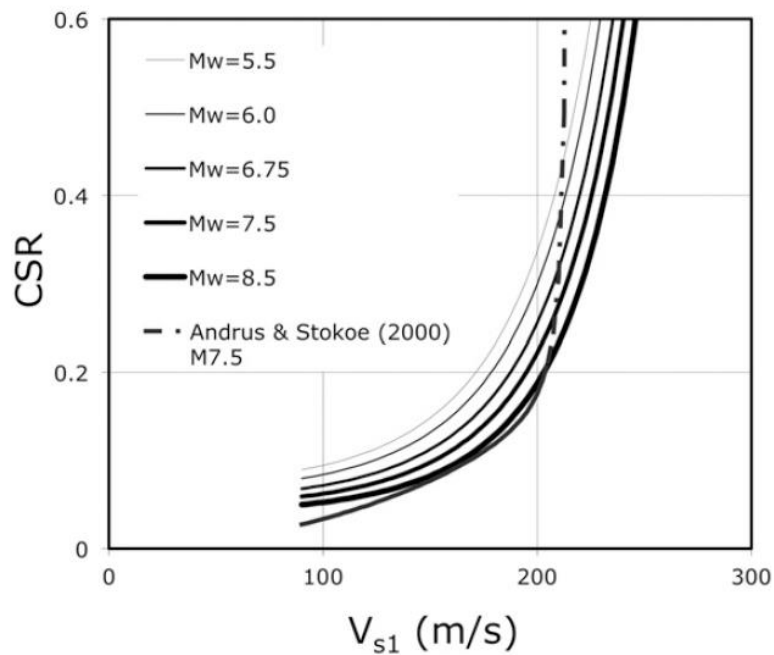


Figure 5.13 Curves of  $CRR$  for a)  $N$ -based method and b)  $V_{s1}$ -based method for the prediction of liquefaction

Values of *CRR* calculated with the *N*-based method are relatively low between 0.143 and 0.234, while the values calculated with the  $V_{sI}$ -based method are relatively high between 0.448 and 2.34. This is resulted from high values of measured  $V_{sI}$  and low values of measured *N*. Since the *MASW* is sensitive to the void ratio  $e$ , hence sensitive to the type of soils and amount of fines content but less sensitive to the relative density (Kayen et al., 2013), the  $V_{sI}$  values might not fully reflect the loose state of the silt deposit, which explains why the *FS* calculated based on  $V_{sI}$  are significantly higher. Furthermore,  $V_s$  is related to very small strain in the elastic range, far from liquefaction conditions. Besides, the *SPT* is sensitive to the soil fines content. Indeed, the *N* values tend to reduce in presence of soil fines. Hence, *N* values might also not be fully representative of the exact density of the soils. Also, *SPT* results are for large strains and plastic behavior, closer to liquefaction conditions. A more realistic factor of safety should be comprised between the values computed using both methods.

## 5.6 Foundation soils spatial variability

In order to assess the critical 2D cross-section to model in the 2D dynamic simulations, 1D dynamic nonlinear ground response analyses are performed on three different soil columns representing three (3) cross-sections (A, B and C) of the embankment. The difference between the 3 cross-sections is the thickness and conditions of the subsoils. The depth of the bedrock varies from 4.9 to 18.0 m from the base of the dike. 1D dynamic nonlinear analyses are performed using DEEPSOIL, to identify the cross-section that would predict the highest crest acceleration. The selection of input motions and the definition of seismic scenarios are presented in chapter 4.

### 5.6.1 Cross-sections A, B and C

Soil columns representative of sections A, B, and C are presented in Figure 5.14. Figure 5.15. presents the  $V_{sI}$  profile of the foundation soils of each section. Note that the soil conditions of the embankment are constant for each section. The  $V_{sI}$  in the embankment are calculated using correlations based on the density of the soils or the  $N$  indices.

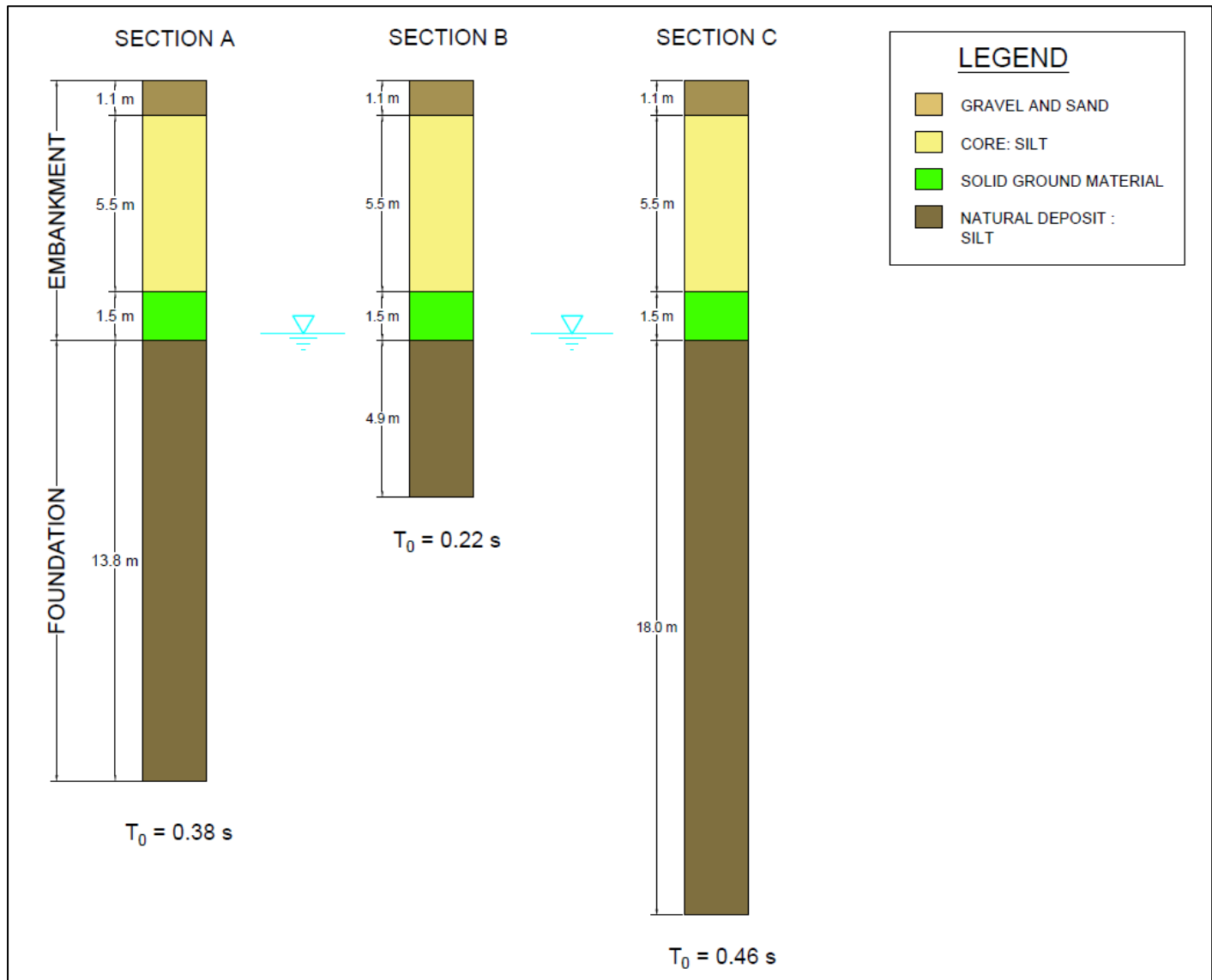


Figure 5.14 Soil column of cross-sections A, B and C of the dike

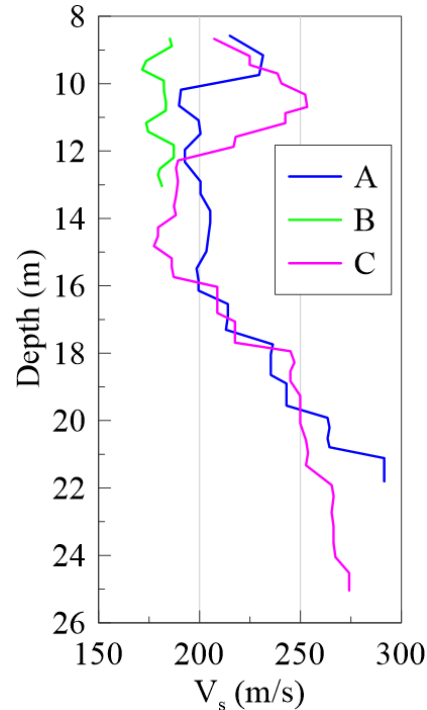


Figure 5.15  $V_s$  profiles of sections A, B and C

#### 5.6.1.1 Presentation of the numerical 1D software DEEPSOIL

DEEPSOIL is a software that can perform equivalent linear and nonlinear 1D ground response analysis (Hashash et al., 2016). Simulations can be performed considering total stresses or effective stresses, i.e. with or without consideration of pore pressure generation. Equivalent-linear simulations are performed in the frequency-domain and nonlinear simulations are performed in the time-domain.

In DEEPSOIL, the soil column and water level must be defined. The soil column is discretized into multiple soil layers, as shown in Figure 5.16, and several parameters are required including the unit weight, the thickness of the layer, the  $V_s$  and the  $MRD$  curves. The type of bedrock must then be defined as an elastic half-space or rigid half-space. Geotechnical properties of the bedrock are also required if the elastic half-space option is chosen. Elastic half-space should be used if an outcrop motion is used, and the rigid half-space should be used if a within motion will be used. Note that an outcrop motion is a motion recorded on the rock at the surface and a within motion is a motion recorded in boring. During the simulations, at each time-step, the following dynamic equation of motion is solved:

$$[M] \{\ddot{u}\} + [C] \{\dot{u}\} + [K] \{u\} = - [M] \{I\} \ddot{u}_g \quad \text{Eq. 5.2}$$

where  $[M]$  is the mass matrix,  $[C]$  is the viscous damping matrix,  $[K]$  is the stiffness matrix,  $\{\ddot{u}\}$  is the vector of nodal relative acceleration,  $\{\dot{u}\}$  is the vector of nodal relative velocities and  $\{u\}$  is the vector of nodal relative displacement,  $\{\ddot{u}_g\}$  is the acceleration at the base of the soil column and  $\{I\}$  is the unit vector.

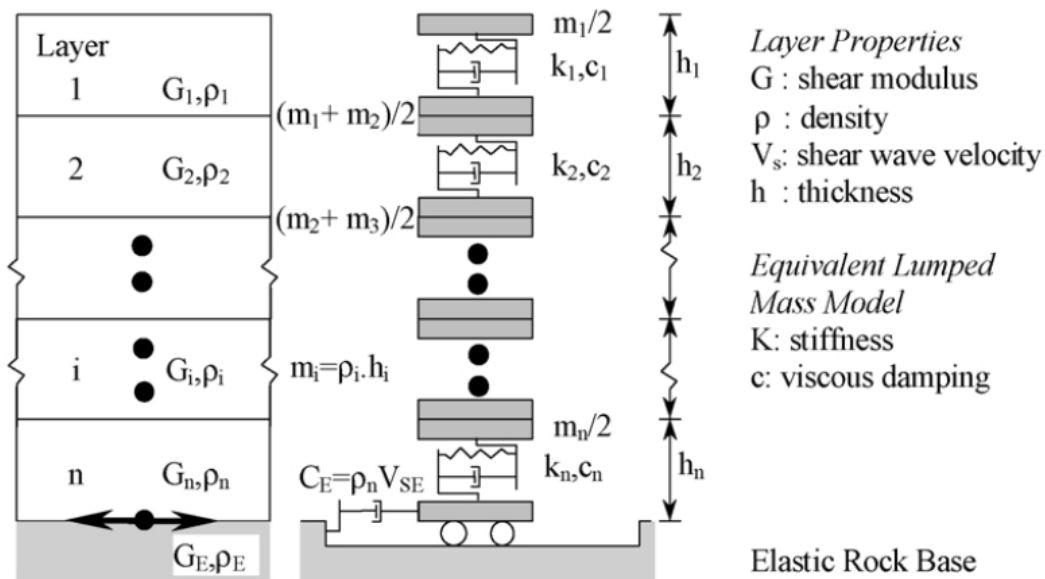


Figure 5.16 One-dimensional horizontally layered deposit shaken at the base, retrieved from Hashash and Park (2001)

## 5.6.2 Non-linear 1D simulations

Nonlinear 1D simulations are performed in DEEPSOIL in the time domain without considering pore pressure generation (i.e. in total stress). The Pressure-Dependent hyperbolic (*MKZ*) model developed by Matasovic (1993) is used to define the backbone curve. Small strain damping is added separately to the model due to the linear shape of the *MKZ* model at small strains. The MRDF Pressure-Dependent Hyperbolic model is used to represent the hysteretic behavior during cyclic loading (Phillips and Hashash, 2009). It is a non-Masing unload-reload formulation that applies a reduction factor that alters the Masing rules. The input *MRD* curves are fit simultaneously.

Each soil profile is discretized into sublayers. The thickness of the sublayers are linked to their stiffness and the maximum frequency to be propagated. Sections A, B and C can respectively propagate maximum frequency of 100, 75 and 100 Hz. For each sublayer, DEEPSOIL requires the following input parameters:

- Thickness
- Unit weight
- Shear wave velocity ( $V_s$ )
- *MRD* curve

The bedrock is defined as an elastic half-space with  $V_s$  of 1500 m/s and input motions are applied as outcrop motions.

### **5.6.3 Results**

The crest average response spectra are presented in Figure 5.17 and compared between sections and for each seismic scenario. Note that the seismic scenarios and motions are presented in chapter 4. The average input motion spectrum at the base is also shown for all scenarios to identify wave amplification or attenuation.

Wave attenuation is observed at all periods except at the degraded fundamental period between 0.53 and 0.73 s. Nonlinearities increase especially in the weaker layers such as in the natural silt leading to wave attenuation in scenarios T1-1 and T1-2. The strongest spectral values ( $S_a$ ) are observed for all scenarios and almost all periods in section A. Hence, section A is selected to represent the embankment.

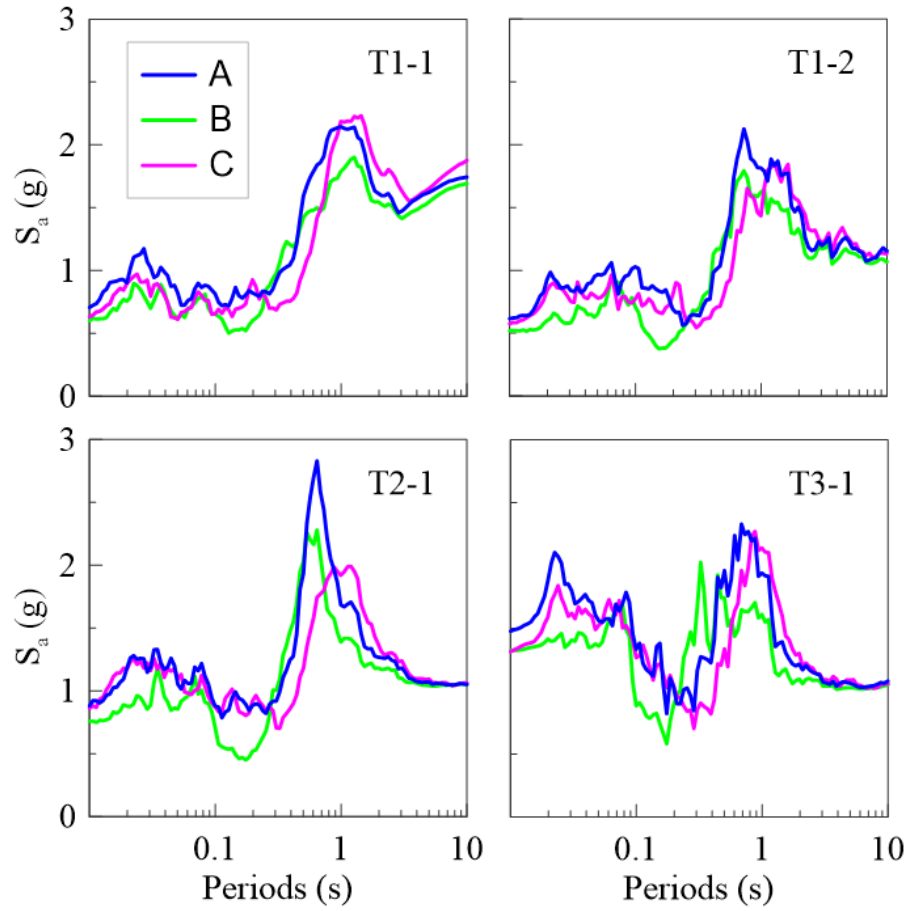


Figure 5.17 Crest response spectra of sections A, B and C

## CHAPTER 6 NUMERICAL MODELING

### 6.1 Introduction

This chapter presents the numerical modeling process used for the 2D dynamic analyses performed in this study. In particular, this section discusses the meshing, the static and dynamic boundary conditions, the input parameters and the soil models used in *FLAC*. Quadrilateral finite elements compose the mesh, which can propagate frequencies of up to 30 Hz. To avoid free movement along the boundaries, roller static boundaries are assigned to the side boundaries and fixed (X and Y) static boundaries are assigned to the base. The initial state of stress is initialized using Mohr-Coulomb soil model assigned to all materials including the bedrock which is modeled as an elastic bedrock with rigidity parameters based on a  $V_s$  of 1500 m/s. The soil input parameters are presented and the choice of hydraulic parameters is discussed. During dynamic analyses, the bottom boundary is modeled as a flexible base to reduce the reflection of outward propagating waves back into the model (Mejia and Dawson, 2006). Quiet boundaries are assigned to the base and free-field conditions are assigned to the lateral boundaries.

Furthermore, the modeling steps to initialize the initial state of stress are presented which are 1- the construction of the model in static equilibrium with empty reservoir and 2- the filling of the reservoir with a decoupled solid-fluid analysis. After that, the slope stability is verified. A static factor of safety of 2.66 is found for the downstream slope.

Since the state of stress of static equilibrium is important for the study of potential of liquefaction, a comparison of the state of stress is performed between 2 methods of construction of the model. In the 1<sup>st</sup> method, the embankment is built with the foundation soil and the model is ran until reaching the static equilibrium. In the 2<sup>nd</sup> method, the dike will be added after the initialization of the state of stress in the foundation soil. Since the embankment is quite short in height (8 m), the state of stress between both methods is not significantly different. Hence, method 1 which is more efficient is used in this project.

After initializing the state of stress with the reservoir at full capacity, the behavior of the model is validated using linear damped simulations. The maximum shear strain, the velocity doubling effect and the effects of lateral boundary locations are verified. The validation is performed with one input motion. The results show that the maximum shear strain recorded is low enough to avoid

material failure and is still inside the range of validity of the Darendeli *MRD* model ( $\gamma \leq 0.3$  %). Also, as the maximum strains are located right underneath the embankment, the location of the side boundaries may be considered adequate. Furthermore, the coefficient in the input stress formula is modified to take into account the velocity doubling effects. Finally, considering the lengthy running time, solutions to increase the timestep and reduce the running time are discussed in this chapter.

## 6.2 Summary of the simulations

The simulations performed for the present study are summarized in table 6.1. Both linear and nonlinear simulations are performed using each ground motion. Note that RSN is the record sequence number.

Table 6.1 Input motions used in the simulations for each scenario.

| Event                                       | Station                   | RSN  | $M_w$ | R (km) | $T_m$ (s) | D (s) | PGA (g) |
|---|---------------------------|------|-------|--------|-----------|-------|---------|
| <b>T1-1: 0.01 – 0.2 s [M5-6; R0-20 km]</b>  |                           |      |       |        |           |       |         |
| Coalinga – 02                               | Oil Fields Fire Station   | 381  | 5.1   | 0.0    | 4.75      | 10.3  | 0.268   |
| Gilroy                                      | Gilroy – Gavilan Coll.    | 2019 | 4.9   | 2.2    | 8.62      | 33    | 0.251   |
| Fruili, Italy – 03                          | Tarcento                  | 3553 | 5.5   | 3.8    | 4.64      | 16.8  | 0.248   |
| Umbria Marche (Aftershock 8), Italy         | Borgo – Cerreto Torre     | 4377 | 5.2   | 8.8    | 6.96      | 19.6  | 0.205   |
| Mineral 2011-08-23                          | SE.NANPP                  | 8571 | 5.7   | 18.5   | 2.82      | 17.4  | 0.313   |
| <b>T1-2: 0.01 – 0.2 s [M6-7; R20-40 km]</b> |                           |      |       |        |           |       |         |
| San Fernando                                | Lake Hughes #4            | 72   | 6.6   | 19.4   | 4.85      | 35    | 0.264   |
| San Fernando                                | Santa Anita Dam           | 87   | 6.6   | 30.7   | 5.48      | 29.7  | 0.264   |
| Whittier Narrow – 01                        | Big Tujunga_Angeles Nat F | 598  | 6.0   | 22.5   | 5.97      | 30.9  | 0.312   |
| San Fernando                                | Lake Hughes #4            | 72   | 6.6   | 19.4   | 4.85      | 35    | 0.253   |
| Big Bear – 01                               | Snow Creek                | 935  | 6.5   | 37.0   | 5.98      | 60    | 0.242   |
| Whittier Narrow – 01                        | Pacoima Kagel Canyon      | 671  | 6.0   | 31.6   | 2.61      | 40    | 0.338   |
| <b>T2-1: 0.2 – 1.0 s [M6-7; R20-40 km]</b>  |                           |      |       |        |           |       |         |
| San Fernando                                | Lake Hughes #4            | 72   | 6.6   | 19.4   | 3.63      | 35    | 0.156   |
| North Palm Springs                          | Anza – Red Mountain       | 511  | 6.1   | 38.2   | 4.48      | 11    | 0.151   |
| Whittier Narrows – 01                       | Big Tujunga_Angeles Nat F | 598  | 6.0   | 22.5   | 4.97      | 30.9  | 0.248   |
| Northridge – 01                             | Big Tujunga_Angeles Nat F | 954  | 6.7   | 19.1   | 4.08      | 30    | 0.127   |
| San Simeon, California                      | San Luis Obispo           | 4016 | 6.5   | 31.3   | 2.12      | 77    | 0.188   |
| <b>T3-1: 1.0 – 10 s [M7-7.5; R40-60 km]</b> |                           |      |       |        |           |       |         |
| Irpinia, Italy – 01                         | Irpinia_Italy-01          | 293  | 6.9   | 59.6   | 1.44      | 52.8  | 0.048   |
| Irpinia, Italy – 01                         | Irpinia_Italy-01          | 294  | 6.9   | 51.7   | 1.11      | 31.9  | 0.035   |
| Taiwan, SMART1 (45)                         | Taiwan SMART1(45)         | 572  | 7.3   | 51.3   | 2.15      | 33    | 0.117   |

## 6.3 Numerical software *FLAC*

*FLAC* (Fast Lagrangian Analysis of Continua, Itasca Consulting Group, 2016) is a two-dimensional explicit finite difference program that simulates the behavior of materials such as soils, rock and other materials under static or dynamic conditions. Dynamic analyses including linear and fully nonlinear simulations can be performed in the time-domain, within the small-strain mode or large-strain mode which allows the grid to freely deform. The soil layers are discretized into multiple finite elements and follow a defined soil constitutive model. Ground water conditions may be defined in the model and then, fully coupled (fluid-solid) analyses or decoupled analyses may be performed to reach equilibrium.

*FLAC* includes built-in constitutive models that can be called directly. If needed, the user may program its own constitutive models, using the built-in programming language *FISH*. Functions might also be written to calculate user-defined parameters. History points are specified at given locations of the model to monitor the results such as the acceleration time series and shear stresses and strains at each time step.

## 6.4 Construction of the model

This section presents the steps followed to build the numerical 2D model in *FLAC*, such as the definition of meshing and boundary conditions. Then, the geometry of the numerical model is presented followed by the input parameters and soil models.

### 6.4.1 Geometry and discretization

#### 6.4.1.1 Grid creation and static boundaries

The first step in the development of the model is to set-up the finite difference grid. The method proposed in the manual is followed (Itasca, 2016). The geometry of the model is drawn in the software and one zoning block is created and extracted. The sides of the model are located at a distance of  $\frac{1}{2} L$  (width) of the dike from its toes. The base of the model is located 11 m below the top of the bedrock. The total width and height of the model are respectively 146.3 and 33.8 m. Note that the location of the boundaries was chosen through trial and error and its validation is further shown in section 6.6.1. The geometry of the model is shown in figure 6.1.

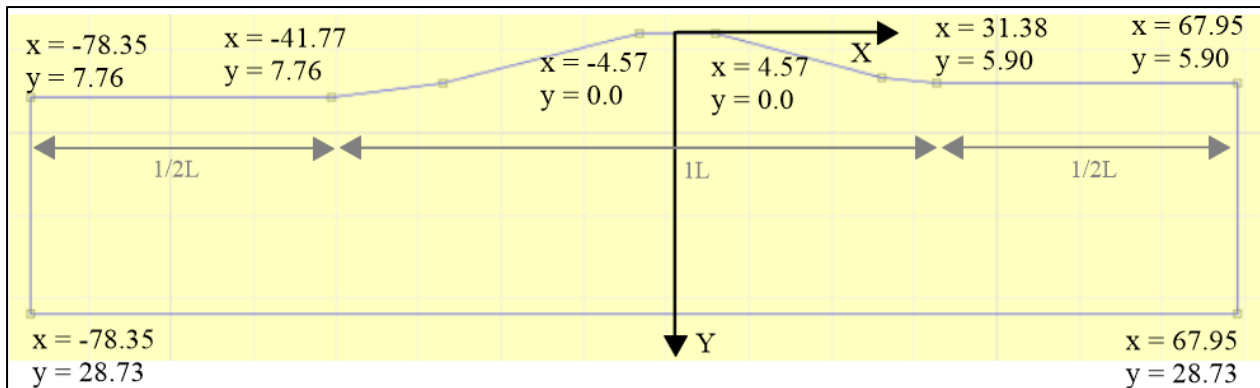


Figure 6.1 Geometry of the model on *FLAC* with coordinates of each point (meter)

This method of building the grid tends to reduce the number of triangular elements, especially along the slopes. As large strain is typically expected during dynamic simulations, it is, therefore, important to minimize the amount of triangular elements inside the model. Triangular elements do not contain overlaid sets of subzones and thus they tend to become badly distorted during dynamic simulations (Itasca, 2016) as compared to quadrilateral elements. This problem is particularly accentuated when triangular elements are present along the slopes.

Roller boundaries are applied to the sides of the model to allow movement in the Y-direction and fix movement in the X-direction. Fixed boundaries are assigned to the base to fix movement in the X and Y directions, otherwise, the foundation would be able to freely move along the base, which may cause unrealistic results.

#### 6.4.1.2 Discretization of the model

The mesh fineness should be selected to provide accurate wave transmission in the model. Logically, a finer mesh propagates a higher range of frequencies. However, a very fine mesh results in a very large running time. Therefore, it is preferable to work with a size mesh that may allow an acceptable range of frequencies to be propagated inside the model while not putting too much burden on the computation times.

For this project, considering the frequency content of the input ground motions and the soil conditions, a frequency range up to 30 Hz to propagate in the model is deemed to be acceptable. The size mesh calculation is based on the work by Kuhmeyer and Lysmer (1973) who have shown that for an accurate representation of wave transmission through the model, the size of an element ( $\Delta L$ ) must be smaller than approximately 1/10 to 1/8 of the wavelength ( $\lambda$ ) associated with the

highest frequency component of the input wave ( $f_{max}$ ), i.e. 30 Hz in this project. The wavelength  $\lambda$  is calculated with equation 6.1 where the  $V_s$  is the smallest shear-wave speed in the model (200 m/s).

$$\lambda = \frac{V_s}{f_{max}} = \frac{200 \text{ m/s}}{30 \text{ Hz}} = 6.7 \text{ m} \quad \text{Eq. 6.3}$$

The  $\Delta L$  is calculated with equation 6.2.

$$\Delta L \cong \frac{\lambda}{10} = \frac{6.7 \text{ m}}{10} = 0.67 \text{ m} \quad \text{Eq. 6.4}$$

As previously mentioned, quadrilateral elements are preferable over triangular elements because the latter tend to become badly distorted under strong motion shaking. A 240 x 54 quadrilateral zone mesh with each element having both dimensions of approximately 0.60 m is generated as shown in figure 6.2. Particular attention is given to the ratio H/V for each element. To improve numerical stability and the accuracy of the results, the ratio should be kept close to 1 which is the case at the center of the model and on the sides. Elements along the slopes are a little elongated due to the topography with a ratio of 1.0H/0.9V.

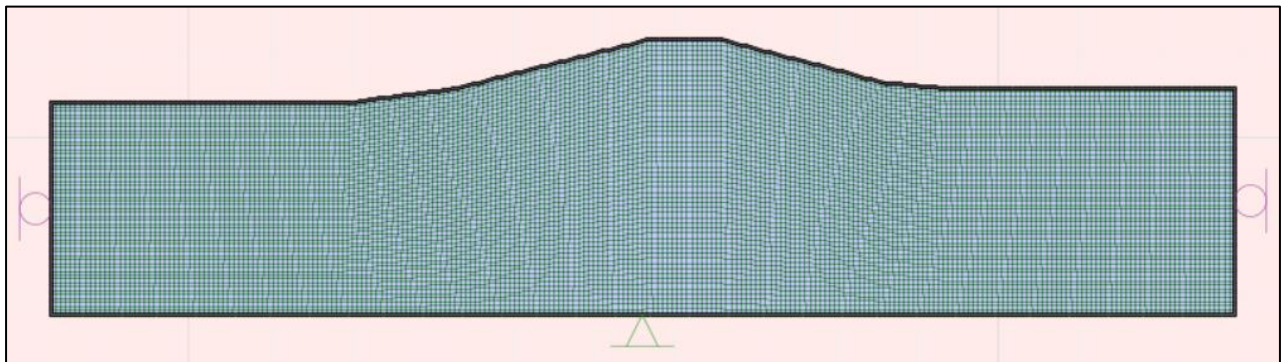


Figure 6.2 Meshing of the model on *FLAC* with 240 x 54 quadrilateral zones

## 6.4.2 Dynamic boundary conditions

Dynamic boundary conditions are an important factor in dynamic numerical modeling. In static analyses, fixed boundaries can be placed at a reasonable distance from the region of interest to fix movement. However, in dynamic analyses, they cause the outward propagating waves to be

reflected back into the model and they do not allow the necessary energy radiation (Mejia and Dawson, 2006). To solve the issue, the boundaries might be placed so far that the soil damping will absorb the reflected waves. On the other hand, this will result in a large computational burden. The alternative is to use dynamic boundaries on the sides and at the base of the model as shown in figure 6.3.

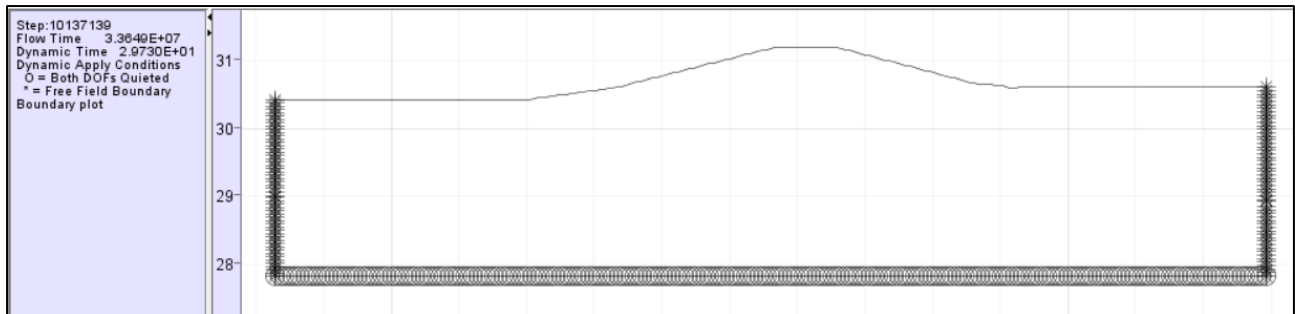


Figure 6.3 Dynamic boundaries of the model on *FLAC*

### Base boundaries

Quiet boundaries in both X and Y directions are applied at the base of the model. *FLAC* uses the viscous boundaries developed by Lysmer and Kuhlemeyer (1969) which operate in the time domain. They are most effective at absorbing the outward propagating waves at an angle of incidence higher than 30 degrees. The scheme's effectiveness has been demonstrated by Kunar et al. (1977) for both finite-element and finite-difference models.

To apply absorbing boundaries at the base, the latter must be modeled as a flexible base. Thus, this requires the input motion to be applied as a shear stress at the base. The velocity time series can be converted to a shear stress time series using equation 6.3.

$$\tau = -K_I(\rho V_s)v(t) \quad \text{Eq. 6.3}$$

where  $\tau$  is the input shear stress,  $K_I$  is an adjustment factor,  $v(t)$  is the input velocity,  $\rho$  the mass density and  $V_s$  the shear-wave speed of the soil layer at the base.

The factor  $K_I$  accounts for the fact that the dynamic boundaries will absorb energy. The *FLAC*'s manual suggests using a factor  $K_I$  of 2 as approximately half of the energy is absorbed. It also suggested that the factor  $K_I$  be adapted to the model to avoid velocity doubling at the base. For this project, a factor  $K_I$  of 1 is used as discussed in section 6.6.1 to reduce velocity doubling effects.

The base of the model is composed of the elastic bedrock. Therefore, the input shear stress is  $-8.103e-6 v(t)$ .

### Side boundaries

For the sides of the model, since the input motion is applied as a boundary condition at the base, quiet boundaries cannot be applied to the sides to avoid the waves to leak out. To avoid this, free-field boundaries are applied to the sides of the model. They model a 1D column of one-unit width which simulates an absorbing quiet boundary.

### Base rotation

For a model with quiet and free-field boundaries, the rotation of the base may develop. It develops because the normal and shear forces do not meet the equilibrium equations at the free-field boundaries. Fortunately, the base rotation has only a minor impact on the results, thus preventing base rotation is for aesthetic purposes. The base rotation on this project is prevented with the *FLAC* built-in command `SET corr_ffrot on`. An adjustment is made every time step so that the resultant reaction normal and shear forces acting along the side boundaries satisfy global force and moment equilibrium.

## **6.4.3 Damping**

Rayleigh viscous damping is used in the simulations to introduce small-strain damping. The scheme uses an input value of  $D_{min}$  and  $f_{min}$  as  $D_{min}$  is reached when the frequency reaches  $f_{min}$ . More details related to the damping is presented in chapter 2 and 3. At large deformations, materials follow the damping curves of Darendeli (2001) when using the hysteretic model.

## **6.4.4 Input parameters and soil models**

In static simulations, the Mohr-Coulomb model is assigned to all materials including the bedrock. Table 6.2 presents the materials used in the model, the geotechnical parameters including the  $\rho$ ,  $K$ ,  $G$ ,  $\phi$  and  $c$  and the hydraulic parameters which are the porosity ( $n$ ) and the hydraulic conductivity ( $k$ ).

Table 6.2 Materials input parameters in *FLAC*

| <b>Materials</b>       | <b><math>\rho</math><br/>(kg/m<sup>3</sup>)</b> | <b>K<br/>(MPa)</b> | <b>G<br/>(MPa)</b> | <b><math>\phi</math><br/>(°)</b> | <b>c<br/>(kPa)</b> | <b>n</b> | <b>k<br/>(cm/s)</b> |
|------------------------|---|--------------------|--------------------|----------------------------------|--------------------|----------|---------------------|
| <b>Rockfill</b>        | 2140.7  | 1 159.5            | 535.2              | 50                               | 0                  | 0.4      | 0.006**             |
| <b>Gravel and sand</b> | 1936.8  | 481.6              | 222.3              | 35                               | 0                  | 0.2      | 0.004**             |
| <b>Clay mat</b>        | 1936.8  | 167.9              | 77.5               | 26                               | 7                  | 0.45     | 0.0001**            |
| <b>Clay ground</b>     | 1936.8  | 377.7              | 174.3              | 26                               | 7                  | 0.33     | 0.0001**            |
| <b>Core: Silt</b>      | 2038.7  | 311.5              | 143.8              | 41                               | 0                  | 0.23     | 0.0005              |
| <b>Medium silt</b>     | 2038.7  | 223.6              | 103.2              | 33.5                             | 0                  | 0.35     | 0.003               |
| <b>Loose silt</b>      | 1987.8  | 196.5              | 90.7               | 29                               | 0                  | 0.47     | 0.004               |
| <b>Bedrock</b>         | 2700  | 13 169             | 6 078              | 50                               | 0                  | 0.25*    | 0.003**             |

The input parameters are based on the results of geotechnical studies, as described in chapter 5. (\*): Typical values are assigned to  $n$  except for the bedrock. Since the true  $n$  of the bedrock is very small and the value of  $n$  affects the computation times by increasing the stiffness of the model, a lower value of  $n$  is assigned to the bedrock. The impact on the results should be small since the pressure-change is related directly to the volume-change and not to porosity-change. A  $n$  value of 0.25 is assigned to the bedrock.

Typical values are assigned to  $k$  of the foundation soils (medium silt and loose silt). (\*\*): The  $k$  for other materials is chosen to reduce the variation of permeability within the model while maintaining consistency between materials. Indeed, a high variation of permeability in the model would significantly reduce the timestep. There should not be a significant difference in the final state between a contrast of 1:20 and 1:200 (Itasca, 2016).

### 6.4.5 Presentation of the model

The geometry and the meshing have been generated and the materials are defined for all zones of the model (Figure 6.4).

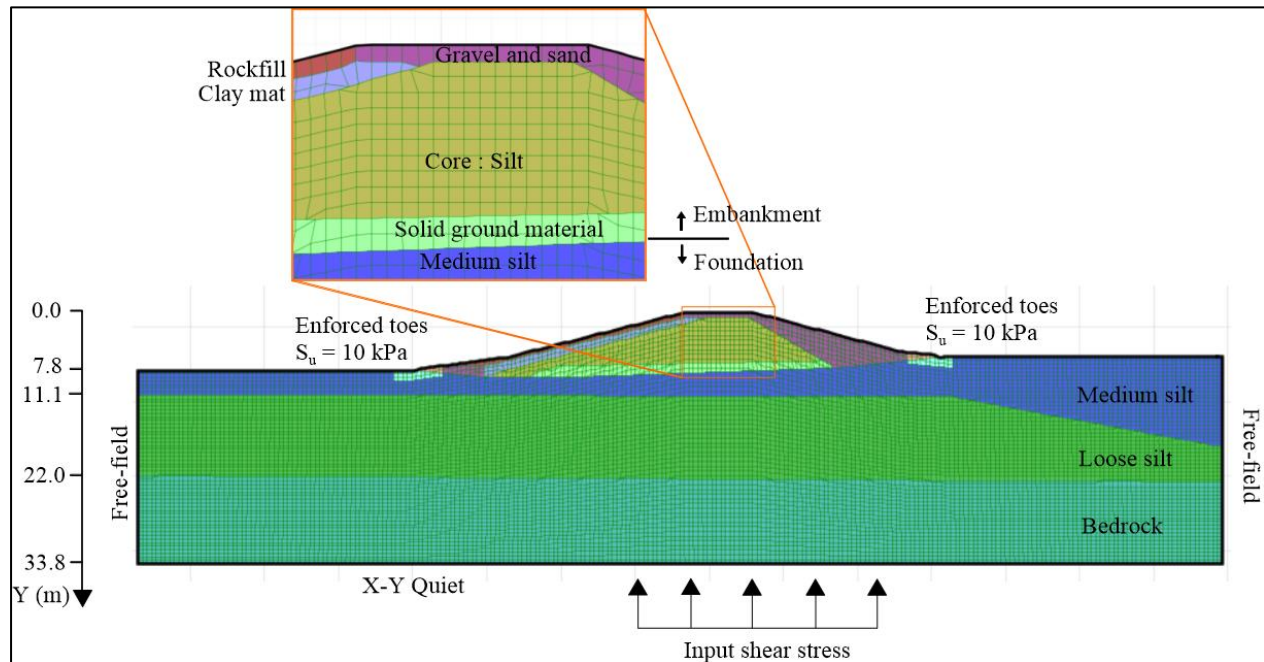


Figure 6.4 Illustration of the model in *FLAC* including materials, dynamic boundary conditions and the input stress

Due to a high concentration of stresses at the toes and very low confining pressure and therefore low resistance, 10 kPa of cohesion is added to the material at the toes to avoid failure during the static state. Since the stiffness remains unchanged, this modification should not affect the final results.

#### 6.4.6 Natural modes

The natural modes correspond to the natural frequencies of the system, the first mode of vibration being the fundamental mode/frequency. The system enters in free oscillation when the period of vibration matches the natural modes of the system. Therefore, great amplification is expected when the motion's range of frequencies matches the natural frequencies of the system.

In order to characterize the natural modes of the system, a 2D dynamic linear simulation in *FLAC* is performed, so that no soil degradation is allowed. Rayleigh damping (viscous) is added to reduce numerical noise. To identify the natural modes, the transfer function (*TF*) between the crest and the base of the model is calculated using equation 6.4.

$$TF = \frac{FAS_{crest}}{FAS_{base}} \quad \text{Eq 6.4}$$

where  $FAS$  is the Fourier amplitude spectrum. The  $TF$  is shown in figure 6.5, and the frequencies of the peaks correspond to the modes of the system. Natural frequencies computed from the  $TF$  are presented in table 6.3.

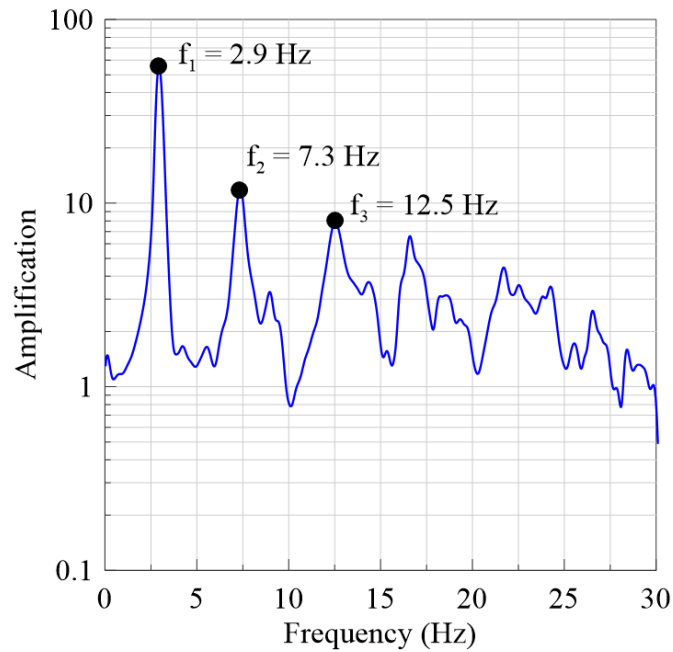


Figure 6.5 Transfer function of the *FLAC* model

Table 6.3 Natural frequencies of the *FLAC* model, obtained using a linear dynamic simulation

| Mode               | Natural frequency (Hz) | Natural mode (s) |
|--------------------|------------------------|------------------|
| 1<br>(fundamental) | 2.9                    | 0.34             |
| 2                  | 7.3                    | 0.14             |
| 3                  | 12.5                   | 0.08             |

To validate the values in table 6.3, the equation 6.5 might be used to provide an estimate of the natural frequencies of the model (Kramer, 1996). Since the equation 6.5 estimates the natural

frequencies of a 1D soil column and that our model is in 2D, the equation only provides an approximation of the true values in 2D.

$$f_n = \frac{V_{s1\_eq}}{4H_m} (2n - 1) \quad \text{Eq. 6.5}$$

An equivalent normalized shear wave velocity ( $V_{s1\_eq}$ ) of 240.2 m/s and a height of the model ( $H_m$ ) of 22 m are considered in the equation 6.5. Table 6.4 presents the estimated natural modes. Natural modes calculated or estimated are quite similar, indicating that the 1D natural frequencies are a reasonable approximation of the modes of the dike.

Table 6.4 Estimated theoretical natural frequencies of a 1D column of soil based on the  $V_{s1}$  and the H of the model

| Mode               | Natural frequency<br>(Hz) | Natural modes<br>(s) |
|--------------------|---------------------------|----------------------|
| 1<br>(fundamental) | 2.77                      | 0.36                 |
| 2                  | 8.30                      | 0.12                 |
| 3                  | 13.83                     | 0.07                 |

## 6.5 Static simulations

Static simulations must be performed to initialize the state of stress in the model before the application of dynamic driving forces. The initial state of shear stresses is particularly important especially for the triggering of liquefaction (Seed and Harder, 1990). Despite that liquefaction is not considered in the numerical simulations due to the constitutive model being used, a special attention was given to the initial state of shear stresses. A comparison is performed between two methods of building the model:

- 1- The embankment is already built;
- 2- The embankment is not built yet (the embankment will be added after the initial state of stress)

Afterward, the state of stress must be initialized with the reservoir at full capacity. This step is performed in decoupled mode, i.e. the pore pressure is first initialized and finally the mechanical pressure (weight of water) is applied. Finally, the static stability of the slopes is evaluated.

### 6.5.1 Static equilibrium

The state of stress must first be initialized before rising of the reservoir. Two modeling methods are compared: 1- the embankment is already built and 2- the embankment is not built yet (embankment added after the initial state of stress). The initial water table is set at a depth of 13.6 m below the crest which corresponds to the water level at the right corner of the model after the rising of the reservoir. The initial state of shear stress is presented for the 1<sup>st</sup> modeling method in figures 6.6a and 6.7a and for the 2<sup>nd</sup> modeling method in figures 6.6b and 6.7b.

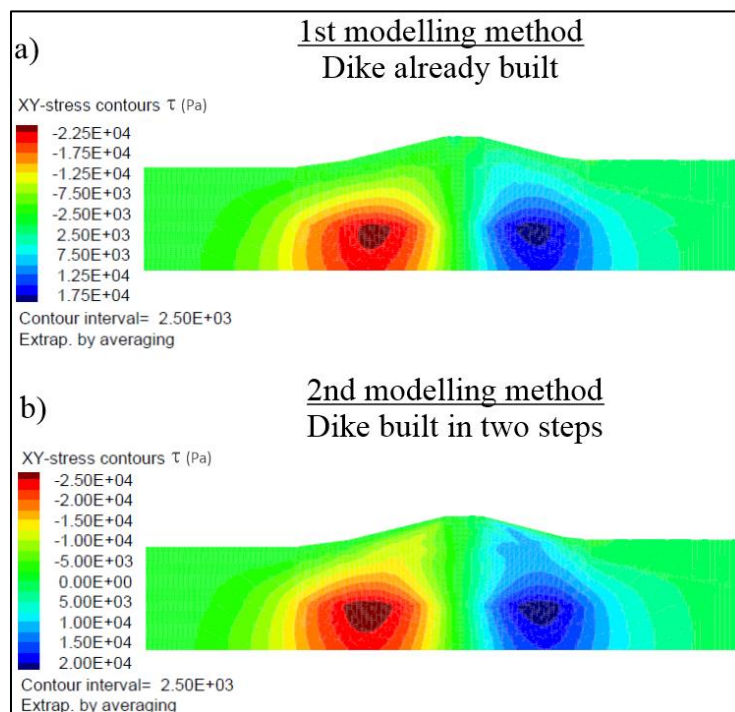


Figure 6.6 Initial state of shear stress  $\tau$  including the weight of the embankment in static state using a) method 1 and b) method 2

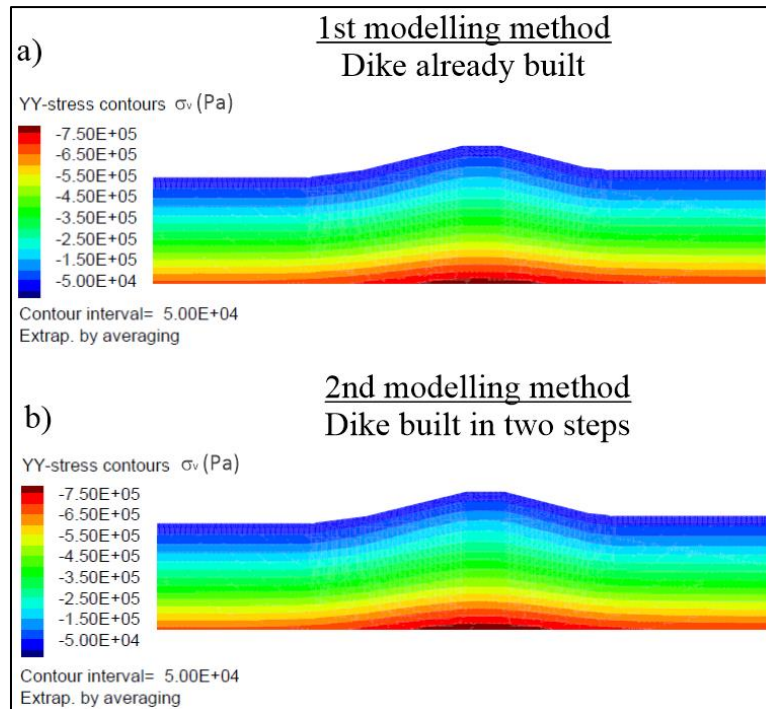


Figure 6.7 Initial state of total vertical stress  $\sigma_v$  including the weight of the embankment in static state with a) method 1 and b) method 2

The initial state of shear stress indicates that for both methods, there are both positive and negative shear stresses acting in the bedrock. These forces indicate a shearing plan at the interface between the natural silt and the bedrock. At the right of the upstream slope, the movements tend to go upward while at the right of the downstream slope, the movements tend to go downward.

Overall, the difference in shear stresses is minimal between both modeling methods. This can be assumed to be due to the embankment being short. The same conclusion might not be valid for a higher embankment. For the rest of the project, modeling method #1 is used which considers that the dike is already constructed on the foundation soils.

## 6.5.2 Initialization of the reservoir

After initializing the initial state of stress, the next step is to raise the reservoir at full capacity. In *FLAC*, there are two different ways to model a hydraulic analysis: the coupled and decoupled analyses. The fully coupled analysis is most realistic as it combines the hydraulic and mechanical parts of the problem, and the distribution of the pore pressures and the stresses and strains are calculated at the same time. This method captures the fluid/solid interaction such as consolidation.

However, the coupled analysis is time-consuming and the benefits to couple both mechanisms might be limited for this project.

The decoupled analysis is less time-consuming as it models the problem by treating the hydraulic part and the mechanical part separately. First, a simulation applies a gradient of pore pressure into the model and stops when it reaches equilibrium. Then, another simulation will input the mechanical pressure induced by the weight of the water.

### 6.5.2.1 Hydraulic pressure

Pore pressure is applied to the model. It is applied as a gradient of pore pressure along the upstream slope to the left-bottom corner of the model. The gradient starts at 0 at the corner to the phreatic level at the upstream slope. Since the phreatic level is below the surface in the downstream section, the pore pressure is fixed at the downstream surface. Figure 6.8 illustrates the applied and fixed pore pressures.

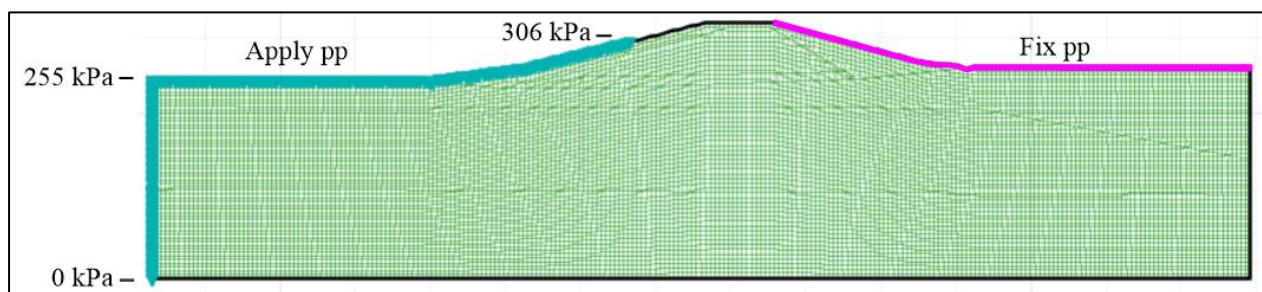


Figure 6.8 Hydraulic input conditions for the initialization of pore pressure while rising the reservoir in static state

Since the analysis is decoupled, mechanical calculations are deactivated. Although the analysis is decoupled, the convergence of the pore pressure is still time-consuming and computational burden adds up because of the great contrast in permeability. To speed the calculations, the fluid bulk-modulus scaling scheme is activated. This scheme is a numerical technique in which local scaling of the fluid bulk modulus is performed so that the critical time step for all gridpoints is approximately the same. Figure 6.9 presents the final distribution of the pore pressure in the model. Monitored water levels are relatively similar to the predicted water levels, providing confidence in the piezometric line computed.

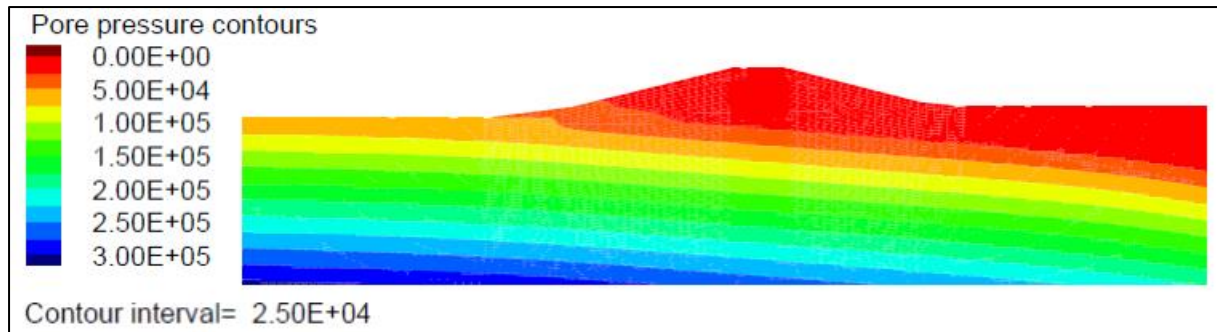


Figure 6.9 Pore pressure distribution in the model with the reservoir at full pool in static state

### 6.5.2.2 Mechanical pressure

Mechanical pressure is applied to the model. It represents the weight of the reservoir and it is applied at the upstream face of the model from the water level to the top-left corner of the model, as illustrated by figure 6.10.

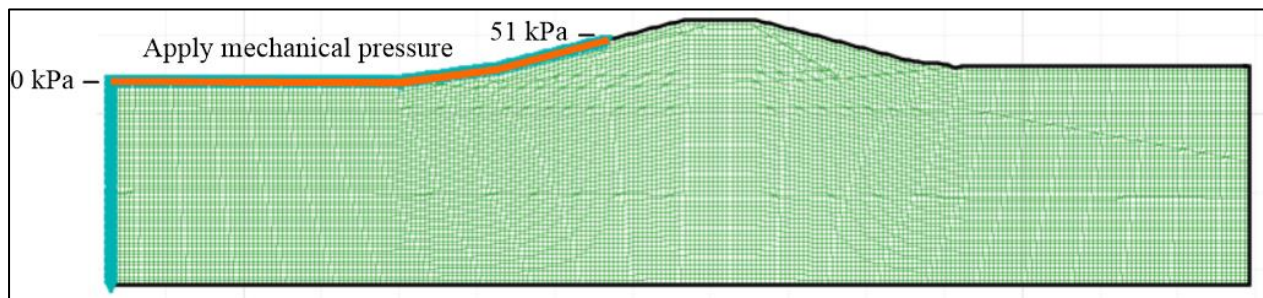


Figure 6.10 Mechanical input condition for the initialization of the state of stress with the reservoir at full pool in static state

Figure 6.11 presents the distribution of shear stresses and total vertical stresses with the reservoir at full capacity.

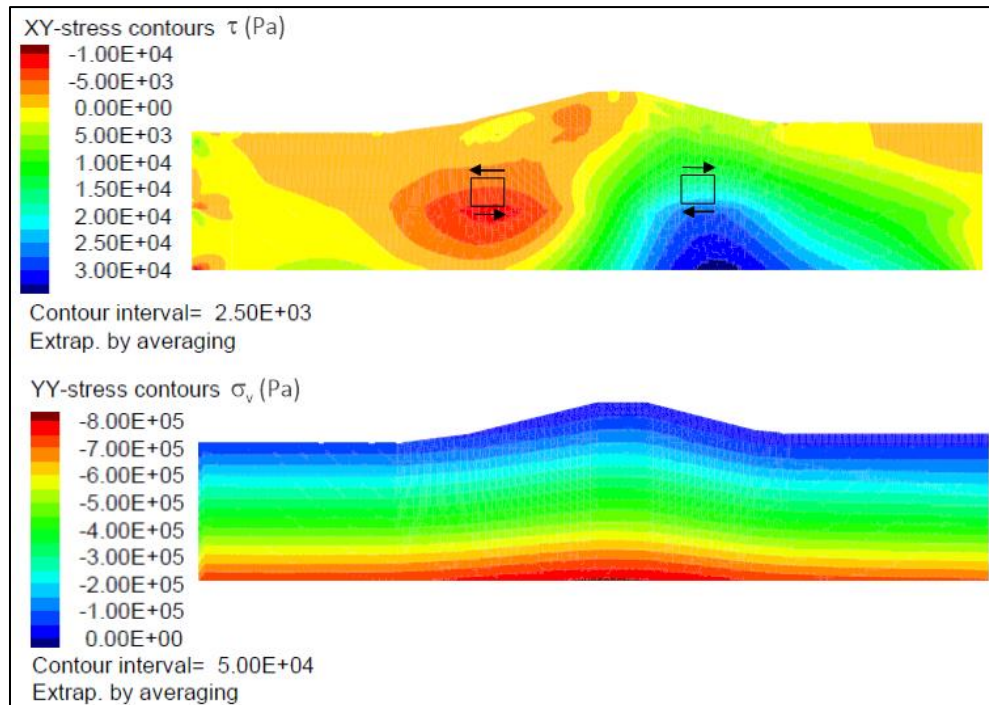


Figure 6.11 Distribution of shear stress and total vertical stress with the reservoir at full pool in static state

Figure 6.11 shows a shearing plan at the center of the model as the downstream face tends to move downward. It becomes more evident in figure 6.12 which presents the horizontal and vertical displacement where the downstream face moves downward to the right. The settlement monitored at the crest is 1.2 mm and the embankment moves up to 1.8 mm to the right.

Strangely, the upstream surface tends to go up, which is impossible since the weight of the reservoir is supposed to apply downward pressure. However, the values are very small with a negative shear stress up to 5 kPa and an upward displacement of 0.8 mm. This strange observation can, therefore, be neglected.

Furthermore, it is important to verify that the shear stress level remains close to zero or is low compared to the total vertical stress  $\sigma_v$ . Otherwise, the shear stress may not be compatible with the hysteretic damping formulation. Figure 6.11 shows that the shear stress is ranging between -10 and 30 kPa which is low because it is always less than 10 % of  $\sigma_v$  (-800 to 0 kPa). Therefore, its effects on the application of the hysteretic damping should be negligible.

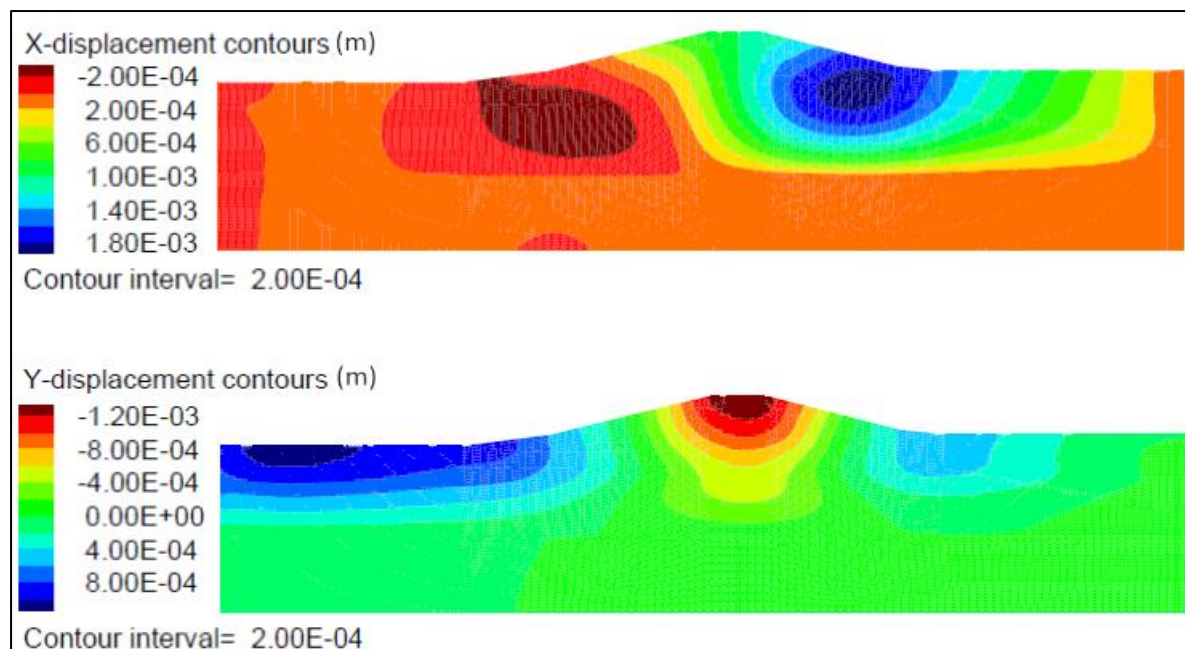


Figure 6.12 Horizontal and vertical displacement with the reservoir at full pool in static state

### 6.5.3 Static slope stability

After filling the reservoir, a static slope stability analysis is performed. Unlike the traditional method which provides an approximate solution using the method of slices, *FLAC* uses a strength reduction technique. It performs a series of simulations while changing the strength properties. Hence, the factor of safety corresponds to the point of stability (Itasca, 2016). Figure 6.13 presents the critical failure surface and the corresponding factor of safety.

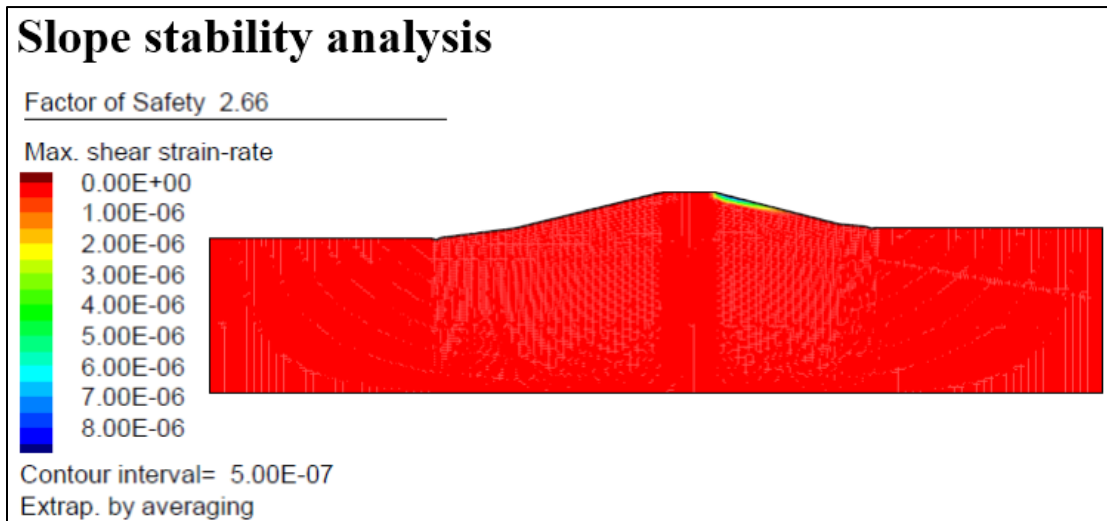


Figure 6.13 Factor of safety of 2.66 for a potential slope failure at the downstream face of the model – Static slope stability analysis

A factor of safety of 2.66 is found and the critical failure surface is located on the downstream face near the crest. Since the factor of safety is large and the critical slip surface is shallow, the slopes are considered stable.

## 6.6 Dynamic linear damped simulations

After initializing the model, the next step is to perform a linear dynamic simulation with elastic-materials. Dynamic forces are applied as shear stresses at the base boundary, as explained in section 6.4.2. As large strain is expected, the large strain mode is activated to provide more accurate deformations.

Rayleigh damping is added to the model to reduce high and low-frequency noise while still simulating linear behavior. One of the objectives of linear simulations is to validate the model, the strength parameters and the level of damping. It is interesting to observe the behavior of the model under seismic loading without it being hidden by attenuation caused by hysteretic damping. Validation of the model under one input ground motion is performed with a linear elastic-materials dynamic simulation, and discussed herein.

### 6.6.1 Validation of the model

Before running fully non-linear simulations, a preliminary run is made to assess for potential problems and to estimate some parameters in the model such as:

- The effect of the side boundary location
- The influence of the free surface (doubling effect)
- The natural frequency ranges
- The necessity for additional damping

A single Rayleigh damped linear elastic-materials simulation was run to validate the model. The preliminary analysis is performed using the input ground motion RSN598H2 of scenario T2-1 (earthquake Whittier Narrows – 01). The *FLAC* model has a predominant frequency of 2.9 Hz.

#### 6.6.1.1 Side boundaries location and maximum level of shear strains

The side boundaries must be far enough to capture all forces increment in the model while still keeping an adequate running time. The location of the side boundaries is selected after monitoring the development of a potential failure surface using elastic-materials. Its position can be determined by observing the shear-strain contour plot illustrated in figure 6.14. The maximum strain is located right underneath the embankment in the loose deposit. Since the soils near the sides of the model

are not affected by the embankment, the location of the side boundaries may be considered adequate.

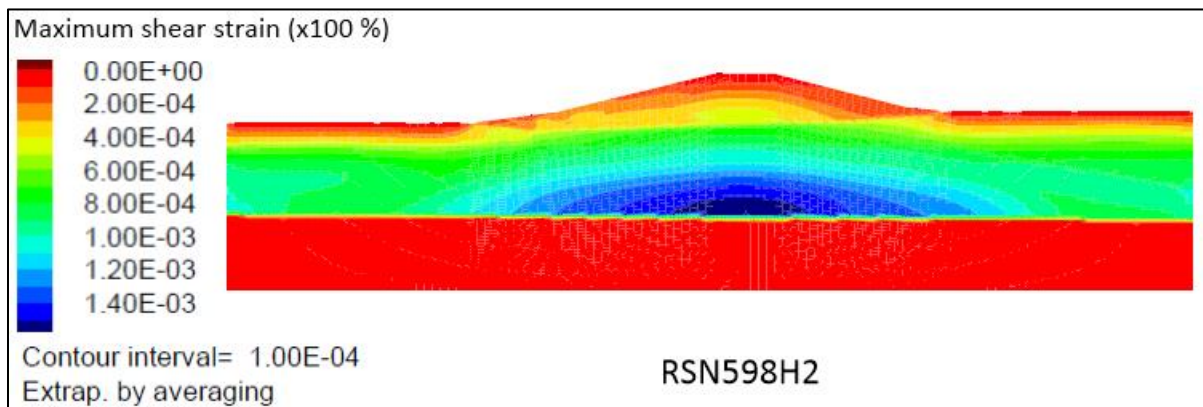


Figure 6.14 Maximum level of shear strain of the preliminary analysis performed using RSN598H2 of scenario T2-1

Since the Darendeli *MRD* model is only defined at strain levels below 0.3 % and that plastic yielding is not allowed, the maximum levels of shear strains should be monitored throughout the model. The results of the elastic simulation performed with ground motion RSN598H2 indicate a maximum shear strain of 0.14 %, though the strains mostly accumulate in the natural silt layer.

#### 6.6.1.2 Influence of the free surface

The velocity doubling effect is an important issue when selecting the location of the bottom boundary. As the base is flexible, the ground motion transformed into input stress introduces upward propagating waves at the base and, at the surface, they are reflected back into the model as downward propagating waves. The quiet boundaries at the base should absorb the downward waves so that the velocity recorded at the base will not double. However, if the model is too shallow, the quiet boundaries will not be as effective to adsorb the downward waves and velocity doubling effects may be observed. To avoid this issue, the model may be deepened so that the bottom boundary exceeds the range of the velocity doubling effect.

The range of the velocity doubling effect of the free surface can be estimated based on the recommendations from the *FLAC* manual (Itasca, 2016). It approximately corresponds to 1/3 to 1/4 of the maximum wavelength  $\lambda$ . For this project, the maximum wavelength of approximately 500 m, hence the bottom boundary should be located at a depth of at least 125 m to avoid velocity

doubling effects. A model that deep would result in an excessively heavy computational burden to the software.

Another solution to this issue is to modify the factor  $K_I$  in the input stress boundary equation. Several runs using elastic-materials can be made to determine an adequate value of  $K_I$  to ensure a better match of the recorded velocity at the base to the input velocity. It is found that a value of 1.0 provides an adequate match with the target velocity as illustrated in figure 6.15. The recorded velocity is compared to the input velocity. The  $S_g$  is also computed at the base and compared to the input motion  $S_g$ . There is only a small amplification due to the doubling effect at the free surface which might be considered acceptable (Itasca, 2016).

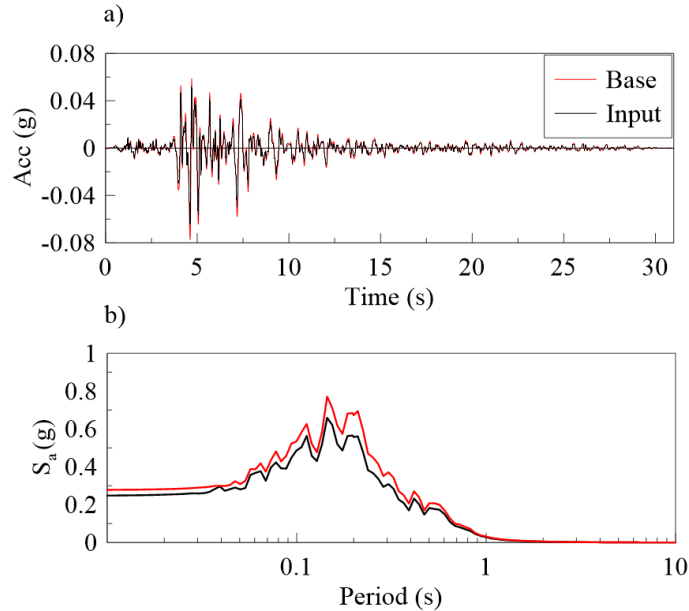


Figure 6.15 Comparison of recorded motion at the base and input motion in terms of a)  $v(t)$  and b)  $S_g$

## 6.7 Calibration of the hysteretic model

The sig4 sigmoidal model is implemented in *FLAC* and it uses 4 coefficients, to be calibrated to match the modulus reduction curve. The equation of the modulus reduction of the model is:

$$\frac{G}{G_{max}} = y_0 + \frac{a}{1 + \exp(-(L - x_0)/b)} \quad (\text{Eq 6.1})$$

In this project, the calibration of the coefficients is performed so that the hysteretic model implemented matches the target *MRD* curves computed using Darendeli's equations (figures 6.16 and 6.17). In particular, the calibration is performed by matching the calibrated backbone curve to the target curve since the backbone curve is more sensitive to an error in the calibration than the *MRD* curves.

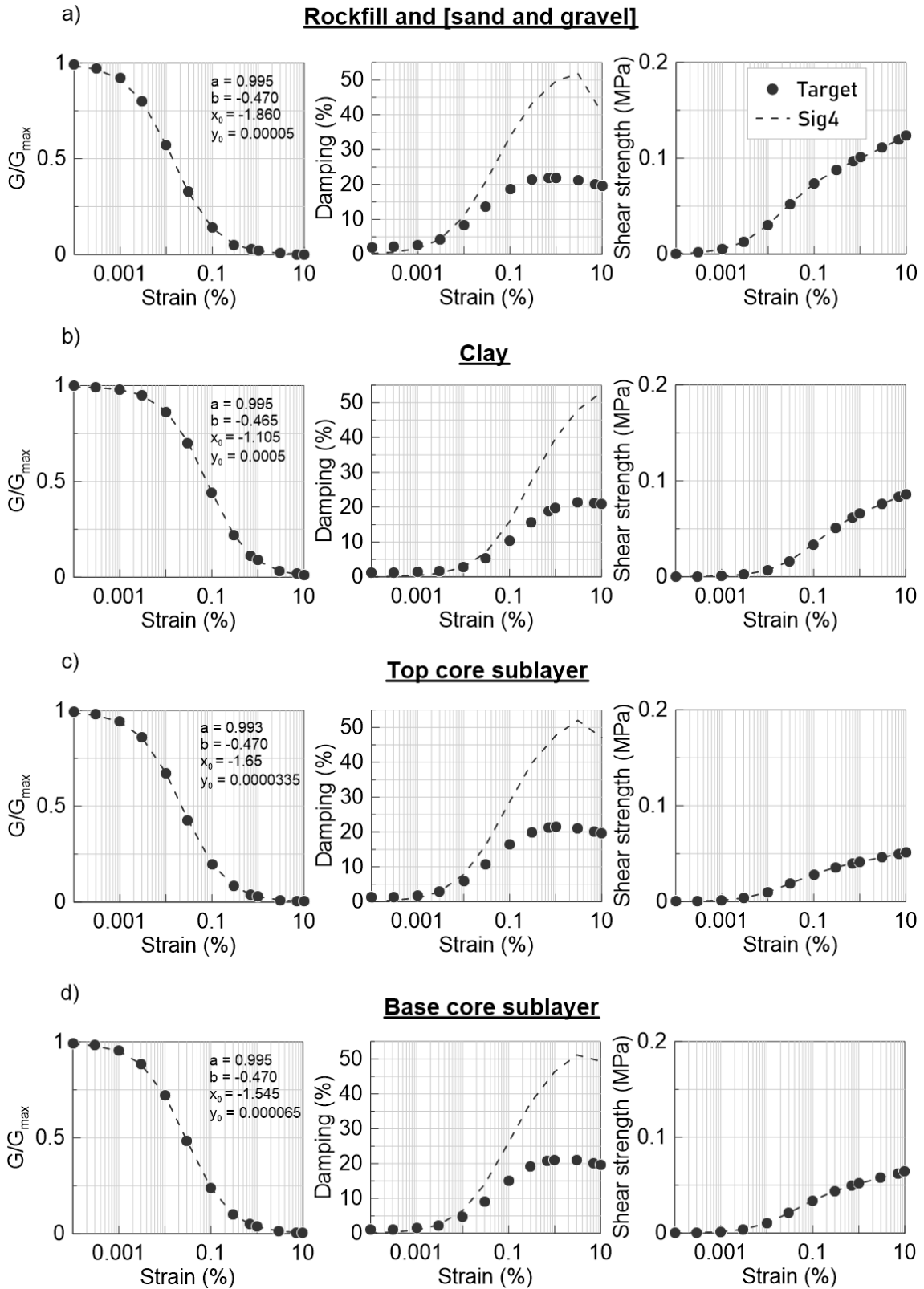


Figure 6.16 Calibration of the hysteretic sig 4 model for a) the rockfill and sand and gravel, b) the clay, c) the top core sublayer and d) the base core sublayer

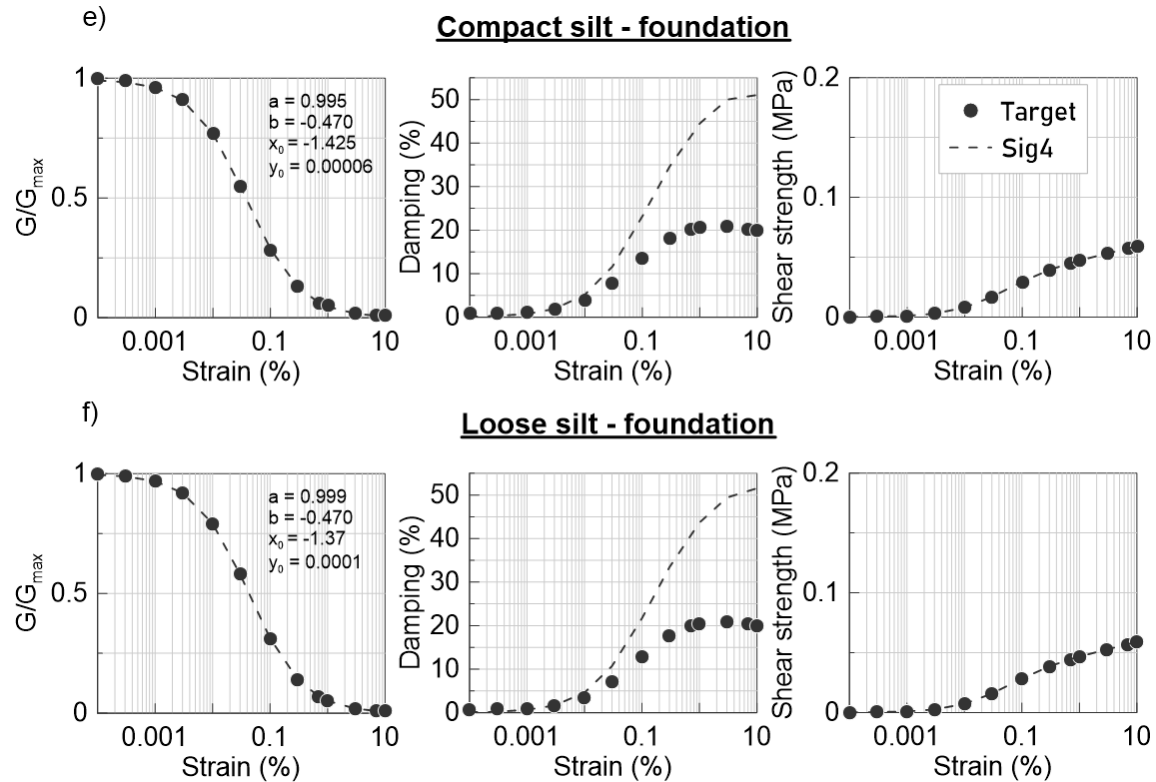


Figure 6.17 Calibration of the hysteretic sig 4 model for the foundation soils: a) compact silt and b) loose silt

The calibrated sig4 curves match closely the target stiffness reduction curves and the backbone curves. Meanwhile the sig4 damping curves match adequately the target damping for strains  $< 0.01$  % but overestimate the target for strains  $> 0.01$  %, especially after  $0.1$  %. This inconsistency between the calibrated damping curves and target curves was also noted by Manika et al. (2014). Hence, the soil response at large strains is expected to be excessively reduced (damped) when strains exceed  $0.1$  %.

## 6.8 Factors affecting the timestep

One of the main reason why simulations on *FLAC* are time consuming is due to the timestep. *FLAC* resolves each equation for each timestep. Hence, the smaller the timestep, the lengthier the time of the simulation. The software uses a minimum value of timestep that avoid instability during the simulation. There are certain factors that significantly influence the timestep such as:

- The Rayleigh damping ratio;
- The center frequency  $f_c$  of Rayleigh damping, etc.
- The stiffness of the model;

### 6.8.1 Materials stiffness

The stiffness of soils influences the equation of continuity. High stiffness reduces the timestep. In the manual of *FLAC*, it is recommended to reduce very high stiffness values and in particular the contrast of stiffness between materials.

For example, since the bedrock is modeled as an elastic bedrock with stiffness and density in this project, its true stiffness is very high but might be reduced to a lower value without significantly affecting the results. Thus, a higher value of porosity  $n$  is selected for the bedrock to reduce the stiffness of the material (see section 6.4.3) as the stiffness is proportional to  $1/n$ .

### 6.8.2 Center frequency $f_c$ of Rayleigh damping

A lower center frequency  $f_c$  considerably reduces the timestep of the simulation. In this project, the  $f_c$  is chosen as the motion center frequency. For example, a nonlinear simulation using a motion with a center frequency  $f_c$  of 4.5 Hz, will be ran with a timestep of  $3.7\text{e-}6$  seconds. Meanwhile, a motion with a lower  $f_c$  of 1.1 Hz will compute a timestep of  $9.2\text{e-}7$  seconds, which is approximately 4 times less. Hence, the simulation time of the latter might be approximately 4 times higher than the other one.

### 6.8.3 Damping ratio of Rayleigh damping

Another factor that may impact the timestep is the damping ratio of Rayleigh damping. A higher value of the damping ratio reduces the timestep and hence increases the running time. The *FLAC*'s manual proposes to reduce the damping ratio to a value of 0.2 %.

To verify this theory, a comparison has been made between 2 simulations:

- 1- using the exact materials damping ratio (approach 1); and
- 2- using a uniform damping ratio value of 0.2 % (approach 2)

The comparison is performed using the motion RSN381H1 (earthquake Coalinga-02) with a *LC* of 0.7 Hz and *HC* of 30 Hz. Simulations using a reduced damping ratio ran 6 times faster than those using the exact materials damping ratios. Meanwhile, the impact of the damping ratio method on the surface spectra at different locations is illustrated in figure 6.18.

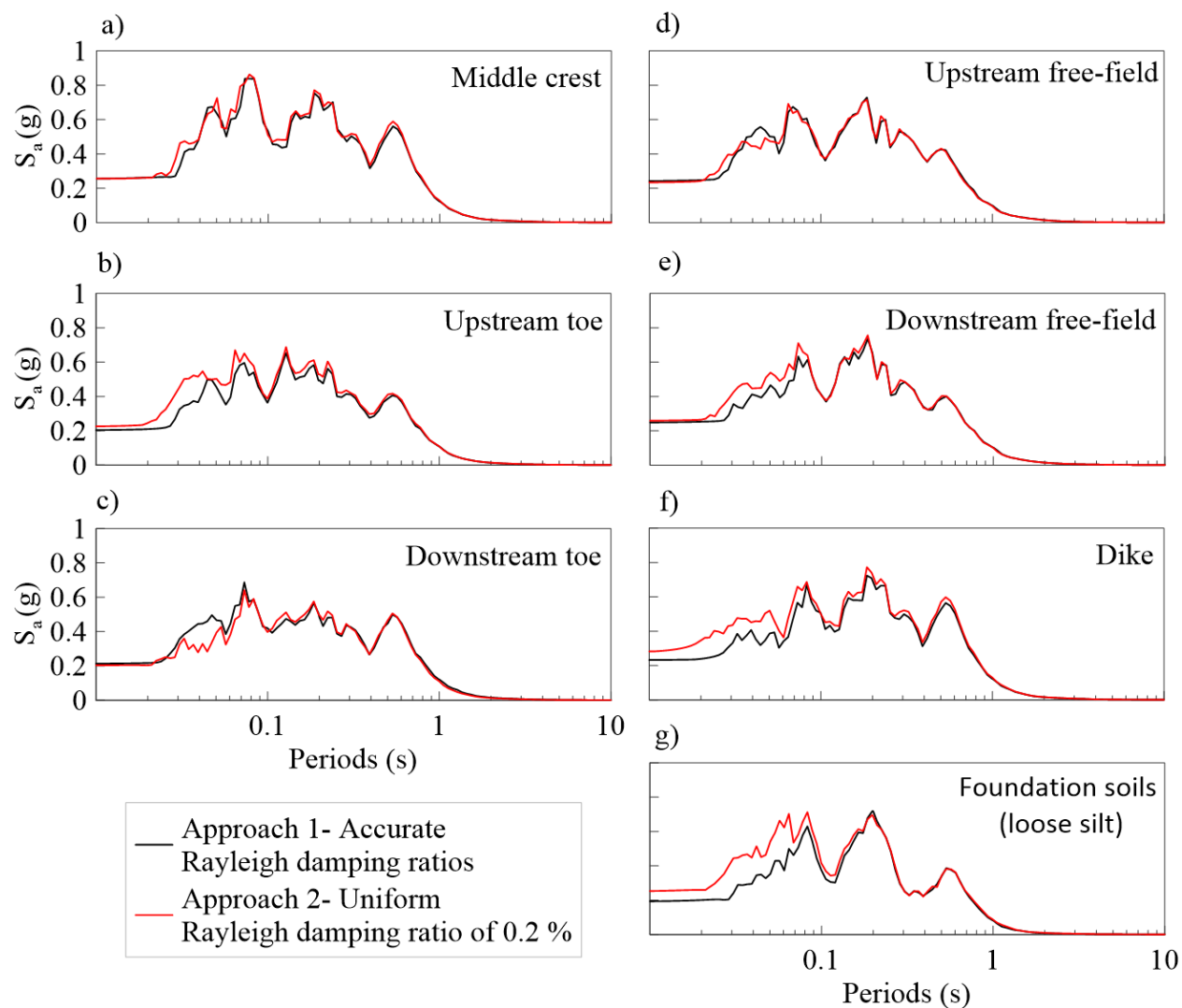


Figure 6.18 Comparison of the response spectrum between approach 1 (accurate values of materials damping ratio) and approach 2 (uniform damping value of 0.2 %) at the a) middle crest, b) upstream toe, c) downstream toe, d) upstream free-field, e) downstream free-field, f) in the dike and g) in the foundation soils (loose silt)

It appears that despite the gain of time, the results are significantly impacted by a reduced damping ratio at short periods (high frequency). The response spectra using approach 2 can be significantly higher than when using approach 1 at short periods, particularly in the dike and the foundation soils. The *PGA* computed with a damping ratio of 0.2 % is up to 30 % more than that of the approach 1. In conclusion, for the geotechnical system simulated here, despite reducing running time, the impact on the results does not justify using a lower value of damping ratio as suggested by the *FLAC*'s manual.

## CHAPTER 7 RESULTS

### 7.1 Introduction

Elastic and nonlinear dynamic simulations are performed using *FLAC*. Acceleration time series, stresses and strains are tracked during the simulations at a few locations of interest: the crest, free-field, toes, mid-slopes, 10 m away from the toes and the centerline of the model.

The spectral amplification is first analyzed followed by the evaluation of the level of soil stiffness degradation. The distribution of *CSR* calculated with *FLAC* is presented alongside the comparison with the *CSR* using the simplified method by Boulanger and Idriss (2008, 2014). Then, several intensity measures (*IM*) are calculated for each location of interest and compared with the input motions and between seismic scenarios. Finally, a brief parametric study is performed to find the most efficient *IM* in the prediction of surface accelerations and *CSR*.

### 7.2 Summary of the results

- Scenario T2-1 returns values of *IM* and spectrum that are fairly average among scenarios with its input spectrum being compatible with the shape of the design spectrum around the  $T_0$ .
- Scenario T1-1 returns weak responses in terms of *IM* due to short input motions ( $D_{75} = \pm 4.5$  s). It returns the weakest *IM* at the surface and weakest values of *CSR*, including *PGV*,  $I_a$ , *CAV*,  $CAV_5$ ,  $CAV_{std}$ ,  $S_a(1.5T_0)$ ,  $S_a(1.0)$  and *SI*.
- Scenario T1-2 returns very high responses in terms of *IM*, *CSR* and spectrum because its input motions exceed the design spectrum  $S(T)$  in the medium periods and its input integration-based *IM* are significantly higher than other scenarios. While T1-1 and T1-2 are both characteristic of the same design spectrum period range (between 0.01 and 0.2 s), the resulting  $I_a$ , *CAV*,  $CAV_5$  and  $CAV_{std}$  of T1-2 are up to 3.7 times higher than T1-1. The scenario T1-2 is also the scenario that shows the weakest amplification. Its input motions having high shaking amplitudes lead to more soil degradation and higher soil damping which contribute to lower amplification.

- Scenario T3-1 has the best potential for amplification among scenarios and shows *IM* comparable to other scenarios (*I<sub>a</sub>*, *CAV*, *CAV<sub>5</sub>*, *CAV<sub>std</sub>* and *SI*) although it being the weakest in terms of input shaking amplitudes and input spectral values. Its high response might be explained by a longer duration of motions ( $\pm 20$  s) and smaller input *IM* among other scenarios, leading to less degradation and more amplification. Also, high long period energy (high frequency) resulted in less degradation and it induced very little to no topographic effects as observed in the spectrum.
- Same level of degradation between T1-1, T1-2 and T2-1 with the degraded fundamental period of the model at  $\pm 0.53$  s, except T3-1 where the *T<sub>0</sub>* lengthens to  $\pm 0.44$  s.
- *PGA* is a poor indicator of the intensity of a motion. Indeed, an amplification of almost all calculated *IM* and response spectrum at the surface is observed, meanwhile the resulting *PGA* is reduced.
- Most degradation takes place in the foundation soils since the degraded fundamental period of the model is already apparent at the free-field and remained unchanged at the crest. Also, the mean period *T<sub>m</sub>* is stable between the crest and the free-field, indicating that the natural period does not continue to elongate.
- The level of spectral amplification is similar in the dike between all scenarios. This is observed by comparing the response at the free-field and the crest.
- Topographic effects are observed in most *IM* (*I<sub>a</sub>*, *CAV*, *CAV<sub>5</sub>*, *CAV<sub>std</sub>*, *ASI*, *SI*, *SIR<sub>75</sub>* and *SIR<sub>95</sub>*). Those *IM* are the highest at the crest which is in agreement with the literature. Topographic effects are not observed in the spectrum of low frequency motions, but are observed in all *IM*.
- The maximum *CSR* is calculated along the downstream face of the dike, near the toe and *CSR* is high as well below the downstream toe where it diminishes gradually with depth. Concentrations of *CSR* are also observed along the upstream face of the dike to the toe.
- Values of *CSR* calculated with the simplified method proposed by Boulanger and Idriss (2008, 2014) are much smaller than those calculated with *FLAC* and the scenarios containing more long-period energy (T2-1 and T3-1) showed lower values of *CSR* due to lower *PGA* which is contrary to what is observed in *FLAC*.

- Except for peak values, the *CSR* are relatively similar for all scenarios below the downstream toe with all scenarios exhibiting liquefaction.
- The parametric study showed that the resulting *PGA* is best correlated with the input *PGA*,  $S_a(0.1)$  and *ASI*, the resulting spectral values are best correlated with the input spectral values of the same period. Also, the *CSR* showed a better correlation with integration-based *IM* such as *CAV*, *CAV<sub>5</sub>*, *CAV<sub>std</sub>*, *I<sub>a</sub>* and *ASI*. Besides, the input spectrum and *PGA* showed the least efficiency in the prediction of *CSR*, which could question the procedure of selecting input motions which is based on the shape of input spectrum.

### 7.3 Tracked variables and history points

In *FLAC*, data is saved only at specific history points defined by the user. The response is monitored at critical locations, such as the crest, on the faces of the dike, on the toes, near the toes, at the free-fields and a profile of history points at the centerline of the model. The defined history point locations are presented in figure 7.1.

For models with topographic irregularities, the crest, toes, slopes, and the vicinity of the toes are the regions that may experience the greatest amplification or attenuation. The free-field is interesting to assess the level of amplification without topographic effects. Several history points were also placed along the centerline of the model to obtain a profile of data.

The following variables are monitored at each history point:

- Acceleration time series;
- Cyclic shear stress ( $\tau$ );
- Cyclic shear strain ( $\gamma$ );

Maximum values for the entire duration of the earthquake are also monitored for each element:

- Maximum peak ground acceleration *PGA*;
- Maximum cyclic shear stress ( $\tau$ );
- Maximum cyclic shear strain ( $\gamma$ );

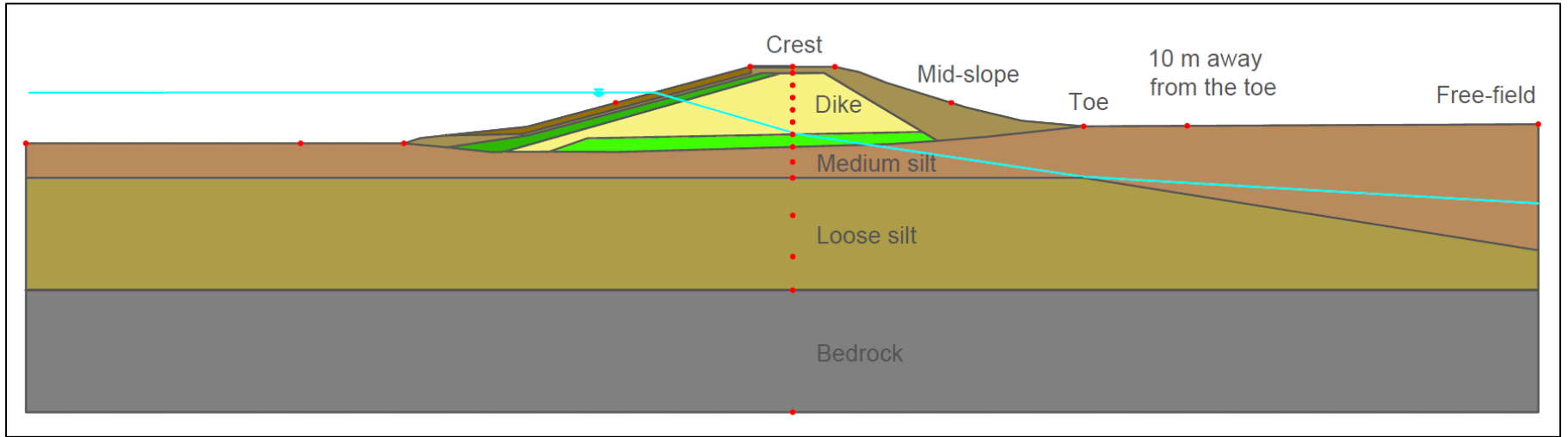


Figure 7.1 Location of history points in the 2D *FLAC* model

## 7.4 Scenario-specific study of the seismic behavior of the dike

The consequences of each scenario are evaluated by performing nonlinear simulations in *FLAC*. The response spectra and intensity measures (*IM*) at different locations of the model are compared between the scenarios. The results of the simulation performed with the event below are discarded from the study due to the simulation not converging; several nodes showed a modulus reduction  $G/G_{max}$  of 0 to nearly 0.

- Whittier Narrow – 01 in California (RSN671H1) of scenario T1-2

### 7.4.1 Spectral response and spectral amplification

#### 7.4.1.1 Amplification of the waves between the crest and the input spectrum of the model

Figure 7.2 presents the average spectral response (*mean S<sub>g</sub>*) calculated at the crest and the input spectrum applied at the base. Figure 7.3 presents a comparison of the *mean S<sub>g</sub>* calculated at the crest between scenarios. Figure 7.4 shows the amplification ratios, calculated between the *mean S<sub>g</sub>* of the crest and the input *mean S<sub>g</sub>* at the base.

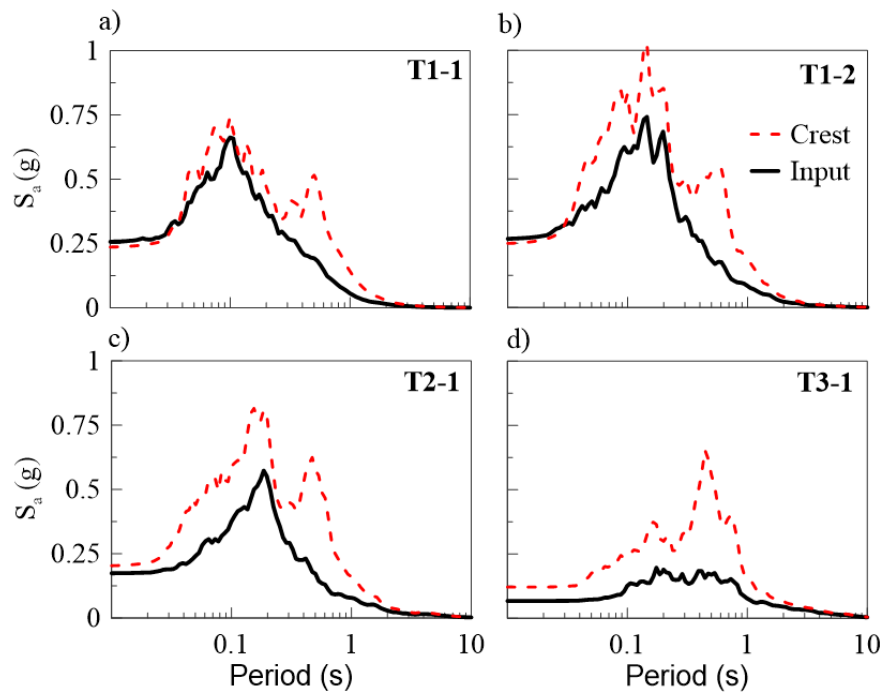


Figure 7.2 Average spectral response calculated at the crest and compared to the input spectrum of scenarios a) T1-1, b) T1-2, c) T2-1 and d) T3-1

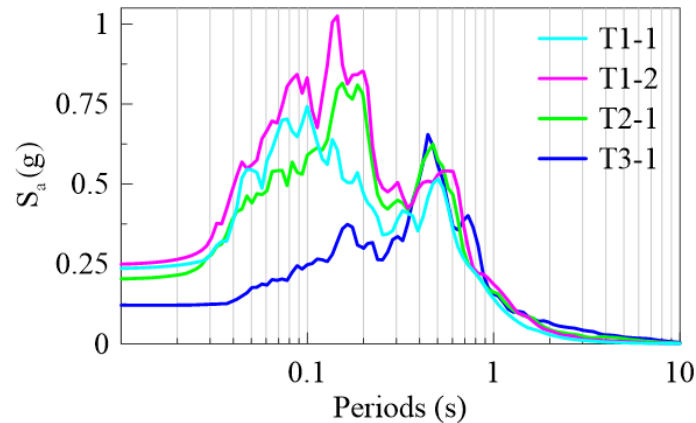


Figure 7.3 Average spectral response calculated at the crest for each scenario

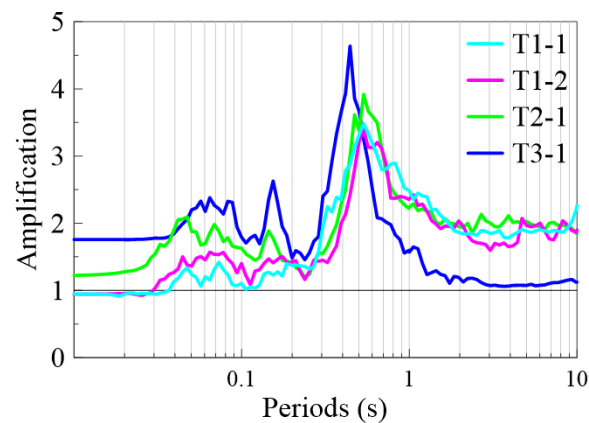


Figure 7.4 Amplification ratios calculated between the average spectral response at the crest and the input average spectral response

The principal observations that can be made based on figures 7.2 to 7.4:

- 1- The *mean*  $S_g$  calculated at the crest is almost always amplified compared to the input spectrum (amplification ratios  $\geq 1$ ). This observation agrees with the results of several past studies. Note that the *PGA* of T1-1 and T1-2 are slightly attenuated at the crest (ratio of 0.94), which may be a result of strong shaking leading to smaller peak amplitudes. Note that spectral values below 0.03 s are only representative of the *PGA* because these frequencies were mostly filtered out during processing of the ground motion records.
- 2- Similar levels of amplification for T1-1, T1-2 and T2-1 are observed at all periods, although T2-1 is more amplified at shorter periods with an amplification ratio of 1.22 for the *PGA* compared to 0.94 (attenuation) for T1-1 and T1-2. This might be due to a lower input spectrum at short periods for T2-1 resulting in less degradation and hence a better potential

for wave amplification. This is also observed in section 7.4.1.2 where the spectrum of T2-1 is amplified in the free-field at short periods compared to T1-1 and T1-2.

- 3- Elongation of the initial fundamental period  $T_0$ , to  $\pm 0.53$  s for T1-1, T1-2 and T2-1 and to  $\pm 0.44$  s for T3-1.
- 4- Lower degree of soil degradation for T3-1 due to weaker seismic waves, leading to a higher level of amplification and less elongation of the  $T_0$ .
- 5- Shape of the *mean*  $S_g$  of T3-1 different from others with less frequency content in the low periods.
- 6- The  $S_a$  at the degraded  $T_0$  is generally similar between scenarios, varying between 0.50 g and 0.65 g with T3-1 being the highest.

#### **7.4.1.2 Amplification of the waves between the crest and the free-field**

Figure 7.5 presents the *mean*  $S_g$  calculated at the crest, at the downstream free-field and the input spectrum applied at the base. A comparison between the crest and the free-field shows the amplification of the waves caused by the dike, by excluding the foundation soils. Figure 7.6 presents the *mean*  $S_g$  calculated at the free-field of each scenario.

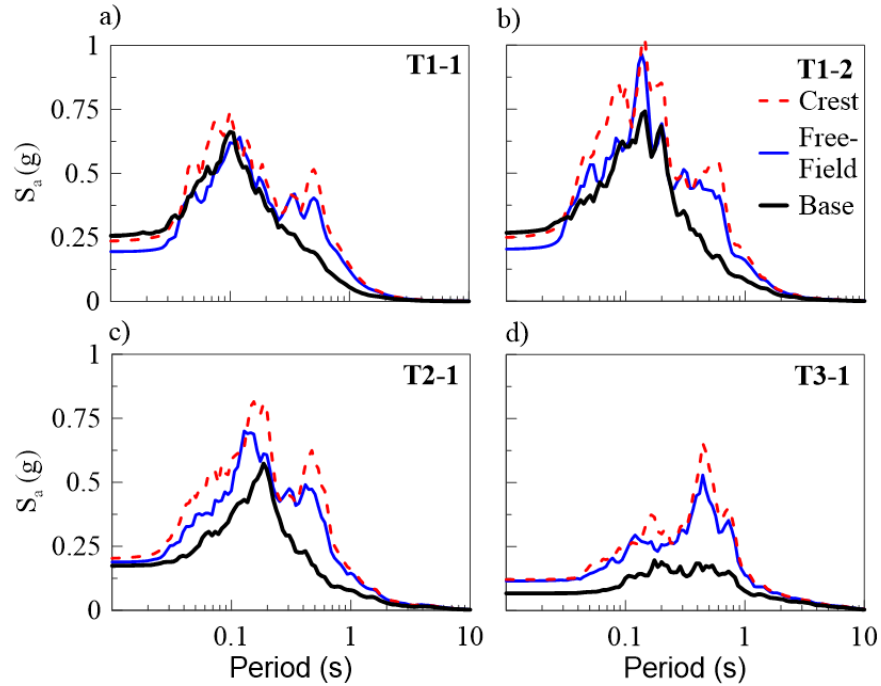


Figure 7.5 Average spectral response calculated at the crest and compared to the free-field and the applied input spectrum of scenarios a) T1-1, b) T1-2, c) T2-1 and d) T3-1

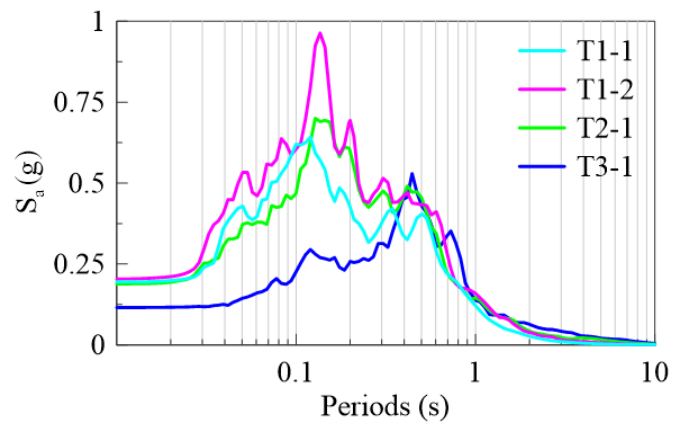


Figure 7.6 Average spectral response calculated at the free-field

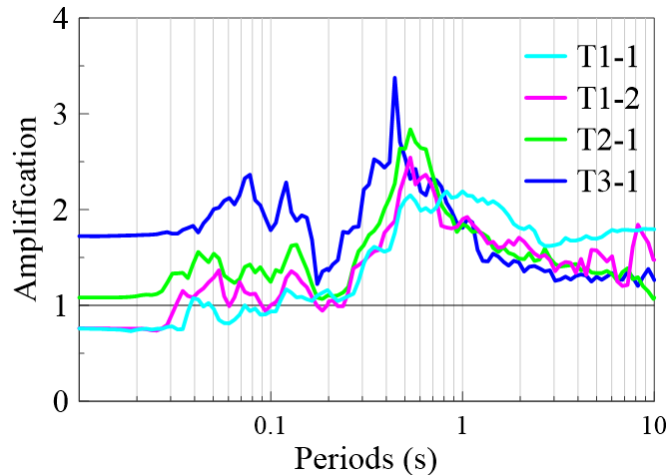


Figure 7.7 Amplification ratios calculated between the average spectral response at the free-field and the applied input spectrum at the base

Here is a list of the principal observations based on figures 7.5 to 7.7:

- The response of the model is generally controlled by the foundation soils. Indeed, the shape of the free-field *mean S<sub>g</sub>* is similar to the crest's.
- Most of the soil degradation takes place in the foundation soils and not in the dike since the degraded  $T_0$  is already apparent in the free-field spectrum (0.53 s for T1-1, T1-2 and T2-1 and 0.44 s for T3-1). Thus, materials composing the dike exhibit very little degradation.
- Under T1-1 and T1-2, figure 7.5 shows that the amplification below 0.53 s observed at the crest is mostly due to materials composing the dike. The *mean S<sub>g</sub>* of T1-1 and T1-2 is neither amplified nor attenuated, with amplification ratios oscillating around 1.0, except around the degraded fundamental period (0.53 s).
- Meanwhile, T2-1 and T3-1 exhibit significant amplification at the free-field at all periods.

The next figure presents the amplification ratios calculated between the crest and the free-field. It shows the amplification solely caused by the dike.

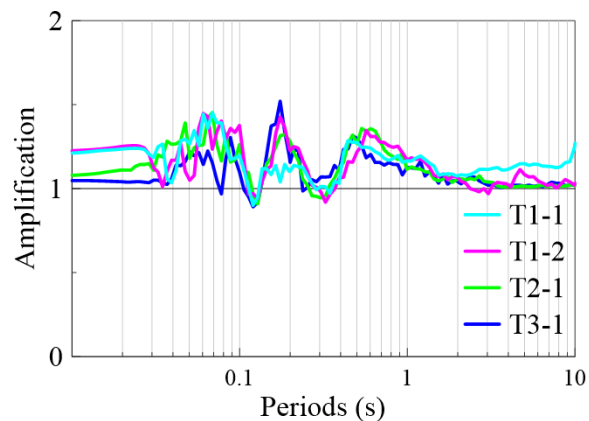


Figure 7.8 Amplification ratios calculated between the *mean*  $S_g$  of the crest and the free-field. The level of amplification of the waves passing through the dike are fairly similar between scenarios, particularly from 0.12 s and except for the *PGA* showing significant variations.

## 7.4.2 Soils nonlinearity

### 7.4.2.1 Natural modes degradation

Figure 7.9 presents the degraded modes determined from the amplification ratios between the *mean*  $S_g$  at the crest and the input spectra (refer to chapter 6 – section 6.4.6.).

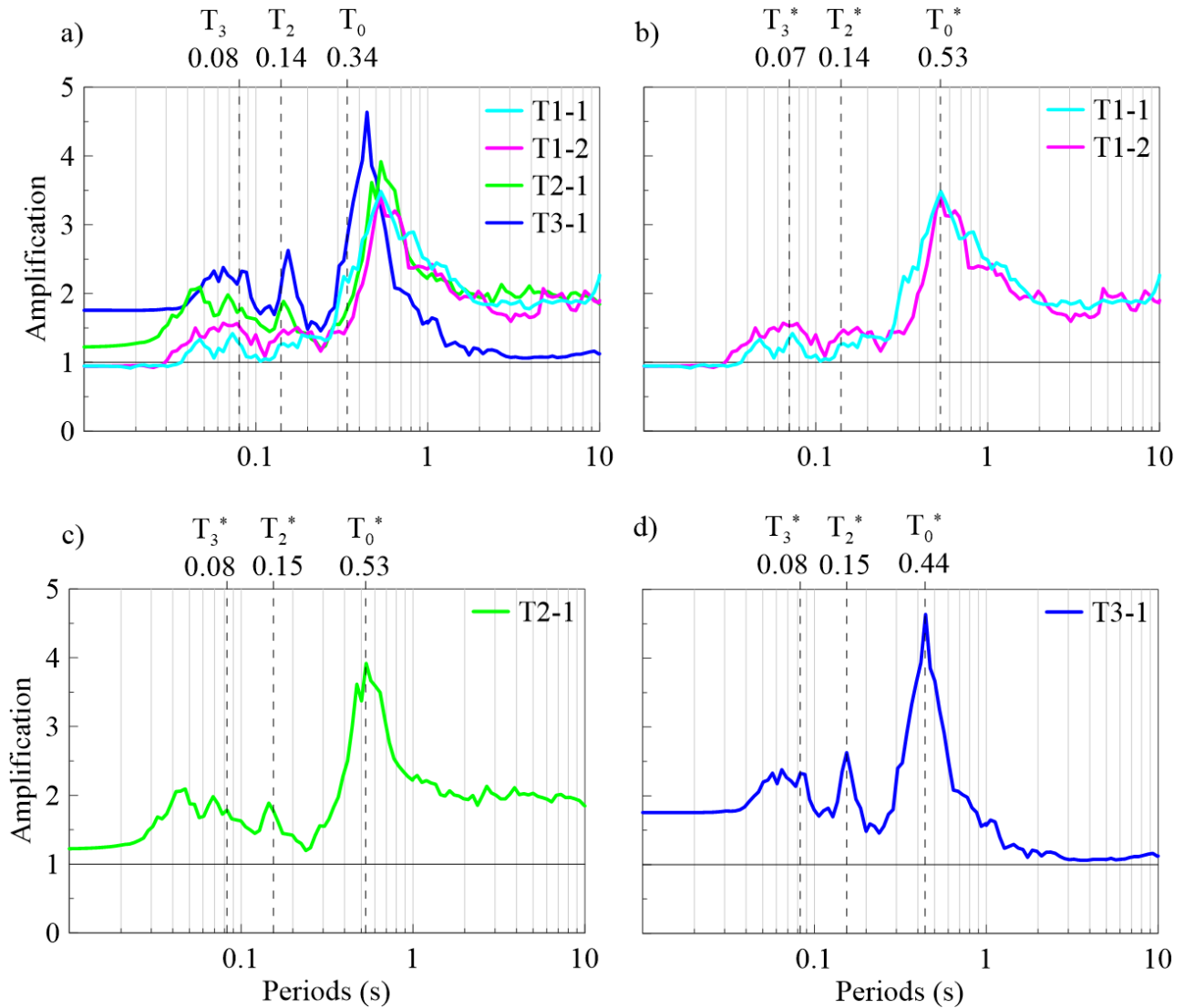


Figure 7.9 Degradation of the natural modes of scenarios a) T1-1, b) T1-2, c) T2-1 and d) T3-1

Soils degradation may be observed with the lengthening of the natural periods. The fundamental period  $T_0$  lengthens from 0.34 s initially to 0.53 s (T1-1, T1-2 and T2-1) and 0.44 s (T3-1). Moreover, the value of the degraded  $T_0$  (0.53 s) calculated based on T1-1, T1-2 and T2-1 also matches more or less the estimated value of  $1.5T_0$  suggested by the literature (Bray and Travasarou, 2007) which is 0.51 s. Besides, a lower degree of soils degradation has led to a shorter degraded  $T_0$  (T3-1). Interestingly, there is no significant degradation observed for the 2<sup>nd</sup> and 3<sup>rd</sup> modes as they showed little to no variations.

### 7.4.2.2 Degree of nonlinearities

A comparison of the results between linear and nonlinear dynamic simulations might be performed to adequately evaluate the level of soils degradation. Figure 7.10 presents the response spectrum at the crest calculated for both linear and nonlinear simulations for each scenario. Then, figure 7.11 presents a ratio representing the level of degradation; the ratio is calculated between the spectral values  $S_a$  considering an elastic behavior on the  $S_a$  considering a nonlinear behavior.

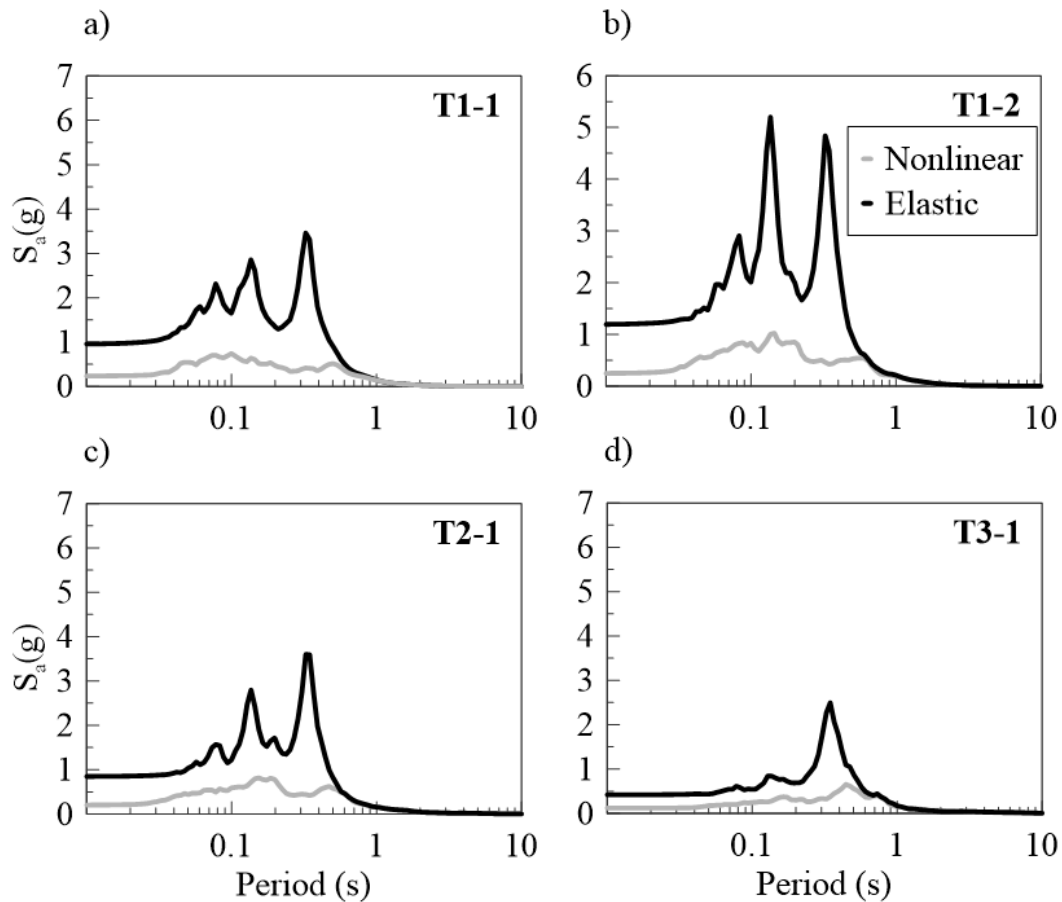


Figure 7.10 Average spectral response calculated at the crest using elastic and nonlinear properties for scenarios a) T1-1, b) T1-2, c) T2-1 and d) T3-1

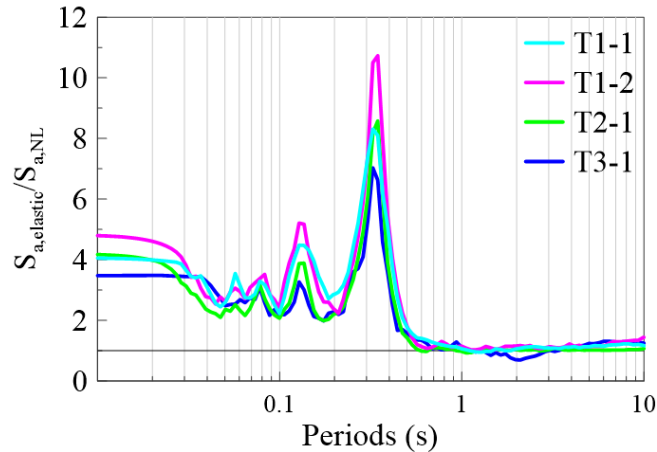


Figure 7.11 Influence of nonlinearity evaluated at the crest as the ratio between the *mean*  $S_g$  obtained from elastic and nonlinear simulations

Soil nonlinearity has considerably damped waves propagating in the model. The figure 7.11 shows that in average, nonlinear  $S_a$  are 1.7 to 12.8 times less than elastic  $S_a$ , meaning that nonlinearities have considerably diminished (damped) the *mean*  $S_g$ . Furthermore, damping is more significant at the 1<sup>st</sup> and 2<sup>nd</sup> natural periods of the model corresponding to 0.34 s and 0.14 s. Note that the damping curves modeled with the sig4 hysteretic model are significantly higher than the Darendeli curves for strains > 0.1 % (see ch6 – section 6.7).

Between scenarios, T1-2 shows the most nonlinearities with ratios of 5.7 for the  $PGA$  and 12.8 for the  $T_0$ . Scenarios T1-1 and T2-1 have a fairly similar degree of nonlinearity and scenario T3-1 has the lowest degree of nonlinearity, although comparable to T1-1 and T2-1. For periods longer than  $T_0$ , the difference between nonlinear and linear simulations drops to an almost null level for all scenarios.

#### 7.4.2.3 Variation of frequency content

Beyond the degradation observed at the crest for nonlinear simulations, soils degradation may also be observed through the model. Figure 7.12 shows the mean period  $T_m$  in the centerline of the model. The  $T_m$  may roughly represent the frequency content of the monitored motions and therefore, a shift in the frequency content might be observed.

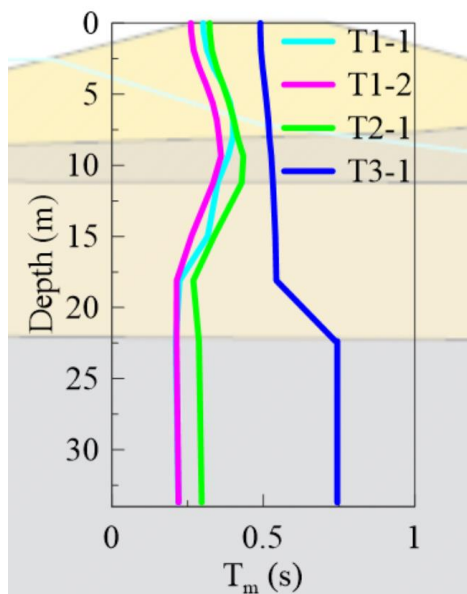


Figure 7.12 Profile of  $T_m$  in the centerline

The  $T_m$  is relatively stable in the bedrock as deformation is minimal. For T1-1, T1-2 and T2-1, recorded motions in the loose silt deposit contain more long-period energy as indicated by an increase of  $T_m$ . Motion frequency content shifts to the lower frequency range while the soil stiffness reduces. Then, the  $T_m$  decreases in the medium density silt and in the embankment, which corresponds to the motion frequency content shifting to higher frequency. Since the soils are stiffer, the soils do not tend to degrade as much as in the loose silt.

The variation of  $T_m$  is different for T3-1. The frequency content shifts to higher frequencies (lower period) once in the soil deposit and remain fairly constant up to the crest. This might be attributed to the high frequency content being more significantly amplified when compared to the other scenarios (see figure 7.7).

The variation of the frequency content may be observed in figure 7.13. It shows the *mean*  $S_g$  at several locations in the centerline profile of the model.

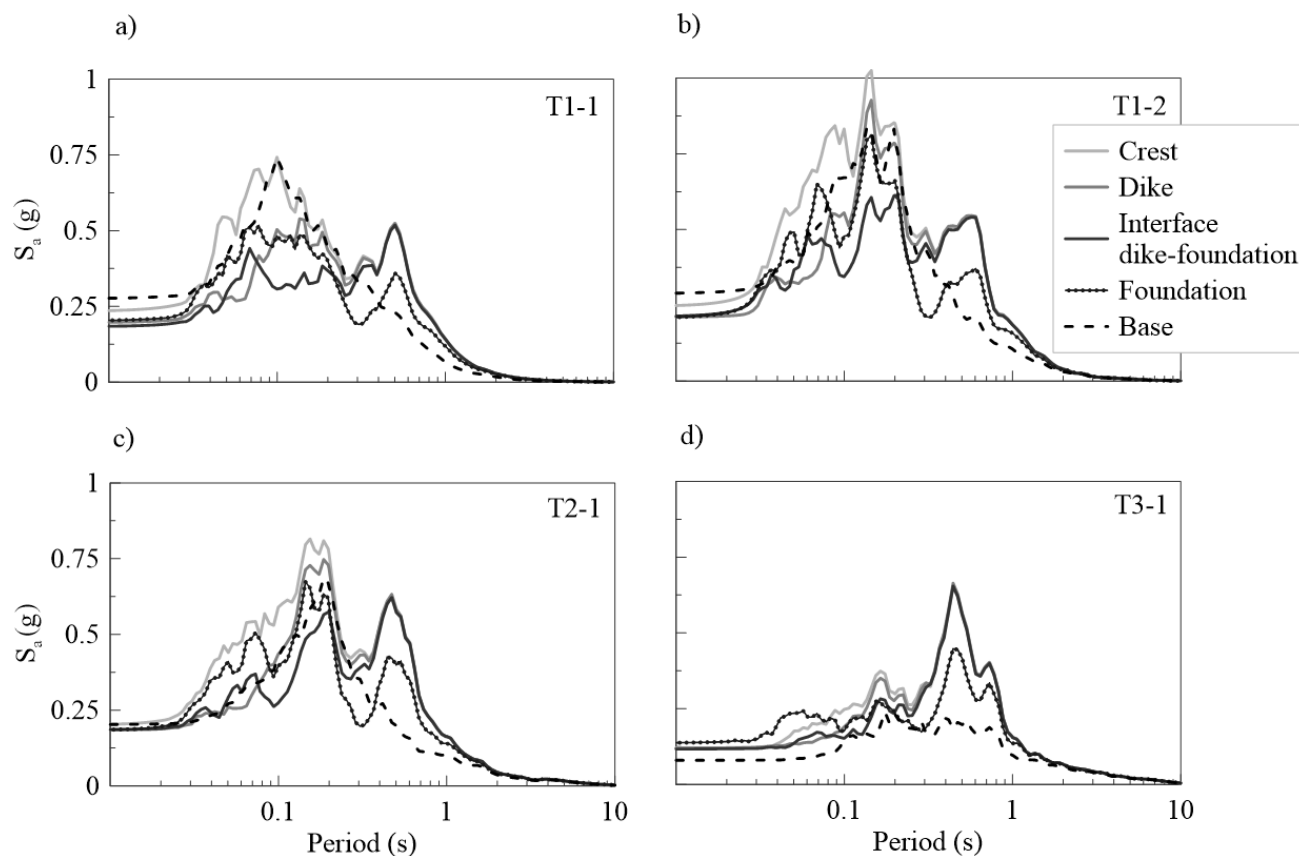


Figure 7.13 Average spectral response in the centerline at several depths of scenarios a) T1-1, b) T1-2, c) T2-1 and d) T3-1

Under T1-1, T1-2 and T2-1, the figure 7.13 shows a shift towards the long-period energy (low frequency) once in the foundation soils and a shift back towards the short-period energy (high frequency) once in the dike. Since the dike is much more rigid than the foundation soils, the waves tend to get amplified at short periods rather than attenuated as in the soft soils.

The shift in the long periods due to the foundation soils is less apparent in the free-field (figure 7.5) as the spectrum is either amplified (T2-1 and T3-1) or is more or less similar than the input spectrum (T1-1 and T1-2). It is possible that soil-structure interactions between the dike and the foundation have influenced the spectrum at the interface. Besides, the *mean*  $S_a$  at all periods are amplified for scenario T3-1 once in the foundation soils, including low periods.

Moreover, the degraded natural periods are already apparent in the foundation soils, further agreeing with the previous observation which is that most degradation takes place in the foundation

soils rather than in the dike. Then, the *mean*  $S_g$  amplifies as the waves propagate from the interface between the dike and the foundation soils up to the crest.

### 7.4.3 Amplification of intensity measures *IM*

The spatial distribution of *IM* is presented in this section:  $PGA$ ,  $PGV$ ,  $I_a$ ,  $CAV$ ,  $CAV_5$ ,  $CAV_{std}$ ,  $S_a(T_0)$ ,  $S_a(1.5T_0)$ ,  $S_a(0.1)$ ,  $S_a(1.0)$ ,  $S_a(10)$ ,  $T_m$ ,  $ASI$ ,  $SI$ ,  $SIR_{75}$  and  $SIR_{95}$ . The definitions of each *IM* are presented in chapter 2-Literature review. The *IM* are calculated at the surface of the model and are averaged for each scenario.

#### 7.4.3.1 Peak amplitudes *IM* – $PGA$ and $PGV$

Peak amplitudes *IM*:  $PGA$  and  $PGV$  represent the highest amplitude of a motion. The figure 7.14 shows the peak amplitudes *IM* and the figure 7.15 the amplification of those *IM*.

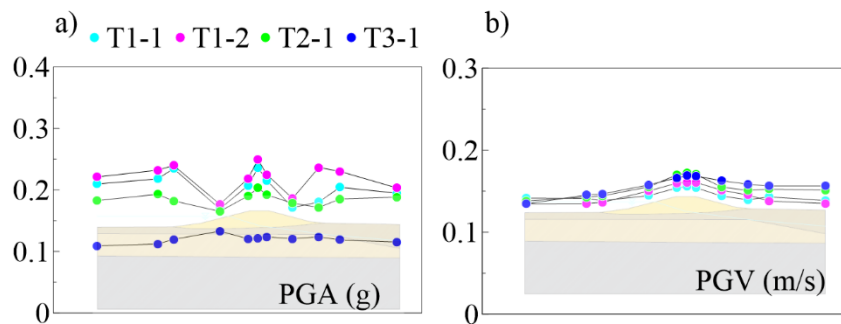


Figure 7.14 Amplitude-based *IM* at the surface of the model including a)  $PGA$  and b)  $PGV$

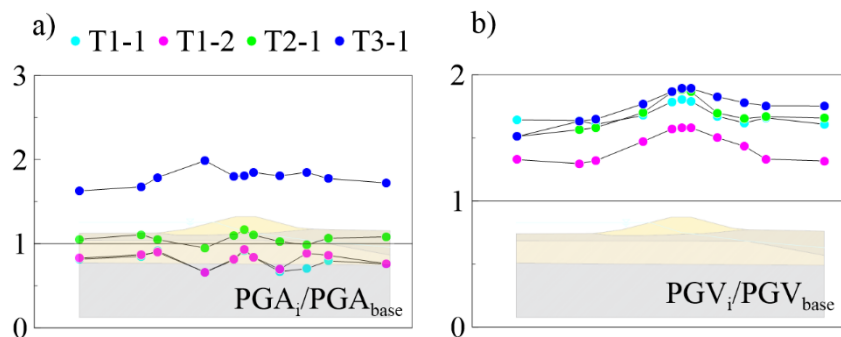


Figure 7.15 Amplification ratios of amplitude-based *IM* at the surface of the model including a)  $PGA$  and b)  $PGV$

Scenario T3-1 generally exhibits the highest amplification of  $PGA$  and  $PGV$  with T1-2 showing the lowest level of amplification. Meanwhile, the highest  $PGA$  values are monitored under T1-2.

At the surface of the model, the highest value of *PGA* is generally monitored at the middle crest where waves propagating in the dike have amplified due to the high rigidity of the materials composing the dike and where it benefited from the superposition of waves due to topographic effects. Besides, the *PGA* of T3-1 is fairly unaffected by topographic effects.

The *PGA* at the middle of the slopes generally shows the highest attenuation. This observation is possibly part of the attenuation/amplification pattern generally observed along the slopes in the literature (Géli et al., 1988). If there were more monitoring points on the slopes, this pattern may possibly have been observed. Also, frequency content along the slopes may shift as mentioned in section 7.3.3.4 and therefore affects the amplitudes of accelerations.

The *PGA* of T1-1 and T1-2 are slightly attenuated following strong shaking resulting in an increase of nonlinearities and damping. Meanwhile, the *PGA* of T2-1 and T3-1 are generally amplified. Finally, the *PGV* is amplified at all monitored locations on the surface and for all scenarios. The amplification ratios generally vary between 1.2 and 2.0.

#### **7.4.3.2 Integration-based IM – $I_a$ , *CAV*, *CAV*<sub>5</sub>, *CAV*<sub>std</sub>, *ASI*, *SI*, *SIR*<sub>75</sub> and *SIR*<sub>95</sub>**

The integration-based *IM* analyzed are *CAV*, *CAV*<sub>5</sub>, *CAV*<sub>std</sub>, *ASI*, *SI*, *SIR*<sub>75</sub> and *SIR*<sub>95</sub>. They are presented in figure 7.16 and their amplification ratios in figure 7.17.

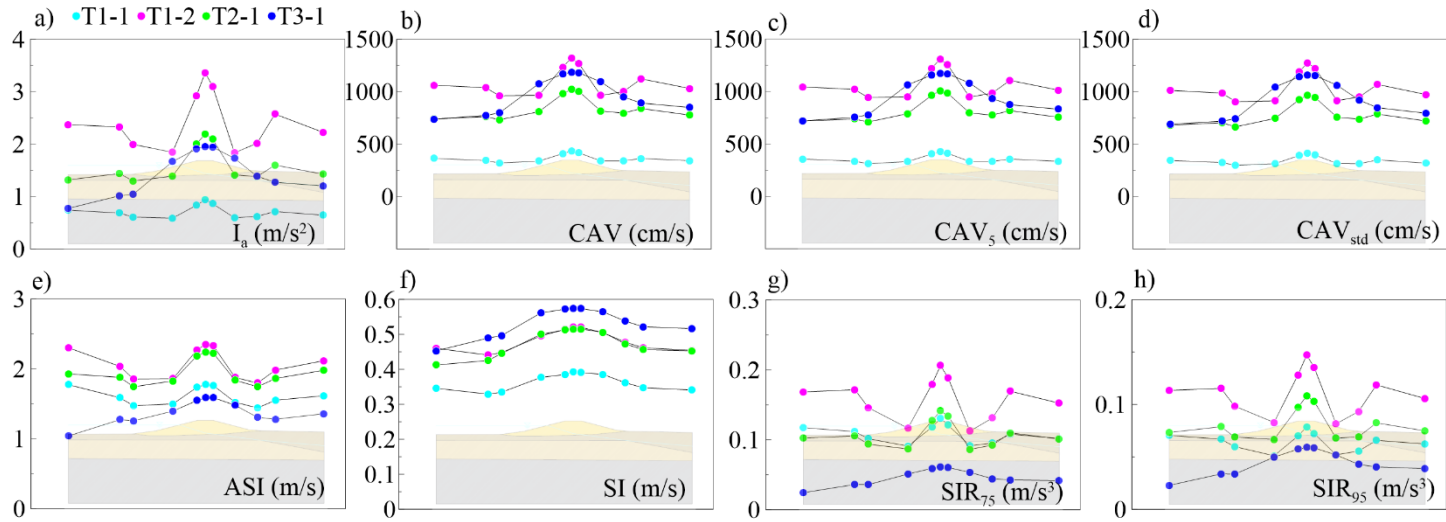


Figure 7.16 Integration-based  $IM$  at the surface of the model including a)  $I_a$ , b)  $CAV$ , c)  $CAV_5$ , d)  $CAV_{std}$ , e)  $ASI$ , f)  $SI$ , g)  $SIR_{75}$  and h)  $SIR_{95}$

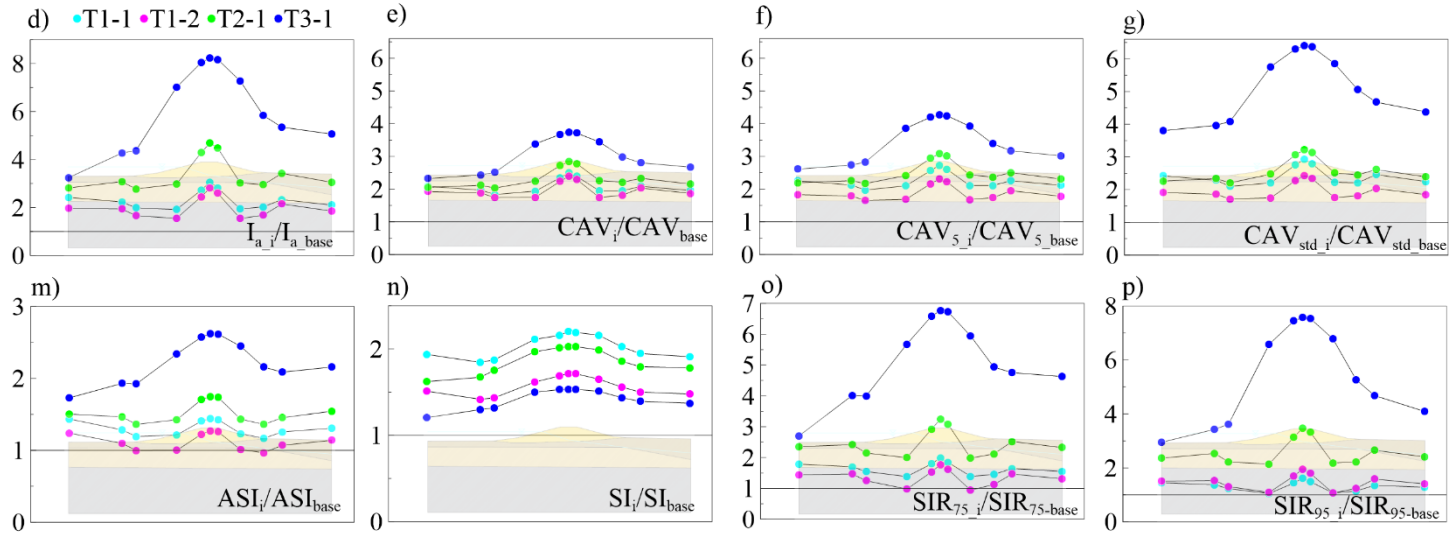


Figure 7.17 Amplification ratios of the integration-based  $IM$  at the surface a)  $I_a$ , b)  $CAV$ , c)  $CAV_5$ , d)  $CAV_{std}$ , e)  $ASI$ , f)  $SI$ , g)  $SIR_{75}$  and h)  $SIR_{95}$

The integration-based *IM* represent the amplitude, the frequency content and the duration of the monitored motions. As such, they are less influenced by processing and high spikes in acceleration time series. Hence, these *IM* may be considered more reliable in describing the content of a motion.

The *IM* all showed amplification at all monitored locations on the surface for all scenarios. Moreover, topographic effects are significant with *IM* being more amplified towards the dike. The level of amplification is generally slightly smaller at the toes than at the free-field, which may indicate a certain defocusing of waves from the toes.

The strongest seismic waves at the surface are observed under the influence of T1-2 and T3-1. They have resulted in the largest values of  $I_a$ ,  $CAV$ ,  $CAV_5$ ,  $CAV_{std}$  and  $SI$  due to the input integration-based *IM* of T1-2 significantly exceeding other scenarios and T3-1 having very long duration of motions ( $D_{75} = \pm 20$  s). Meanwhile, the weakest motions monitored at the surface are observed with T1-1 due to short acceleration time series ( $D_{75} = 4.5$  s). Besides, T2-1 shows average values of integration-based *IM* among scenarios. It is interesting that even though the average response spectrum of T3-1 is the weakest among scenarios, its results are still comparable to other scenarios due to its input motions being very long ( $D_{75} = \pm 20$  s). This is also observed with the  $SIR_{75}$  and  $SIR_{95}$  which divides the  $I_a$  by the duration and then drops to the lowest value among all scenarios.

#### 7.4.3.3 Spectral-based *IM* – $S_a(T_0)$ , $S_a(1.5T_0)$ , $S_a(0.1)$ , $S_a(1.0)$ and $S_a(10)$

The spectral-based *IM* are  $S_a(T_0)$ ,  $S_a(1.5T_0)$ ,  $S_a(0.1)$ ,  $S_a(1.0)$  and  $S_a(10)$ . They are presented in figure 7.18 and amplification ratios in figure 7.19.

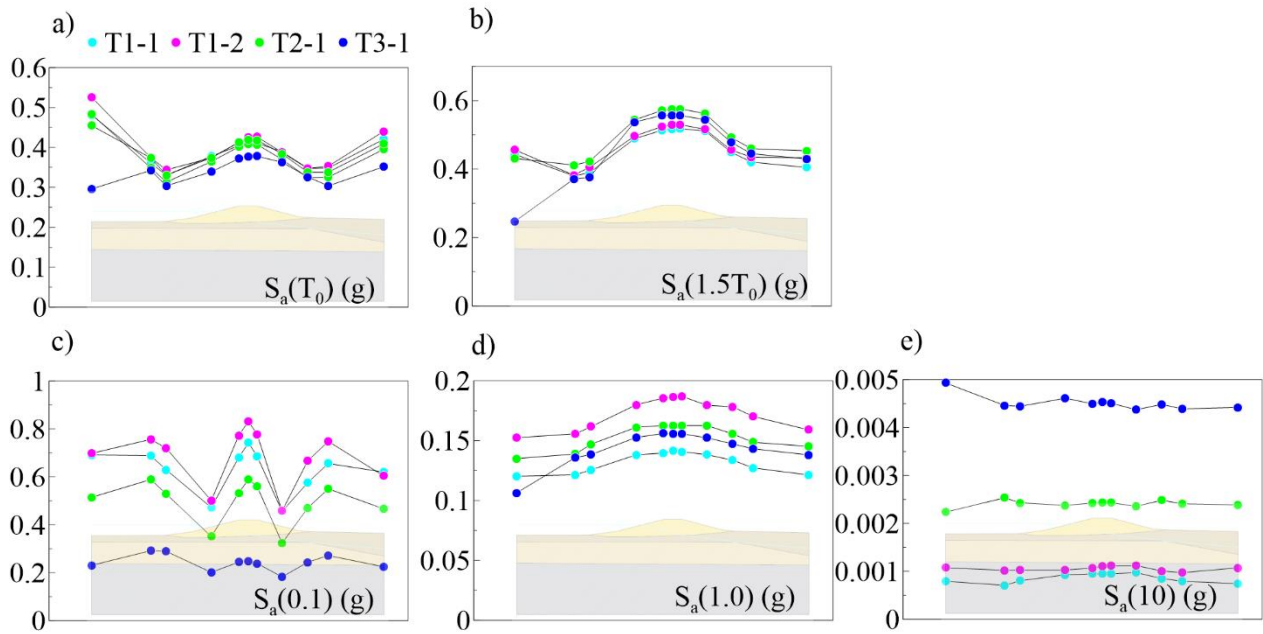


Figure 7.18 Spectral-based *IM* at the surface of the model including a)  $S_a(T_0)$ , b)  $S_a(1.5T_0)$ , c)  $S_a(0.1)$ , d)  $S_a(1.0)$  and e)  $S_a(10)$

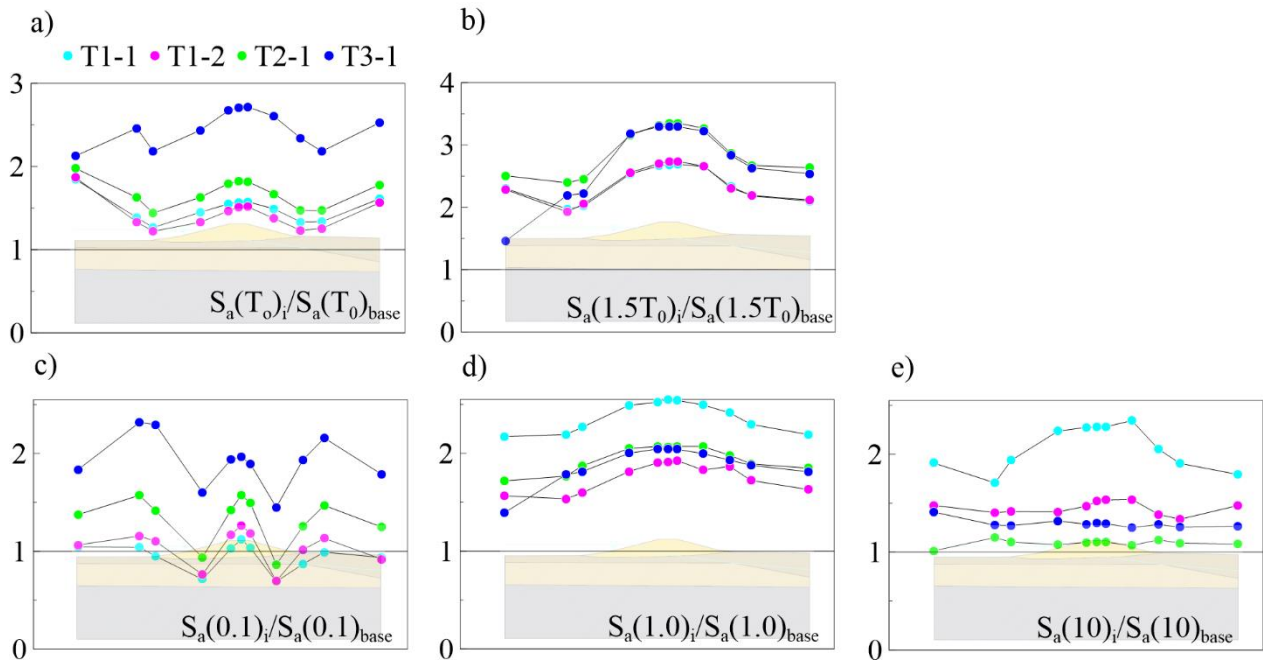


Figure 7.19 Amplification ratios of spectral-based *IM* at the surface of the model including a)  $S_a(T_0)$ , b)  $S_a(1.5T_0)$ , c)  $S_a(0.1)$ , d)  $S_a(1.0)$  and e)  $S_a(10)$

Spectral values are generally amplified for all scenarios, such as mentioned in the previous sections. The level of amplification of spectral values for periods near the degraded  $T_0$  is higher than for short periods. For scenarios with high content of high frequencies such as T1-1 and T1-2, high frequency waves are damped by the passage in the foundation soils as observed by the attenuation of  $S_a(0.1)$  at the free-field and are amplified again once in the dike (amplification of  $S_a(0.1)$  at the crest). Topographic effects are observed with  $S_a$  being more amplified at the vicinity of the crest, except at 10 s where the frequency content is poor and the potential for amplification is almost null.

#### 7.4.3.4 Modification of the frequency content – $T_m$

A variation of the motion frequency content may be observed by monitoring the mean period  $T_m$ . The  $T_m$  of each scenario is presented in figure 7.20a and its amplification ratio in figure 7.20b.

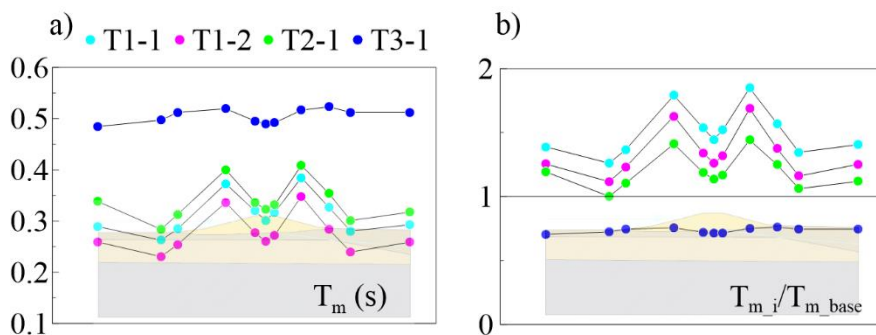


Figure 7.20 Frequency-based  $IM$  at the surface of the model with values of a)  $T_m$  and b) amplification ratios of  $T_m$

The ratio  $T_m/T_{m,base}$  is elongated for all scenarios except T3-1, meaning that motions are shifting to longer periods (lower frequency) while motions subjected to T3-1 are shifting to shorter periods (higher frequency). An elongation of the periods is a result of soil degradation. The  $T_m$  is similar at the crest and the free-field, further supporting the idea that most of the degradation has already took place in the foundation soils. The  $T_m$  is longer at mid-slopes, indicating that more content is shifted to longer periods. The figure 7.21 shows the *mean*  $S_g$  calculated at mid-slopes compared to the crest.

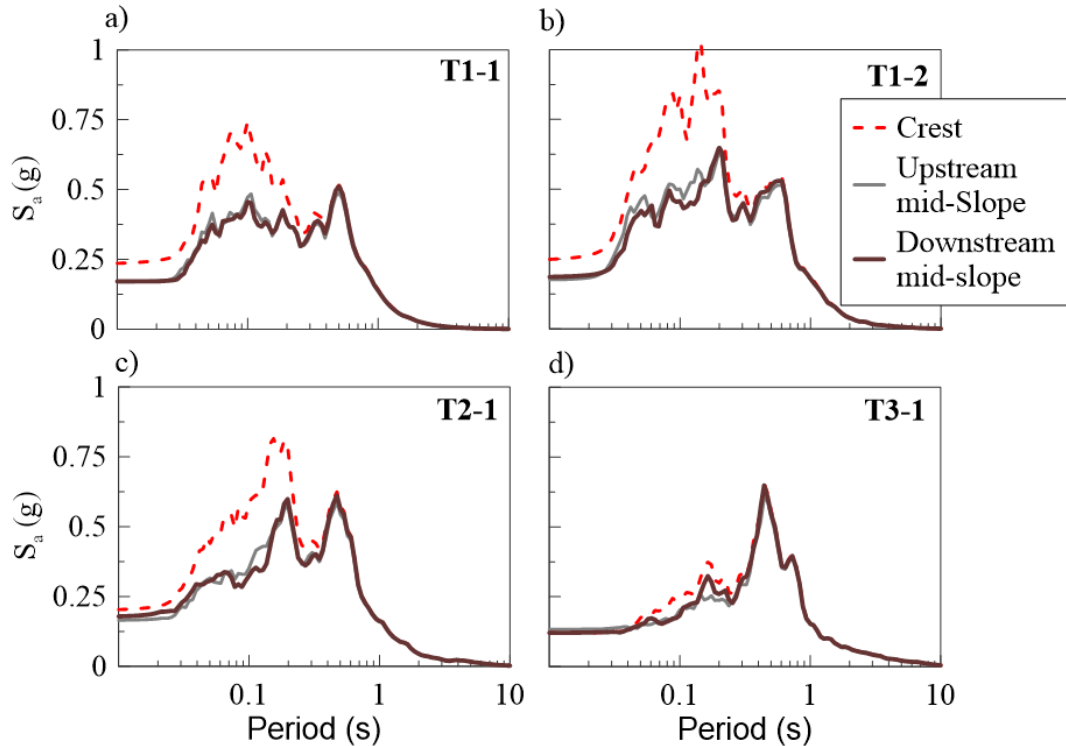


Figure 7.21 Average spectral response calculated at mid-slopes and compared to the crest of scenarios a) T1-1, b) T1-2, c) T2-1 and d) T3-1

Figure 7.21 shows that the *mean*  $S_g$  at mid-slopes is significantly lower than the crest from the *PGA* to the degraded  $T_0$ , contributing to the elongation of the  $T_m$  since motions contain more long-period energy. Furthermore, the *mean*  $S_g$  at mid-slopes are fairly similar between the upstream and downstream faces.

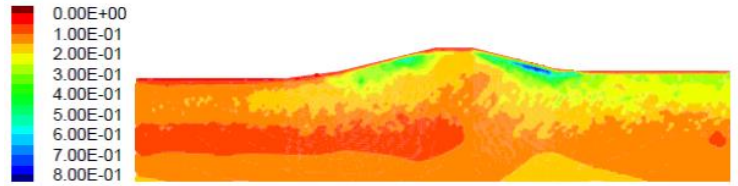
## 7.5 Cyclic stress ratio (*CSR*)

### 7.5.1 Distribution of *CSR*

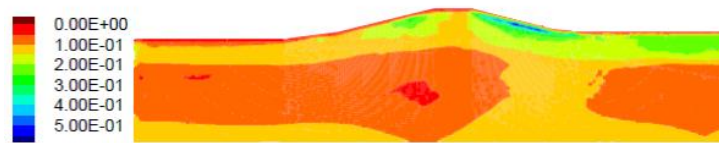
The cyclic stress ratio *CSR* is calculated at each point for each simulation as the ratio between the maximum shear stress  $\tau_{xy}$  during the simulation and the effective vertical stress  $\sigma'_v$ . The computation is performed in *FLAC* by using a user-defined function to compute the maximum  $\tau_{xy}$  and the built-in parameter  $\sigma'_v$  at each node of the model. In a few locations near the surface the effective stress,  $\sigma'_v$  approaches 0, resulting in very high *CSR* values. These high values of *CSR* are limited to a maximum value of 5, to allow a fair comparison with the rest of the model.

The *CSR* is calculated for each simulation of all scenarios and the distribution of *CSR* is shown in figures 7.22 to 7.25.

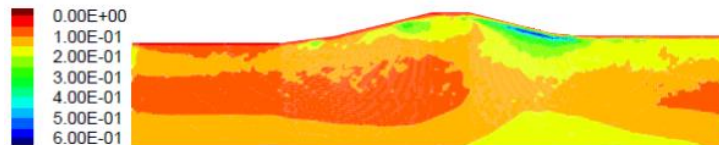
### T1-1 - Distribution of CSR



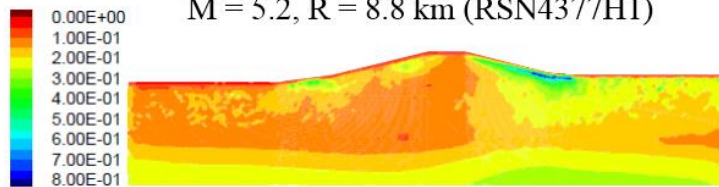
Coalinga - 02, M = 5.1, R = 0 km (RSN381H1)



Gilroy, M = 4.9, R = 2.2 km (RSN2019H2)



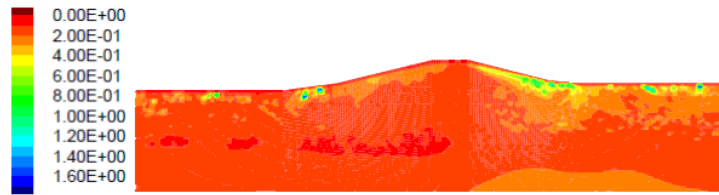
Umbria Marche (Aftershock 8), Italy  
M = 5.2, R = 8.8 km (RSN4377H1)



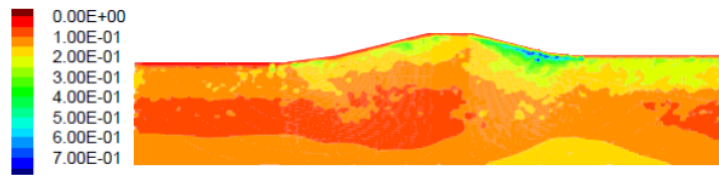
Mineral 2011-08-23, M = 5.7, R = 18.5 km (RSN8571H2)

Figure 7.22 Distribution of CSR of each simulation of scenario T1-1

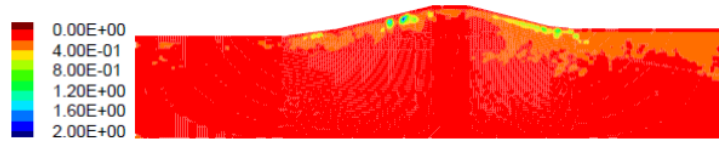
### T1-2 - Distribution of CSR



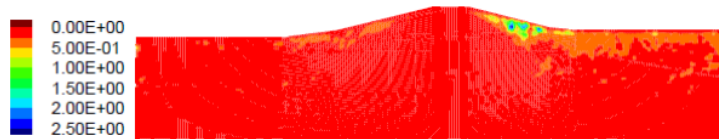
San Fernando, M = 6.6, R = 19.4 km (RSN72H1)



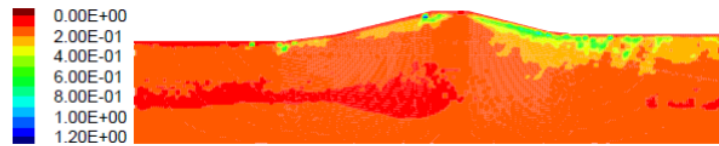
San Fernando, M = 6.6, R = 30.7 km (RSN87H2)



Whittier Narrow - 01, M = 6.0, R = 22.5 km (RSN598H2)



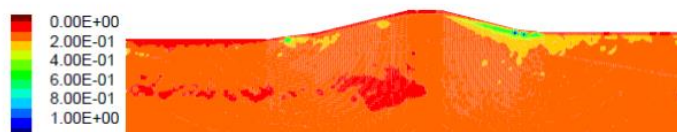
San Fernando, M = 6.6, R = 19.4 km (RSN72H2)



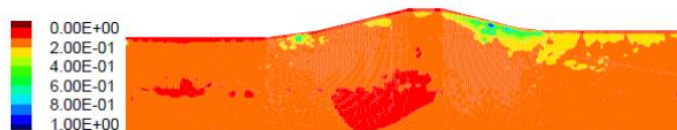
Big Bear - 01, M = 6.5, R = 37.0 km (RSN935H1)

Figure 7.23 Distribution of CSR of each simulation of scenario T1-2

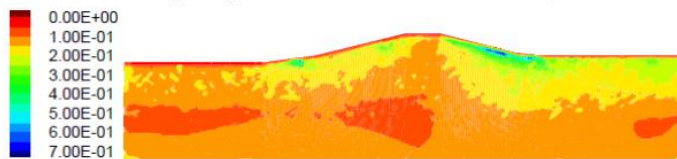
### T2-1 - Distribution of CSR



San Fernando,  $M = 6.6$ ,  $R = 19.4$  km (RSN72H2)



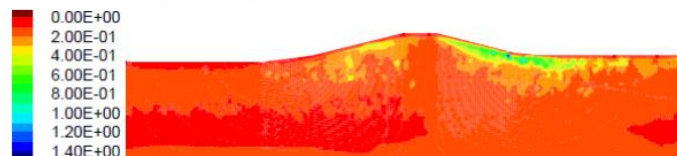
North Palm Springs,  $M = 6.1$ ,  $R = 38.2$  km (RSN511H1)



Whittier Narrows - 01,  $M = 6.0$ ,  $R = 22.5$  km (RSN598H2)



Northridge - 01,  $M = 6.7$ ,  $R = 19.1$  km (RSN954H1)



San Simeon, California,  $M = 6.5$ ,  $R = 31.3$  km (RSN4016H1)

Figure 7.24 Distribution of CSR of each simulation of scenario T2-1

### T3-1 - Distribution of CSR

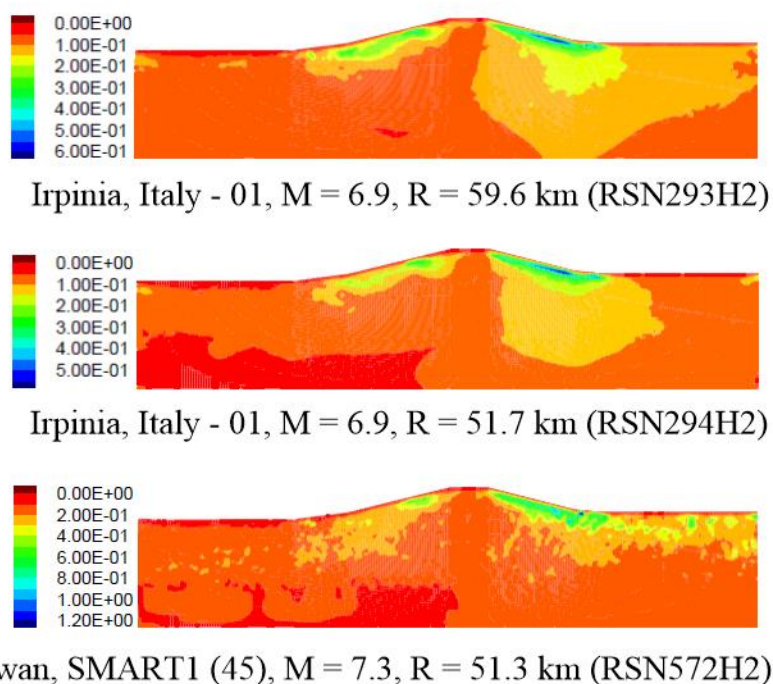


Figure 7.25 Distribution of CSR of each simulation of scenario T3-1

The figures 7.22 to 7.25 show that the distribution of *CSR* is relatively uniform between scenarios; with higher *CSR* along the slopes, close to both toes and on the downstream side of the landside. Therefore, it is important to verify that materials composing dikes are well compacted, especially at the downstream slope so that the materials behave as dilating materials. Conversely, the *CSR* is lower in the center of the dike and also in the foundation soils under the central part of the dike to the upstream landside. Furthermore, the *CSR* in the free field is generally higher near the surface (low confining pressure) and diminishes gradually with depth.

In general, the *CSR* is highest along the slopes of the dike and most critical near the bottom of the downstream slope to the toe. Moreover, *CSR* values are relatively high under the downstream toe of the dike, in the foundation soils. If dikes are built on loose materials of low consistency, these materials constituting the downstream base could be susceptible to liquefaction. In our case, the materials composing the toe of the slope consist of a natural deposit of silt of medium density to very loose at depth, partially saturated, which rendered them susceptible to liquefaction. Outside the locations where there are concentrations of high *CSR*, the values of *CSR* are relatively low, between 0.15 to 0.2 for all scenarios.

It is worth mentioning that the results of Athanasopoulos-Zekkos (2008) have also shown that concentrations of *CSR* are located beneath the toes. Besides, the author found that the highest *CSR* is located at the upstream toe, contrary to our study, which might be due to a different geometry as the dikes in Athanasopoulos-Zekkos (2008) have a landside much higher than the waterside. The table 7.1 presents the average values of maximum *CSR* and of the *CSR* below the downstream toe.

Table 7.1 Average values of maximum *CSR* and of *CSR* below the downstream toe

| Scenario | Average maximum <i>CSR</i> | Average <i>CSR</i> below downstream toe |
|----------|----------------------------|---|
| T1-1     | 0.68                       | 0.45                                    |
| T1-2     | 1.70                       | 0.65                                    |
| T2-1     | 1.32                       | 0.52                                    |
| T3-1     | 0.77                       | 0.56                                    |

As mentioned, the maximum *CSR* is generally calculated inside the dike at the downstream slope. The peak values are highest for T1-2 which contains the most powerful input motions, followed by T2-1 and scenarios T3-1 and T1-1. At the downstream toe, the scenarios in descending order with the highest *CSR* are about the same order than the maximum *CSR*: T1-2, T3-1, T2-1 and T1-1.

Besides, the equivalent number of cycles at a stress level of  $0.65\tau_{max}$  is calculated at the downstream toe and the downstream mid-slope which is near the location where the maximum *CSR* was monitored (figure 7.26).

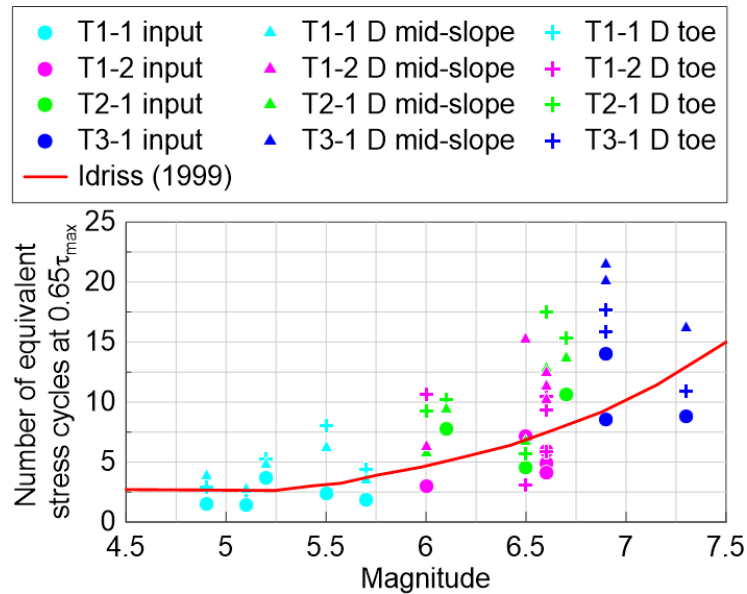


Figure 7.26 Number of equivalent stress cycles at  $0.65\tau_{max}$  at critical locations for liquefaction triggering

The number of equivalent cycles at  $0.65\tau_{max}$  generally increases at both locations compared to the input motions for all scenarios, meaning that there are more cycles resulting in a greater potential for liquefaction, particularly at the downstream toe. The number of equivalent cycles at the downstream toe is superior to the downstream mid-slope except for T3-1 due to less topographic effects resulting from lower frequency content (refer to section 7.6).

## 7.5.2 Evaluation of the potential of liquefaction

The factor of safety against liquefaction potential may be calculated by comparing the *CRR* and the *CSR*. The *CRR* is calculated based on *SPT* values (blow-counts *N*-values) with the method proposed by Boulanger and Idriss (2014) and based on the  $V_s$  with the method proposed by Kayen et al. (2013) (refer to chapter 2: Literature review). A profile of *CRR* and *CSR* is calculated at the downstream toe where concentrations of *CSR* were observed and is presented in figure 7.27. The figure 7.28 then presents the factors of safety against triggering of liquefaction.

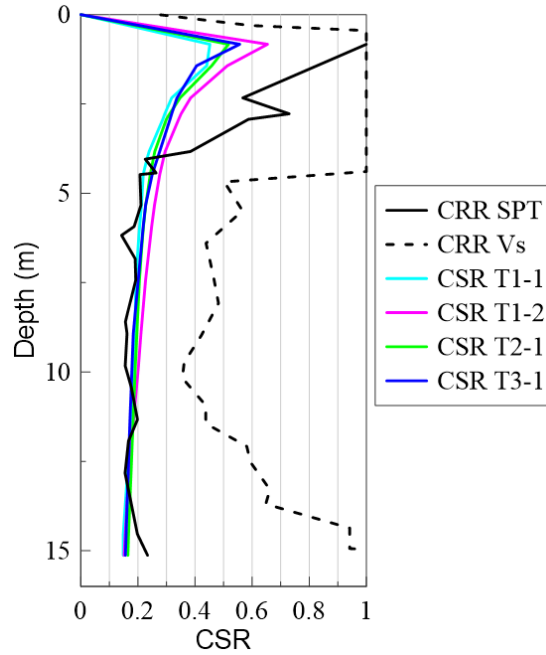


Figure 7.27 Profile of *CSR* at the downstream toe obtained with *FLAC* and *CRR* calculated using the method based on *SPT* and  $V_s$  results

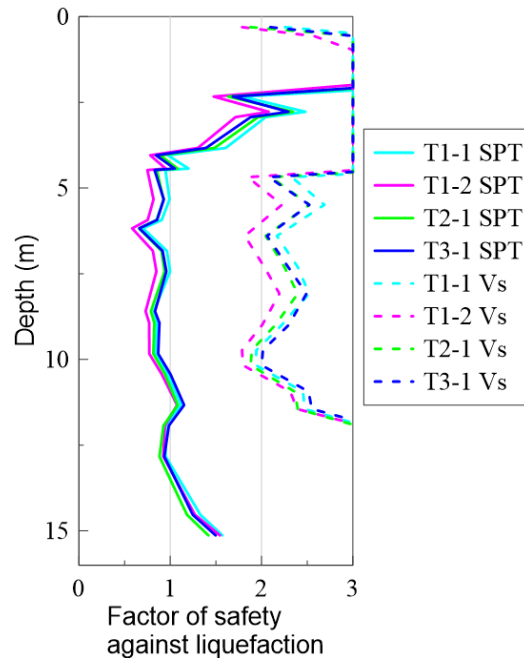


Figure 7.28 Factors of safety against liquefaction by comparing the *CRR* using the method based on *SPT* and  $V_s$  results and the *CSR* obtained with *FLAC*

A concentration of *CSR* is observed at the downstream toe, near the surface at very low confining pressure at around 0.8 m under the surface and the *CSR* suddenly drops then reduces gradually with

depth. Values of *CSR* are relatively similar between scenarios as the difference of *CSR* reduces with depth; with a difference of around 0.2 at the peak (at 0.8 m) and less than 0.02 at the interface with the bedrock.

The *FS* is always less than 1 using the method based on *SPT* results, meanwhile, the *SF* are always more than 1 with the method based on  $V_s$  due to high *CRR* (refer to chapter 3). Despite both methods showing contradictive results, the factors of safety against liquefaction (figure 7.28) are similar between scenarios, meaning that the same conclusions may be drawn regardless of the scenario considered.

### 7.5.3 Comparison of liquefaction triggering using the simplified method

In practice, one of the simplest, fastest and most widespread ways of evaluating the liquefaction potential is to calculate the *CSR* using the method of Boulanger and Idriss (2014) based on the input *PGA* and reduction factors considering a 1D wave propagation problem. Hence, it might be interesting to compare the *CSR* between the simplified method and the *CSR* computed with *FLAC*. To compare the *CSR* on the same basis, the 0.65 reduction factor is excluded in the calculation of *CSR*.

To do this, *CSR* profiles were calculated with the simplified method for both critical locations identified in the *CSR* distribution graphs (figures 7.14 to 7.17) and at the crest:

- 1- At the downstream toe
- 2- Near the bottom of the downstream slope
- 3- Crest

A soil class D ( $PGA = 0.360$  g) is considered. The *CSR* profiles are presented in figure 7.29.

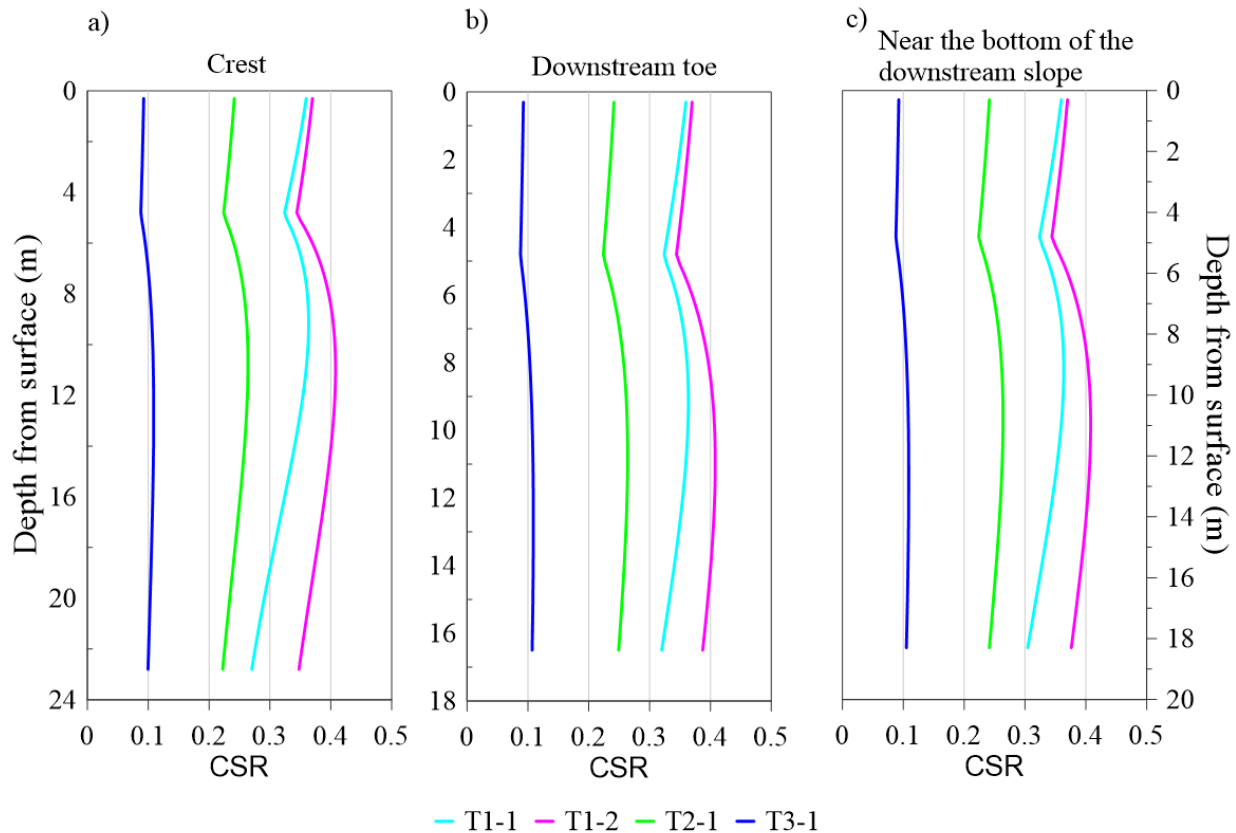


Figure 7.29 CSR profiles calculated with the simplified method at the a) the crest, b) downstream toe and the c) near the bottom of the downstream slope

The simplified method gives CSR results of less than 0.4 for all scenarios at the three (3) locations considered. Values of CSR are significantly different between scenarios, meanwhile the CSR distributions with *FLAC* (see fig. 7.14 to 7.17) and the profile of CSR below the landside toe (figure 7.19) showed that the variation of CSR between scenarios should be minimal outside the locations where there are concentrations of CSR.

Given that the *PGA* of T2-1 and T3-1 is smaller because they contain motions with more long-period energy, both scenarios result in the lowest CSR with the simplified method. But on the contrary, by considering the topographic effects, the nonlinearity of the materials, the geotechnical characteristics of the materials and the complete time series of the accelerations with *FLAC*, all scenarios return rather similar values of CSR, except for the peak values near the surface.

The factors of safety against liquefaction triggering are calculated at the downstream toe using the *SPT* results and the  $V_s$  results (figure 7.30).

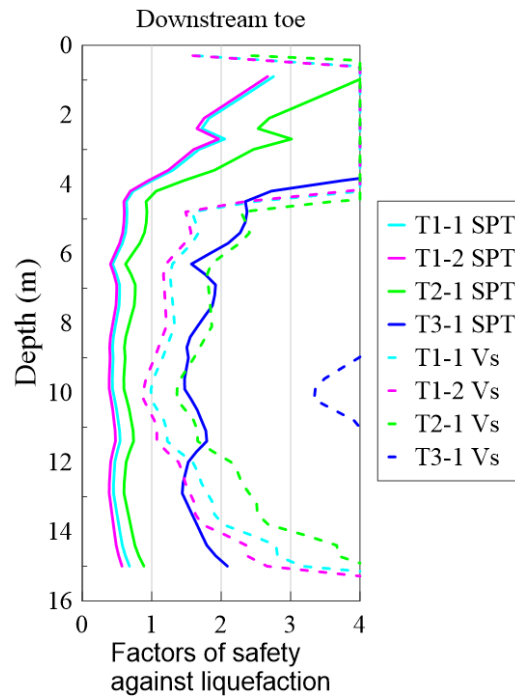


Figure 7.30 Factors of safety against liquefaction triggering at the downstream toe using *CSR* calculated with the simplified method and considering the *CRR* by SPT results and the *CRR* by  $V_s$

The figure 7.30 shows that all scenarios exhibit liquefaction of the foundation soils at the downstream toe with the exception of T3-1. The *SF* calculated with the  $V_s$  results are almost always  $> 1$  due to higher *CRR*. Contrary to the *SF* obtained from *FLAC*, it is worth mentioning that the *SF* calculated with the simplified method vary significantly between scenarios with short periods scenarios exhibiting a greater potential for liquefaction (higher *PGA*).

In conclusion, the simplified method is directly linked to the input *PGA* which does not reflect the frequency content nor the duration of the motions and the long-period energy of a motion. It returns values of *CSR* highly influenced by the input motion unlike the results from *FLAC* showing relatively stable values of *CSR* between scenarios. Hence, the simplified method does not return satisfactory results for the evaluation of the liquefaction potential of dikes and the soils located around the dike.

## 7.6 Topographic effects

The presence of a topographic irregularity induces topographic effects. Based on literature, 2D effects are generally concentrated on the top of the irregularity resulting in the amplification of the

waves at the crest, an amplification or attenuation at the toes depending on the motions frequency content and a pattern of amplification and attenuation along the slopes and at the vicinity of the irregularity.

The results obtained of the model have shown that the maximum wave acceleration is monitored on the crest, especially in the middle of the crest, indicating that wave focusing resulting in wave superposition may have amplified the acceleration in the crest centerline. Figure 7.31 presents the ratios of the  $IM$  at the crest and the free-field for  $PGA$ ,  $PGV$ ,  $I_a$ ,  $CAV$ ,  $CAV_5$ ,  $CAV_{std}$ ,  $ASI$ ,  $SI$ ,  $SIR_{75}$  and  $SIR_{95}$ .

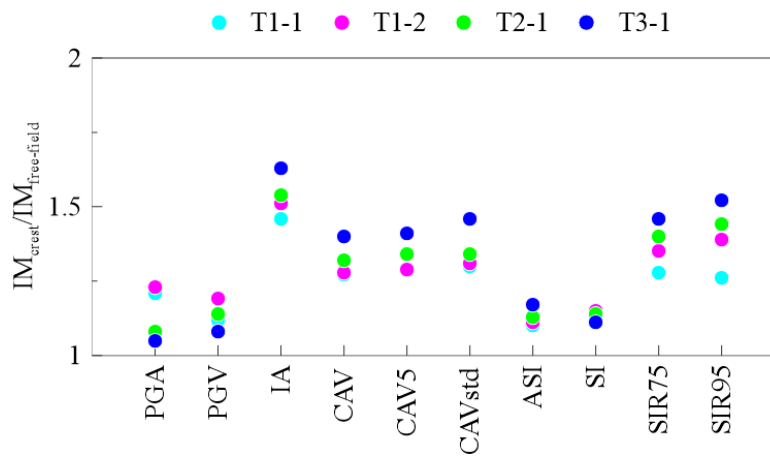


Figure 7.31 Amplification ratios of  $IM$  calculated between the crest and the free-field

Most amplitudes and integration-based  $IM$  showed higher values at the crest than other locations of the surface. Values are 5 to 63 % higher than the free-field with integration-based  $IM$  being the most amplified. Furthermore, the amplification at the crest compared to the free-field is generally higher with T3-1 among all scenarios.

Besides, the amplification of the waves is less apparent at the toes for most  $IM$  (figures 7.14 to 7.20). The figure 7.32 show the  $mean S_g$  calculated at the crest, the mid-slopes, the toes and the free-field. Note that the  $mean S_g$  presented in this figure at the mid-slopes and the toes are the average between the upstream and downstream faces.

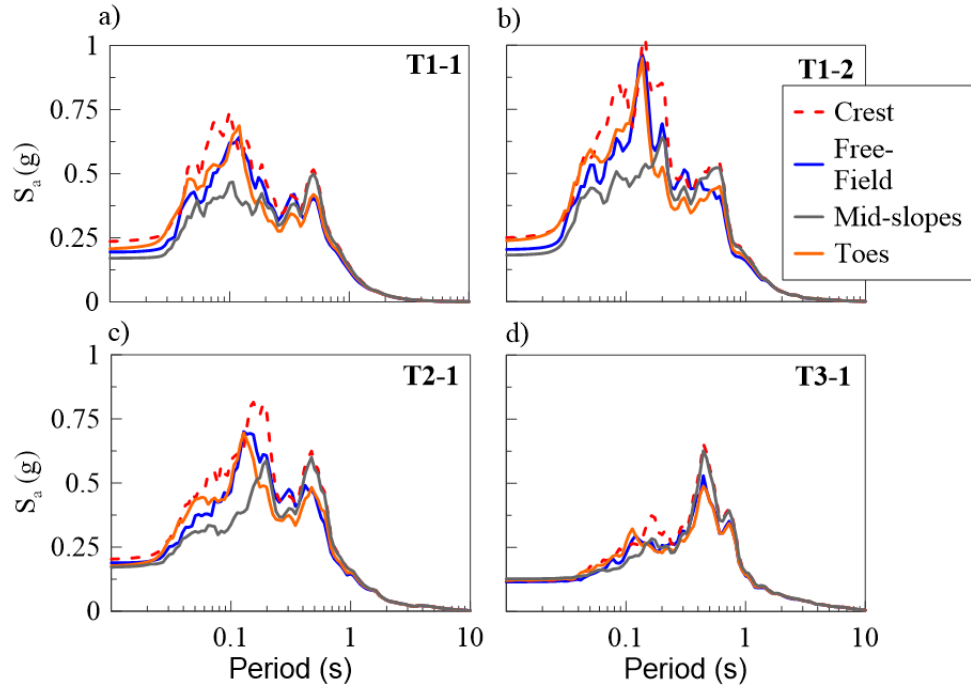


Figure 7.32 Average spectral response at the crest, the mid-slopes, the toes and the free-field for  
a) T1-1, b) T1-2, c) T2-1 and d) T3-1

The variation of *mean*  $S_g$  at the surface is relatively small under the influence of T3-1 (average center frequency of 1.6 Hz) which is in agreement with the results of Ashford et al. (1997) and Nguyen and Gatmiri (2007). The authors found that low frequency motions tend to induce little to no topographic effects. However, even though topographic effects are not observed in the spectrum, topographic effects are observed in all *IM* considered with *IM* being higher on the dike than at the vicinity of the dike.

## 7.7 Impact of seismic hazard in the short-period range

This section focuses on the impact of seismic hazard in the short-period range. In the literature, it is usually accepted that the short-period spectrum in *ENA* is dominated by earthquakes of low  $M$  and short  $R$  (Atkinson, 2009). However, as shown in chapter 4, the short-period spectrum between 0.01 and 0.2 s can be broken down into 2 scenarios:

- 1-  $M5-6$  and  $R0-20$  km (T1-1), and
- 2-  $M6-7$  and  $R20-40$  km (T1-2)

The scenario T1-1 represents low-to-moderate-intensity earthquakes occurring at short distances while T1-2 represents stronger earthquakes at moderate distances. This section will present the differences between both scenarios in terms of selected input motions and seismic response of the embankment.

### 7.7.1 Input ground motions

Figure 7.33 presents the *IM* of the selected and scaled input ground motions for both scenarios T1-1 and T1-2. Refer to chapter 4 for the input motions *IM* of all scenarios.

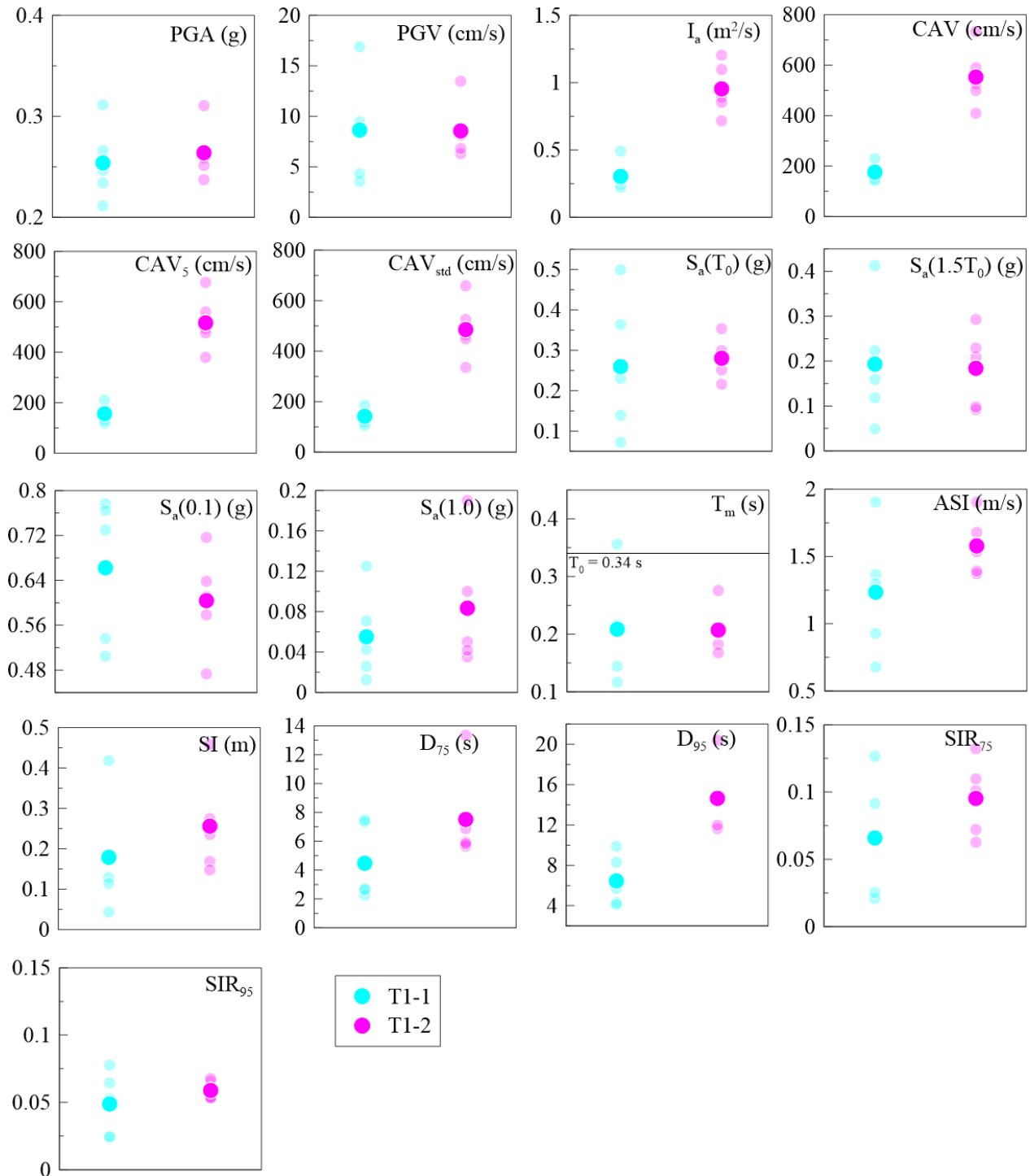


Figure 7.33 Input motions intensity measures  $IM$  of T1-1 and T1-2

All intensity-based  $IM$  indicate that T1-2 contains stronger and longer motions. Despite both scenarios have the same  $T_{RS}$  (between 0.01 and 0.2 s), the integration-based  $IM$ , i.e. the  $I_a$ ,  $CAV$ ,  $CAV_5$  and  $CAV_{std}$  of T1-2 are up to 3 times higher than T1-1. The duration-based  $IM$ , i.e.  $D_{75}$  and

$D_{95}$  of T1-2 are up to 2.5 times higher than T1-1. Amplitude, duration and frequency content being the most contributing parameters to the damage potential of an earthquake, a stronger response of the model subjected under T1-2 is hence expected.

Besides, despite  $IM$  based on amplitude, duration and frequency content clearly showed that T1-2 is more intense than T1-1, this tendency is less reflected in the response spectrum with the  $PGA$  being similar between both scenarios. Also, figure 7.34 presents a comparison of the shape of the  $S_g$  of the selected and scaled input motions and the average input  $S_g$  of scenarios T1-1 and T1-2.

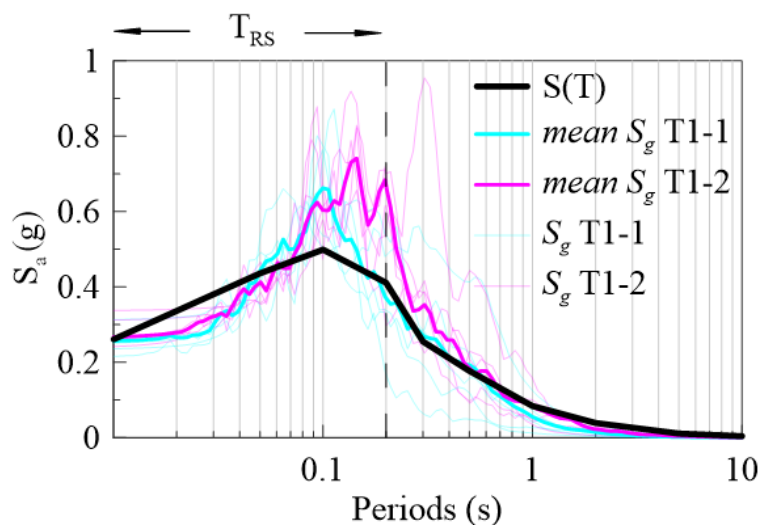


Figure 7.34 Shape of input motions  $mean S_g$  of T1-1 and T1-2 and  $S_T(T)$

The shape of T1-2 input spectrum is higher than T1-1's of about 1-83 % at medium to long periods which is fairly moderate compared to the excess of the  $IM$  but their shape is mostly the same at short periods ( $< 0.1$  s).

As mentioned in chapter 4, the input spectrum of both scenarios are significantly higher than the  $S_T(T)$ , especially at the peak (0.1 s). For scenario T1-2, in addition to the incompatibility of the spectrum's shape, the frequency content is shifted to longer periods (low frequency). Indeed, the peak is slightly shifted to longer periods (0.14 s) and the shape of the spectrum is higher than  $S_T(T)$  after 0.14 s which may lead to an exaggerated response of the dike.

### 7.7.2 Impact on the seismic response

The figure 7.35 presents the amplitude of the acceleration in terms of  $PGA$ ,  $PGV$ ,  $I_a$ ,  $S_a(T_0)$ ,  $S_a(1.5T_0)$ ,  $S_a(0.1)$ ,  $S_a(1.0)$ ,  $T_m$ ,  $ASI$ ,  $SI$ ,  $SIR_{75}$  and  $SIR_{95}$ . Based on the figure, integration-based  $IM$

of T1-2 such as  $I_a$ ,  $CAV$ ,  $CAV_5$  and  $CAV_{std}$  are 1.8 to 2.6 times higher than T1-1's. Since those  $IM$  integrate the 3 most important components of seismic damage potential (amplitude, frequency content and duration), it might be concluded that the T1-2 produce waves acceleration and damage potential more significant than T1-1.

Also, the level of dispersion of the results is different for each  $IM$  with results  $I_a$ ,  $CAV$ ,  $CAV_5$  and  $CAV_{std}$  oscillating around the average values. To quantify the dispersion between the results of each  $IM$ , the standard deviation is calculated and is presented on the table 7.2.

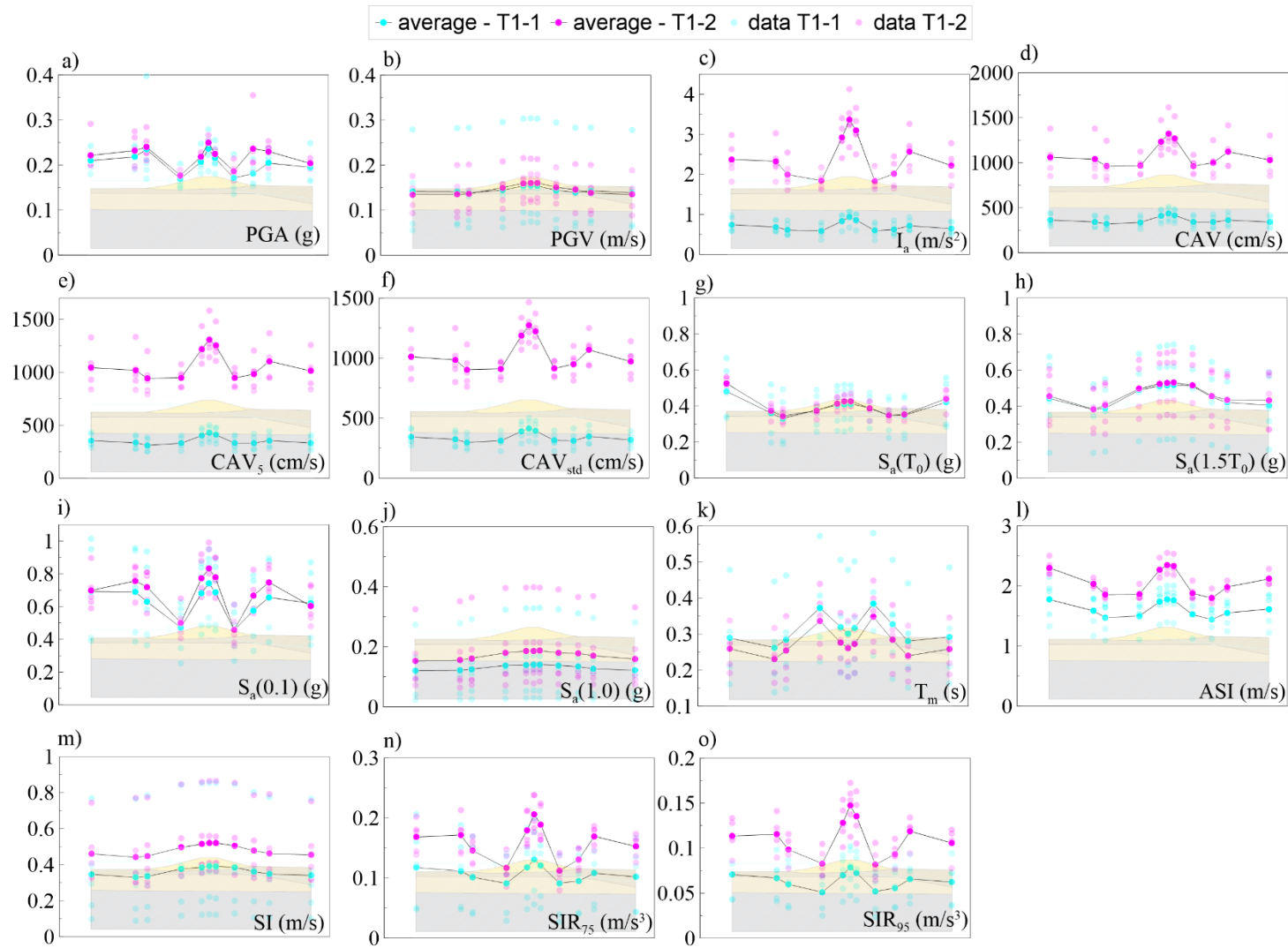


Figure 7.35 Comparison of amplitude, frequency and duration-based *IM* at the surface of the model between T1-1 and T1-2, including a)  $PGA$ , b)  $PGV$ , c)  $I_a$ , d)  $CAV$ , e)  $CAV_5$ , f)  $CAV_{std}$ , g)  $S_a(T_0)$ , h)  $S_a(1.5T_0)$ , i)  $S_a(0.1)$ , j)  $S_a(1.0)$ , k)  $T_m$ , l)  $ASI$ , m)  $SI$ , n)  $SIR_{75}$  and o)

$SIR_{95}$

Table 7.2 Standard deviation of resulting intensity measures  $IM$  at the surface of the model for scenarios T1-1 and T1-2

| Type of IM                       | IM  | Standard deviation |         |         |
|----------------------------------|---|--------------------|---------|---------|
|                                  |   | average            | minimum | maximum |
| Integration-based in time domain | $I_a, CAV, CAV_5, CAV_{std}$                | 17%                | 7%      | 31%     |
| Peak amplitude-based             | $PGA$                                       | 13%                | 3%      | 40%     |
|                                  | $PGV$                                       | 44%                | 20%     | 64%     |
| Spectral-based                   | $S_a(T_0), S_a(1.5T_0), S_a(0.1), S_a(1.0)$ | 39%                | 6%      | 86%     |
| Frequency-based                  | $T_m$                                       | 32%                | 22%     | 45%     |
| Other integration-based          | $ASI, SI, SIR_{75}, SIR_{95}$               | 33%                | 3%      | 80%     |

The table 7.2 shows that the dispersion between the results of T1-1 and T1-2 for  $I_a, CAV, CAV_5$  and  $CAV_{std}$  is fairly low with an average of 17 %. The  $PGA$  also shows a narrow range of values with an average standard deviation of 13 %. In comparison, the rest of the  $IM$  showed a strong dispersion of the results with an average standard deviation of around 30 to 45 %.

In summary, considering that the  $IM I_a, CAV, CAV_5$  and  $CAV_{std}$  present a smaller dispersion of the results and therefore a better precision, it might be concluded that these  $IM$  showed that T1-2 generate a much stronger response of the model at the surface than T1-1, despite them both representing the same scenario-specific period range  $T_{RS}$ . A comparison between the response spectrum calculated at the crest is presented in the figure 7.32, and shows that the spectrum at the crest is similar below 0.11 s despite the difference observed with the  $IM$  and is higher for T1-2 at medium to long periods as for the input spectrum.

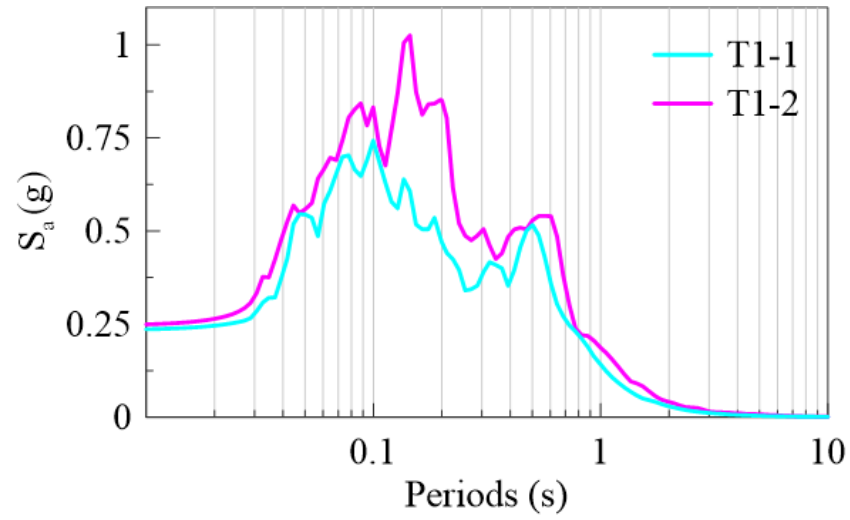


Figure 7.36 Response spectrum calculated at the crest with T1-1 and T1-2

## 7.8 Parametric study: Ground motions intensity measures *IM* to evaluate damage measures *DM*

This section's main objective is to offer insight on input motion intensity measures *IM* capable of predicting the seismic response of an embankment. The limited number of considered simulations (18) may not adequately capture the best *IM* to predict the seismic response of the embankment, but this study may help to determine the most promising *IM*.

A parametric study may offer insight on an optimum *IM* for the selection and scaling of input ground motions which may substantially reduce variability in the predicted response of an embankment and eventually reduce the number of records to achieve the same accuracy in the seismic response prediction. As the input ground motion is one of the most important parameter that may affect the outcome of dynamic analyses, hence, selection and scaling of ground motions is a crucial step in dynamic analyses.

In the past few years, several authors have studied *IM* for predicting the seismic response of earth dams (e.g. Bray and Travararou (2007), Beaty and Perlea (2012), Armstrong (2018)). However, their studies are based on tall dams of more than 40 m high (for details, refer to chapter 2: Literature review). No studies were performed to determine effective *IM* on small embankments which motivates this study.

As defined by Shome and Cornell (1999) and Luco and Cornell (2001), an adequate *IM* should be “efficient”, “sufficient” and “predictable”, which means that an efficient *IM* should be closely related to the damage measures *DM*, a sufficient *IM* should not be conditionally dependent of the *M* and *R* and a predictable *IM* should be accurately determined through ground motion models (*GMM*).

Note that the sufficiency and predictability is not evaluated in this project. Using scaling factors to match the input ground motions to the  $S_T(T)$  impacted the compatibility of motions to their corresponding *M* and *R*. Furthermore, while the *GMM* in *WNA* are developed based on empirical data, *GMM* in *ENA* are heavily based on simulations due to the lack of historical ground motions recorded in the range of *M* and *R* of interest (Atkinson and Adams, 2013; Pezeshk et al., 2011). As a result, there is an uncertainty associated to the *GMPE* in *ENA*. In addition, as soil conditions and

topography may significantly impact the soil response, the *GMM* are developed for plane surface, thus are not adapted for embankments.

### 7.8.1 Damage measures *DM* and candidate intensity measures *IM*

Several candidate input motion intensity measures *IM* are evaluated for their efficiency in the prediction of damage measures *DM* at the surface of the model. Table 7.3 presents a list of *DM* studied at the crest, the downstream free-field and the downstream and upstream toes and mid-slopes. The maximum value of *CSR* and the *CSR* at the downstream toe are also evaluated as *DM* in this study. The values of *CSR* are normalized to a  $M = 7.5$  to allow comparison on the same basis. The candidate input motions *IM* are listed in table 7.4.

Table 7.3 Damage measures *DM* and locations considered in the parametric study

| <b><i>DM</i></b>               | <b>Location of <i>DM</i></b>   |
|--------------------------------|--|
| <i>PGA</i>                     | Crest<br>Downstream free-field<br>Downstream and upstream mid-slopes<br>Downstream and upstream toes |
| $S_a(T_0)$                     |  |
| $S_a(1.5T_0)$                  |  |
| $S_a(0.1)$                     |  |
| $S_a(1)$                       |  |
| $S_a(10)$                      |  |
| Maximum $CSR_{M=7.5}$          | Along the downstream slope, near the toe<br>(See section 7.5)  |
| Downstream toe's $CSR_{M=7.5}$ | Downstream toe   |

Table 7.4 Candidate input motions intensity measures  $IM$  in the parametric study

| ID | Type                                    | IMs           |
|----|---|---------------|
| 1  | Amplitude-based                         | $PGA$         |
| 2  |   | $PGV$         |
| 3  |   | $PGD$         |
| 4  | Amplitude, frequency and duration-based | $I_a$         |
| 5  |   | $CAV$         |
| 6  |   | $CAV_5$       |
| 7  |   | $CAV_{STD}$   |
| 8  | Amplitude-based                         | $S_a(T_0)$    |
| 9  |   | $S_a(1.5T_0)$ |
| 10 |   | $S_a(0.1)$    |
| 11 |   | $S_a(1.0)$    |
| 12 | Frequency-based                         | $T_m$         |
| 13 | Amplitude, frequency and duration-based | $ASI$         |
| 14 |   | $SI$          |
| 15 | Duration-based                          | $D_{75}$      |
| 16 |   | $D_{95}$      |
| 17 | Amplitude, frequency and duration-based | $SIR_{75}$    |
| 18 |   | $SIR_{95}$    |

### 7.8.2 Efficiency of candidate input motions $IM$ in the prediction of damage measures $DM$

The efficiency of candidate input motions  $IM$  in the prediction of  $DM$  at the crest, mid-slopes, toes and the free-field is presented in figure 7.37. An efficient  $IM$  should show a good correlation with the  $DM$  (refer to the chapter 2-section 2.3.3.). A smaller value of efficiency means less uncertainty in the prediction of the  $DM$ .

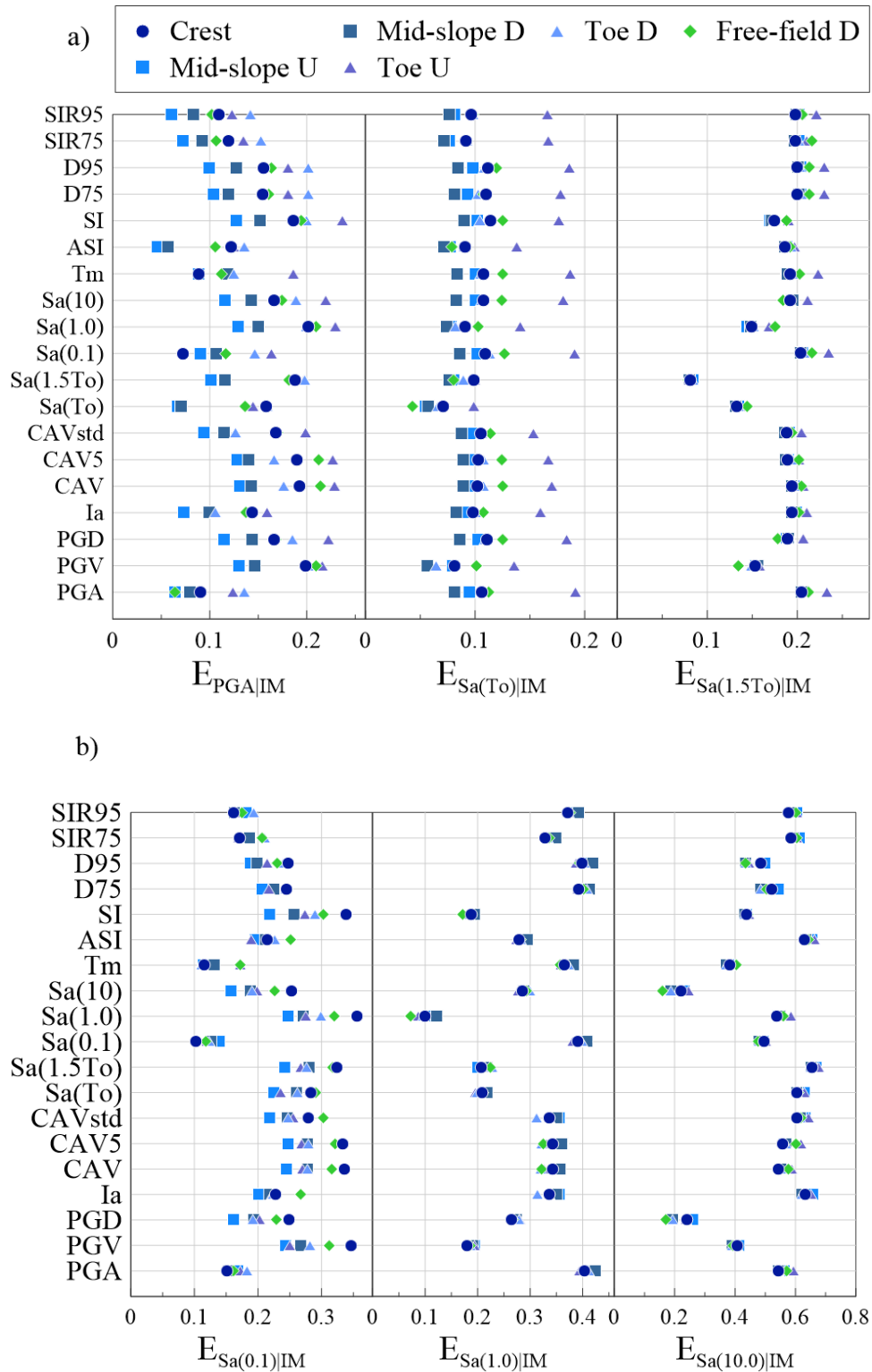


Figure 7.37 Efficiency of candidate input motion  $IM$  for the prediction of a)  $PGA$ ,  $S_a(T_0)$  and  $S_a(1.5T_0)$  and b)  $S_a(0.1)$ ,  $S_a(1.0)$  and  $S_a(10.0)$  at the crest, both mid-slopes and the toes and the free-field

In general, the variation of the efficiency of candidates  $IM$  is small between the different locations on the surface, i.e. a candidate  $IM$  is just as efficient at the peak as at the free-field for example. To predict the  $PGA$  at different locations on the surface of the model, the  $IM$  corresponding to short period spectral values, such as the input  $PGA$  and  $S_a(0.1)$  are the most efficient  $IM$  in the prediction of the resulting  $PGA$ . Indeed, these  $IM$  show the lowest standard deviation of the residuals. Furthermore, the input  $ASI$ , which correspond to the integral of the response spectrum between 0.1 and 0.5 s, indicate a satisfying efficiency in the prediction of the  $PGA$ .

For the prediction of spectral values  $S_a$  at different periods and locations on the surface, they are the most influenced by the input response spectrum, particularly the  $S_a$  at the same period. For example, the resulting  $S_a(T_0)$  is best correlated with the  $S_a(T_0)$  of the input motion.

Besides, knowing which input parameters are the best correlated with the  $CSR$  might help to improve the selection of input motions for the prediction of liquefaction. The figure 7.38 show the efficiency of candidate input  $IM$  in the prediction of the maximum value of  $CSR$  in the model and the  $CSR$  at the downstream toe.

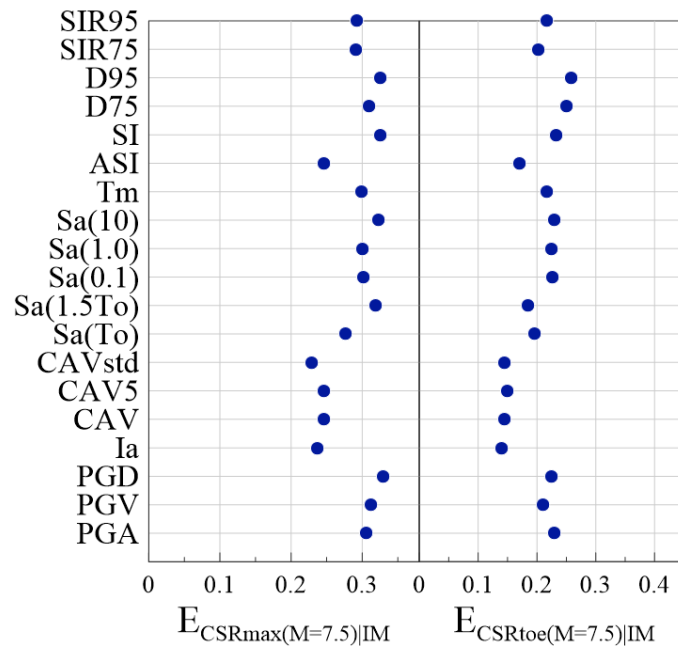


Figure 7.38 Efficiency of candidate  $IM$  for the prediction of the maximum  $CSR$  and the  $CSR$  at the downstream toe

For the prediction of both maximum  $CSR$  and  $CSR$  at the downstream toe, the integration-based input  $IM$  show the lowest standard deviation of the residuals (most efficient), such as the  $I_a$ , the

cumulative absolute velocity parameters ( $CAV$ ,  $CAV_5$  and  $CAV_{std}$ ) and the  $ASI$ . On the contrary, input spectral values are the least efficient in the prediction of both  $CSR$ .

Based on this observation, the selection of input motions is entirely based on the shape of the response spectrum, as commonly done in practice, is questionable, because this study showed that the input spectral values are the least correlated with the liquefaction triggering parameter  $CSR$ .

Also, the input  $PGA$  shows a high standard deviation of the residuals and hence is not an efficient  $IM$  in the prediction of both  $CSR$ , which also question the fact that the  $PGA$  is the only parameter related to the seismic demand used in the simplified liquefaction triggering analysis.

## CHAPTER 8 CONCLUSION

### 8.1 Summary and conclusion

In practice, the seismic design of a dike can be based on several different analyses, from simple ones such as the pseudo-static analysis to more complex ones such as nonlinear deformation analyses. The latter require the selection of ground motion recordings based on seismic scenarios representative of the seismicity of the region, i.e. the seismic hazard, for the period range of interest, based on a deaggregation analysis of the seismic hazard. Thus, the selection of seismic scenarios is a very important step because it directly influences the selection of input ground motions and hence the results of simulations.

The main objectives of this study are the evaluation of the impact of seismic hazard on the seismic response of an earth dike in *ENA*, and finding candidate *IM* capable of predicting *DM* to reduce the uncertainty associated to the selection of input motions. Hence, the response of a dike in a fictitious site in Montreal is evaluated and compared for different seismic scenarios.

The specific objectives are:

- Define seismic scenarios based on the deaggregation analysis of the seismic hazard in Montreal
- Assess the difference in terms of input motions *IM* between scenarios
- Study the response of the model with nonlinear simulations:
  - Compare the *DM* between scenarios
  - Compare the level of amplification due to soil conditions and topographic effects in terms of *IM* characterizing the amplitude, duration and/or frequency content of response motions;
- Assess the efficiency of candidate *IM* in the prediction of *DM* by performing a parametric study.

The conclusions of this study are presented herein.

### 8.1.1 Seismic hazard and selection and scaling of input motions

**Seismic scenarios:** In *ENA*, based on the literature, the seismic hazard is dominated by a combination of events of low  $M$  and short  $R$  in the short-period range and events of high  $M$  and long  $R$  in the long-period range. However, the analysis of the deaggregation in Montreal showed that the seismic hazard at short periods are characterized by not one but two scenarios. A total of 4 scenarios are defined for the entire period range.

- Between periods 0.01 and 0.2 s, the hazard is dominated by 2 scenarios:
  - T1-1 with M5-6 and R0-20 km and;
  - T1-2 with M-6-7 and R20-40 km;
- One scenario characterizes the hazard between 0.2 and 1.0 s:
  - T2-1 with M6-7 and R20-40 km;
- One scenario characterizes the hazard between 1.0 and 10 s:
  - T3-1 with M7-7.5 and R40-60 km

**Selection of input motions:** Input motions are selected from the PEER database (NGAEast and NGAWest2), processed and scaled using the *S<sub>Ia</sub>* method. Five ground motions are selected for T1-1, six for T1-2, five for T2-1 and three for T3-1.

**Compatibility issue:** Short period scenarios (T1-1 and T1-2) have an average input spectrum that exceeds the target spectrum, especially T1-2 which contain very strong ground motions of M6-7. The selected motions, which in majority come from the NGAWest2 database, have a richer lower frequency content, hence, the shape of the spectrum of the selected motions is usually lower in short periods and higher in medium to long periods which is the opposite than the spectrum of the site and could lead to a potential high response. T2-1 matches adequately the target spectrum and T3-1 has its average spectrum being significantly lower than the target at low to medium periods.

**Intensity measures (*IM*) of input motions:** Scenario T1-1 shows strong amplitude with *PGA* and  $S_a(T_0)$  of 0.25 g and 0.21 g respectively, and frequency content relatively close to  $T_0$  with 0.26 s compared to 0.34 s but a short duration of less than 5 s. The scenario T1-2 contains the most intense motions in terms of all *IM* considered. Its cumulative absolute velocities are 3 to 4 times higher than T1-1 and its  $D_{75}$  is 72 % higher than T1-1. The large difference between the *IM* of T1-2

compared to other scenarios may be due to the compatibility issue of motions with the  $S_T(T)$ . The scenario T2-1 contains motions with frequency content closest to the natural frequency of the model (2.9 Hz). Its average center frequency is 3.5 Hz. Also, the scenario T2-1 characterizes the hazard at the  $T_0$  which will further lead to higher amplification in the model. Although the scenario T3-1 contains the weakest motions in terms of amplitude and has its frequency content far from  $T_0$ , its  $D_{75}$  is the highest among all scenarios with 20.4 s.

### 8.1.2 Results of nonlinear simulations and parametric study

When analyzing the results of the nonlinear simulations, the surface acceleration is analyzed in terms of parameters characterizing the amplitude, frequency content and duration of surface movements.

**Scenario-specific study of the seismic behavior of the dike:** The scenario T2-1 resulted in fairly average response among scenarios while T1-1 returned the weakest response, T1-2 exaggeratedly high response and T3-1 response comparable among scenarios. Although T1-2 returns the highest surface acceleration, it also returns the lowest amplification factors for the  $IM$  considered. The surface acceleration is a result of the initial intensity of the input motions of T1-2 because it initially exceeded the  $S_T(T)$ . Meanwhile, although T3-1 has weak input motions amplitudes, its resulting  $IM$  are still comparable to other scenarios due to its very long duration ( $\pm 20$  s). However, T3-1 does not induce or induces very little topographic effects in the spectrum due to its frequency content. In the contrary, T1-1 returns the weakest response due to its motions being short ( $D_{75} = \pm 4.5$  s). Besides, the level of degradation is similar between T1-1, T1-2 and T2-1 as the degraded fundamental period at the crest has lengthened to  $\pm 0.53$  s ( $\pm 0.44$  s for T3-1).

**Topographic effects:** Topographic effects are observed in all scenarios in most  $IM$  (except the spectrum for T3-1), especially the integration-based  $IM$  while the  $PGA$  showed a reduction at the surface, meaning that the  $PGA$  is a poor indicator of the intensity of a motion. Besides, most degradation takes place in the foundation soils since the degraded fundamental period  $T_0$  is already apparent at the free-field and remained unchanged at the crest.

**Cyclic stress ratio (liquefaction):** The  $CSR$  is evaluated in the  $FLAC$  model and the distribution of  $CSR$  showed that there are concentrations of  $CSR$  along the sloping faces and below the toes, especially in the downstream side. Under the downstream toe, the  $CSR$  values are fairly similar

between scenarios meaning that the same conclusions may be drawn regarding triggering of liquefaction, regardless of the scenario. Then, the *CSR* obtained with *FLAC* are compared to the values obtained using the simplified method by Boulanger and Idriss (2008, 2014) and the latter computed values inferior to those obtained with *FLAC*. This is especially true for scenarios T2-1 and T3-1 which exhibit very low *CSR* with the simplified method due to low *PGA*.

**Parametric study:** A simplified parametric study is performed to correlate the input motions *IM* to the surface acceleration and resulting *CSR*. The efficiency of each candidate *IM* is calculated based on their prediction of surface acceleration and *CSR*. The resulting surface *PGA* is best correlated with the input *PGA*,  $S_a(0.1)$  and *ASI*; the resulting spectral values are best correlated with the input spectral values at the same period. Also, the *CSR* showed a better correlation with integration-based *IM* such as *CAV*,  $CAV_5$ ,  $CAV_{std}$ ,  $I_a$  and *ASI*. Besides, the input spectrum and *PGA* showed the least efficiency in the prediction of *CSR*, which could question the procedure of selecting input motions which is entirely based on the shape of input spectrum. Hence, engineers in practice should not rely solely on the shape of the response spectrum during selection of input motions, but should consider other parameters that showed adequate efficiency in the prediction of the sought damage measures such as *CAV*,  $CAV_5$ ,  $CAV_{std}$ ,  $I_a$  or *ASI* when assessing potential of liquefaction.

### 8.1.3 Scope of research

The results of this thesis have led to many interesting conclusions. However, these conclusions are submitted to limitations which lead to some prospects for improvement:

- Evaluate the influence of considering input motions *IM* during the selection of ground motions: Since one conclusion of this study is that engineers should not rely exclusively on the shape of the input spectrum for the selection of input motions, but also consider other parameters that showed adequate efficiency with the sought *DM*.
- Use of artificially generated input motions: this approach was discarded at the beginning of this project, but input motions generated artificially using algorithms such as with the SeismoArtif software, or stochastically simulated records (Atkinson 2009) are sometimes used. Although these motions have a reasonable spectrum, their duration and cumulative

effects are generally unrealistic. However, the extent of their limitations has not been studied in depth.

- Increase the number of input motions per scenario: As the conclusions of this study are based on a total number of 17 nonlinear simulations, the conclusions might be further validated using more input motions.
- Model multiple dikes and dams: This study focused on only one existing dike of a particular geometry since simulations are time consuming. However, it could be interesting to evaluate the response of dikes of different geometry and stratigraphy.

## REFERENCES

- Ancheta, T. D., Darragh, R. B., Stewart, J. P., Seyhan, E., Silva, W. J., Chiou, B. S. J., Wooddell, K. E., Graves, R. W., Kottke, A. R., Boore, D. M., Kishida, T. and Donahue, J. L. (2013). *PEER NGA-West2 Database* (Report no 2013/03). Retrived from [https://peer.berkeley.edu/sites/default/files/2013\\_03\\_ancheta\\_7.3.2020.pdf](https://peer.berkeley.edu/sites/default/files/2013_03_ancheta_7.3.2020.pdf)
- Arias, A., (1970). A measure of earthquake intensity. In Hansen, R. J. (ed.), *Seismic Design for Nuclear Power Plants*. Cambridge: MIT Press.
- Armstrong, R. J. (2018). *Relationship between earthquake ground motion intensity measures and embankment dam deformations* [Seminar session]. SMIP17 Seminar, California. [https://www.conservation.ca.gov/cgs/Documents/Program-SMIP/Seminar/SMIP17\\_P6\\_Paper%20by%20Armstrong.pdf](https://www.conservation.ca.gov/cgs/Documents/Program-SMIP/Seminar/SMIP17_P6_Paper%20by%20Armstrong.pdf)
- Ashford, S. A., and Sitar, N. (1997). Analysis of topographic amplification of inclined shear waves in a steep coastal bluff. *Bulletin of the Seismological Society of America*, 87(3), 692-700. <https://pubs.geoscienceworld.org/ssa/bssa/article/87/3/692/120235>
- Athanasopoulos-Zekkos, A. (2008). *Select topics on the static and dynamic response and performance of earthen levees* (Doctoral dissertation, University of California). ProQuest Dissertations & Theses. <https://search.proquest.com/docview/304696297?pq-origsite=gscholar&fromopenview=true>
- Athanasopoulos-Zekkos, A. (2010). *Variability in earthen levee seismic response due to time-history selection*. [Paper presentation], 5<sup>th</sup> International Conference on Recent Advances in Geotechnical Earthquake Engineering and Soil Dynamics, San Diego, California. <https://scholarsmine.mst.edu/icrageesd/05icrageesd/session03/18/>
- Athanasopoulos-Zekkos, A. and Seed, R. B. (2013). Simplified methodology for consideration of two-dimensional dynamic response of levees in liquefaction-triggering evaluation. *Journal of Geotechnical and Geoenvironmental Engineering*, 139(11), 1911-1922. [https://doi.org/10.1061/\(ASCE\)GT.1943-5606.0000913](https://doi.org/10.1061/(ASCE)GT.1943-5606.0000913).
- Atkinson, G. M. (2009). Earthquake time histories compatible with the 2005 National building code of Canada uniform hazard spectrum. *Canadian Journal of Civil Engineering*, 36(6), 991-1000. <https://doi.org/10.1139/L09-044>.
- Atkinson, G. and Adams, J. (2013). Ground motion prediction equations for application to the 2015 Canadian national seismic hazard maps, *Canadian Journal of Civil Engineering*, 40(10): 988-998. <https://doi.org/10.1139/cjce-2012-0544>
- Andrus, R. D. and Stokoe II, K. H. (2000). Liquefaction resistance of soils from shear-wave velocity, *Journal of Geotechnical and Geoenvironmental Engineering*, 126(11), 1015-1025. [https://doi.org/10.1061/\(ASCE\)1090-0241\(2000\)126:11\(1015\)](https://doi.org/10.1061/(ASCE)1090-0241(2000)126:11(1015))
- Baker, J. W. (2011). Conditional mean spectrum: Tool for ground motion selection. *Journal of Structural Engineering*, 137(3), 322-331. [https://doi.org/10.1061/\(ASCE\)ST.1943-541X.0000215](https://doi.org/10.1061/(ASCE)ST.1943-541X.0000215)
- Bard, P. Y. (1999). Ground shaking site effects: main characteristics. In Institute of Engineering Seismology and Earthquake Engineering (Eds.), *Local effects on strong ground motion: Physical basis and estimation methods in view of microzoning studies* (1<sup>st</sup> ed., pp. 233-257). [https://www.researchgate.net/publication/235623266\\_Local\\_effects\\_of\\_strong\\_ground\\_motion\\_Basic\\_physical\\_phenomena\\_and\\_estimation\\_methods\\_for\\_microzoning\\_studies](https://www.researchgate.net/publication/235623266_Local_effects_of_strong_ground_motion_Basic_physical_phenomena_and_estimation_methods_for_microzoning_studies)
- Bazzurro, P. and Cornell, C. A. (1999). Disaggregation of seismic hazard. *Bulletin of the Seismological Society of America*, 89(2), 501-520. <https://pubs.geoscienceworld.org/ssa/bssa/article/89/2/501/342641>
- Beaty, M. H. and Perlea, V. G. (2012). *Effect of ground motion characteristics on liquefaction modeling of dams*. [Paper presentation], GeoCongress, Oakland, California. <https://doi.org/10.1061/9780784412121.216>
- Boore, D. M. and Bommer, J. J. (2005). Processing of strong-motion accelerograms: needs, options and consequences. *Soil Dynamics and Earthquake Engineering*, 25(2005), 93-115. <https://doi.org/10.1016/j.soildyn.2004.10.007>
- Boore, D. M. (2010). Orientation-independent, nongeometric-mean measures of seismic intensity from two horizontal components of motion. *Bulleting of Seismological Society of America*, 100(4), 1830-1835. <https://doi.org/10.1785/0120090400>
- Boore, D. M, Sisi, A. A. and Akkar, S. (2012). Using pad-stripped acausally filtered strong-motion data, *Bulletin of the Seismological Society of America*, 102(2): 751-760. <https://doi.org/10.1785/0120110222>.
- Boulanger, R. W. and Idriss, M. (2008). *Soil liquefaction during earthquakes* (1<sup>st</sup> ed.). Earthquake Engineering Research Institute.

- Boulanger, R. W. and Idriss, I. M. (2014). *CPT and SPT based liquefaction triggering procedures* (Report no. UCD/CGM-14/01). Retrieved from [http://www.ce.memphis.edu/pezeshk/PDFs/Software/Liquefaction/Boulanger\\_Idriss\\_CPT\\_and\\_SPT\\_Liq\\_triggering\\_CGM-14-01\\_20141.pdf](http://www.ce.memphis.edu/pezeshk/PDFs/Software/Liquefaction/Boulanger_Idriss_CPT_and_SPT_Liq_triggering_CGM-14-01_20141.pdf)
- Bowles, J. E. (1997). *Foundation analysis and design* (5<sup>th</sup> ed.). Peoria, Illinois: McGraw-Hill.
- Bradley, B. A., Cubrinovski, M., Dhakal, R. P. and MacRae, G. A. (2008). Intensity measures for the seismic response of pile foundations. *Soil Dynamics and Earthquake Engineering*, 29: 1046-1058, <https://doi.org/10.1016/j.soildyn.2002.12.002>.
- Bradley, B. A. (2012a). Empirical correlations between cumulative absolute velocity and amplitude-based ground motion intensity measures. *Earthquake Spectra*, 28(1): 37-54. <https://doi.org/10.1193/1.3675580>
- Bradley, B. A. (2012b). Empirical correlations between peak ground velocity and spectrum-based intensity measures. *Earthquake Spectra*, 28(1): 17-35. <https://doi.org/10.1193/1.3675582>
- Bray, J. D. (2007). Chapter 14: Simplified seismic slope displacement procedures. [Paper presentation], 4<sup>th</sup> International Conference on Earthquake Geotechnical Engineering – Invited Lectures, K. D. Pitilakis. <https://calgeo.memberclicks.net/assets/docs/bray2007.pdf>
- Bray, J. D. and Travasarou, T. (2007). Simplified procedure for estimating earthquake-induced deviatoric slope displacements. *Journal of Geotechnical and Geoenvironmental Engineering*, 133(4), 381-392. [https://doi.org/10.1016/\(ASCE\)1090-0241\(2007\)133:4\(381\)](https://doi.org/10.1016/(ASCE)1090-0241(2007)133:4(381))
- Bullock, Z., Dashti, S., Liel, A. B., Porter, K. A. and Karimi, Z. (2019). Assessment supporting the use of outcropping rock evolutionary intensity measures for prediction of liquefaction consequences. *Earthquake Spectra*, 35(4), 1899-1926. <https://doi.org/10.1193/041618EQS094M>
- Campbell, K. W. and Bozorgnia, Y. (2011). Prediction equations for the standardized version of cumulative absolute velocity as adapted for use in the shutdown of U.S. nuclear power plants. *Nuclear Engineering and Design*, 241(7): 2558-2569. <https://doi.org/10.1016/j.nucengdes.2011.04.020>
- Cloud W, K. (1967). Intensity map and structural damage, Parkfield, California earthquake of June 27, 1966. *Bulletin of the Seismological Society of America*, 57(6), 1161-1178. <https://pubs.geoscienceworld.org/ssa/bssa/article/57/6/1161/101484>
- Converse, A. M. and Brady, A. G. (1992). *BAP: Basic strong-motion accelerogram processing software, version 1.0* (Report n. 92-296A). [https://escweb.wr.usgs.gov/nsmp-data/bap/BAP\\_v10.pdf](https://escweb.wr.usgs.gov/nsmp-data/bap/BAP_v10.pdf)
- Darendeli, M. B. (2001). *Development of a new family of normalized modulus reduction and material damping curves*. (Doctoral dissertation, The University of Texas at Austin, Austin, Texas). ProQuest Dissertations & Theses. <https://repositories.lib.utexas.edu/handle/2152/10396>
- Dashti, S. Bray, J. D., Pestana, J. M., Riemer, M. and Wilson, D. (2010). Centrifuge testing to evaluate and mitigate liquefaction-induced building settlement mechanisms. *Journal of Geotechnical and Geoenvironmental Engineering*, 136(7), 918-929. [https://doi.org/10.1061/\(ASCE\)GT.1943-5606.0000306](https://doi.org/10.1061/(ASCE)GT.1943-5606.0000306)
- Finn, W. L., and Wightman, A. (2003). Ground motion amplification factors for the proposed 2005 edition of the National Building Code of Canada. *Canadian Journal of Civil Engineering*, 30(2), 272-278. <https://doi.org/10.1139/l02-081>.
- Géli, L., Bard, P.-Y. & Jullien, B. (1988). The effect of topography on earthquake ground motion: A review and new results. *Bulletin of the Seismological Society of America*, 78(1), 42-63. <https://pubs.geoscienceworld.org/bssa/article-lookup/78/1/42>
- Goudarzy, M., Rahman, M. M., König, D. and Schanz, T. (2016). Influence of non-plastic fines content on maximum shear modulus of granular materials, *Soils and Foundations*, 56(6), 973-983. <https://doi.org/10.1016/j.sandf.2016.11.003>
- Goulet, C., Bozorgnia, Y., Abrahamson, N., Kuehn, N., Atik, L. A., Youngs, R., Graves, R. and Atkinson, G. (2018). *Central and Eastern North America Ground-Motion Characterization – NGA-East Final Report* (Report no. 2018/08). [https://apps.peer.berkeley.edu/publications/peer\\_reports/reports\\_2018/NGA-East\\_1MainReport\\_FINAL.pdf](https://apps.peer.berkeley.edu/publications/peer_reports/reports_2018/NGA-East_1MainReport_FINAL.pdf)
- Halchuk, S., Adams, J., Kolaj, M. and Allen, T. (2019). Deaggregation of NBCC 2015 seismic hazard for selected canadian cities [Paper presentation]. 12<sup>th</sup> Canadian Conference on Earthquake Engineering, Quebec, QC, Canada. [https://www.earthquakescanada.ca/hazard-alea/2019\\_12CCEE/12CCEE\\_Halchuk\\_et\\_al\\_Deaggregation\\_192-DMSa-149.pdf](https://www.earthquakescanada.ca/hazard-alea/2019_12CCEE/12CCEE_Halchuk_et_al_Deaggregation_192-DMSa-149.pdf)
- Hardin, B. O. and Drnevich, V. P. (1972). Shear modulus and damping in soils: Design equations and curves. *Journal of Soil Mechanics and Foundation Engineering Division*, 98(7), 667-692.

[https://www.researchgate.net/publication/247509918\\_Shear\\_Modulus\\_and\\_Damping\\_in\\_Soils\\_Design\\_Equations\\_and\\_Curves](https://www.researchgate.net/publication/247509918_Shear_Modulus_and_Damping_in_Soils_Design_Equations_and_Curves)

- Hashash, Y. M. A. and Park, D. (2001). Nonlinear one-dimensional seismic ground motion propagation in the Mississippi embayment. *Engineering Geology*, 62(1-3), 185-206. [https://doi.org/10.1016/S0013-7952\(01\)00061-8](https://doi.org/10.1016/S0013-7952(01)00061-8)
- Hashash, Y. M. A., Musgrove, M. I., Harmon, J. A., Groholski, D. R., Phillips, C. A. and Park, D. (2016). "DEEPSOIL 6.1, user manual"
- Hashash, Y. M. A., Phillips, C. and Groholski, D. R. (2010). *Recent advances in non-linear site response analysis* [Paper presentation]. 5<sup>th</sup> International Conference on Recent Advances in Geotechnical Earthquake Engineering, San Diego, California. <https://scholarsmine.mst.edu/icrageesd/05icrageesd/session12/8/>
- Housner, G.W. (1959). Behavior of structures during earthquakes, *Journal of the Engineering Mechanics Division*, 85(4), 109-130.
- Humar, J. (2015). Background to some of the seismic design provisions of the 2015 National Building Code of Canada. *Canadian Journal of Civil Engineering*, 42(11), 940-952. <https://doi.org/10.1139/cjce-2014-0385>
- Idriss, I. M. (1990). *Response of soft soil sites during earthquakes* [Paper presentation]. H. Bolton Seed Memorial Symposium, Berkeley, California
- Idriss, I. M. (1991). *Earthquake ground motions at soft soil sites* [Paper presentation]. 2<sup>nd</sup> International Conference on Recent Advances in Geotechnical Earthquake Engineering and Soil Dynamics, St-Louis, Missouri. <https://scholarsmine.mst.edu/cgi/viewcontent.cgi?article=3564&context=icrageesd>
- Idriss, I. M. (1999). *An update to the Seed-Idriss simplified procedure for evaluating liquefaction potential* [Paper presentation]. Transportation Research Board Workshop on New Approaches to Liquefaction, Washington, DC.
- Itasca Consulting Group Inc. (2016). Fast Lagrangian Analysis of Continua v8, User's guide, 6<sup>th</sup> edition, Minneapolis, Minnesota.
- Joyner, W. B. and Boore, D. M. (1988). *Measurement, characterization and prediction of strong ground motion*. Paper presented at Earthquake and Soil Dynamics II – Recent Advances in Ground-Motion Evaluation, Geotechnical Special Publication, New York (pp. 43-102). [http://www.daveboore.com/pubs\\_online/joyner\\_boore\\_park\\_city\\_1988.pdf](http://www.daveboore.com/pubs_online/joyner_boore_park_city_1988.pdf)
- Kammerer, A., Coleman, J., Hashash, Y. M. A., Johnson, J. J., Kennedy, R. P., Whittaker, A. S. and Yu, C.-C. (2018). *Nonlinear soil-structure-interaction analysis in support of seismic design and probabilistic risk assessment of nuclear facilities* (Report no. INL/EXT-18-50155). [https://www.researchgate.net/publication/330986316\\_Nonlinear\\_soil-structure-interaction\\_analysis\\_in\\_support\\_of\\_seismic\\_design\\_and\\_probabilistic\\_risk\\_assessment\\_of\\_nuclear\\_facilities](https://www.researchgate.net/publication/330986316_Nonlinear_soil-structure-interaction_analysis_in_support_of_seismic_design_and_probabilistic_risk_assessment_of_nuclear_facilities)
- Karray, M. (2010). *Shear wave velocity in geotechnical engineering* [Paper presentation]. International Conference on Geotechnical Engineering, Hammamet, Tunisia. [https://www.researchgate.net/profile/Mourad\\_Karray/publication/267038559\\_Shear\\_wave\\_velocity\\_in\\_geotechnical\\_engineering/links/544328fe0cf2a76a3ccb0add/Shear-wave-velocity-in-geotechnical-engineering.pdf](https://www.researchgate.net/profile/Mourad_Karray/publication/267038559_Shear_wave_velocity_in_geotechnical_engineering/links/544328fe0cf2a76a3ccb0add/Shear-wave-velocity-in-geotechnical-engineering.pdf)
- Kawase, H. and Aki, K. (1990). Topography effect at the critical SV-wave incidence: possible explanation of damage pattern by the Whittier Narrows, California, Earthquake of 1 October 1987. *Bulletin of the Seismological Society of America*, 80(1), 1-22. <https://pubs.geoscienceworld.org/ssa/bssa/article/80/1/1/119281/topography-effect-at-the-critical-sv-wave>
- Kayen, R., Moss, R. E. S., Thompson, E. M., Seed, R. B., Cetin, K. O., Der Kiureghian, A., Tanaka, Y. and Tokimatsu, K. (2013). Shear-wave velocity-based probabilistic and deterministic assessment of seismic soil liquefaction potential. *Journal of Geotechnical and Geoenvironmental Engineering*, 139(3), 407-419. [https://doi.org/10.1061/\(ASCE\)GT.1943-5606.0000743](https://doi.org/10.1061/(ASCE)GT.1943-5606.0000743)
- Kostadinov, M. V. and Towhata, I. (2002). Assessment of liquefaction-induced peak ground velocity and frequency of horizontal ground shaking at onset of phenomenon. *Soil Dynamics and Earthquake Engineering*, 22(4), 309-322. doi:10.1016/S0267-7261(02)00018-0
- Kramer, S. L. (1996). *Geotechnical earthquake engineering* (1<sup>st</sup> ed.), Upper Saddle River, N. J., United States: Prentice Hall.
- Krawinkler, H. and Rahnama, M. (1992). *Effects of soft soils on design spectra*. Paper presented at 10<sup>th</sup> World Conference on Earthquake Engineering, Rotterdam (pp. 5841-5846). [https://www.iitk.ac.in/nicee/wcee/article/10\\_vol10\\_5841.pdf](https://www.iitk.ac.in/nicee/wcee/article/10_vol10_5841.pdf)

- Krinitzky, E. L. and Chang, F. K. (1978). *State-of-the-art for assessing earthquake hazards in the United States: Specifying peak motions for design earthquakes* (Report no. 7). <https://hdl.handle.net/11681/20720>
- Kuhlemeyer, R. L. and Lysmer, J. (1973). Finite element method accuracy for wave propagation problems, *Journal of Soil Mechanics and Foundations Div.*, 99(SM5), 421-427.
- Kunar, R. R., Beresford, P. J. and Cundall, P. A. (1977). *A tested soil-structure model for surface structures* [Symposium session]. Symposium on Soil-Structure Interaction, India (pp. 137-144)
- Kwok, A. O. L., Stewart, J. P., Hashash, Y. M. A., Matasovic, N., Pyke, R., Wang, Z. and Yang, Z. Y. (2007). Use of exact solutions of wave propagation problems to guide implementation of nonlinear seismic ground response analysis procedures, *Journal of Geotechnical and Geoenvironmental Engineering*, 133(11), 1385-1398, [https://doi.org/10.1061/\(ASCE\)1090-0241\(2007\)133:11\(1385\)](https://doi.org/10.1061/(ASCE)1090-0241(2007)133:11(1385))
- Lanzo, G., Vucetic, M. and Doroudian, M. (1997). Reduction of shear modulus at small strains in simple shear, *Journal of Geotechnical and Geoenvironmental Engineering*, 123(11), 1035-1042. [https://doi.org/10.1061/\(ASCE\)1090-0241\(1997\)123:11\(1035\)](https://doi.org/10.1061/(ASCE)1090-0241(1997)123:11(1035))
- Leroueil, S. and Tavenas, F. (1983). Propriétés caractéristiques des argiles de l'est du Canada, *Canadian Geotechnical Journal*, 20, 681-705. <https://cdnsiencepub.com/doi/pdf/10.1139/t83-076>
- Luco, N. and Cornell, C. A. (2001). Structure-specific scalar intensity measures for near-source and ordinary earthquake ground motions. *Earthquake Spectra*, 23(2), 357-392. <https://doi.org/10.1193/1.2723158>
- Lysmer, J. and Kuhlemeyer, R. L. (1969). Finite dynamic model for infinite media, *Journal of the Engineering Mechanics Division*, 95(4), 859-877.
- Makdisi, F. I. and Seed, H. B. (1978). *Simplified procedure for estimating dam and embankment earthquake-induced deformations* (Report no. UCB/EERC-77/19). <https://nehprsearch.nist.gov/static/files/NSF/PB276820.pdf>
- Manika, M., Ovando, E. and Botero, E. (2014). Assessment of damping models in FLAC, *Computers and Geotechnics*, 59(2014), 12-20, <https://doi.org/10.1016/j.compgeo.2014.02.007>
- Masing, G. (1926). Eigenspannumyen und verfeshungung beim messing, Paper presented in 2<sup>nd</sup> International Congress on Applied Mechanics, Zurich, Switzerland (pp. 332-335).
- Matesovic, N. (2003). *Seismic response of composite horizontally-layered soil deposits*. (Doctoral dissertation, University of California, Los Angeles). <https://search.proquest.com/pqdtglobal/docview/304053070/FDCFF3C9686E49CAPQ/1?accountid=40695>
- Mejia, L. H. and Dawson, E. M. (2006). *Earthquake deconvolution for FLAC*. Paper presented at 4<sup>th</sup> International Symposium on Numerical modeling in Geomechanics, Madrid, Spain. <http://citeseerx.ist.psu.edu/viewdoc/download?doi=10.1.1.454.5241&rep=rep1&type=pdf>
- Michaud, D., and Léger, P. (2014). Ground motions selection and scaling for nonlinear dynamic analysis of structures located in Eastern North America. *Canadian Journal of Civil Engineering*, 41(3), 232-244. <https://doi.org/10.1139/cjce-2012.0339>.
- Michigan Technological University. (2020, October 24). *What is Seismology?*. UPSeis. <http://www.geo.mtu.edu/UPSeis/waves.html#:~:text=Body%20waves%20can%20travel%20through,both%20body%20and%20surface%20waves.&text=The%20P%20wave%20can%20move,liquid%20layers%20of%20the%20earth.>
- Nason, R. D. (1971). Shattered earth at Wallaby Street, Sylmar. In Geological Survey (ed.), *Geological Survey Professional Paper* (pp. 97-98). [https://books.google.ca/books?hl=fr&lr=&id=DxXV3Wzk\\_rSC&oi=fnd&pg=PA97&dq=nason+1971+shattered+san+fernando+&ots=plmcmhe0VQ&sig=ooAV6WbvVifUo\\_fSPhtLaKPJlGc#v=onepage&q=nason%201971%20shattered%20san%20fernando&f=false](https://books.google.ca/books?hl=fr&lr=&id=DxXV3Wzk_rSC&oi=fnd&pg=PA97&dq=nason+1971+shattered+san+fernando+&ots=plmcmhe0VQ&sig=ooAV6WbvVifUo_fSPhtLaKPJlGc#v=onepage&q=nason%201971%20shattered%20san%20fernando&f=false)
- NCRHP. (2010). *LRFD design and construction of shallow foundations for highway bridge structures* (Report no. 651). [ftp://ftp.odot.state.or.us/techserv/Geo-Environmental/Geotech/Retaining%20Structures/Retaining\\_wall\\_references/NCHRP\\_651\\_LRFD\\_design\\_shallow\\_fdn\\_bridges/nchrp\\_rpt\\_651.pdf](ftp://ftp.odot.state.or.us/techserv/Geo-Environmental/Geotech/Retaining%20Structures/Retaining_wall_references/NCHRP_651_LRFD_design_shallow_fdn_bridges/nchrp_rpt_651.pdf)
- Nechtschein, S., Bard, P. Y., Gariel, J. C., Meneroud, J. P., Dervin, P., Cushing, M. ... Duval, A. M. (1995). *A topographic effect study in the Nice region* [Paper presentation]. 5<sup>th</sup> International Conference on Seismic Zonation, Nice, France. [https://www.researchgate.net/profile/Edward\\_Cushing2/publication/235623130\\_A\\_topographic\\_effect\\_study\\_in\\_the\\_Nice\\_region/links/5888b264a6fdcc9a35c10e9c/A-topographic-effect-study-in-the-Nice-region.pdf](https://www.researchgate.net/profile/Edward_Cushing2/publication/235623130_A_topographic_effect_study_in_the_Nice_region/links/5888b264a6fdcc9a35c10e9c/A-topographic-effect-study-in-the-Nice-region.pdf)

- NERHP. (1994). *1994 Recommended provisions for seismic regulations of new buildings: Part 1, provisions* (Report no. P-750). [https://www.fema.gov/media-library-data/20130726-1730-25045-1580/femap\\_750.pdf](https://www.fema.gov/media-library-data/20130726-1730-25045-1580/femap_750.pdf)
- Nguyen, K.-V. and Gatmiri, B. (2007). Evaluation of seismic ground motion induced by topographic irregularity, *Soil Dynamics and Earthquake Engineering*, 27(2007), 183-188, <https://doi.org/10.1016/j.soildyn.2006.06.005>
- NRC, (2015a). *Commentary J-NBCC 2015, Design for seismic effects*, no. Issued by the Canadian Commission on Buildings and Fire Codes. Ottawa, ON: National Research Council of Canada.
- NRC. (2015b). *National Building Code of Canada*. National Research Council, Ottawa, ON, Canada.
- O'Hara, T. F. and Jacobson, J. P. (1991). *Standardization of the cumulative absolute velocity* (Report no. EPRI TR-100082-T2), Palo Alto, California.
- Ohtsuki, A. and Harumi, K. (1983). Effect of topography and subsurface inhomogeneities on seismic SV waves. *Earthquake Engineering and Structural Dynamics*, 11 (4), 441-462. <https://doi.org/10.1002/eqe.4290110402>
- Peck, R. B., Hanson, W. E. and Thornburn, T. H. (1974). *Foundation Engineering* (2<sup>nd</sup> ed.). Illinois, United States: John Wiley & Sons, Inc.
- Pezeshk, S., Zandieh, A. and Tavakoli, B. (2011). Hybrid empirical ground-motion prediction equations for Eastern North America using NGA models and updated seismological parameters. *Bulletin of the Seismological Society of America*, 101(4), 1859-1870, <https://doi.org/10.1785/0120100144>
- Phillips, C. and Hashash, Y.M. A. (2009). Damping formulation for non-linear 1D site response analyses. *Soil Dynamics and Earthquake Engineering*, 29(7), 1143-1158. <https://doi.org/10.1016/j.soildyn.2009.01.004>
- Rathje, E. M., Abrahamson, N. A. and Bray, J., D., (1998). Simplified content estimates of earthquake ground motions. *Journal of Geotechnical and Geoenvironmental Engineering*, 124(2), 150-159. [https://doi.org/10.1061/\(ASCE\)1090-0241\(1998\)124:2\(150\)](https://doi.org/10.1061/(ASCE)1090-0241(1998)124:2(150))
- Rathje, E. M., Faraj, F., Russel, S. and Bray, J. D. (2004). Empirical relationships for frequency content parameters of earthquake ground motions. *Earthquake Spectra*, 20(1), 119-144. <https://doi.org/10.1193/1.1643356>
- Rathje, E. M., Idriss, I. M., Somerville, P., Ansal, A., Bachhuber, J., Baturay, M., Erdik, M., Frost, D., Lettis, W., Sozer, B., Stewart, J. and Ugras, T. (2001). Strong ground motion site effects. *Earthquake Spectra*, 16(1), 65-96. <https://doi.org/10.1193/1.1586147>
- Rayleigh, J. W. S and Lindsay, R. B. (1945). *The theory of sound* (2<sup>nd</sup> ed.). New York: Dover Publications.
- Reed, J. W. and Kassawara, R. (1988). A criterion for determining exceedance of the operating basis earthquake. *Nuclear Engineering and Design*, 123(2-3), 387-396. [https://doi.org/10.1016/0029-5493\(90\)90259-Z](https://doi.org/10.1016/0029-5493(90)90259-Z)
- Seed, H. B. and Idriss, I. M. (1970). *Soil moduli and damping factors for dynamic response analyses* (Report no. EERC 70-10). <https://ntrl.ntis.gov/NTRL/dashboard/searchResults/titleDetail/PB197869.xhtml>
- Seed, H. B. and Idriss, I. M. (1971). Simplified procedure for evaluating soil liquefaction potential, *Journal of Soil Mechanics and Foundations Division*, 97(SM9), 1249-1273.
- Seed, H. B., Idriss, I. M., Makdisi, F. and Banerjee, N. (1975). *Representation of irregular stress time histories by equivalent uniform stress series in liquefaction analyses* (Report no. EERC 75-29), Earthquake Engineering Research Center, University of Berkeley, California
- Seed, H. B., Wong, R. T., Idriss, I. M., and Tokimatsu, K. (1986). Moduli and damping factors for dynamic analyses of cohesionless soils. *Journal of Geotechnical Engineering*, 112(11), 1016-1032. [https://doi.org/10.1061/\(ASCE\)0733-9410\(1986\)112:11\(1016\)](https://doi.org/10.1061/(ASCE)0733-9410(1986)112:11(1016))
- Seed, R. B. and Harder Jr., L. F. (1990). *SPT-based analysis of cyclic pore pressure generation and undrained residual strength*. Paper presented at HB Seed Memorial Symposium, Berkeley pp. 351-376). [https://www.google.com/url?sa=t&rct=j&q=&esrc=s&source=web&cd=&cad=rja&uact=8&ved=2ahUKEwi3z86K4JDrAhWphOAKHYFEBtUQFjABegQIBxAB&url=https%3A%2F%2Fwww.u-cursos.cl%2Fingenieria%2F2006%2F1%2FCI79F%2F1%2Fmaterial\\_docente%2Fbajar%3Fid\\_material%3D91603&usq=AOvVaw2FpUle-sYDLn6brnVD6LRF](https://www.google.com/url?sa=t&rct=j&q=&esrc=s&source=web&cd=&cad=rja&uact=8&ved=2ahUKEwi3z86K4JDrAhWphOAKHYFEBtUQFjABegQIBxAB&url=https%3A%2F%2Fwww.u-cursos.cl%2Fingenieria%2F2006%2F1%2FCI79F%2F1%2Fmaterial_docente%2Fbajar%3Fid_material%3D91603&usq=AOvVaw2FpUle-sYDLn6brnVD6LRF)
- Shome, N. and Cornell, A. C. (1999). *Probabilistic seismic demand analysis of nonlinear structures* (Report no. RMS-35). <https://nehrpsearch.nist.gov/article/PB99-143372/XAB>
- Tremblay, R., Atkinson, G. M., Bouaanani, N., Daneshvar, P., Léger, P., and Koboevic, S. (2015). *Selection and scaling of ground motion time histories for seismic analysis using NBCC 2015* [Paper presentation]. 11th Canadian Conference on Earthquake Engineering, Victoria, BC, Canada. [https://www.caee.ca/pdf/Paper\\_99060.pdf](https://www.caee.ca/pdf/Paper_99060.pdf)

- Trifunac, M. D. and Hudson, D. E. (1971). Analysis of the Pacoima dam accelerogram – San Fernando, California, earthquake of 1971. *Bulletin of the Seismological Society of America*, 61(5), 1393-1411. <https://pubs.geoscienceworld.org/ssa/bssa/article/61/5/1393/116979>
- Vahdani, S. and Wikstrom, S. (2002). Response of the Tarzana strong motion site during the 1994 Northridge earthquake., *Soil Dynamics and Earthquake Engineering*, 22(9-12), 837-848. [https://doi.org/10.1016/S0267-7261\(02\)00106-9](https://doi.org/10.1016/S0267-7261(02)00106-9)
- Vucetic, M. (1990). Normalized behavior of clay under irregular cyclic loading. *Canadian Geotechnical Journal*, 27(1), 29-46. <https://doi.org/10.1139/t90-004>
- Vucetic, M., Lanzo, G. and Doroudian, M. (1998). Damping at small strains in cyclic simple shear test. *Journal of Geotechnical and Geoenvironmental Engineering*, 124(7), 585-594, [https://doi.org/10.1061/\(ASCE\)1090-0241\(1998\)124:7\(585\)](https://doi.org/10.1061/(ASCE)1090-0241(1998)124:7(585))
- Watson-Lamprey, J. and Abrahamson, N. (2005). Selection of ground motion time series and limits on scaling. *Soil Dynamics and Earthquake Engineering*. 26(5), 477-482. <https://doi.org/10.1016/j.soildyn.2005.07.001>
- Wolff, T. F. (1989). Pile capacity prediction using parameter functions. In American Society of Civil Engineers (Eds.), *Predicted and Observed Axial Behavior of Piles: Results of a Pile Prediction Symposium* (pp. 396). Evanston, Illinois, United States: Geotechnical Special Publication.
- Yang, J. and Liu, X. (2016). Shear wave velocity and stiffness of sand: the role of non-plastic fines. *Géotechnique*, 66(6), 500-514. <https://doi.org/10.1680/jgeot.15.P.205>
- Yniesta, S., Brandenberg, S. J. and Shafiee, A. (2017). ARCS: A one dimensional nonlinear soil model for ground response analysis. *Soil Dynamics and Earthquake Engineering*, 102(2017), 75-85. <https://doi.org/10.1016/j.soildyn.2017.08.015>
- Youd, T. L., Idriss, I. M., Andrus, R. D., Arango, I., Castro, G., Christian, J. T., Dobry, R., Finn, W. D. L., Harder Jr., L. F., Hynes, M. E., Ishihara, K., Koester, J. P., Liao, S. S. C., Marcuson III, W. F., Martin, G. R., Mitchell, J. K., Moriwaki, Y., Power, M. S., Robertson, P., .... and Stokoe II, K. H. (2001). Liquefaction resistance of soils: Summary report from the 1996 NCEER and 1998 NCEER/NSF workshops on evaluation of liquefaction resistance of soils. *Journal of Geotechnical and Geoenvironmental Engineering*, 127(4), 817-833. [https://doi.org/10.1061/\(ASCE\)1090-0241\(2001\)127:4\(297\)](https://doi.org/10.1061/(ASCE)1090-0241(2001)127:4(297))

## APPENDIX A DETAILS OF THE SELECTED, PROCESSED AND SCALED INPUT GROUND MOTIONS

### Scenario T1-1

Coalinga – 02, 1983,  $M_w = 5.1$ ,  $D = 0.0$  km (RSN381H1)

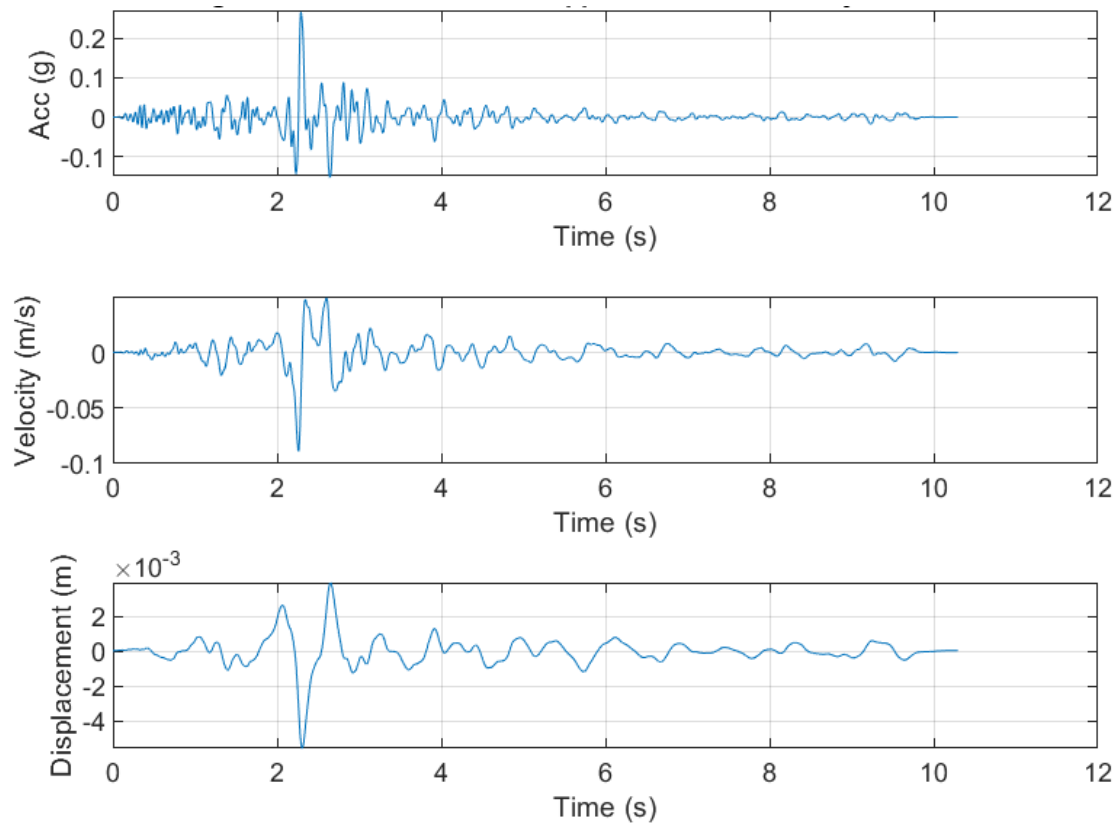


Figure 8.1 Acceleration, velocity and displacement time series of the event Coalinga – 02 (RSN381H1)

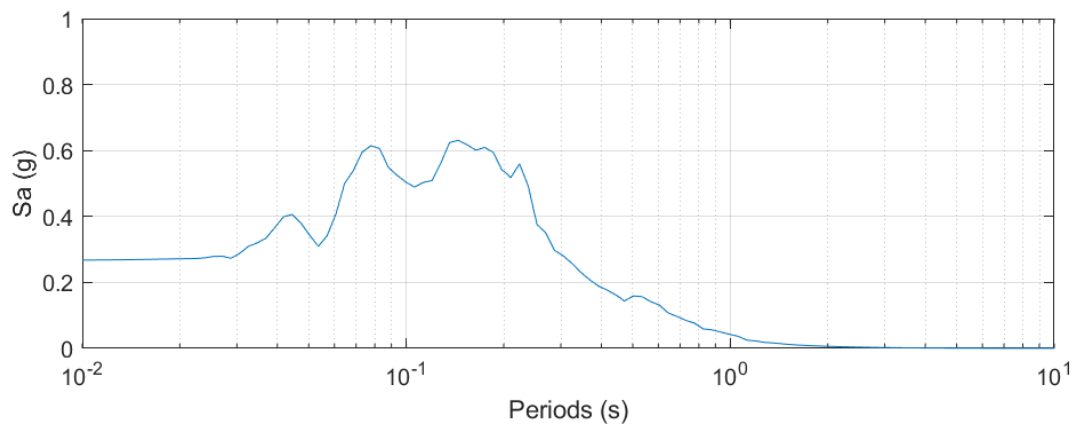


Figure 8.2 Response spectrum of the event Coalinga - 02 (RSN381H1)

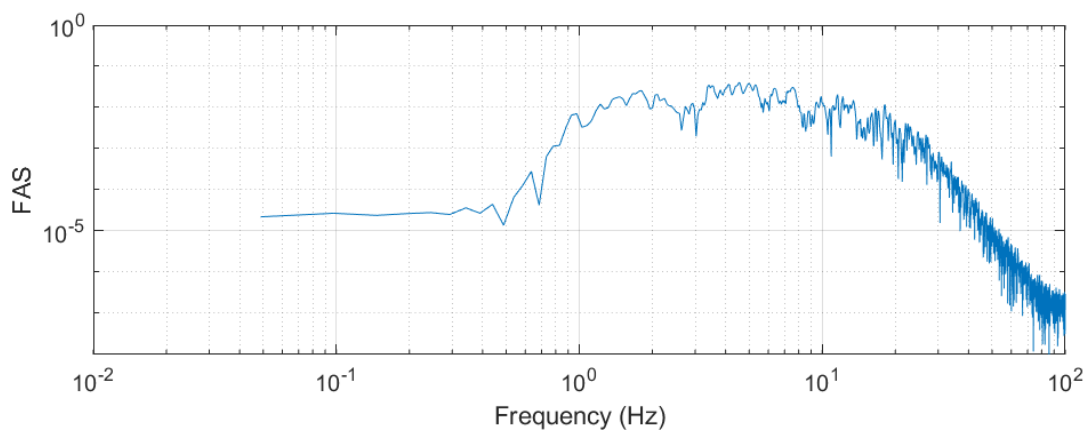


Figure 8.3 Fourier amplitude spectrum of the event Coalinga - 02 (RSN381H1)

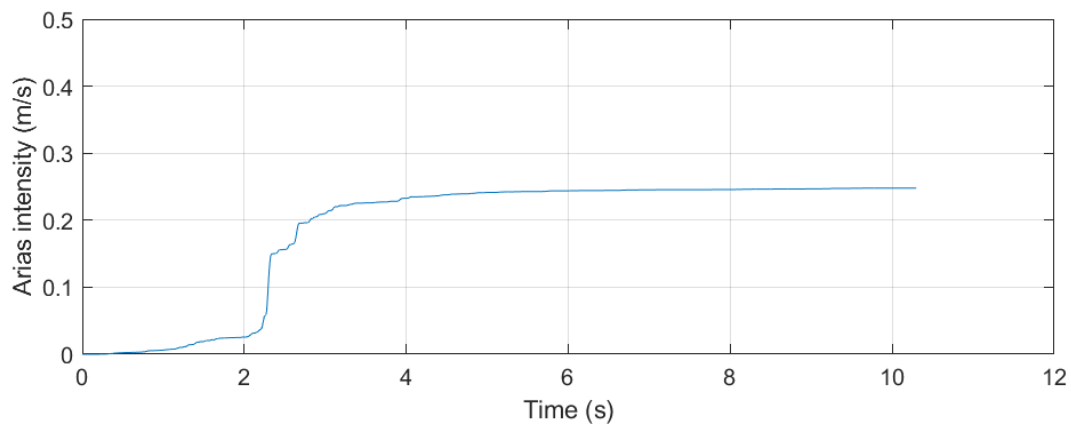


Figure 8.4 Arias intensity of the event Coalinga - 02 (RSN381H1)

Gilroy, 2002,  $M_w = 4.9$ ,  $D = 2.2$  km (RSN2019H2)

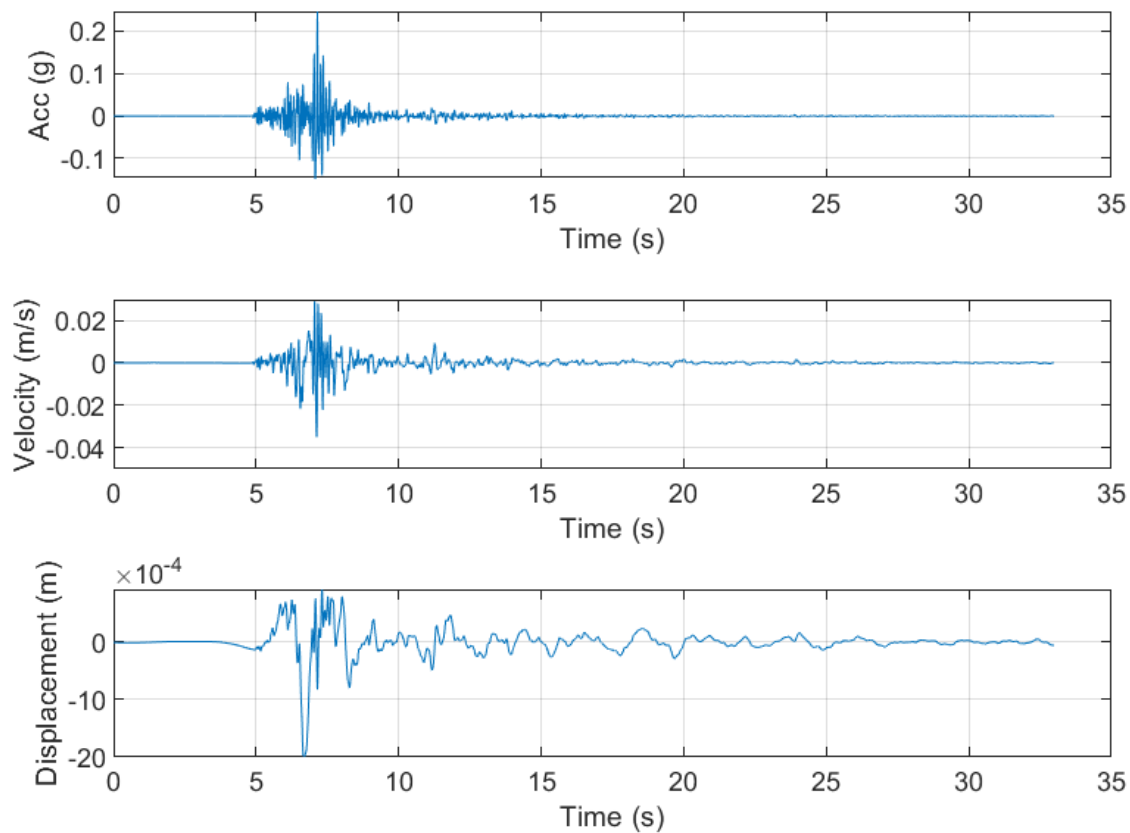


Figure 8.5 Acceleration, velocity and displacement time series of the event Gilroy (RSN2019H2)

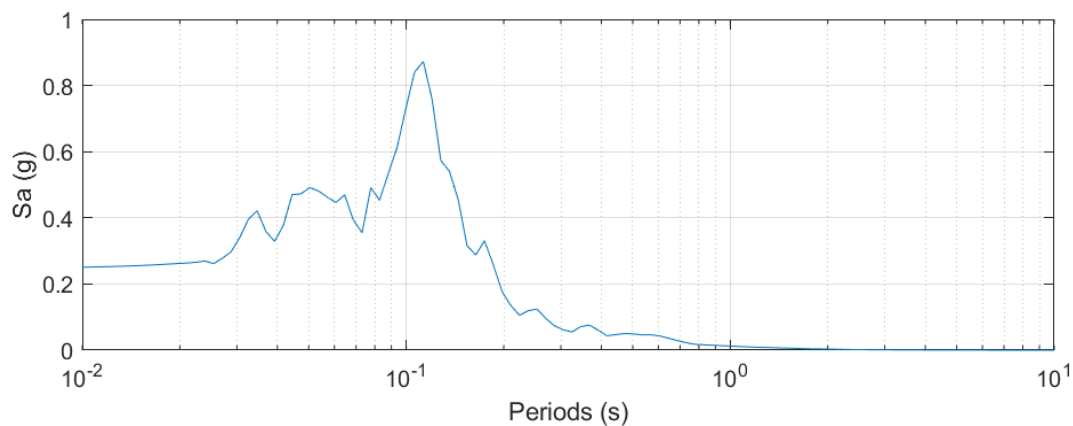


Figure 8.6 Response spectrum of the event Coalinga - 02 (RSN381H1)

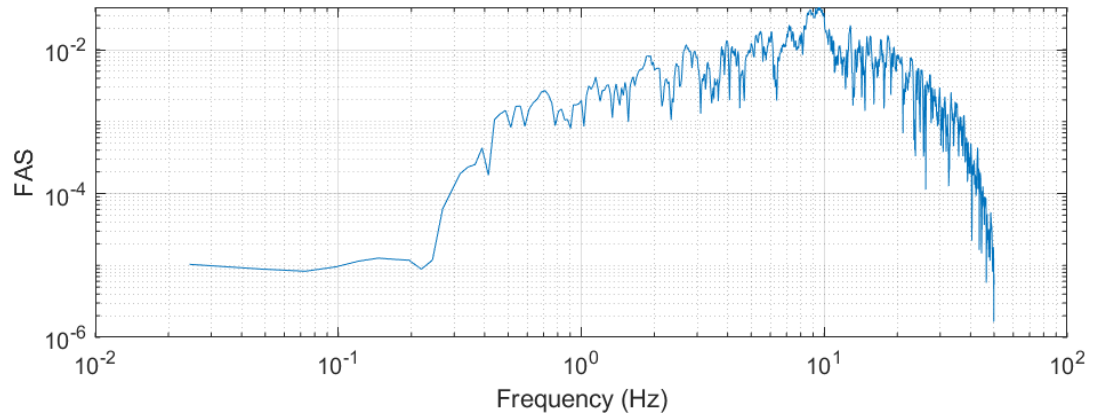


Figure 8.7 Fourier amplitude spectrum of the event Gilroy (RSN2019H2)

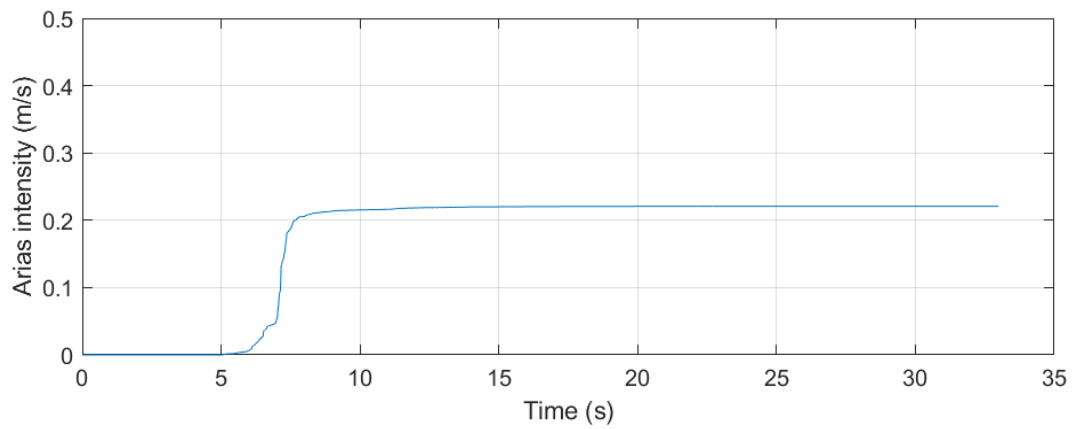


Figure 8.8 Arias intensity of the event Gilroy (RSN2019H2)

Fruili, Italy – 03, 1976,  $M_w = 5.5$ ,  $D = 16.8$  km (RSN3553H1)

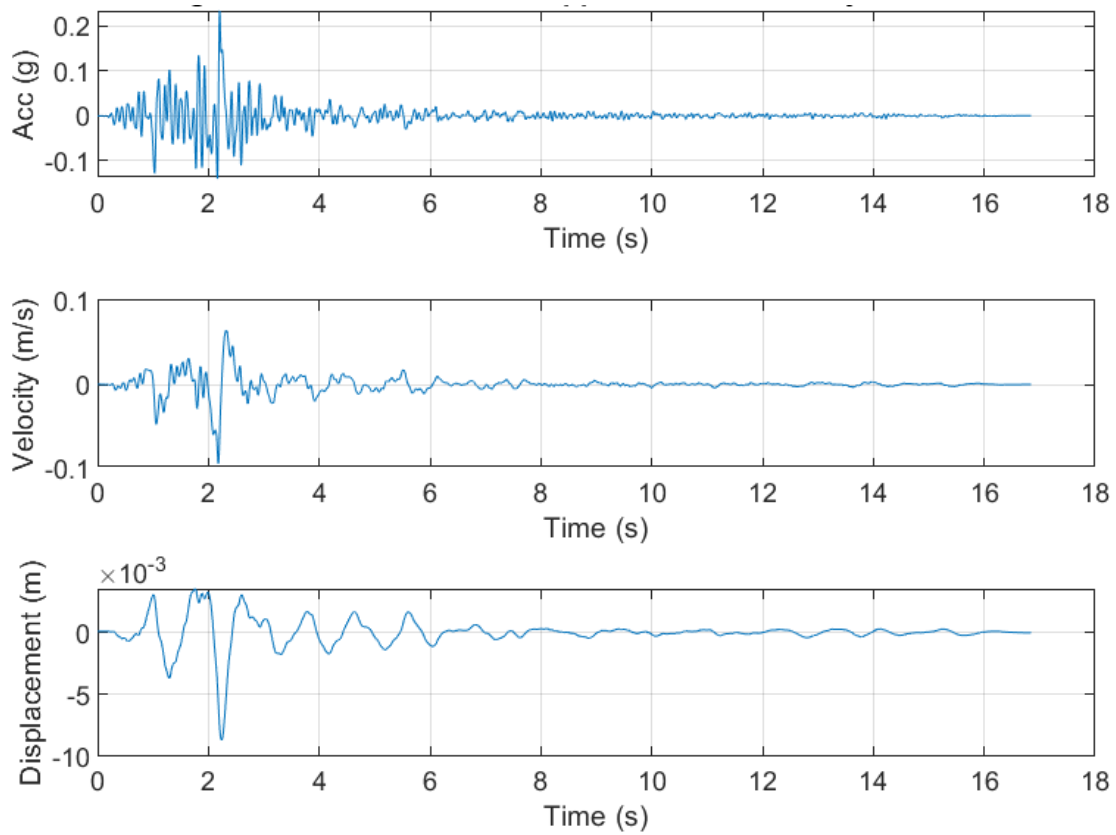


Figure 8.9 Acceleration, velocity and displacement time series of the event Fruili, Italy – 03 (RSN3553H1)

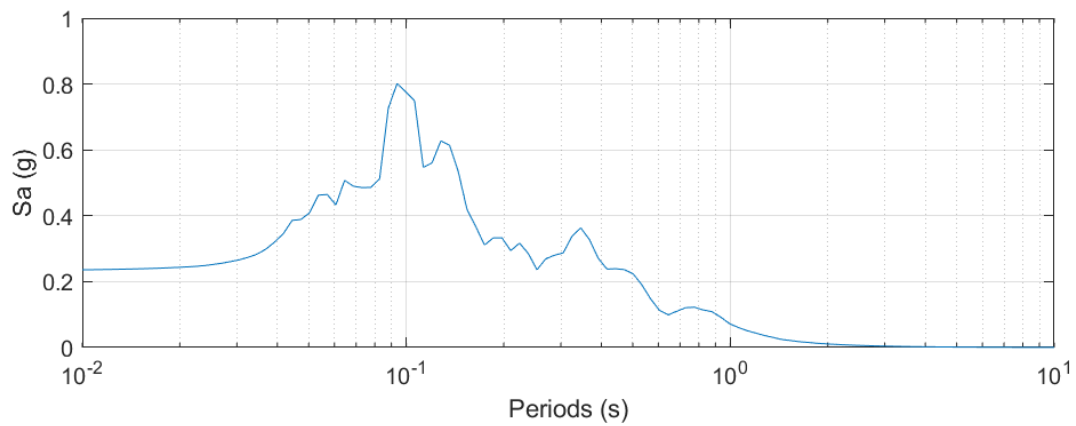


Figure 8.10 Response spectrum of the event Fruili, Italy – 03 (RSN3553H1)

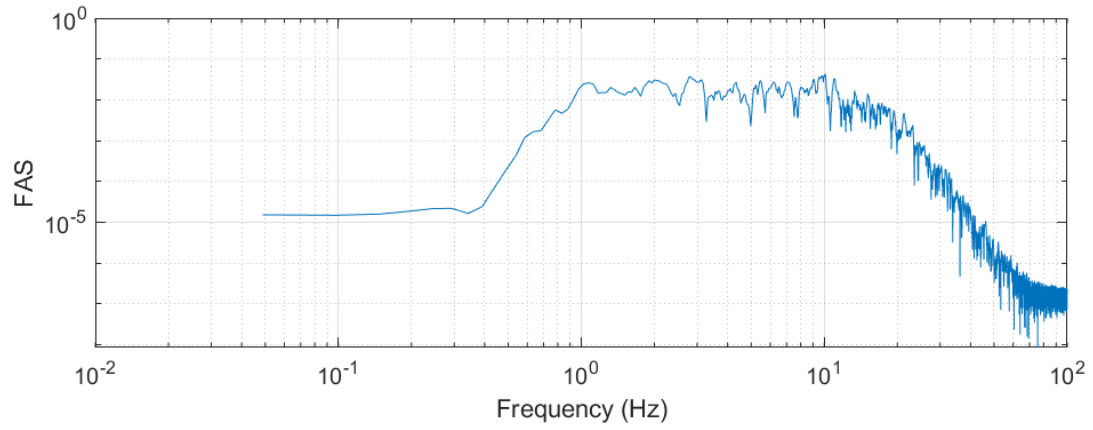


Figure 8.11 Fourier amplitude spectrum of the event Fruii, Italy – 03 (RSN3553H1)

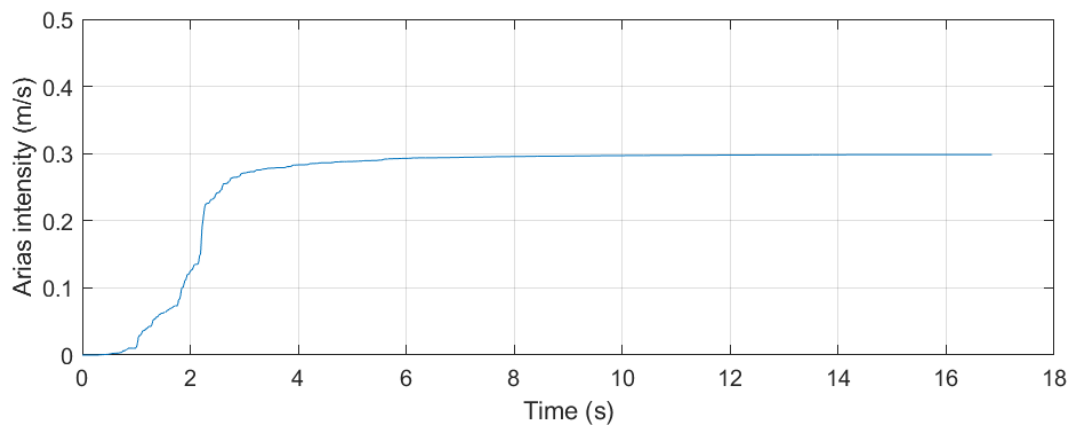


Figure 8.12 Arias intensity of the event Fruii, Italy – 03 (RSN3553H1)

Umbria Marche (Aftershock 8), Italy, 1997,  $M_w = 5.2$ ,  $D = 8.8$  km (RSN4377H1)

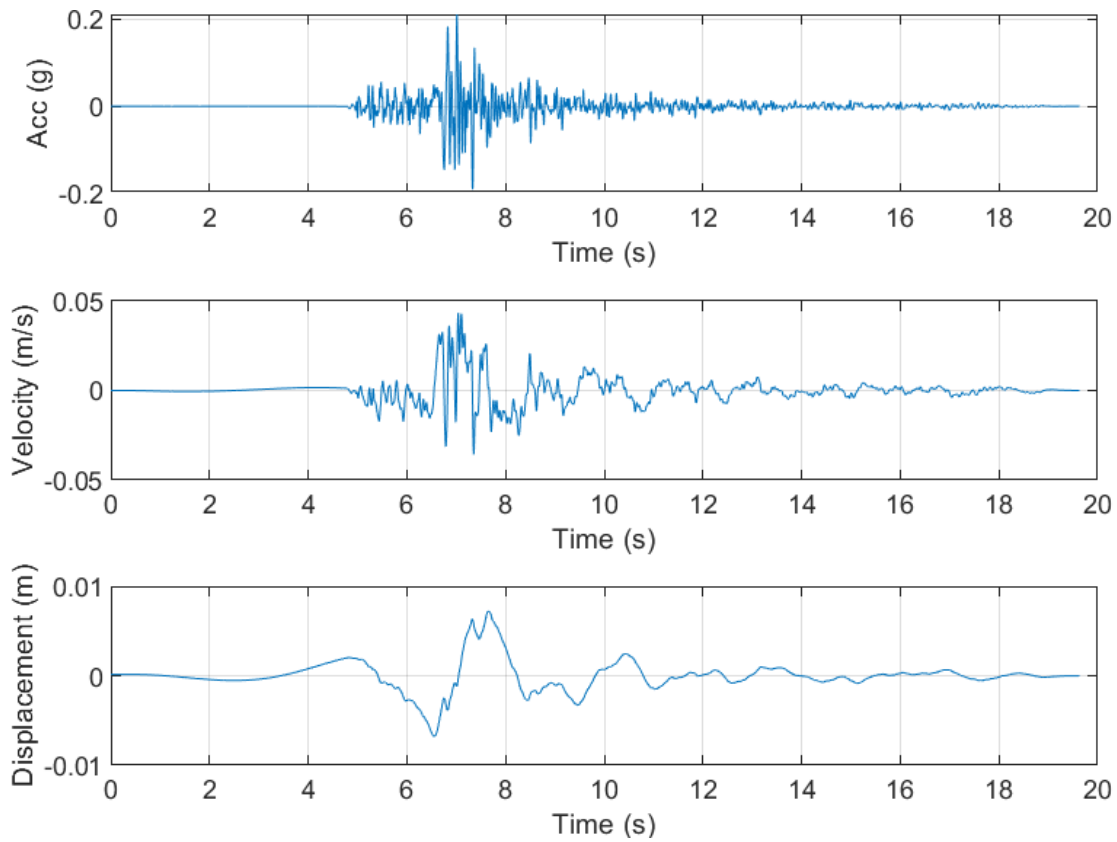


Figure 8.13 Acceleration, velocity and displacement time series of the event Umbria Marche (Aftershock 8), Italy (RSN4377H1)

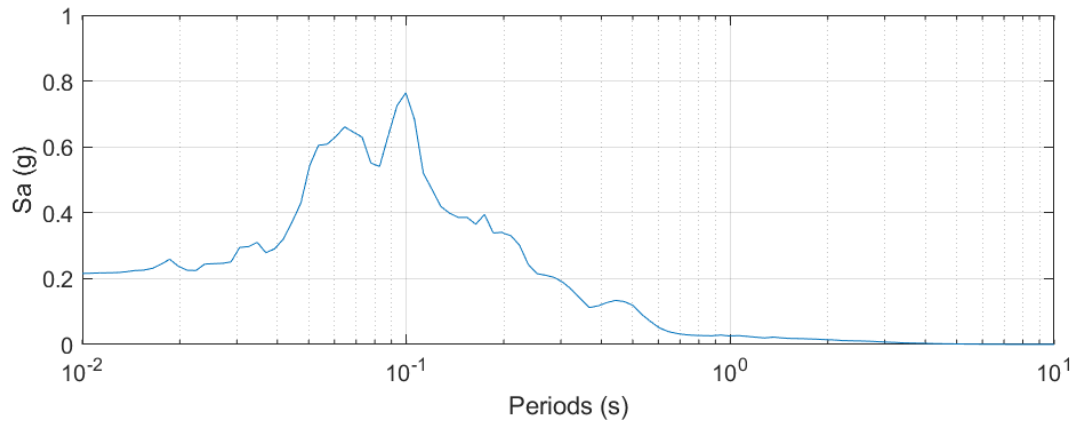


Figure 8.14 Response spectrum of the event Umbria Marche (Aftershock 8), Italy (RSN4377H1)

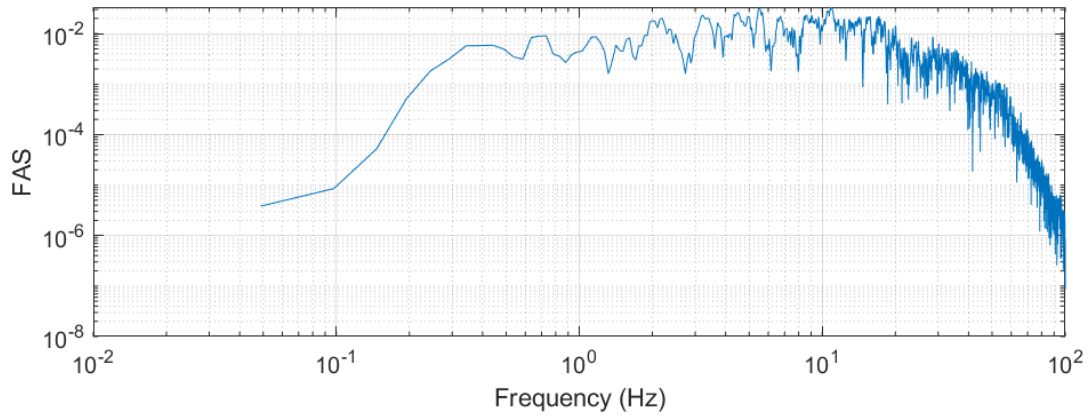


Figure 8.15 Fourier amplitude spectrum of the event Umbria Marche (Aftershock 8), Italy (RSN4377H1)

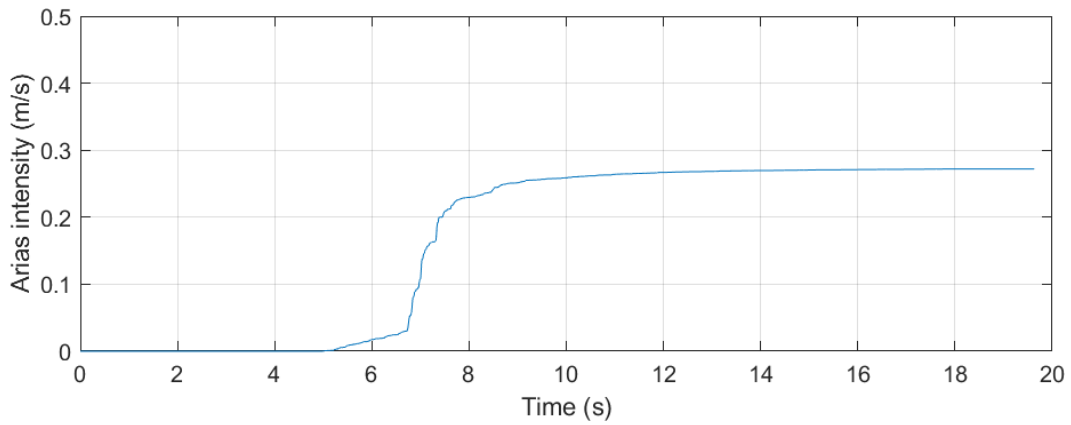


Figure 8.16 Arias intensity of the event Umbria Marche (Aftershock 8), Italy (RSN4377H1)

Mineral 2011-08-23, 2011,  $M_w = 5.7$ ,  $R = 18.5$  km (RSN8571H2)

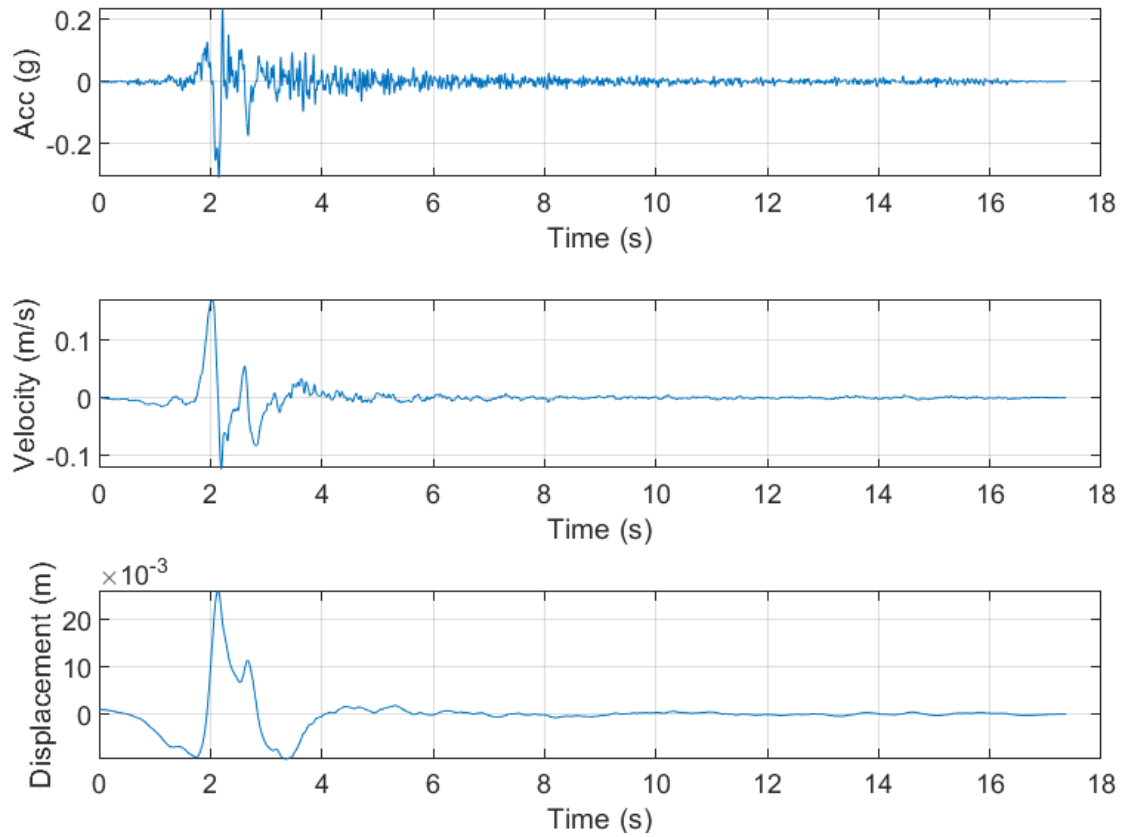


Figure 8.17 Acceleration, velocity and displacement time series of the event Mineral 2011-08-23 (RSN8571H2)

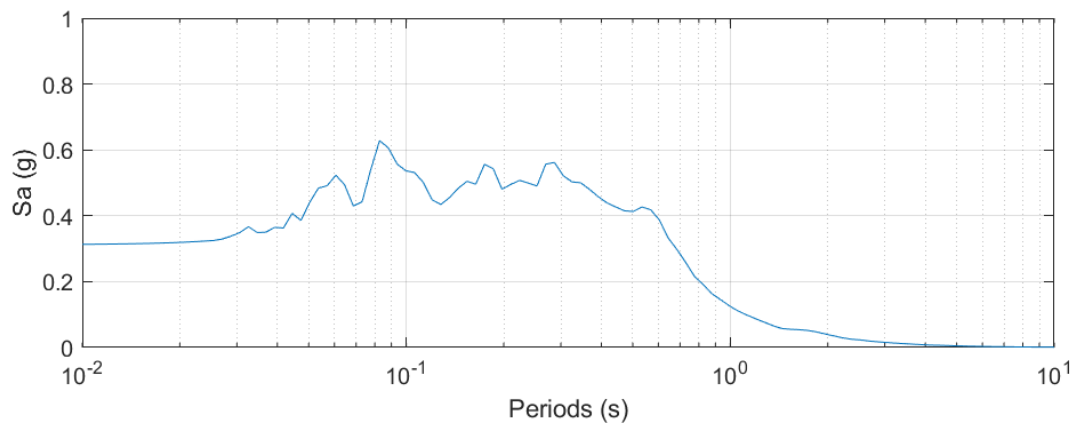


Figure 8.18 Response spectrum of the event Mineral 2011-08-23 (RSN8571H2)

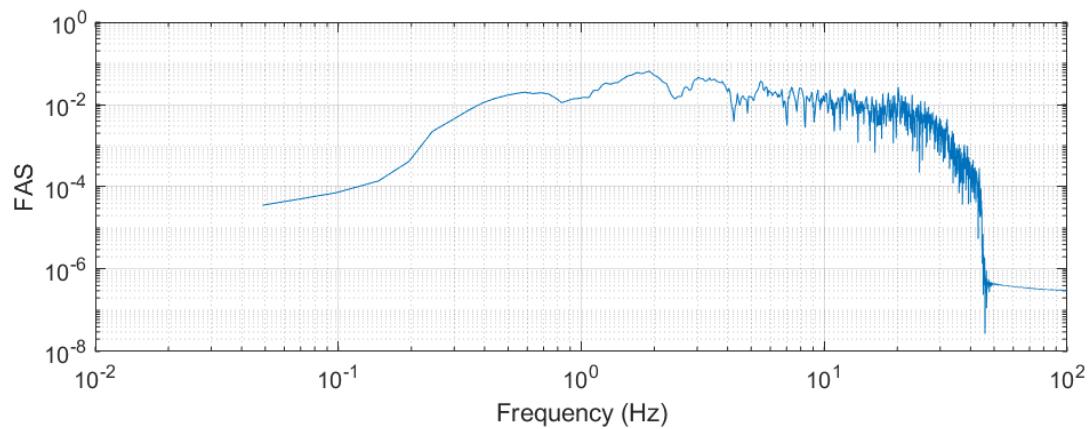


Figure 8.19 Fourier amplitude spectrum of the event Mineral 2011-08-23 (RSN8571H2)

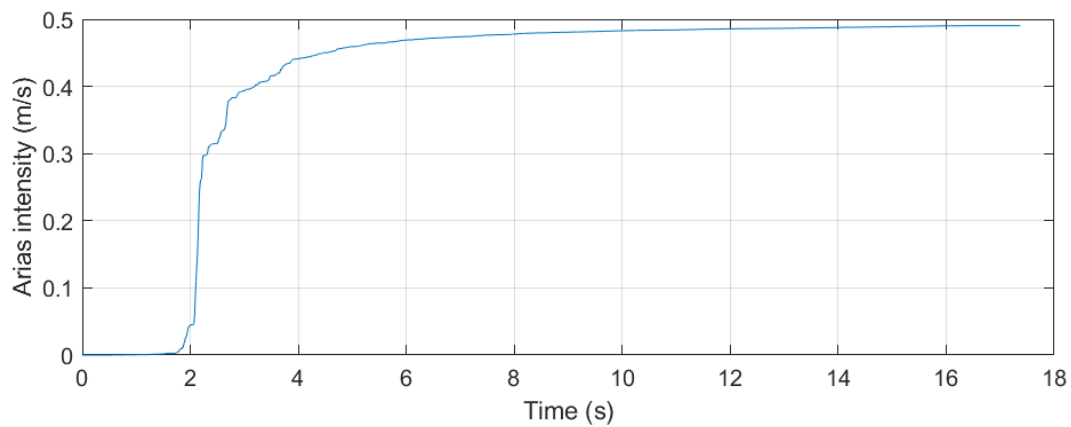


Figure 8.20 Arias intensity of the event Mineral 2011-08-23 (RSN8571H2)

**Scenario T1-2**

San Fernando, 1971,  $M_w = 6.6$ ,  $R = 19.4$  km (RSN72H1)

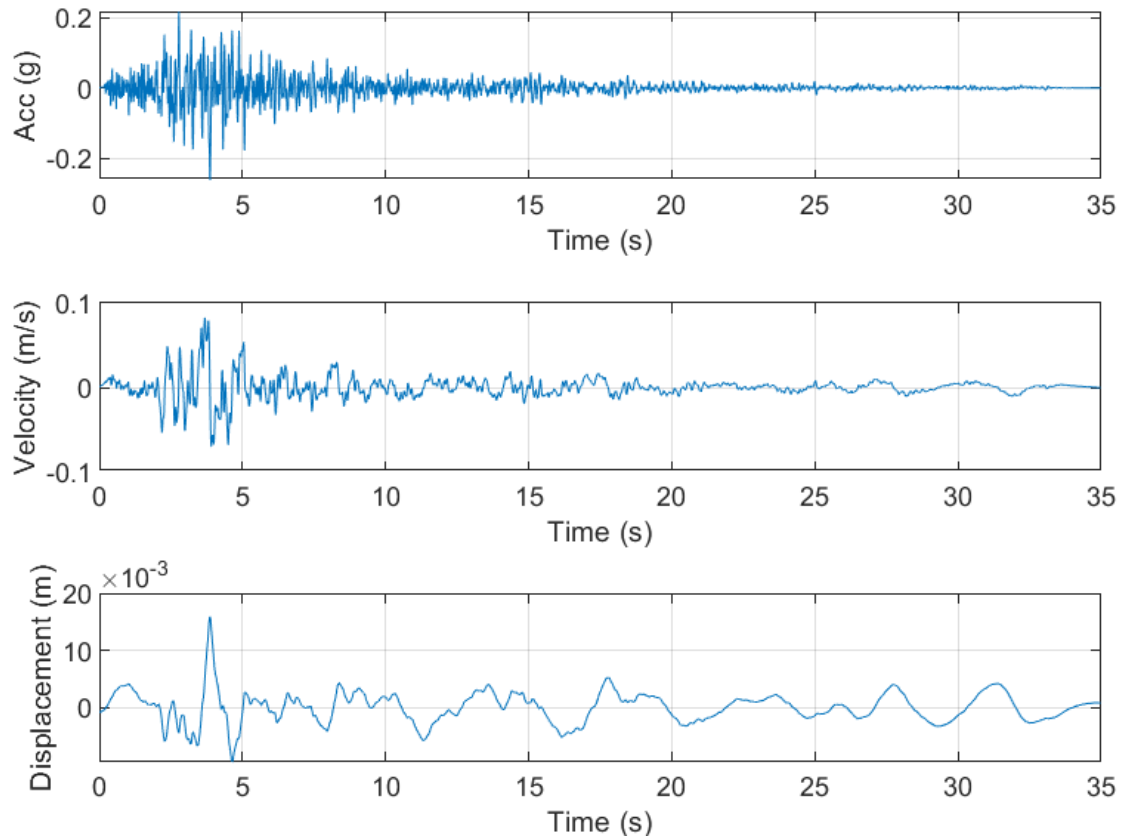


Figure 8.21 Acceleration, velocity and displacement time series of the event San Fernando (RSN72H1)

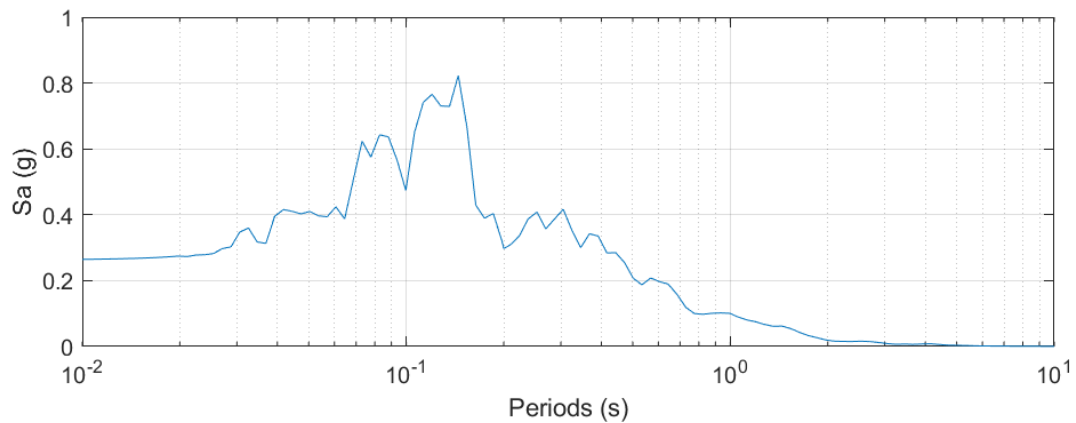


Figure 8.22 Response spectrum of the event San Fernando (RSN72H1)

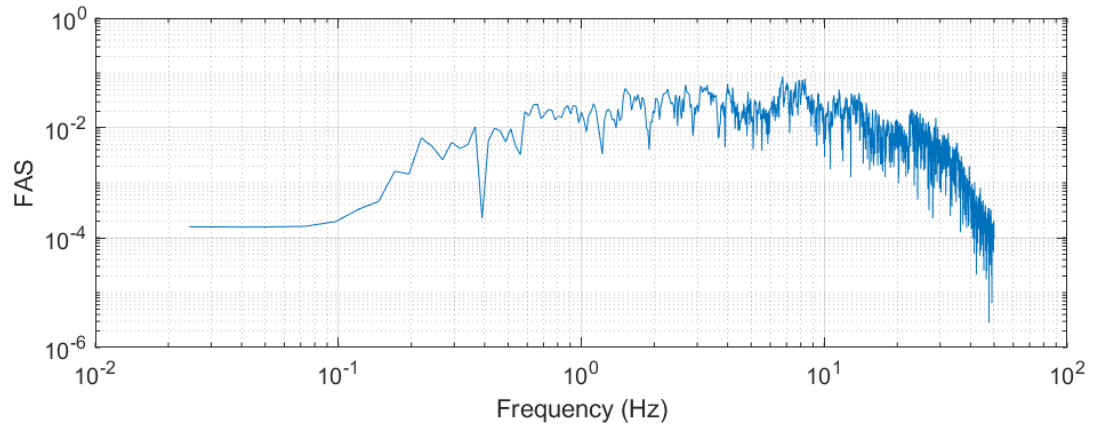


Figure 8.23 Response spectrum of the event San Fernando (RSN72H1)

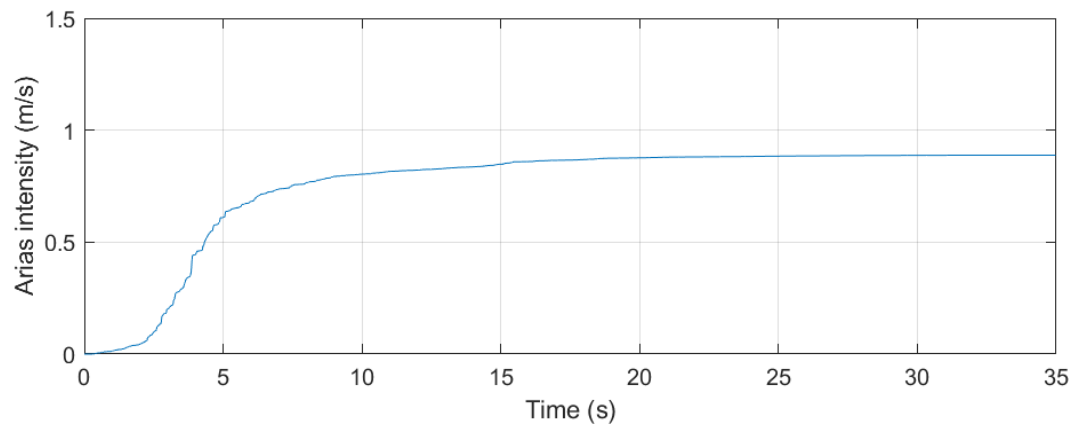


Figure 8.24 Arias intensity of the event San Fernando (RSN72H1)

San Fernando, 1971,  $M_w = 6.6$ ,  $R = 19.4$  km (RSN72H2)

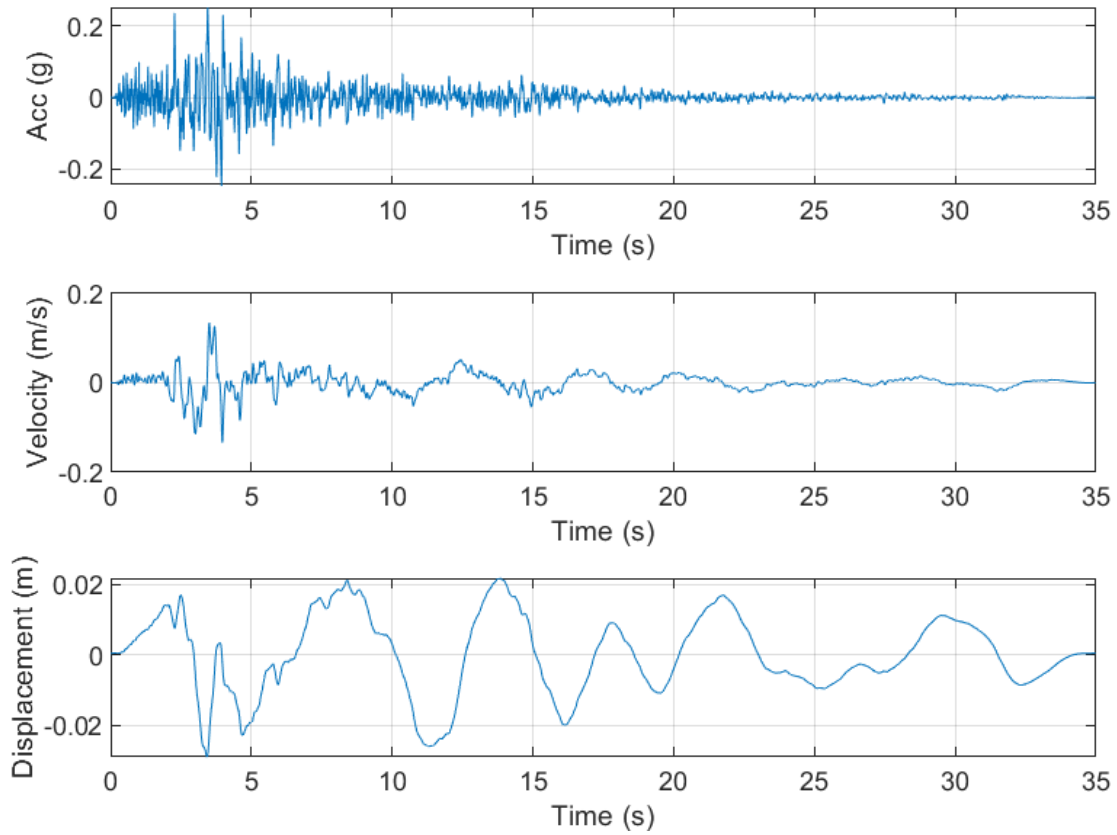


Figure 8.25 Acceleration, velocity and displacement time series of the event San Fernando (RSN72H2)

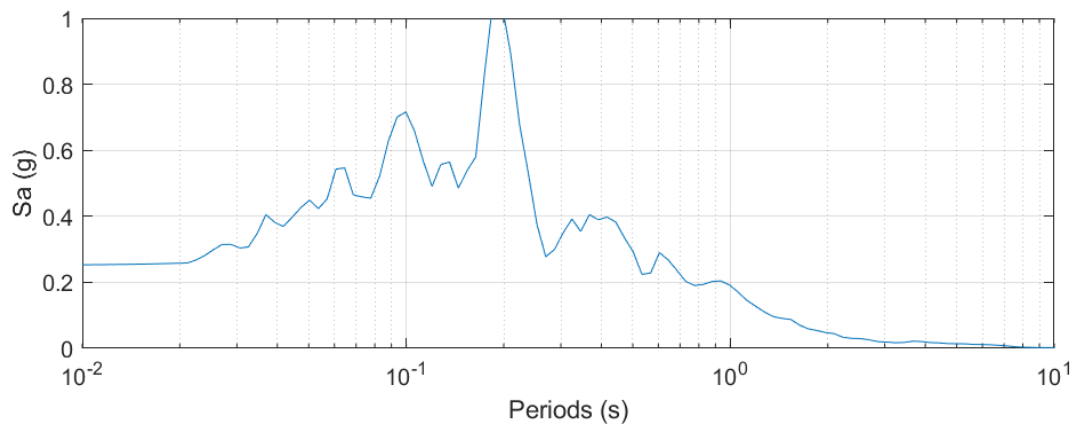


Figure 8.26 Response spectrum of the event San Fernando (RSN72H2)

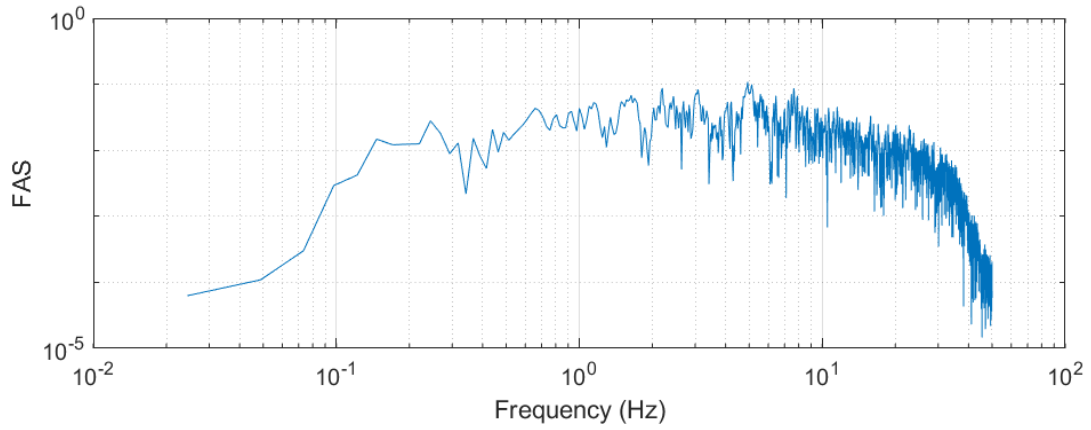


Figure 8.27 Fourier amplitude spectrum of the event San Fernando (RSN72H2)

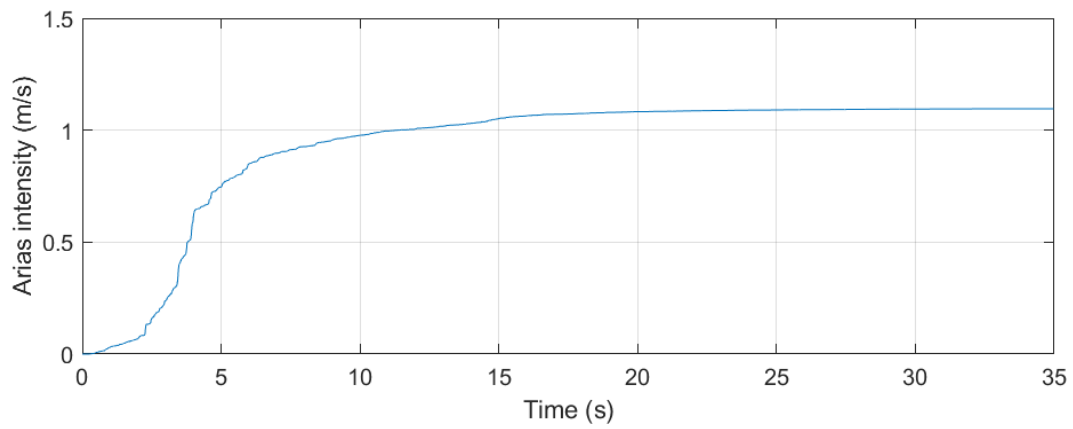


Figure 8.28 Arias intensity of the event San Fernando (RSN72H2)

San Fernando, 1971,  $M_w = 6.6$ ,  $R = 30.7$  km (RSN87H2)

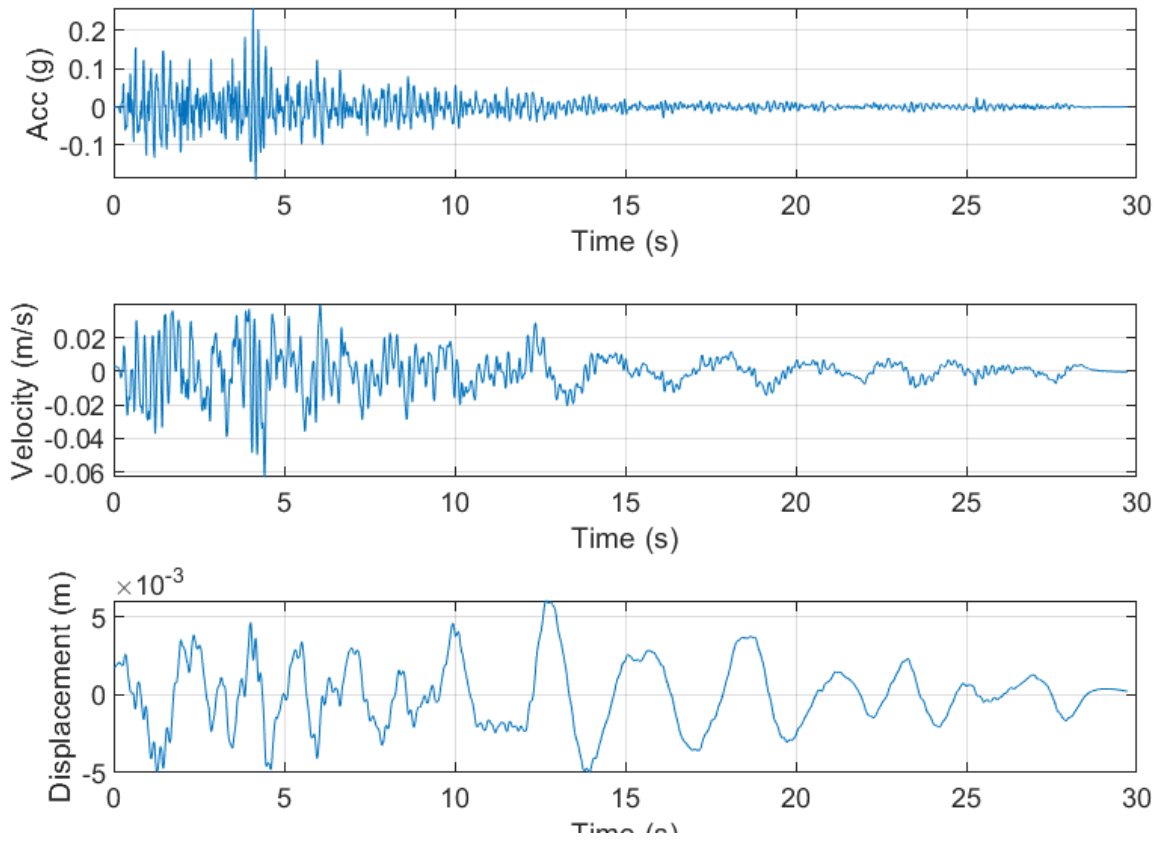


Figure 8.29 Acceleration, velocity and displacement time series of the event San Fernando (RSN87H2)

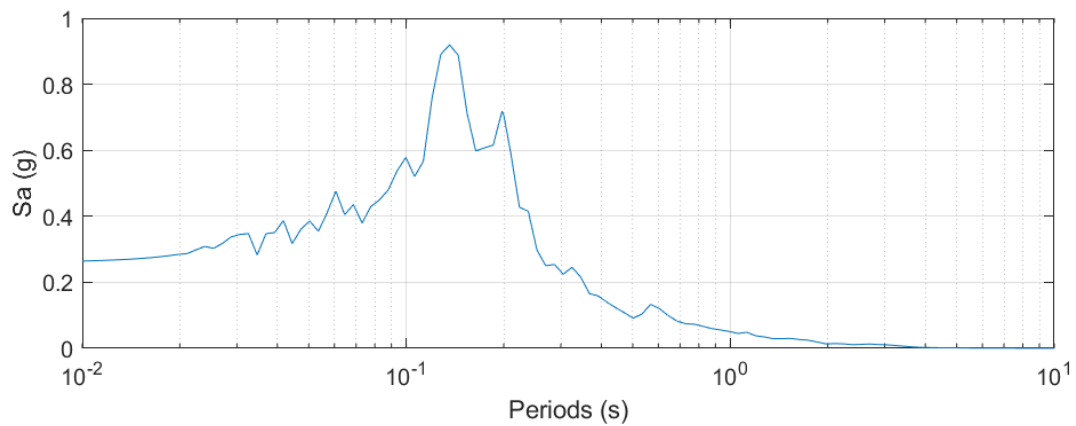


Figure 8.30 Response spectrum of the event San Fernando (RSN87H2)

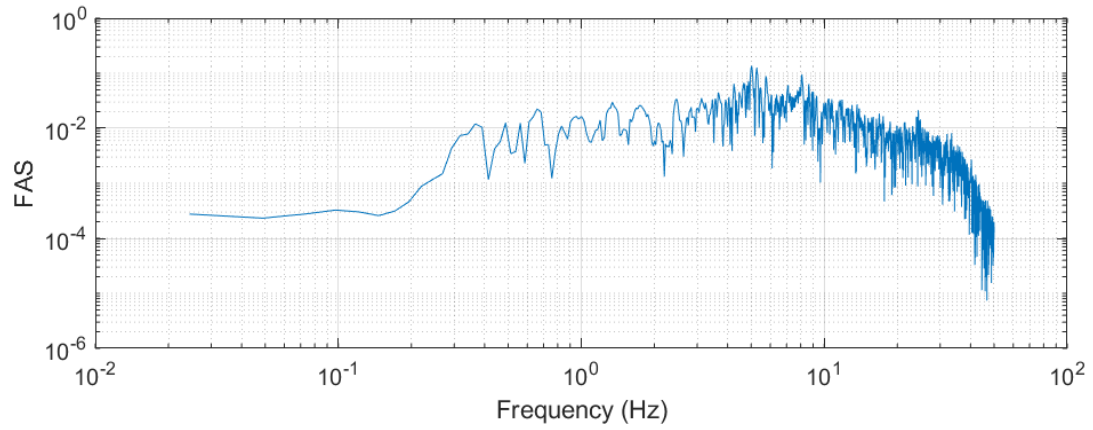


Figure 8.31 Fourier amplitude spectrum of the event San Fernando (RSN87H2)

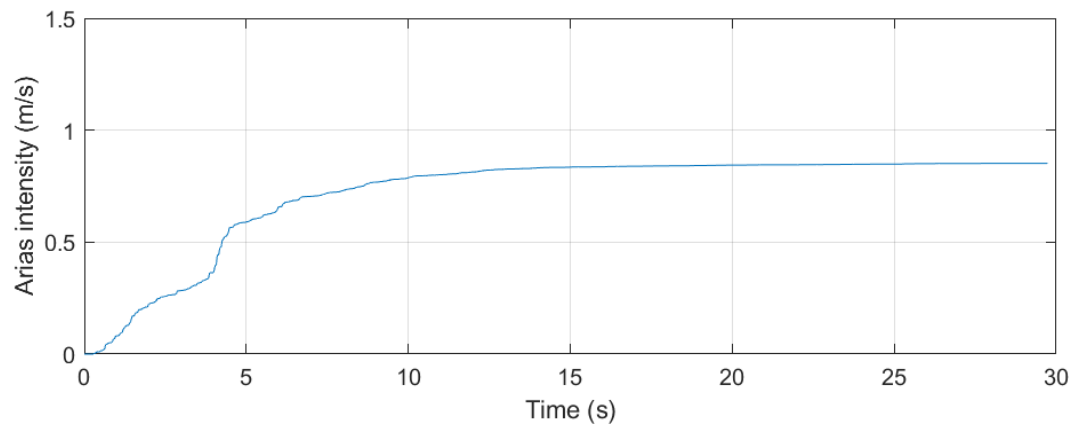


Figure 8.32 Arias intensity of the event San Fernando (RSN87H2)

Whittier Narrow – 01, 1987,  $M_w = 6.0$ ,  $R = 22.5$  km (RSN598H2)

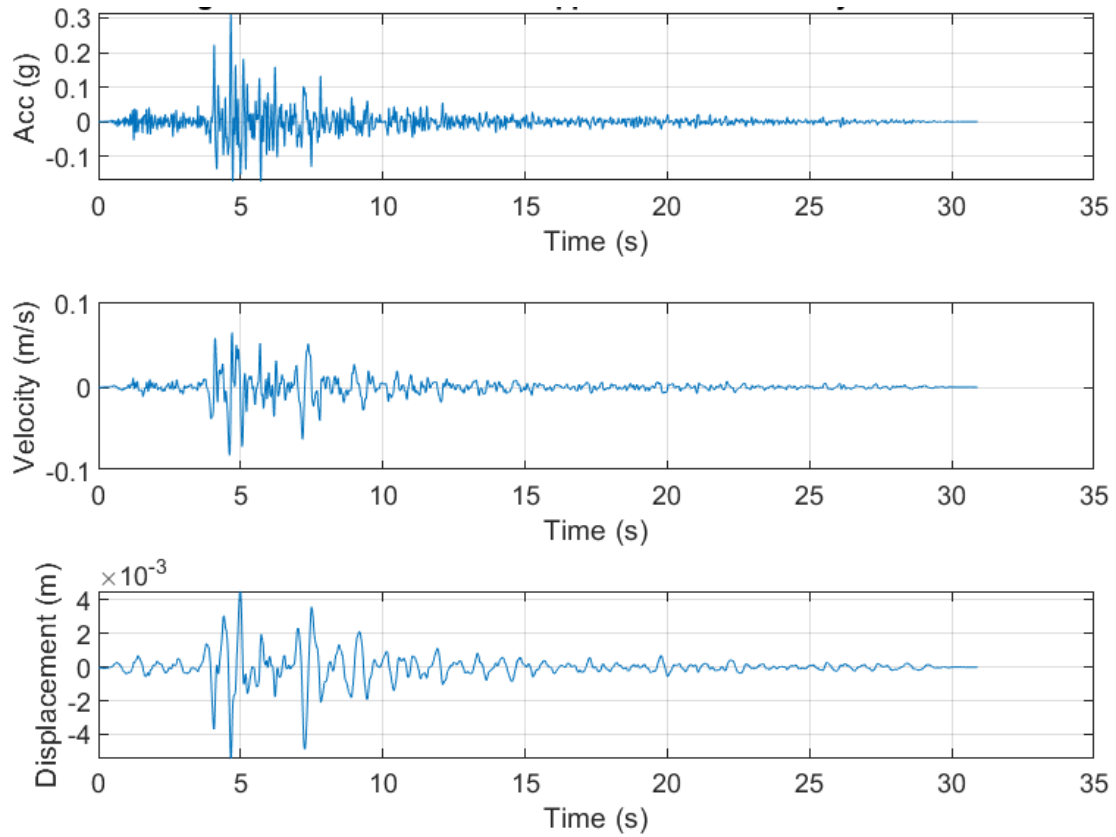


Figure 8.33 Acceleration, velocity and displacement of the event Whittier Narrow – 01 (RSN598H2)

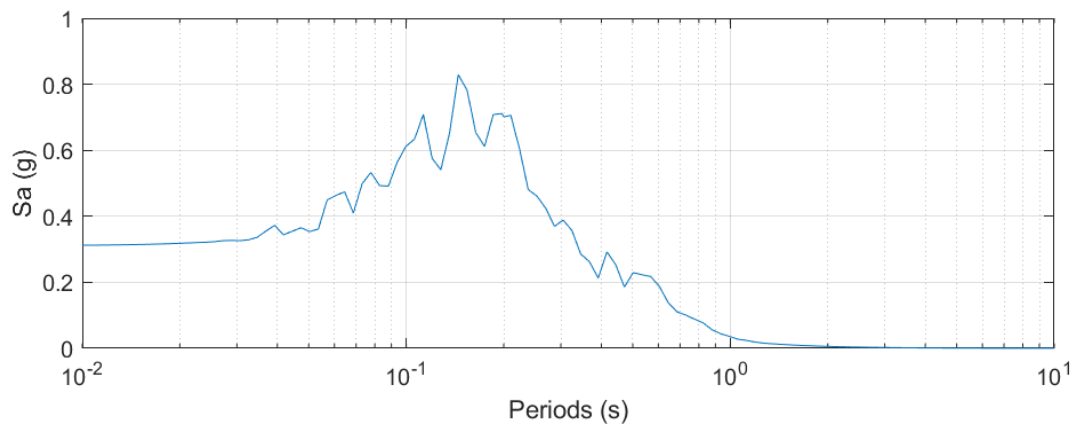


Figure 8.34 Response spectrum of the event Whittier Narrow – 01 (RSN598H2)

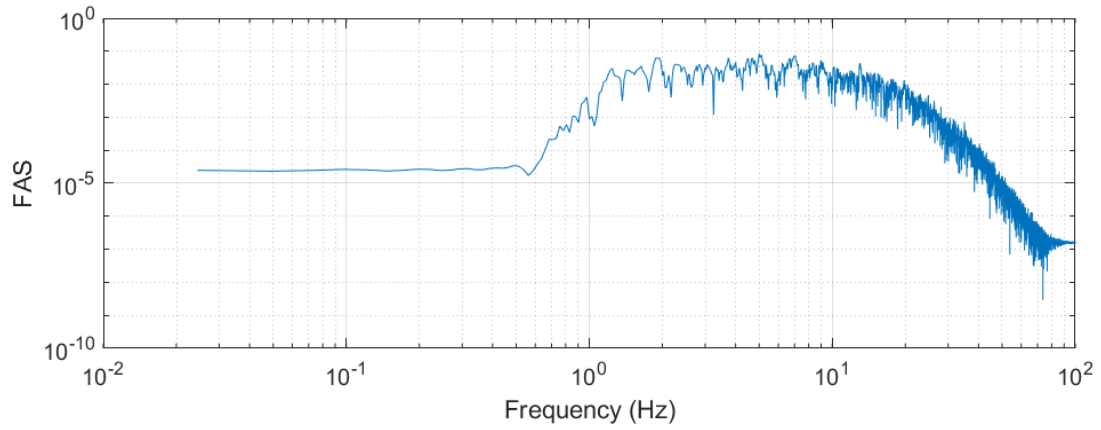


Figure 8.35 Fourier amplitude spectrum of the event Whittier Narrow - 01 (RSN598H2)

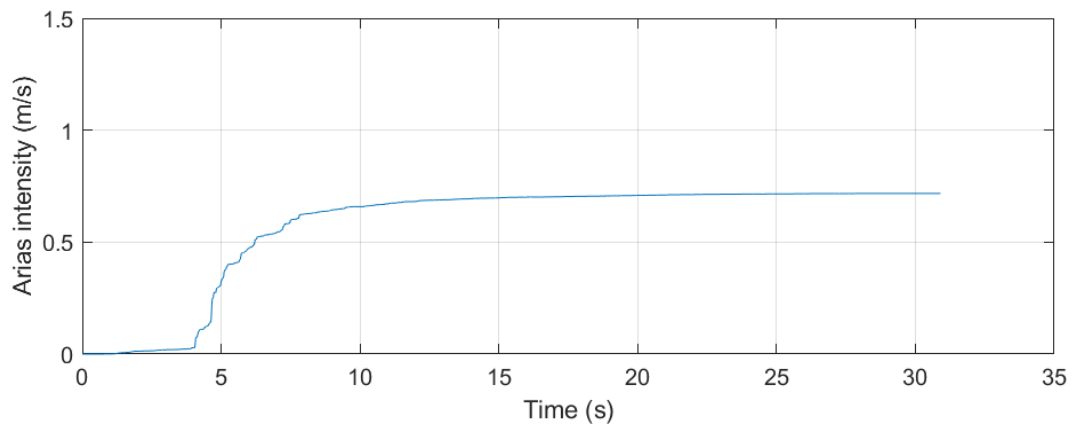


Figure 8.36 Arias intensity of the event Whittier Narrow - 01 (RSN598H2)

Big Bear – 01, 1992m  $M_w = 6.5$ ,  $R = 37.0$  km (RSN935H1)

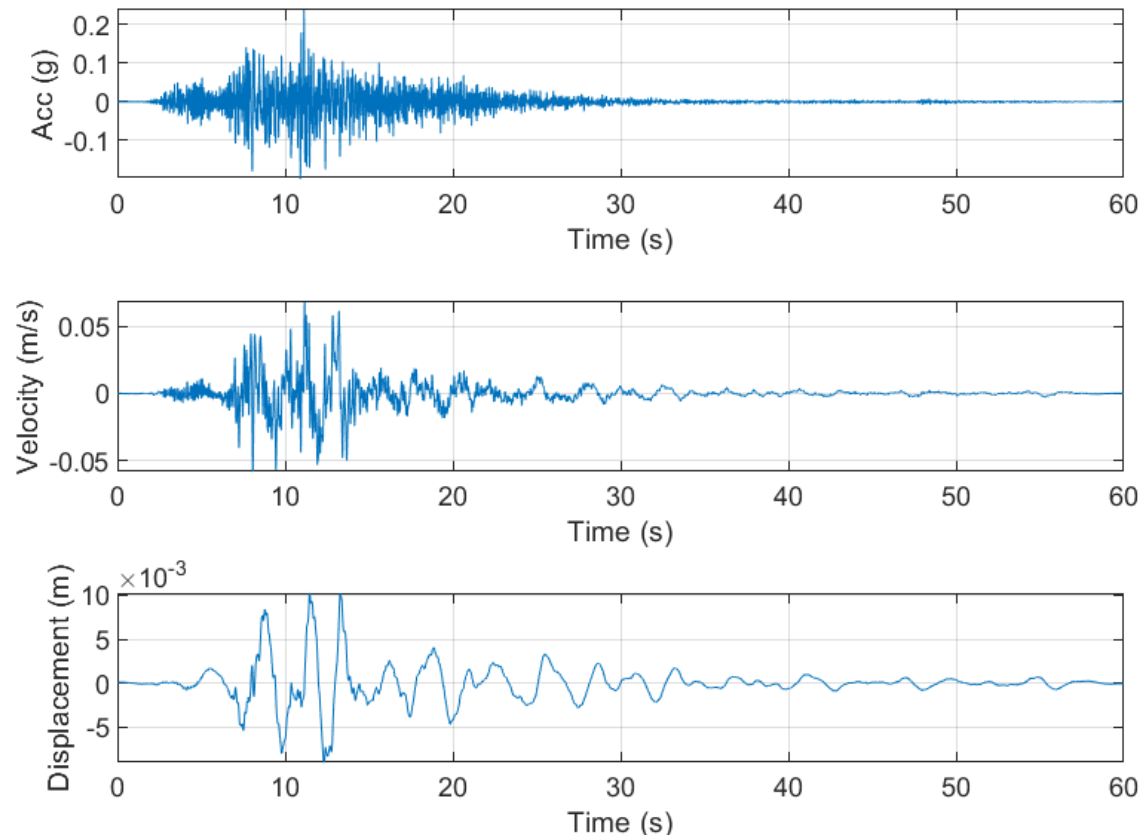


Figure 8.37 Acceleration, velocity and displacement time series of the event Big Bear – 01 (RSN935H1)

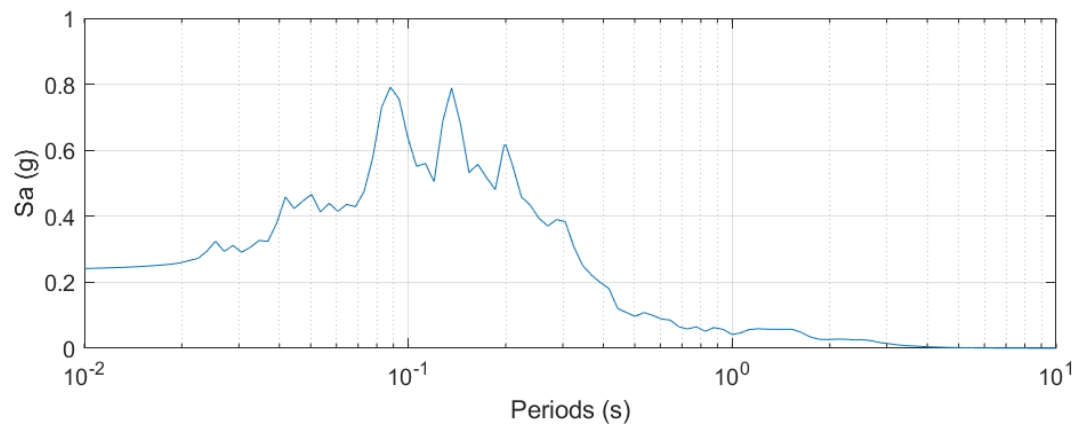


Figure 8.38 Response spectrum of the event Big Bear – 01 (RSN935H1)

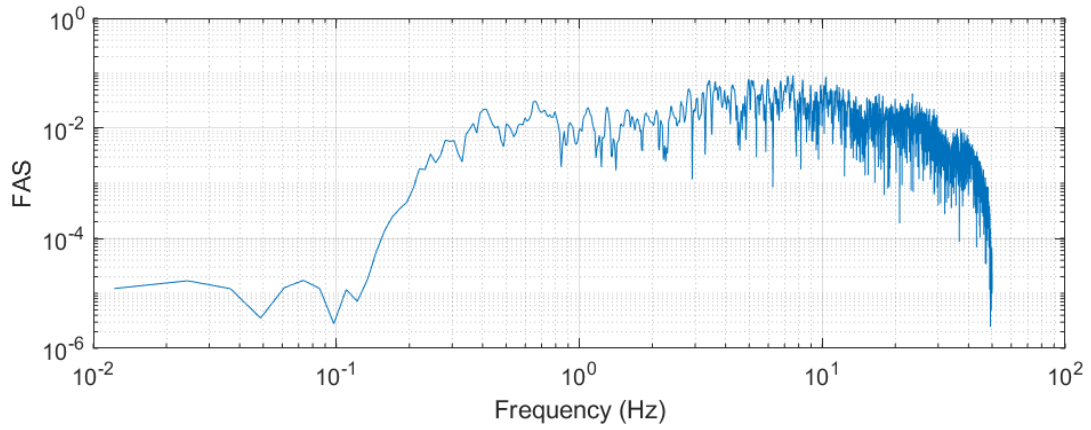


Figure 8.39 Fourier amplitude spectrum of the event Big Bear – 01 (RSN935H1)

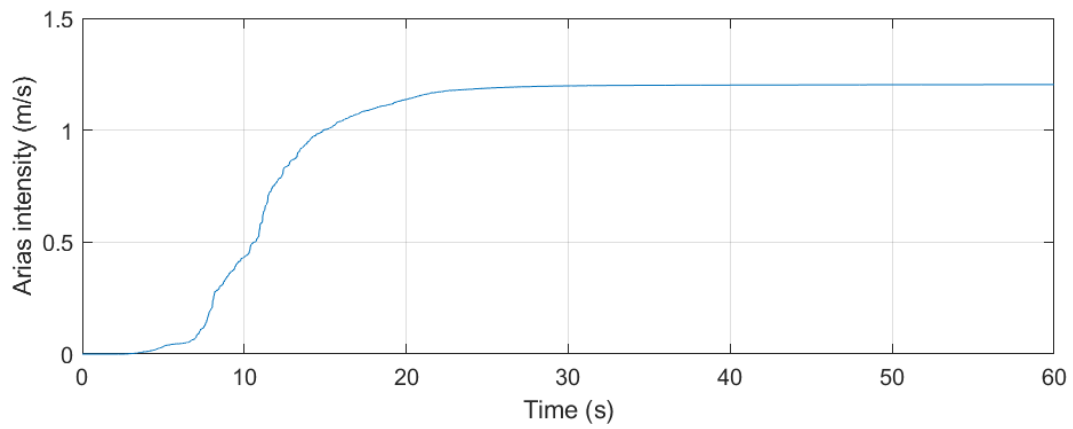


Figure 8.40 Arias intensity of the event Big Bear – 01 (RSN935H1)

Whittier Narrow – 01, 1987,  $M_w = 6.0$ ,  $R = 31.6$  km (RSN671H1)

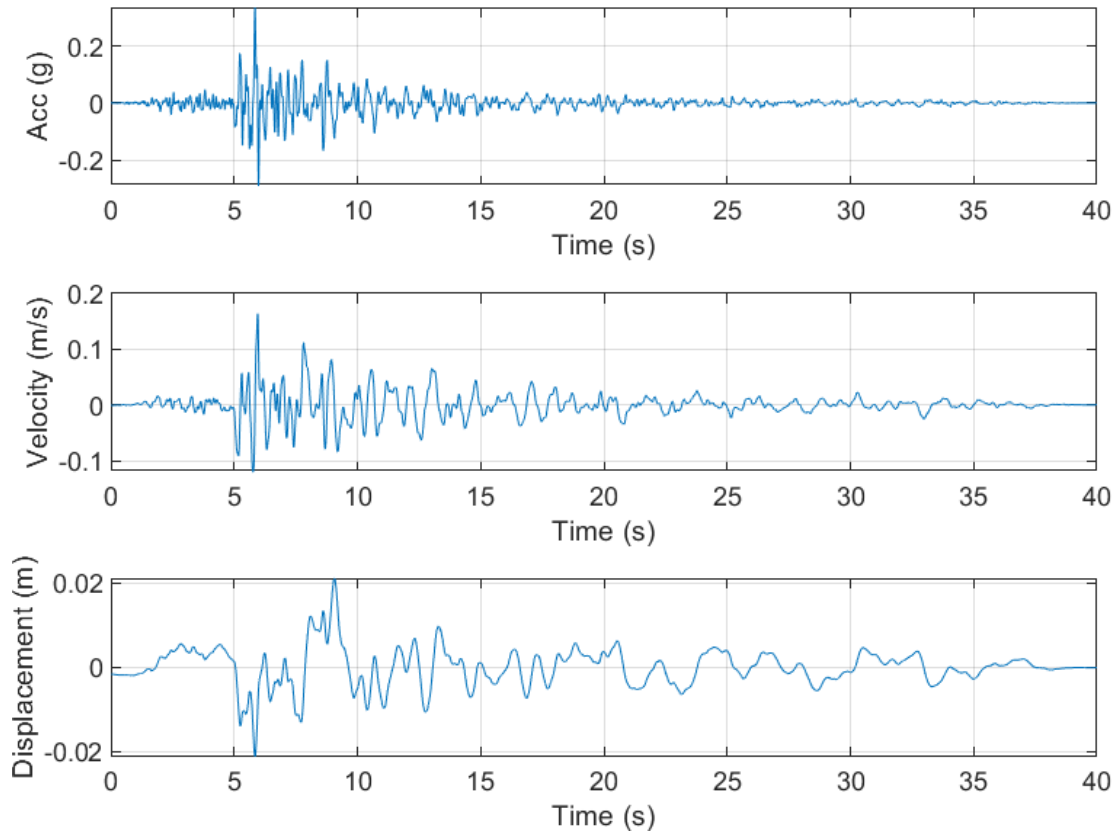


Figure 8.41 Acceleration, velocity and displacement time series of the event Whittier Narrow – 01 (RSN671H1)

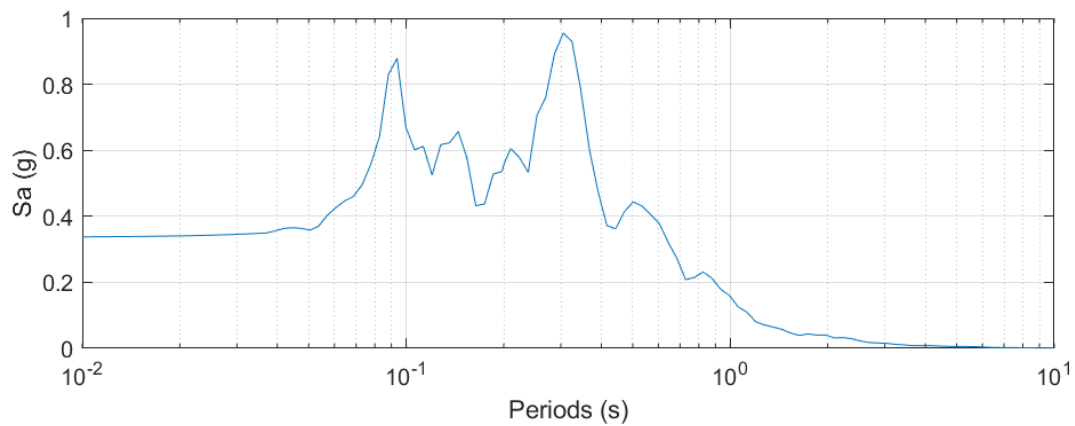


Figure 8.42 Response spectrum of the event Whittier Narrow – 01 (RSN671H1)

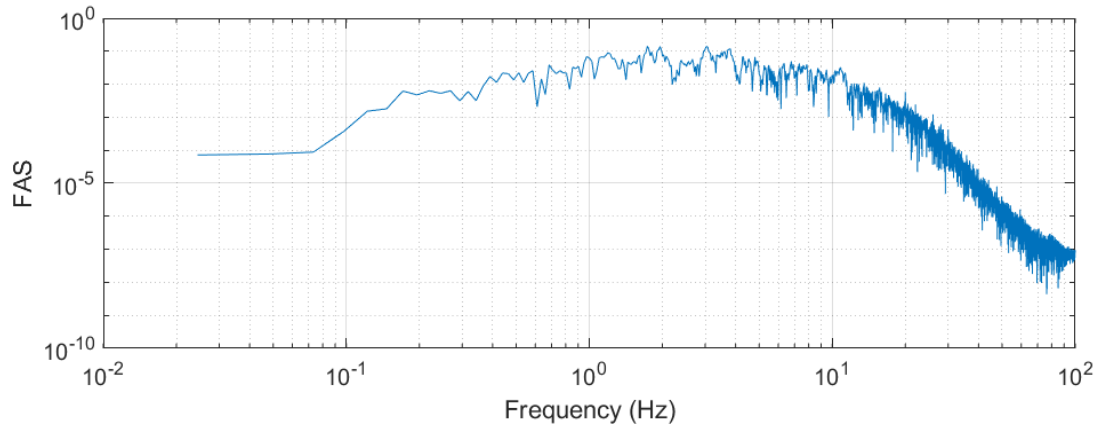


Figure 8.43 Fourier amplitude spectrum of the event Whittier Narrow – 01 (RSN671H1)

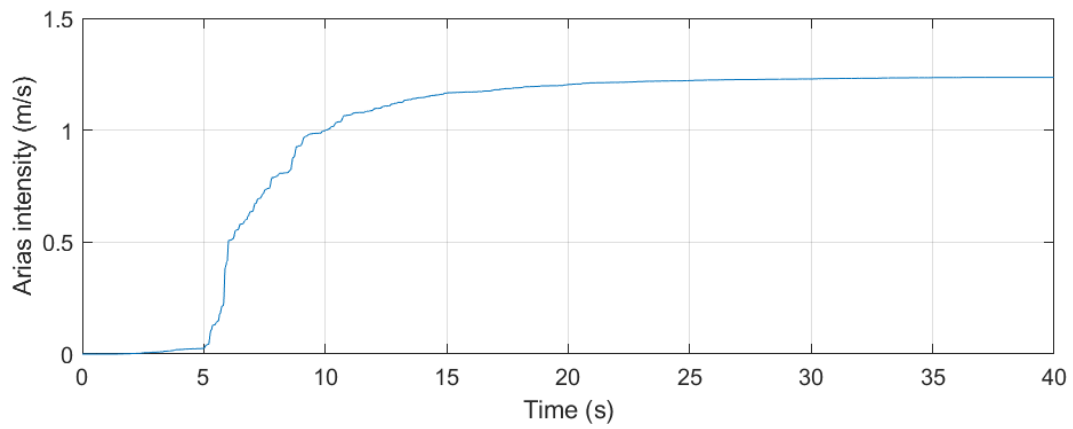


Figure 8.44 Arias intensity of the event Whittier Narrow – 01 (RSN671H1)

**Scenario T2-1**

San Fernando, 1971,  $M_w = 6.6$ ,  $R = 19.4$  km (RSN72H2)

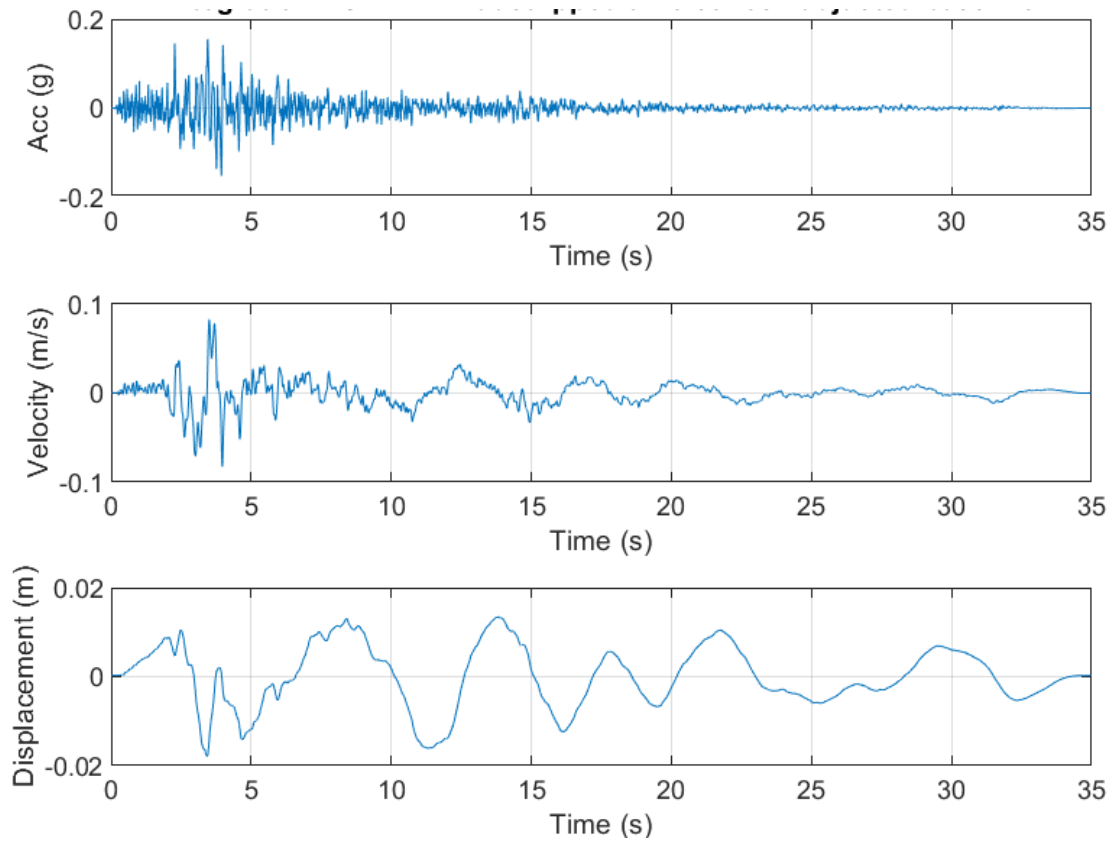


Figure 8.45 Acceleration, velocity and displacement time series of the record San Fernando (RSN72H2)

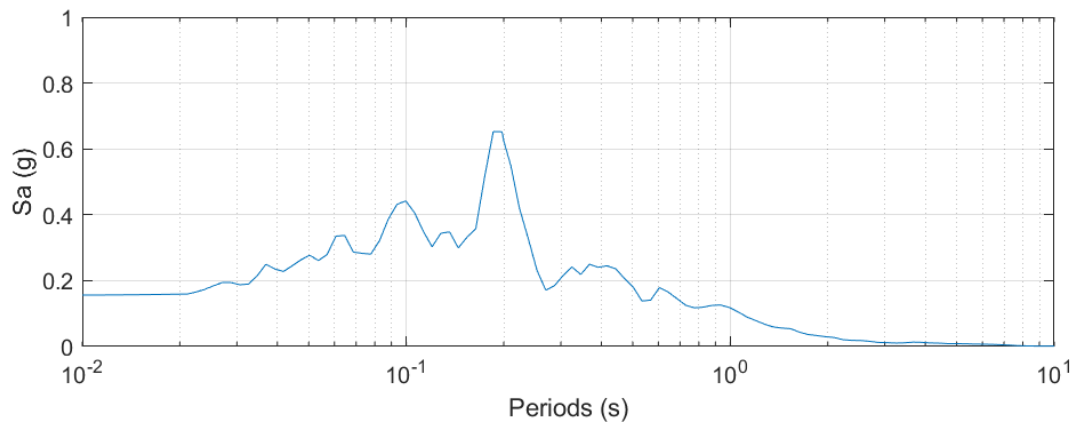


Figure 8.46 Response spectrum of the record San Fernando (RSN72H2)

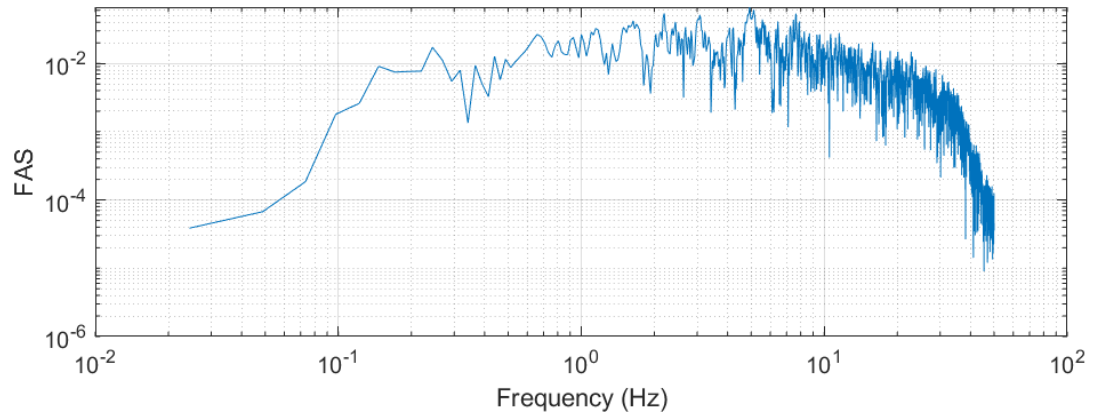


Figure 8.47 Fourier amplitude spectrum of the record San Fernando (RSN72H2)

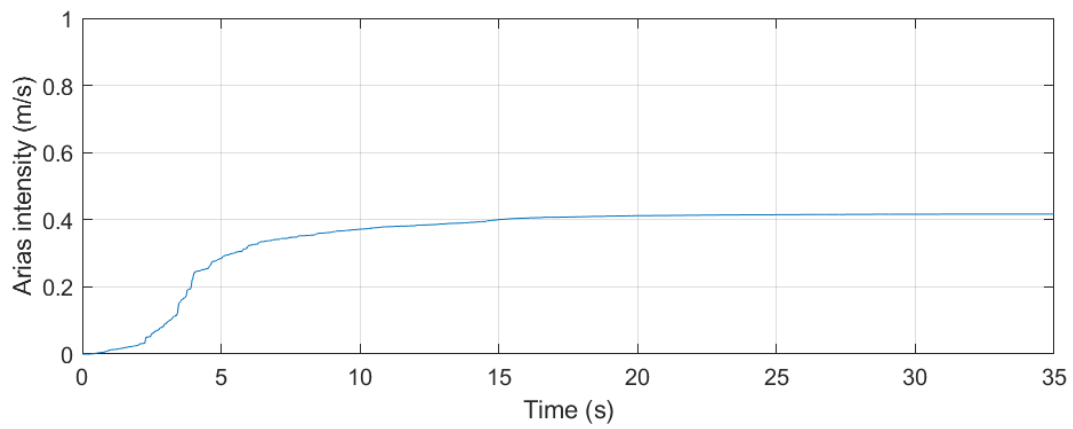


Figure 8.48 Arias intensity of the record San Fernando (RSN72H2)

North Palm Springs, 1986,  $M_w = 6.1$ ,  $R = 38.2$  km (RSN511H1)

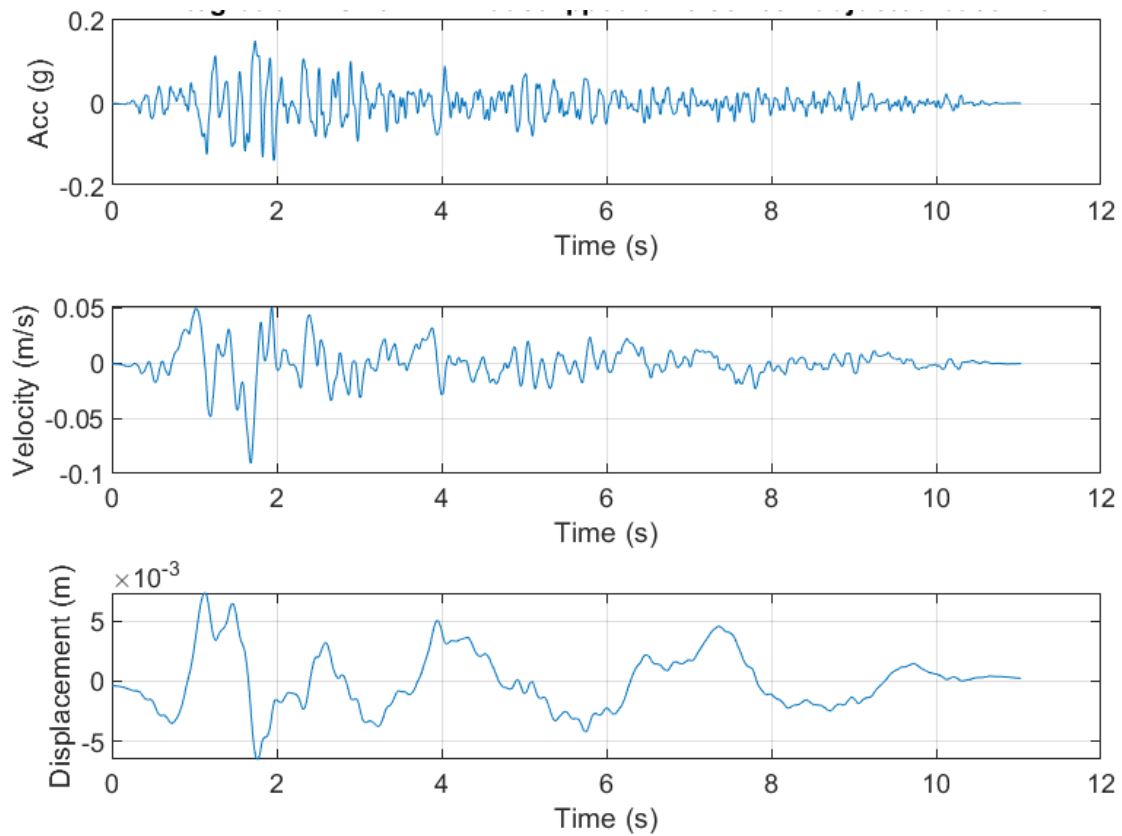


Figure 8.49 Acceleration, velocity and displacement time series of the record North Palm Springs (RSN511H1)

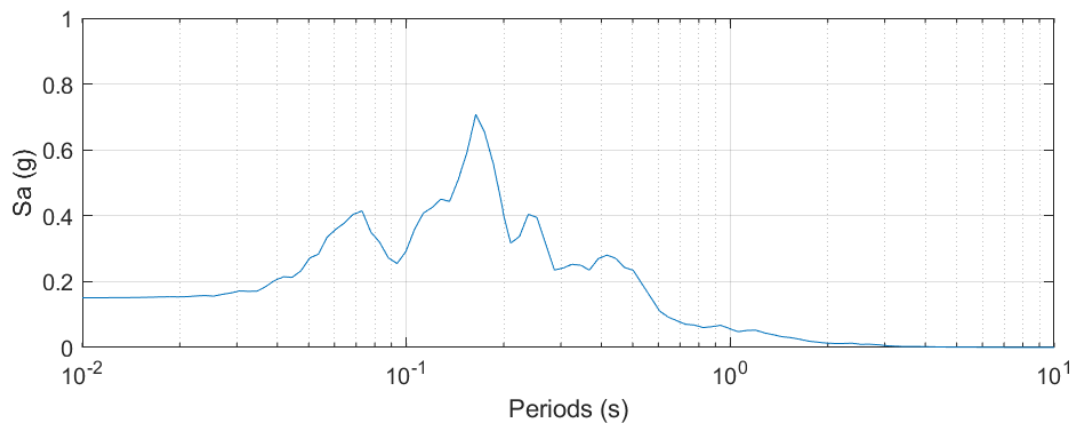


Figure 8.50 Response spectrum of the record North Palm Springs (RSN511H1)

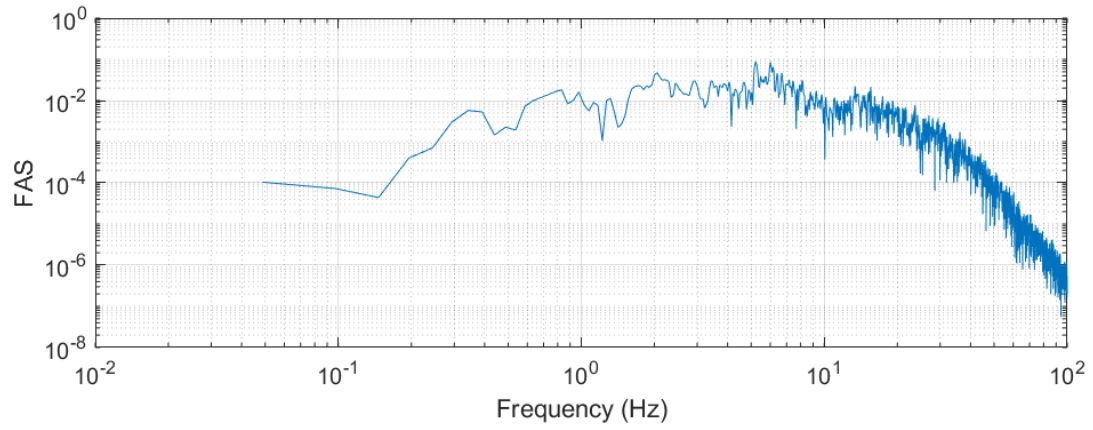


Figure 8.51 Fourier amplitude spectrum of the record North Palm Springs (RSN511H1)

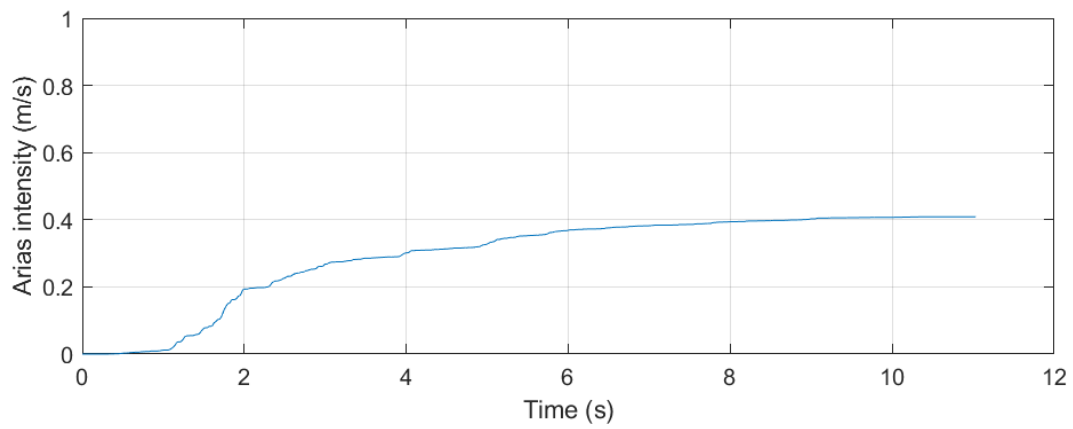


Figure 8.52 Arias intensity of the record North Palm Springs (RSN511H1)

Whittier Narrows – 01, 1987,  $M_w = 6.0$ ,  $R = 22.5$  km (RSN598H2)

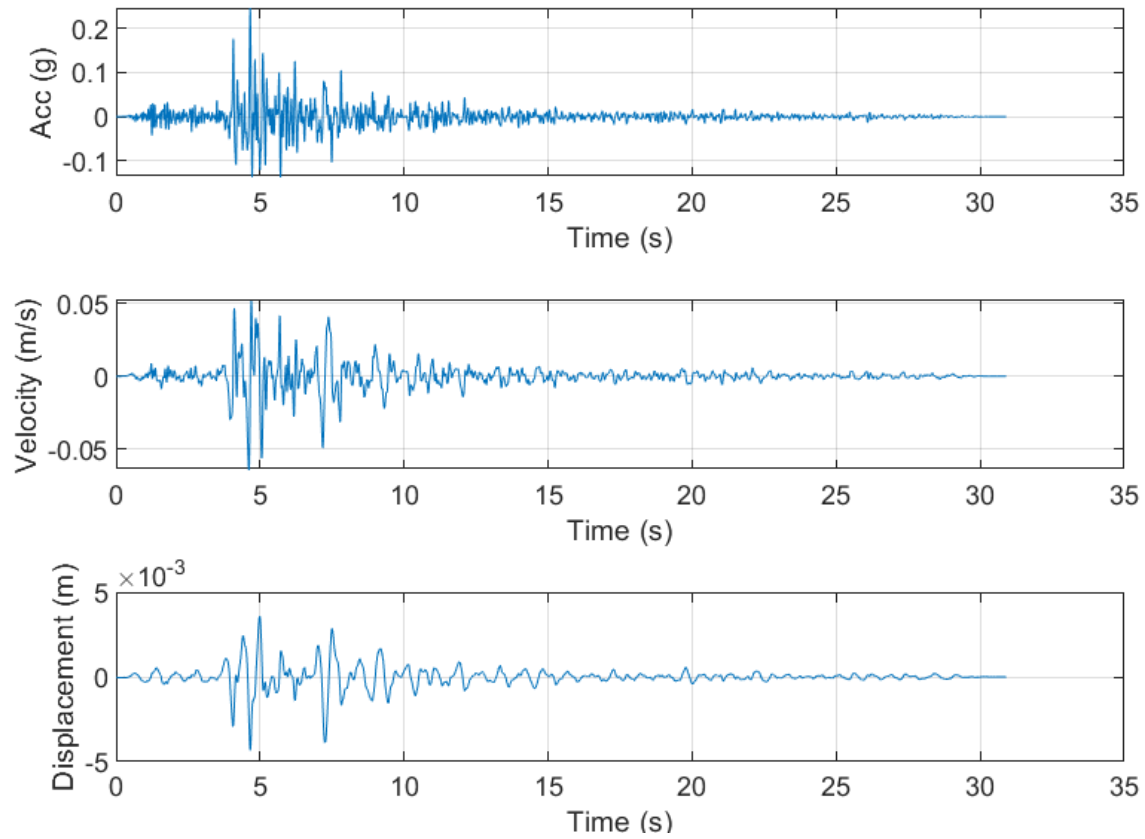


Figure 8.53 Acceleration, velocity and displacement time series of the event Whittier Narrows – 01 (RSN598H2)

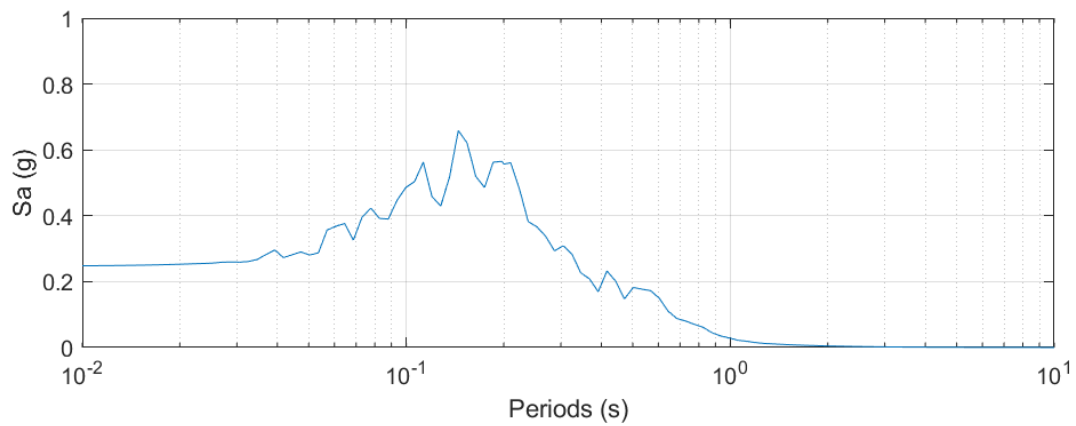


Figure 8.54 Response spectrum of the event Whittier Narrows – 01 (RSN598H2)

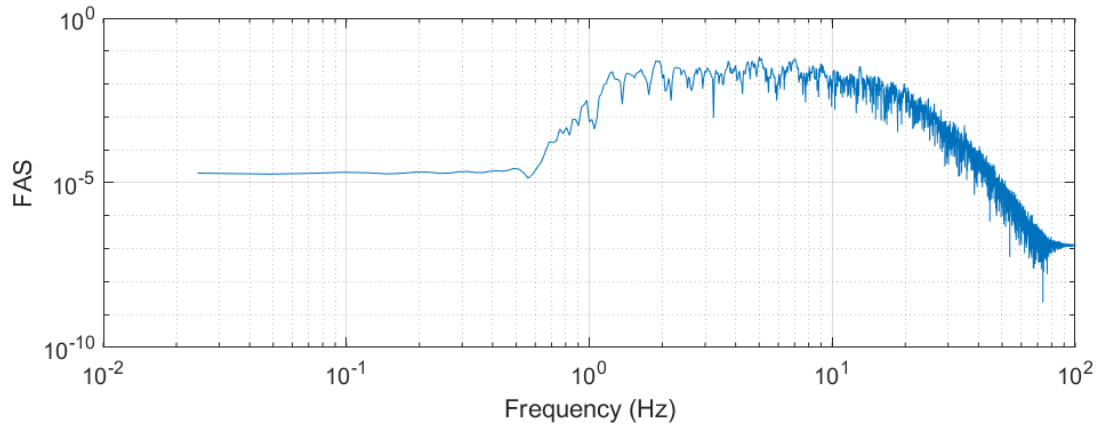


Figure 8.55 Fourier amplitude spectrum of the event Whittier Narrows – 01 (RSN598H2)

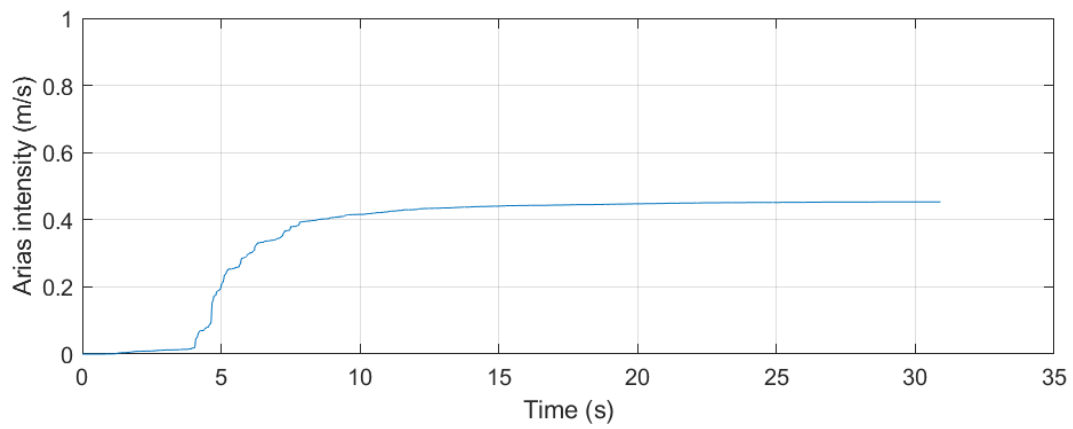


Figure 8.56 Arias intensity of the event Whittier Narrows – 01 (RSN598H2)

Northridge – 01, 1994,  $M_w = 6.7$ ,  $R = 19.1$  km (RSN954H1)

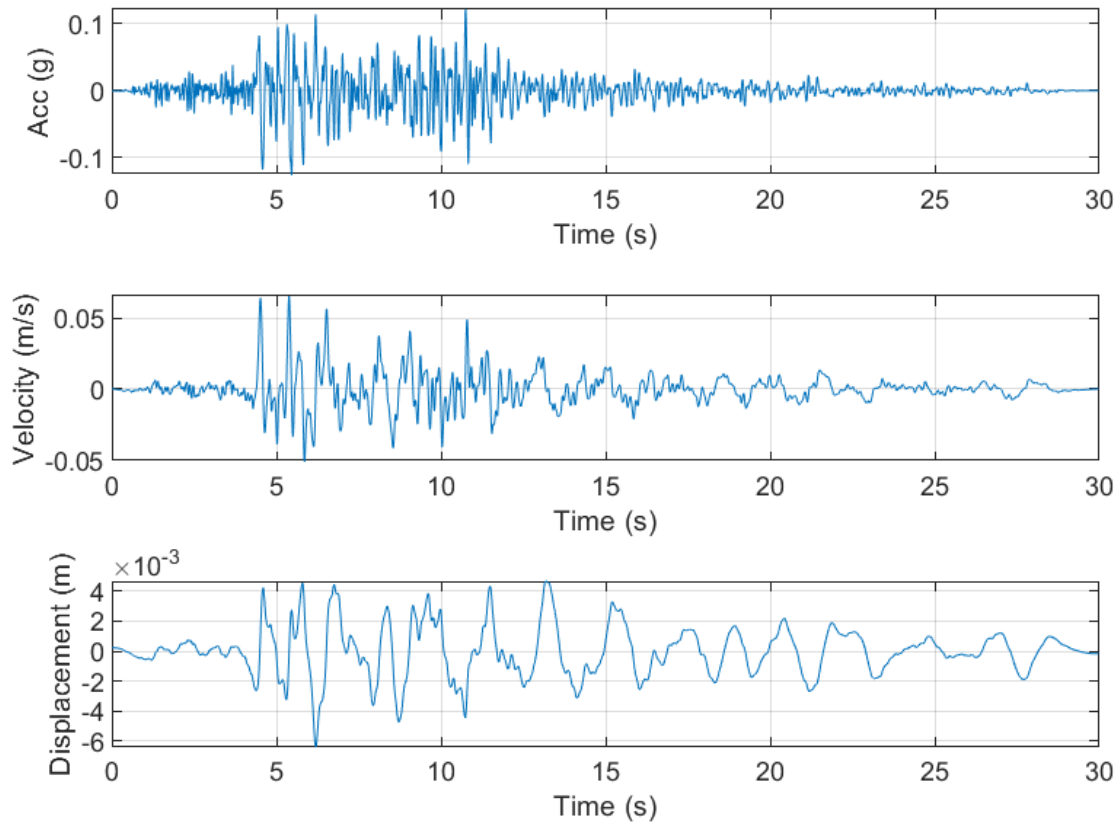


Figure 8.57 Acceleration, velocity and displacement time series of the event Northridge (RSN954H1)

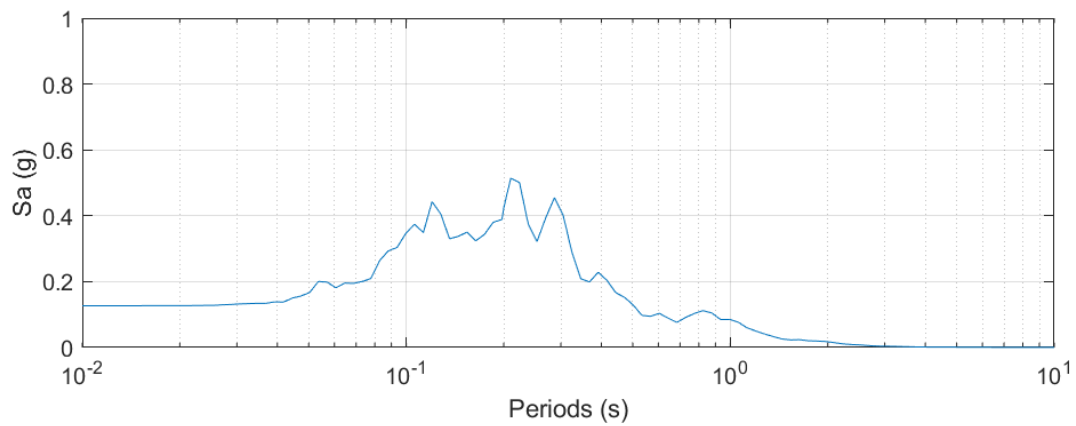


Figure 8.58 Response spectrum of the event Northridge (RSN954H1)

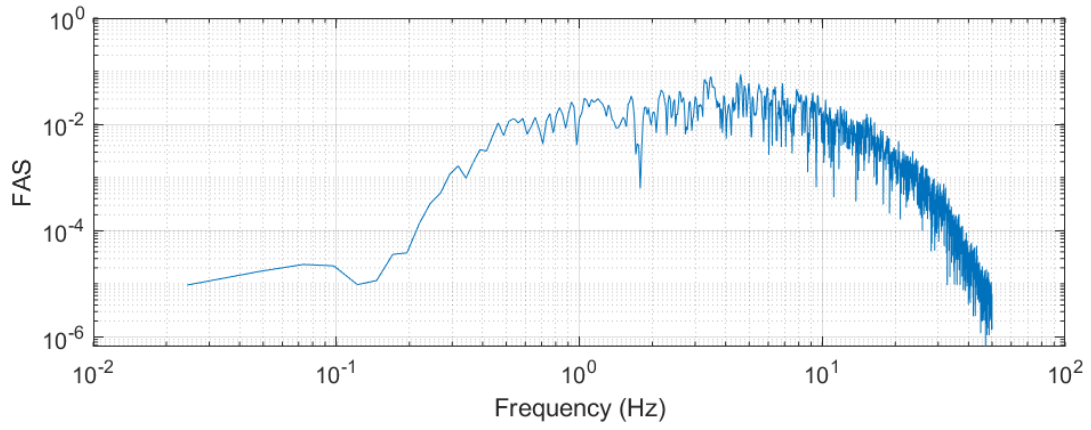


Figure 8.59 Fourier amplitude spectrum of the event Northridge (RSN954H1)

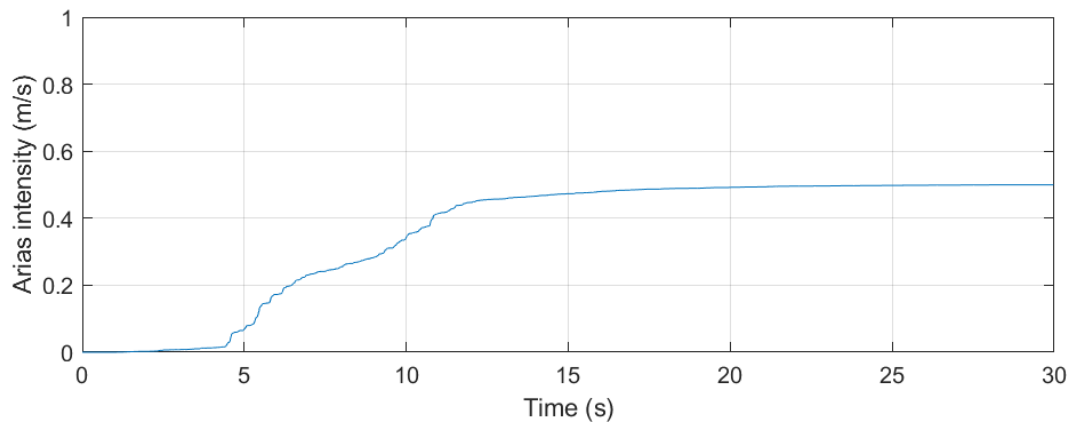


Figure 8.60 Arias intensity of the event Northridge (RSN954H1)

San Simeon, California, 2003,  $M_w = 6.2$ ,  $R = 31.3$  km (RSN4016H1)

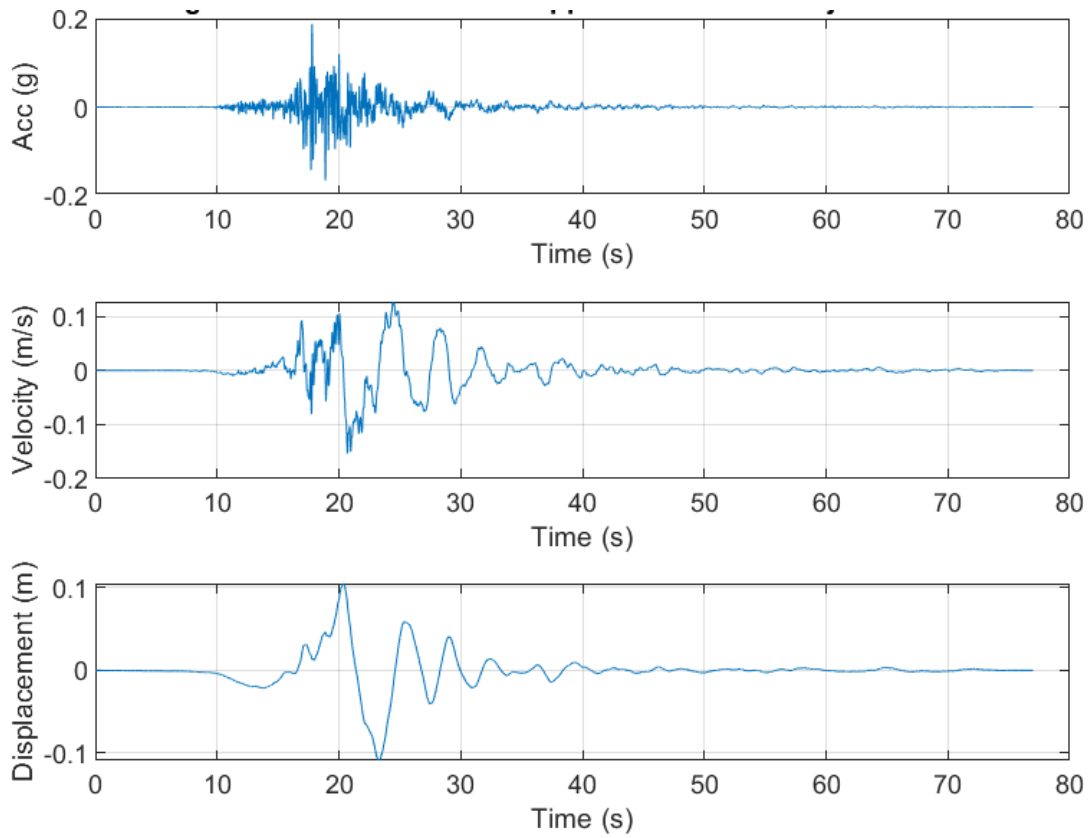


Figure 8.61 Acceleration, velocity and displacement time series of the event San Simeon (RSN4016H1)

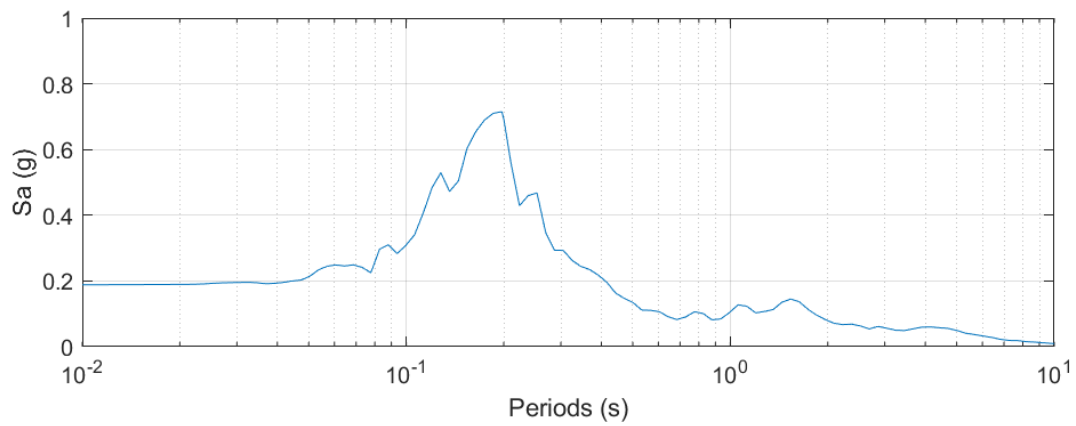


Figure 8.62 Response spectrum of the event San Simeon (RSN4016H1)

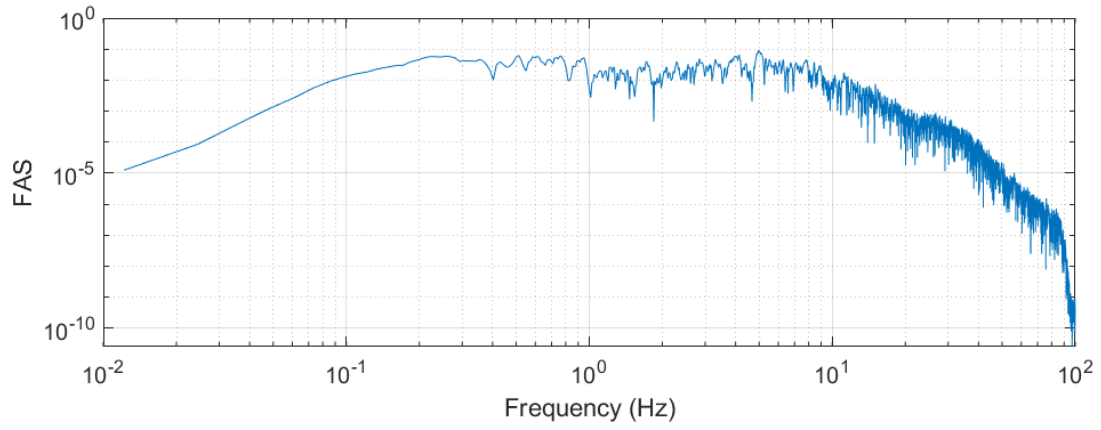


Figure 8.63 Fourier amplitude spectrum of the event San Simeon (RSN4016H1)

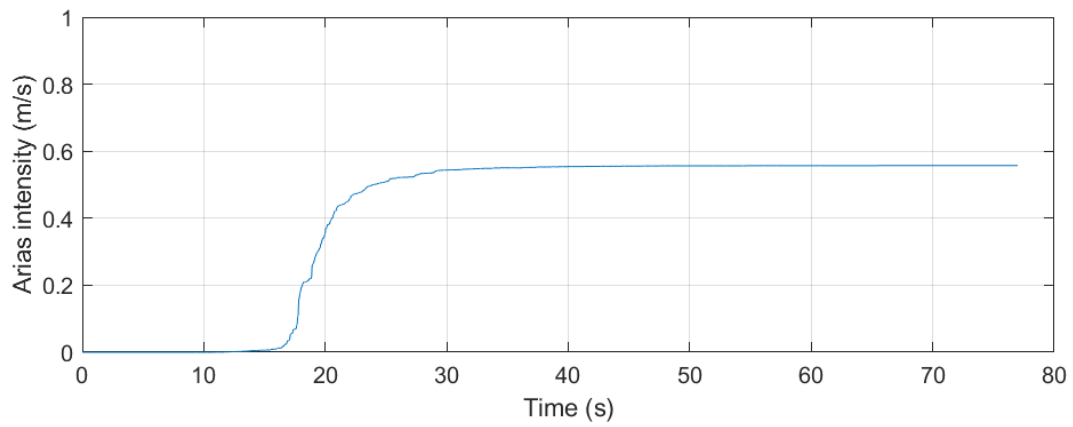


Figure 8.64 Arias intensity of the event San Simeon (RSN4016H1)

**Scenario T3-1**

Irpinia, Italy – 01, 1980,  $M_w = 6.9$ ,  $R = 59.6$  km (RSN293H2)

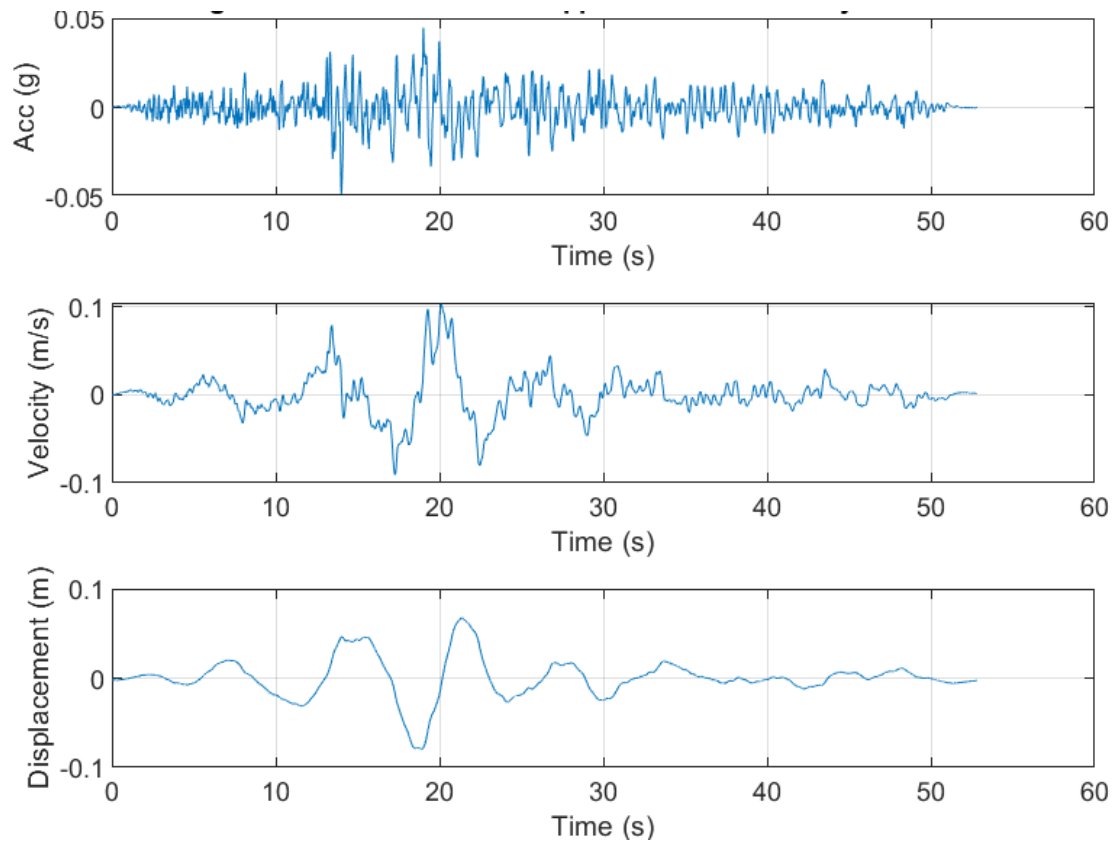


Figure 8.65 Acceleration, velocity and displacement time series of the event Irpinia, Italy (RSN293H2)

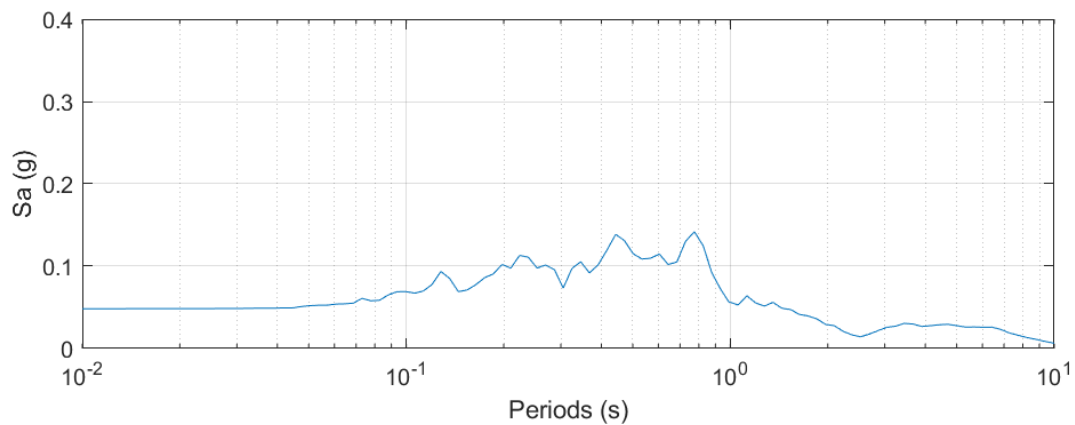


Figure 8.66 Response spectrum of the event Irpinia, Italy (RSN293H2)

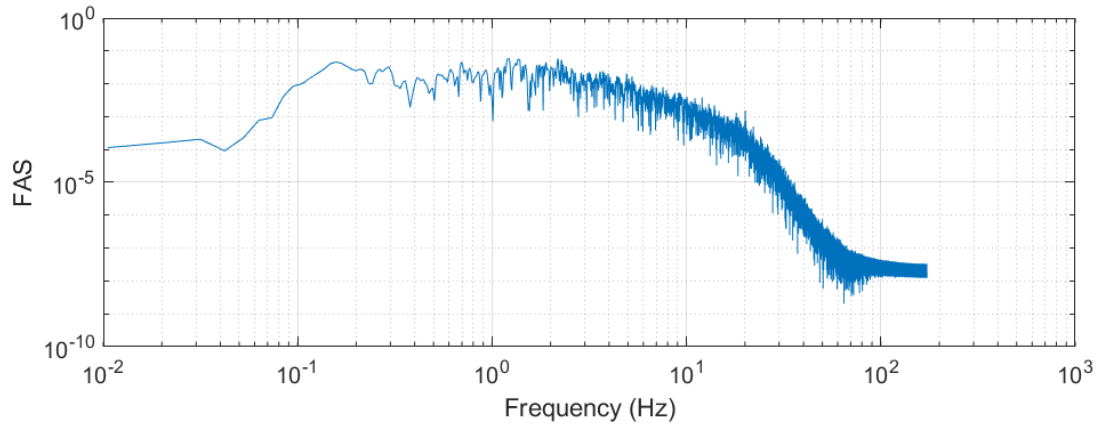


Figure 8.67 Fourier amplitude spectrum of the event Irpinia, Italy (RSN293H2)

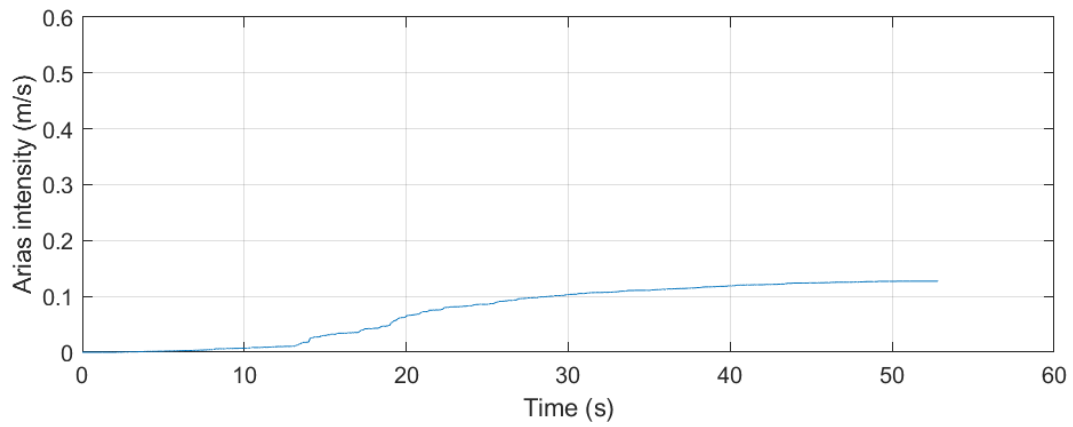


Figure 8.68 Arias intensity of the event Irpinia, Italy (RSN293H2)

Irpinia, Italy – 01, 1980,  $M_w = 6.9$ ,  $R = 59.6$  km (RSN294H2)

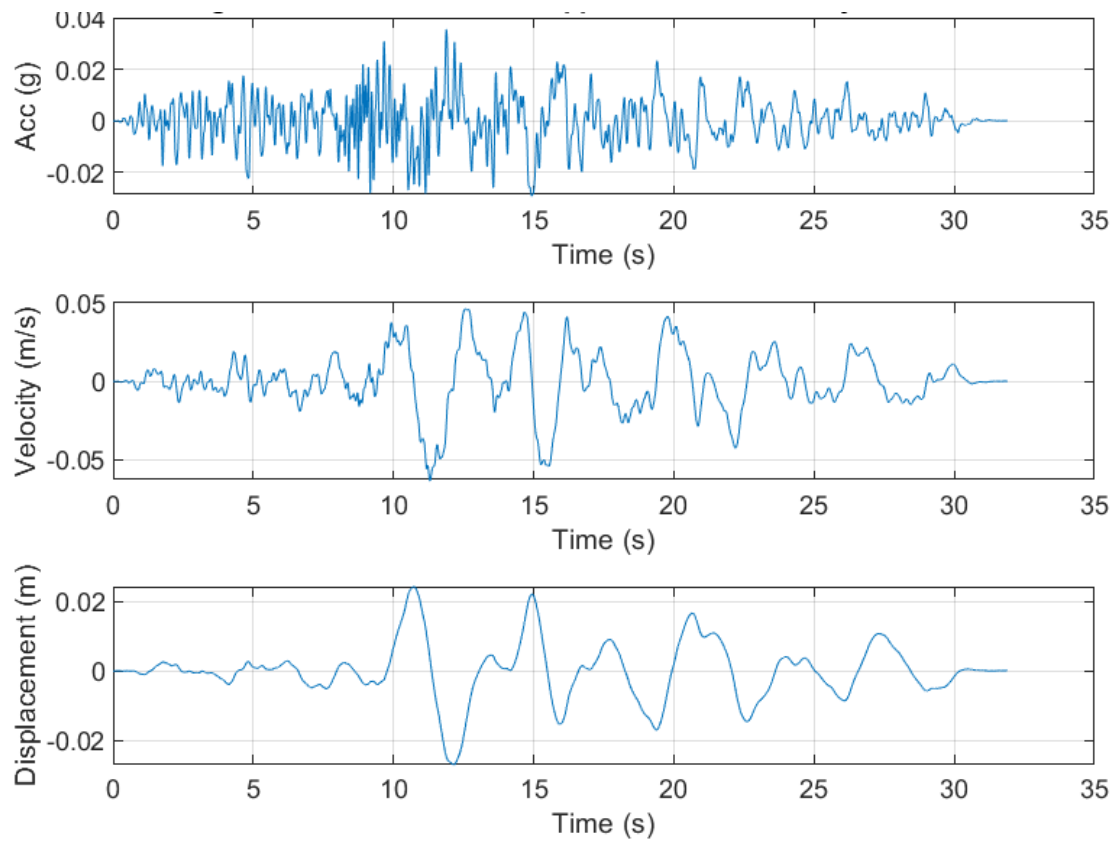


Figure 8.69 Acceleration, velocity and displacement time series of the event Irpinia, Italy (RSN294H2)

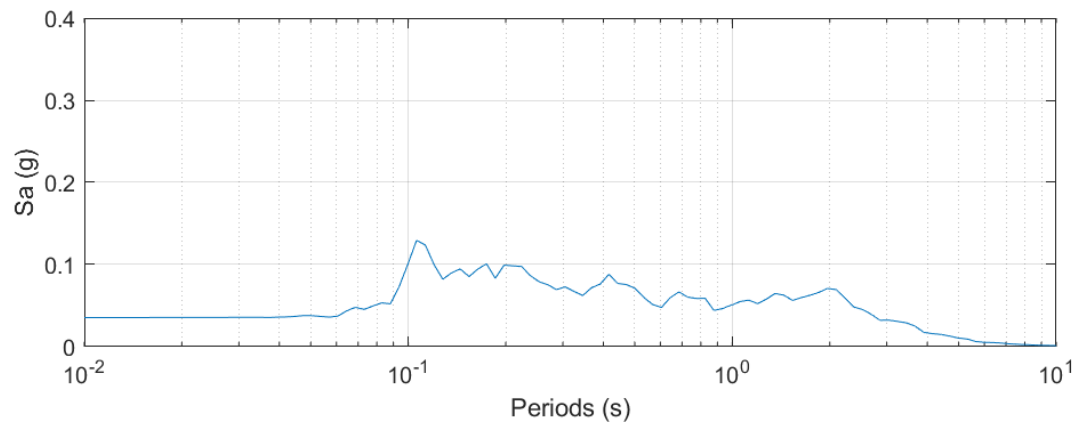


Figure 8.70 Response spectrum of the event Irpinia, Italy (RSN294H2)

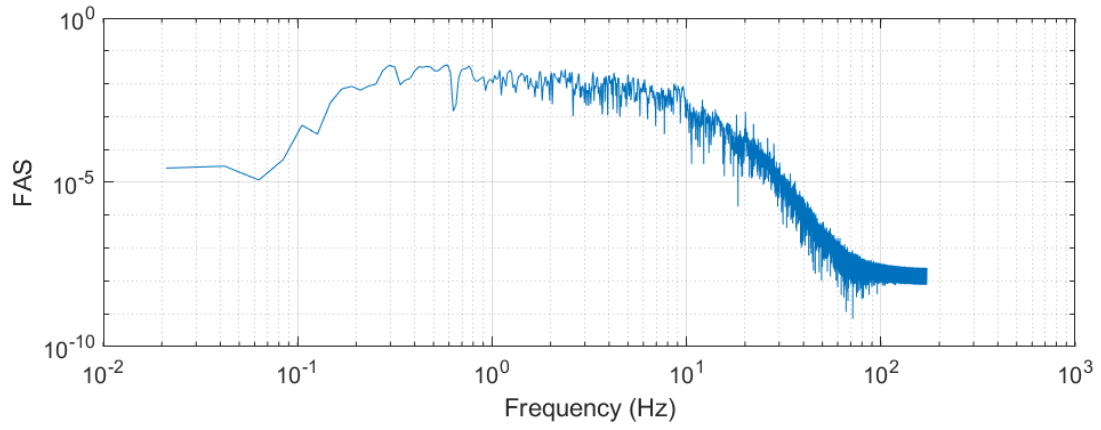


Figure 8.71 Fourier amplitude spectrum of the event Irpinia, Italy (RSN294H2)

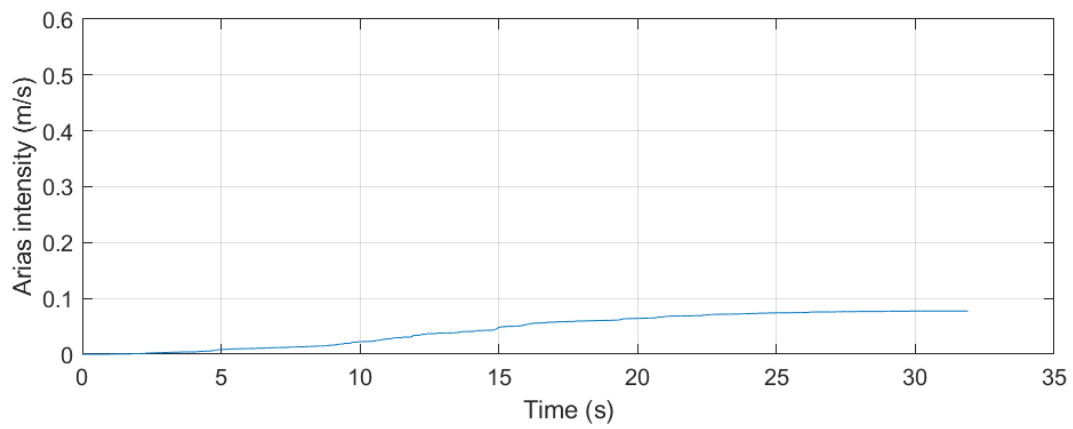


Figure 8.72 Arias intensity of the event Irpinia, Italy (RSN294H2)

Taiwan, SMART1 (45), 1986,  $M_w = 7.3$ ,  $R = 51.3$  km (RSN572H2)

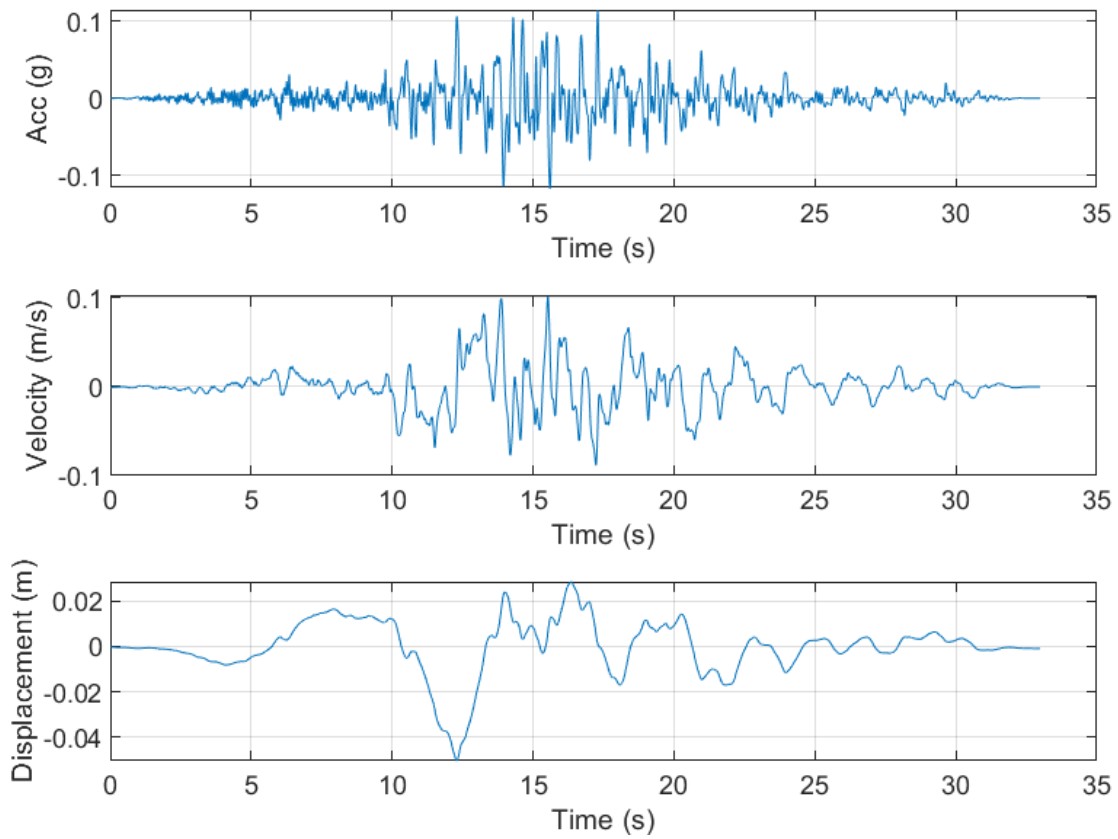


Figure 8.73 Acceleration, velocity and displacement time series of the event Taiwan, SMART1 (45) (RSN572H2)

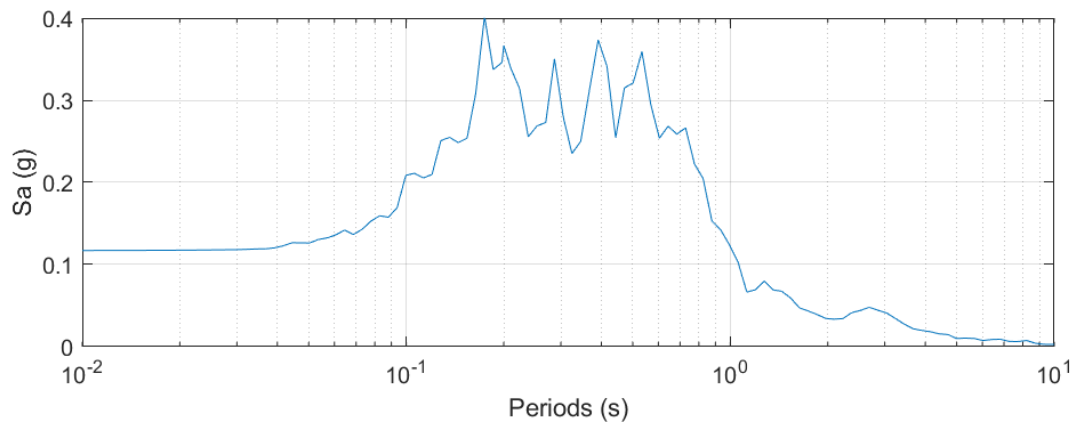


Figure.8.74 Response spectrum of the event Taiwan, SMART1 (45) (RSN572H2)

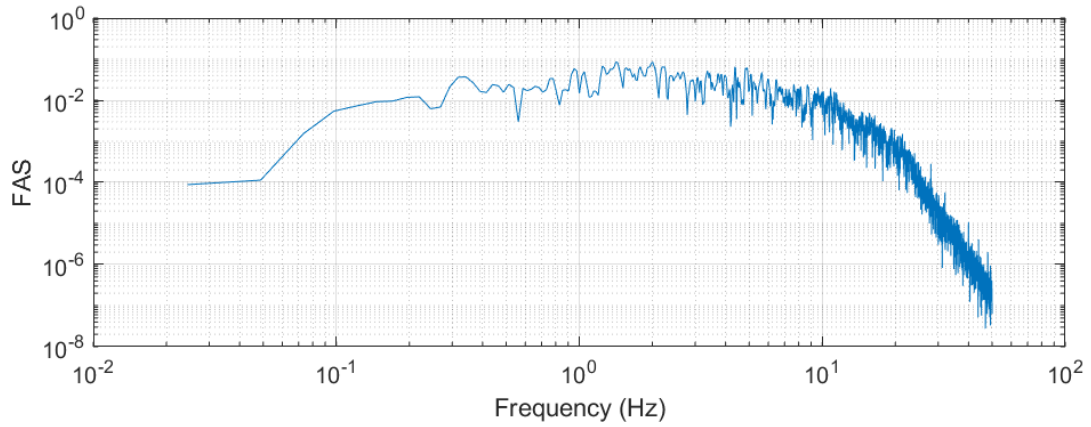


Figure 8.75 Fourier amplitude spectrum of the event Taiwan, SMART1 (45) (RSN572H2)

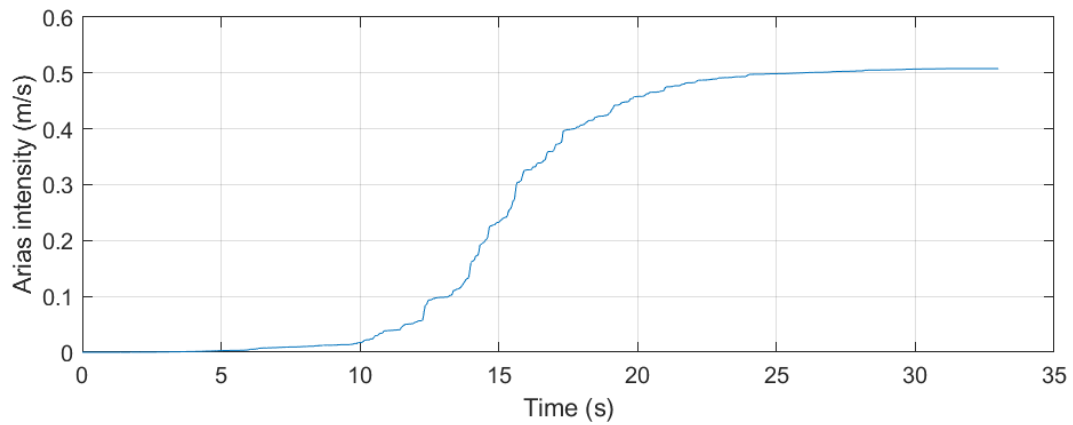


Figure 8.76 Arias intensity of the event Taiwan, SMART1 (45) (RSN572H2)

## APPENDIX B BOREHOLE REPORTS

a)

| <b>BOREHOLE BH-1</b>  |                                      |   |        |                          |             |       |         |              |            |            |                  |   |
|---|--------------------------------------|---|--------|--------------------------|-------------|-------|---------|--------------|------------|------------|------------------|---|
| Date:   |                                      |   |        |                          |             |       |         |              |            |            |                  |   |
| Nord (Y)<br>Est (X)<br>Depth of bedrock: 78.00 m      Elevation : 100.00 m (Z)<br>End of borehole:  |                                      |   |        |                          |             |       |         |              |            |            |                  |   |
| State of sampling<br><input type="checkbox"/> Intact <input type="checkbox"/> Remoulded <input type="checkbox"/> Lost <input type="checkbox"/> Coring |                                      |   |        |                          |             |       |         |              |            |            |                  |   |
| <b>TYPE OF SAMPLES</b><br>CF Split spoon<br>CR Coring   |                                      |   |        |                          |             |       |         |              |            |            |                  |   |
| Depth (feet)  | Depth (m)                            | Stratigraphy  | SYMBOL | Waterlevel (m)<br>/ DATE | Type/Number | State | CALIBRE | Recovery (%) | Blow/15 cm | "N" ou RQD | Results          | TESTS   |
|   | Elevation (m)<br>100.00<br>Depth (m) | DESCRIPTION OF SOILS AND ROCK   |        |                          |             |       |         |              |            |            |                  | Wp    W    W <sub>L</sub><br>20 40 60 80 100 120<br>Undrained shear strength<br>Dynamic cone penetration<br>20 40 60 80 100 120 |
| 1   |                                      | Sandy gravel with traces of silt.<br>Gray-brown. Relatively dry. With<br>cobbles and boulders (1-2 %).<br>Symbol: GW  |        |                          |             |       |         |              |            |            |                  |   |
| 2   |                                      |   |        |                          |             |       |         |              |            |            |                  |   |
| 3   |                                      | <b>Core:</b><br>Sand and silt with traces<br>of clay becoming silt and<br>sand with traces of clay.<br>Gray-brown. Humid.<br>Symbol: SM<br>Density: medium to very<br>dense |        |                          |             |       |         |              |            |            |                  |   |
| 4   | 98.90<br>1.10                        |   |        |                          |             |       |         |              |            |            |                  |   |
| 5   |                                      |   |        |                          | CF-1        |       |         | 95           |            | 125        | AG<br>w = 12.3 % |   |
| 6   |                                      |   |        |                          | CF-2        |       |         | 66           |            | 96         | AG<br>w = 13.9 % |   |
| 7   |                                      |   |        |                          |             |       |         |              |            |            |                  |   |
| 8   |                                      |   |        |                          |             |       |         |              |            |            |                  |   |
| 9   |                                      |   |        |                          |             |       |         |              |            |            |                  |   |
| 10  |                                      |   |        |                          |             |       |         |              |            |            |                  |   |
| 11  |                                      |   |        |                          |             |       |         |              |            |            |                  |   |
| 12  |                                      |   |        |                          |             |       |         |              |            |            |                  |   |
| 13  |                                      |   |        |                          |             |       |         |              |            |            |                  |   |
| 14  |                                      |   |        |                          |             |       |         |              |            |            |                  |   |
| 15  |                                      |   |        |                          |             |       |         |              |            |            |                  |   |
| 16  |                                      |   |        |                          |             |       |         |              |            |            |                  |   |
| 17  |                                      |   |        |                          |             |       |         |              |            |            |                  |   |
| 18  |                                      |   |        |                          |             |       |         |              |            |            |                  |   |
| 19  |                                      |   |        |                          |             |       |         |              |            |            |                  |   |
| 20  |                                      |   |        |                          |             |       |         |              |            |            |                  |   |
| <b>Notes:</b><br><br>Equipment: NW/NQ   |                                      |   |        |                          |             |       |         |              |            |            |                  |   |
|   |                                      |   |        |                          |             |       |         |              |            |            | Page: 1 de 3     |   |

|              |           |               |   |        |                       |             |       |         |              | BOREHOLE BH-1             |            |                  |  |    |    |    |     |     |
|--------------|-----------|---------------|---|--------|-----------------------|-------------|-------|---------|--------------|---------------------------|------------|------------------|--|----|----|----|-----|-----|
|              |           |               |   |        |                       |             |       |         |              | Date:                     |            |                  |  |    |    |    |     |     |
|              |           |               |   |        |                       |             |       |         |              | Nord (Y)                  |            |                  |  |    |    |    |     |     |
|              |           |               |   |        |                       |             |       |         |              | Est (X)                   |            |                  |  |    |    |    |     |     |
|              |           |               |   |        |                       |             |       |         |              | Depth of bedrock: 78.00 m |            |                  |  |    |    |    |     |     |
|              |           |               |   |        |                       |             |       |         |              | Elevation : 100.00 m (Z)  |            |                  |  |    |    |    |     |     |
|              |           |               |   |        |                       |             |       |         |              | End of borehole: m        |            |                  |  |    |    |    |     |     |
| Stratigraphy |           |               |   | TESTS  |                       |             |       |         |              |                           |            |                  |  |    |    |    |     |     |
| Depth (feet) | Depth (m) | Elevation (m) | DESCRIPTION OF SOILS AND ROCK   | SYMBOL | Waterlevel (m) / DATE | Type/Number | State | CALIBRE | Recovery (%) | Blow/15 cm                | "N" ou RQD | Results          | TENEUR EN EAU ET LIMITES (%)                         |    |    |    |     |     |
|              |           |               |   |        |                       |             |       |         |              |                           |            |                  | Wp   | WL |    |    |     |     |
|              |           |               |   |        |                       |             |       |         |              |                           |            |                  | 20   | 40 | 60 | 80 | 100 | 120 |
|              |           |               |   |        |                       |             |       |         |              |                           |            |                  | Undrained shear strength<br>Dynamic cone penetration |    |    |    |     |     |
|              |           |               |   |        |                       |             |       |         |              |                           |            |                  | 20   | 40 | 60 | 80 | 100 | 120 |
|              |           |               |   |        |                       | CF-3        |       |         | 66           |                           | 65         | AG<br>w = 16.3 % |  |    |    |    |     |     |
|              |           |               |   |        |                       | CF-4        |       |         | 82           |                           | 131        | AG<br>w = 13.5 % |  |    |    |    |     |     |
|              |           | 92.20         |   |        |                       | CF-5        |       |         | 79           |                           | 126        | AG<br>w = 13.6 % |  |    |    |    |     |     |
|              |           | 7.90          |   |        |                       |             |       |         |              |                           |            |                  |  |    |    |    |     |     |
|              |           | 91.90         |   |        |                       |             |       |         |              |                           |            |                  |  |    |    |    |     |     |
|              |           | 8.10          | Frundation soils:<br>Silt with traces of clay and fine sand. Becomes a silt with little fine sand and traces of clay at 11.6 m.<br>Density: medium becoming loose to very loose at 11.2 m |        |                       | CF-6        |       |         | 66           |                           | 32         | AG<br>w = 23.3 % |  |    |    |    |     |     |
|              |           |               |   |        |                       | CF-7        |       |         | 49           |                           | 15         | AG<br>w = 25.5 % |  |    |    |    |     |     |
|              |           |               |   |        |                       | CF-8        |       |         | 89           |                           | 13         | AG<br>w = 20.7 % |  |    |    |    |     |     |
|              |           |               |   |        |                       | CF-9        |       |         | 45           |                           | 4          | AG<br>w = 23.7 % |  |    |    |    |     |     |
|              |           |               |   |        |                       | CF-10       |       |         | 79           |                           | 9/15 cm    | AG<br>w = 20.3 % |  |    |    |    |     |     |

|              |           |               |           |                               |        |                       |             |       |         |              |            | BOREHOLE BH-1             |                  |                              |  |    |    |     |     |     |
|--------------|-----------|---------------|-----------|-------------------------------|--------|-----------------------|-------------|-------|---------|--------------|------------|---------------------------|------------------|------------------------------|--|----|----|-----|-----|-----|
|              |           |               |           |                               |        |                       |             |       |         |              |            | Date:                     |                  |                              |  |    |    |     |     |     |
|              |           |               |           |                               |        |                       |             |       |         |              |            | Nord (Y)                  |                  |                              |  |    |    |     |     |     |
|              |           |               |           |                               |        |                       |             |       |         |              |            | Est (X)                   |                  |                              |  |    |    |     |     |     |
|              |           |               |           |                               |        |                       |             |       |         |              |            | Depth of bedrock: 78.00 m |                  |                              |  |    |    |     |     |     |
|              |           |               |           |                               |        |                       |             |       |         |              |            | Elevation : 100.00 m (Z)  |                  |                              |  |    |    |     |     |     |
|              |           |               |           |                               |        |                       |             |       |         |              |            | End of borehole: m        |                  |                              |  |    |    |     |     |     |
| Stratigraphy |           |               |           |                               |        |                       |             |       |         |              |            | TESTS                     |                  |                              |  |    |    |     |     |     |
| Depth (feet) | Depth (m) | Elevation (m) | Depth (m) | DESCRIPTION OF SOILS AND ROCK | SYMBOL | Waterlevel (m) / DATE | Type/Number | State | CALIBRE | Recovery (%) | Blow/15 cm | "N" ou RQD                | Results          | TENEUR EN EAU ET LIMITES (%) |  |    |    |     |     |     |
|              |           |               |           |                               |        |                       |             |       |         |              |            |                           |                  | Wp                           | W  | WL |    |     |     |     |
|              |           |               |           |                               |        |                       |             |       |         |              |            |                           |                  | 20                           | 40   | 60 | 80 | 100 | 120 |     |
|              |           |               |           |                               |        |                       |             |       |         |              |            |                           |                  |                              | Undrained shear strength<br>Dynamic cone penetration |    |    |     |     |     |
|              |           |               |           |                               |        |                       |             |       |         |              |            |                           |                  |                              | 20   | 40 | 60 | 80  | 100 | 120 |
|              | 15        |               |           |                               |        |                       | CF-11       |       |         | 78           |            | 7                         | AG<br>w = 19.2 % |                              |  |    |    |     |     |     |
|              | 15.96     |               |           |                               |        |                       |             |       |         |              |            |                           |                  |                              |  |    |    |     |     |     |
|              | 16        | 84.04         |           | End of borehole.              |        |                       |             |       |         |              |            |                           |                  |                              |  |    |    |     |     |     |
|              | 17        |               |           |                               |        |                       |             |       |         |              |            |                           |                  |                              |  |    |    |     |     |     |
|              | 18        |               |           |                               |        |                       |             |       |         |              |            |                           |                  |                              |  |    |    |     |     |     |
|              | 19        |               |           |                               |        |                       |             |       |         |              |            |                           |                  |                              |  |    |    |     |     |     |
|              | 20        |               |           |                               |        |                       |             |       |         |              |            |                           |                  |                              |  |    |    |     |     |     |
|              | 21        |               |           |                               |        |                       |             |       |         |              |            |                           |                  |                              |  |    |    |     |     |     |
|              | 22        |               |           |                               |        |                       |             |       |         |              |            |                           |                  |                              |  |    |    |     |     |     |
|              | 23        |               |           |                               |        |                       |             |       |         |              |            |                           |                  |                              |  |    |    |     |     |     |

b)

| <b>BOREHOLE BH-2</b>   |  |                       |             |                       |         |              |                |            |         |       |                               |  |  |             |       |         |              |            |            |         |   |  |  |  |  |  |  |  |  |  |  |  |  |      |   |  |    |                |    |  |  |  |  |      |   |  |    |                |    |  |  |  |  |      |   |  |    |              |    |  |  |  |  |      |   |  |    |                |    |  |  |  |  |      |   |  |    |            |    |  |  |  |  |      |   |  |    |            |    |  |
|--|--|-----------------------|-------------|-----------------------|---------|--------------|----------------|------------|---------|-------|-------------------------------|--|--|-------------|-------|---------|--------------|------------|------------|---------|---|--|--|--|--|--|--|--|--|--|--|--|--|------|---|--|----|----------------|----|--|--|--|--|------|---|--|----|----------------|----|--|--|--|--|------|---|--|----|--------------|----|--|--|--|--|------|---|--|----|----------------|----|--|--|--|--|------|---|--|----|------------|----|--|--|--|--|------|---|--|----|------------|----|--|
| Date: _____  |  |                       |             |                       |         |              |                |            |         |       |                               |  |  |             |       |         |              |            |            |         |   |  |  |  |  |  |  |  |  |  |  |  |  |      |   |  |    |                |    |  |  |  |  |      |   |  |    |                |    |  |  |  |  |      |   |  |    |              |    |  |  |  |  |      |   |  |    |                |    |  |  |  |  |      |   |  |    |            |    |  |  |  |  |      |   |  |    |            |    |  |
| Nord (Y)<br>Est (X)<br>Depth of bedrock: 17.15 m    Elevation : 94.1 m (Z)    End of borehole: 19.53 m   |  |                       |             |                       |         |              |                |            |         |       |                               |  |  |             |       |         |              |            |            |         |   |  |  |  |  |  |  |  |  |  |  |  |  |      |   |  |    |                |    |  |  |  |  |      |   |  |    |                |    |  |  |  |  |      |   |  |    |              |    |  |  |  |  |      |   |  |    |                |    |  |  |  |  |      |   |  |    |            |    |  |  |  |  |      |   |  |    |            |    |  |
| State of sampling<br><input type="checkbox"/> Intact <input checked="" type="checkbox"/> Remoulded <input type="checkbox"/> Lost <input type="checkbox"/> Coring |  |                       |             |                       |         |              |                |            |         |       |                               |  |  |             |       |         |              |            |            |         |   |  |  |  |  |  |  |  |  |  |  |  |  |      |   |  |    |                |    |  |  |  |  |      |   |  |    |                |    |  |  |  |  |      |   |  |    |              |    |  |  |  |  |      |   |  |    |                |    |  |  |  |  |      |   |  |    |            |    |  |  |  |  |      |   |  |    |            |    |  |
| TYPE OF SAMPLES<br>CF Split spoon<br>CR Coring   |  |                       |             |                       |         |              |                |            |         |       |                               |  |  |             |       |         |              |            |            |         |   |  |  |  |  |  |  |  |  |  |  |  |  |      |   |  |    |                |    |  |  |  |  |      |   |  |    |                |    |  |  |  |  |      |   |  |    |              |    |  |  |  |  |      |   |  |    |                |    |  |  |  |  |      |   |  |    |            |    |  |  |  |  |      |   |  |    |            |    |  |
| Depth (feet)<br>Depth (m)<br>Elevation (m)<br>Depth (m)  | <table border="1" style="width:100%; border-collapse: collapse;"> <thead> <tr> <th style="width: 15%;">Stratigraphy</th> <th style="width: 10%;">SYMBOL</th> <th style="width: 10%;">Waterlevel (m) / DATE</th> <th colspan="5">SAMPLES</th> <th style="width: 10%;">TESTS</th> </tr> <tr> <th>DESCRIPTION OF SOILS AND ROCK</th> <th></th> <th></th> <th>Type/Number</th> <th>State</th> <th>CALIBRE</th> <th>Recovery (%)</th> <th>Blow/15 cm</th> <th>"N" ou RQD</th> <th>Results</th> </tr> </thead> <tbody> <tr> <td style="vertical-align: top;">                             94.10<br/><br/>                             Backfill:<br/>                             generally composed of sand and gravel with cobbles, no sampling                         </td> <td style="text-align: center; vertical-align: middle;"> </td> <td></td> <td></td> <td></td> <td></td> <td></td> <td></td> <td></td> <td></td> </tr> <tr> <td style="vertical-align: top;">                             92.60<br/>1.50<br/><br/>                             Silty deposit:<br/>                             Silt with sometimes some clay and traces of sand.<br/>                             Density: generally medium becoming loose at 7m depth                         </td> <td style="text-align: center; vertical-align: middle;"> </td> <td></td> <td>CF-1</td> <td style="text-align: center;">X</td> <td></td> <td style="text-align: center;">66</td> <td style="text-align: center;">12-10<br/>17-18</td> <td style="text-align: center;">27</td> <td></td> </tr> <tr> <td></td> <td style="text-align: center; vertical-align: middle;"> </td> <td></td> <td>CF-2</td> <td style="text-align: center;">X</td> <td></td> <td style="text-align: center;">50</td> <td style="text-align: center;">16-16<br/>17-20</td> <td style="text-align: center;">35</td> <td></td> </tr> <tr> <td></td> <td style="text-align: center; vertical-align: middle;"> </td> <td></td> <td>CF-3</td> <td style="text-align: center;">X</td> <td></td> <td style="text-align: center;">57</td> <td style="text-align: center;">8-9<br/>12-12</td> <td style="text-align: center;">21</td> <td></td> </tr> <tr> <td></td> <td style="text-align: center; vertical-align: middle;"> </td> <td></td> <td>CF-4</td> <td style="text-align: center;">X</td> <td></td> <td style="text-align: center;">74</td> <td style="text-align: center;">16-11<br/>12-18</td> <td style="text-align: center;">23</td> <td></td> </tr> <tr> <td></td> <td style="text-align: center; vertical-align: middle;"> </td> <td></td> <td>CF-5</td> <td style="text-align: center;">X</td> <td></td> <td style="text-align: center;">57</td> <td style="text-align: center;">8-9<br/>9-9</td> <td style="text-align: center;">18</td> <td></td> </tr> <tr> <td></td> <td style="text-align: center; vertical-align: middle;"> </td> <td></td> <td>CF-6</td> <td style="text-align: center;">X</td> <td></td> <td style="text-align: center;">74</td> <td style="text-align: center;">8-6<br/>7-9</td> <td style="text-align: center;">15</td> <td></td> </tr> </tbody> </table> | Stratigraphy          | SYMBOL      | Waterlevel (m) / DATE | SAMPLES |              |                |            |         | TESTS | DESCRIPTION OF SOILS AND ROCK |  |  | Type/Number | State | CALIBRE | Recovery (%) | Blow/15 cm | "N" ou RQD | Results | 94.10<br><br>Backfill:<br>generally composed of sand and gravel with cobbles, no sampling |  |  |  |  |  |  |  |  |  | 92.60<br>1.50<br><br>Silty deposit:<br>Silt with sometimes some clay and traces of sand.<br>Density: generally medium becoming loose at 7m depth |  |  | CF-1 | X |  | 66 | 12-10<br>17-18 | 27 |  |  |  |  | CF-2 | X |  | 50 | 16-16<br>17-20 | 35 |  |  |  |  | CF-3 | X |  | 57 | 8-9<br>12-12 | 21 |  |  |  |  | CF-4 | X |  | 74 | 16-11<br>12-18 | 23 |  |  |  |  | CF-5 | X |  | 57 | 8-9<br>9-9 | 18 |  |  |  |  | CF-6 | X |  | 74 | 8-6<br>7-9 | 15 |  |
| Stratigraphy   | SYMBOL   | Waterlevel (m) / DATE | SAMPLES     |                       |         |              |                | TESTS      |         |       |                               |  |  |             |       |         |              |            |            |         |   |  |  |  |  |  |  |  |  |  |  |  |  |      |   |  |    |                |    |  |  |  |  |      |   |  |    |                |    |  |  |  |  |      |   |  |    |              |    |  |  |  |  |      |   |  |    |                |    |  |  |  |  |      |   |  |    |            |    |  |  |  |  |      |   |  |    |            |    |  |
| DESCRIPTION OF SOILS AND ROCK  |  |                       | Type/Number | State                 | CALIBRE | Recovery (%) | Blow/15 cm     | "N" ou RQD | Results |       |                               |  |  |             |       |         |              |            |            |         |   |  |  |  |  |  |  |  |  |  |  |  |  |      |   |  |    |                |    |  |  |  |  |      |   |  |    |                |    |  |  |  |  |      |   |  |    |              |    |  |  |  |  |      |   |  |    |                |    |  |  |  |  |      |   |  |    |            |    |  |  |  |  |      |   |  |    |            |    |  |
| 94.10<br><br>Backfill:<br>generally composed of sand and gravel with cobbles, no sampling  |  |                       |             |                       |         |              |                |            |         |       |                               |  |  |             |       |         |              |            |            |         |   |  |  |  |  |  |  |  |  |  |  |  |  |      |   |  |    |                |    |  |  |  |  |      |   |  |    |                |    |  |  |  |  |      |   |  |    |              |    |  |  |  |  |      |   |  |    |                |    |  |  |  |  |      |   |  |    |            |    |  |  |  |  |      |   |  |    |            |    |  |
| 92.60<br>1.50<br><br>Silty deposit:<br>Silt with sometimes some clay and traces of sand.<br>Density: generally medium becoming loose at 7m depth                 |  |                       | CF-1        | X                     |         | 66           | 12-10<br>17-18 | 27         |         |       |                               |  |  |             |       |         |              |            |            |         |   |  |  |  |  |  |  |  |  |  |  |  |  |      |   |  |    |                |    |  |  |  |  |      |   |  |    |                |    |  |  |  |  |      |   |  |    |              |    |  |  |  |  |      |   |  |    |                |    |  |  |  |  |      |   |  |    |            |    |  |  |  |  |      |   |  |    |            |    |  |
|  |  |                       | CF-2        | X                     |         | 50           | 16-16<br>17-20 | 35         |         |       |                               |  |  |             |       |         |              |            |            |         |   |  |  |  |  |  |  |  |  |  |  |  |  |      |   |  |    |                |    |  |  |  |  |      |   |  |    |                |    |  |  |  |  |      |   |  |    |              |    |  |  |  |  |      |   |  |    |                |    |  |  |  |  |      |   |  |    |            |    |  |  |  |  |      |   |  |    |            |    |  |
|  |  |                       | CF-3        | X                     |         | 57           | 8-9<br>12-12   | 21         |         |       |                               |  |  |             |       |         |              |            |            |         |   |  |  |  |  |  |  |  |  |  |  |  |  |      |   |  |    |                |    |  |  |  |  |      |   |  |    |                |    |  |  |  |  |      |   |  |    |              |    |  |  |  |  |      |   |  |    |                |    |  |  |  |  |      |   |  |    |            |    |  |  |  |  |      |   |  |    |            |    |  |
|  |  |                       | CF-4        | X                     |         | 74           | 16-11<br>12-18 | 23         |         |       |                               |  |  |             |       |         |              |            |            |         |   |  |  |  |  |  |  |  |  |  |  |  |  |      |   |  |    |                |    |  |  |  |  |      |   |  |    |                |    |  |  |  |  |      |   |  |    |              |    |  |  |  |  |      |   |  |    |                |    |  |  |  |  |      |   |  |    |            |    |  |  |  |  |      |   |  |    |            |    |  |
|  |  |                       | CF-5        | X                     |         | 57           | 8-9<br>9-9     | 18         |         |       |                               |  |  |             |       |         |              |            |            |         |   |  |  |  |  |  |  |  |  |  |  |  |  |      |   |  |    |                |    |  |  |  |  |      |   |  |    |                |    |  |  |  |  |      |   |  |    |              |    |  |  |  |  |      |   |  |    |                |    |  |  |  |  |      |   |  |    |            |    |  |  |  |  |      |   |  |    |            |    |  |
|  |  |                       | CF-6        | X                     |         | 74           | 8-6<br>7-9     | 15         |         |       |                               |  |  |             |       |         |              |            |            |         |   |  |  |  |  |  |  |  |  |  |  |  |  |      |   |  |    |                |    |  |  |  |  |      |   |  |    |                |    |  |  |  |  |      |   |  |    |              |    |  |  |  |  |      |   |  |    |                |    |  |  |  |  |      |   |  |    |            |    |  |  |  |  |      |   |  |    |            |    |  |
| Notes:<br><br>Equipment: NW/NQ   |  |                       |             |                       |         |              |                |            |         |       |                               |  |  |             |       |         |              |            |            |         |   |  |  |  |  |  |  |  |  |  |  |  |  |      |   |  |    |                |    |  |  |  |  |      |   |  |    |                |    |  |  |  |  |      |   |  |    |              |    |  |  |  |  |      |   |  |    |                |    |  |  |  |  |      |   |  |    |            |    |  |  |  |  |      |   |  |    |            |    |  |
| Page: 1 de 3   |  |                       |             |                       |         |              |                |            |         |       |                               |  |  |             |       |         |              |            |            |         |   |  |  |  |  |  |  |  |  |  |  |  |  |      |   |  |    |                |    |  |  |  |  |      |   |  |    |                |    |  |  |  |  |      |   |  |    |              |    |  |  |  |  |      |   |  |    |                |    |  |  |  |  |      |   |  |    |            |    |  |  |  |  |      |   |  |    |            |    |  |

|              |           |               |           |                               |        |                       |             |       |         | <b>BOREHOLE BH-2</b>                      |            |            |              |                              |                          |    |    |     |     |     |
|--------------|-----------|---------------|-----------|-------------------------------|--------|-----------------------|-------------|-------|---------|---|------------|------------|--------------|------------------------------|--------------------------|----|----|-----|-----|-----|
|              |           |               |           |                               |        |                       |             |       |         | Date:                                     |            |            |              |                              |                          |    |    |     |     |     |
|              |           |               |           |                               |        |                       |             |       |         | Nord (Y)                                  |            |            |              |                              |                          |    |    |     |     |     |
|              |           |               |           |                               |        |                       |             |       |         | Est (X)                                   |            |            |              |                              |                          |    |    |     |     |     |
|              |           |               |           |                               |        |                       |             |       |         | Depth of Elevation : 94.1 m (Z)           |            |            |              |                              |                          |    |    |     |     |     |
|              |           |               |           |                               |        |                       |             |       |         | bedrock: 17.15 m End of borehole: 19.53 m |            |            |              |                              |                          |    |    |     |     |     |
| Stratigraphy |           |               |           | TESTS                         |        |                       |             |       |         |   |            |            |              |                              |                          |    |    |     |     |     |
| Depth (feet) | Depth (m) | Elevation (m) | Depth (m) | DESCRIPTION OF SOILS AND ROCK | SYMBOL | Waterlevel (m) / DATE | Type/Number | State | CALIBRE | Recovery (%)                              | Blow/15 cm | "N" ou RQD | Results      | TENEUR EN EAU ET LIMITES (%) |                          |    |    |     |     |     |
|              |           |               |           |                               |        |                       |             |       |         |   |            |            |              | Wp                           | Wl                       |    |    |     |     |     |
|              |           |               |           |                               |        |                       |             |       |         |   |            |            |              | 20                           | 40                       | 60 | 80 | 100 | 120 |     |
|              |           |               |           |                               |        |                       |             |       |         |   |            |            |              |                              | Undrained shear strength |    |    |     |     |     |
|              |           |               |           |                               |        |                       |             |       |         |   |            |            |              |                              | Dynamic cone penetration |    |    |     |     |     |
|              |           |               |           |                               |        |                       |             |       |         |   |            |            |              |                              | 20                       | 40 | 60 | 80  | 100 | 120 |
| 20           |           |               |           |                               |        |                       |             |       |         |   |            |            |              |                              |                          |    |    |     |     |     |
| 21           |           |               |           |                               |        |                       | CF-7        |       |         | 66  | 4.7<br>5.9 | 12         |              |                              |                          |    |    |     |     |     |
| 22           |           |               |           |                               |        |                       | CF-8        |       |         | 66  | 7.3<br>5.6 | 8          |              |                              |                          |    |    |     |     |     |
| 23           |           |               |           |                               |        |                       | CF-9        |       |         | 74  | 3.5<br>3.2 | 8          |              |                              |                          |    |    |     |     |     |
| 24           |           |               |           |                               |        |                       | &           |       |         |   |            |            |              |                              |                          |    |    |     |     |     |
| 25           |           |               |           |                               |        |                       | CF-10       |       |         | 66  | 6.5<br>5.2 | 10         |              | AG<br>W = 28.0               |                          |    |    |     |     |     |
| 26           |           |               |           |                               |        |                       | CF-11       |       |         | 74  | 2.2<br>3.3 | 5          |              |                              |                          |    |    |     |     |     |
| 27           |           |               |           |                               |        |                       | CF-12       |       |         |   | 4.3<br>2.8 | 5          |              |                              |                          |    |    |     |     |     |
| 28           |           |               |           |                               |        |                       | CF-13       |       |         | 66  | 1.2<br>3.5 | 5          |              |                              |                          |    |    |     |     |     |
| 29           |           |               |           |                               |        |                       | CF-14       |       |         | 66  | 5.4<br>4.4 | 8          |              |                              |                          |    |    |     |     |     |
| 30           |           |               |           |                               |        |                       | CF-15       |       |         | 74  | 3.5<br>5.0 | 10         |              |                              |                          |    |    |     |     |     |
| 31           |           |               |           |                               |        |                       | CF-16       |       |         | 62  | 5.3<br>4.5 | 7          |              |                              |                          |    |    |     |     |     |
| 32           |           |               |           |                               |        |                       | CF-17       |       |         | 41  | 3.4<br>4.4 | 8          |              | AG<br>W = 20.5               |                          |    |    |     |     |     |
| 33           |           | 81.30         |           |                               |        |                       |             |       |         |   |            |            |              |                              |                          |    |    |     |     |     |
| 34           |           | 12.80         |           |                               |        |                       |             |       |         |   |            |            |              |                              |                          |    |    |     |     |     |
| 35           |           |               |           |                               |        |                       |             |       |         |   |            |            |              |                              |                          |    |    |     |     |     |
| 36           |           |               |           |                               |        |                       |             |       |         |   |            |            |              |                              |                          |    |    |     |     |     |
| 37           |           |               |           |                               |        |                       |             |       |         |   |            |            |              |                              |                          |    |    |     |     |     |
| 38           |           |               |           |                               |        |                       |             |       |         |   |            |            |              |                              |                          |    |    |     |     |     |
| 39           |           |               |           |                               |        |                       |             |       |         |   |            |            |              |                              |                          |    |    |     |     |     |
| 40           |           |               |           |                               |        |                       |             |       |         |   |            |            |              |                              |                          |    |    |     |     |     |
| 41           |           |               |           |                               |        |                       |             |       |         |   |            |            |              |                              |                          |    |    |     |     |     |
| 42           |           |               |           |                               |        |                       |             |       |         |   |            |            |              |                              |                          |    |    |     |     |     |
| 43           |           |               |           |                               |        |                       |             |       |         |   |            |            |              |                              |                          |    |    |     |     |     |
| 44           |           |               |           |                               |        |                       |             |       |         |   |            |            |              |                              |                          |    |    |     |     |     |
| 45           |           |               |           |                               |        |                       |             |       |         |   |            |            |              |                              |                          |    |    |     |     |     |
| 46           |           |               |           |                               |        |                       |             |       |         |   |            |            |              |                              |                          |    |    |     |     |     |
| 47           |           |               |           |                               |        |                       |             |       |         |   |            |            |              |                              |                          |    |    |     |     |     |
| 48           |           |               |           |                               |        |                       |             |       |         |   |            |            |              |                              |                          |    |    |     |     |     |
|              |           |               |           |                               |        |                       |             |       |         |   |            |            | Page: 2 de 3 |                              |                          |    |    |     |     |     |

**Sandy deposit:**  
 Sand with various proportions of "silt and sand" to "silty sand".  
 Density: loose to medium.  
 At depth, the proportion of silt increases gradually



c)

|   |              | <b>BOREHOLE BH-3</b>   |   |        |                       |             |       |         |                |            |              |         |
|---|--------------|--|---|--------|-----------------------|-------------|-------|---------|----------------|------------|--------------|---------|
|   |              | Date:  |   |        |                       |             |       |         |                |            |              |         |
|   |              | Nord (Y)<br>Est (X)  |   |        |                       |             |       |         |                |            |              |         |
|   |              | Depth of bedrock: 15.80 m End of borehole: 18.39 m<br>Elevation : 94.1 m (Z) |   |        |                       |             |       |         |                |            |              |         |
| State of sampling<br><input checked="" type="checkbox"/> Intact <input checked="" type="checkbox"/> Remoulded <input type="checkbox"/> Lost <input type="checkbox"/> Coring |              |  |   |        |                       |             |       |         |                |            |              |         |
| TYPE OF SAMPLES<br>CF Split spoon<br>CR Coring  |              |  |   |        |                       |             |       |         |                |            |              |         |
| Depth (feet)  | Stratigraphy |  | SAMPLES   |        |                       |             |       | TESTS   |                |            |              |         |
|   | Depth (m)    | Elevation (m)  | DESCRIPTION OF SOILS AND ROCK   | SYMBOL | Waterlevel (m) / DATE | Type/Number | State | CALIBRE | Recovery (%)   | Blow/15 cm | "N" ou RQD   | Results |
|   | 0.00         | 94.10  | Topsoil and organics  |        |                       | CF-1        | A     | 83      | 1-2<br>3-3     | 4          |              |         |
|   | 0.05         |  | Granular deposit:<br>generally composed of silt with<br>various proportions of sand and<br>traces of clay.<br>Density: Loose becoming<br>medium at 1.5 m depth. Very<br>loose at 15.5 m |        |                       | CF-2        | B     | 83      | 1-2<br>2-5     | 4          |              |         |
| 1   |              |  |   | CF-3   |                       |             | 74    |         | 8-10<br>11-13  | 21         |              |         |
| 2   |              |  |   | CF-4   |                       |             | 82    |         | 9-11<br>12-14  | 23         |              |         |
| 3   |              |  |   | CF-5   |                       |             | 68    |         | 7-9<br>11-14   | 20         |              |         |
| 4   |              |  |   | CF-6   |                       |             | 57    |         | 9-13<br>13-18  | 26         |              |         |
| 5   |              |  |   | CF-7   |                       |             | 49    |         | 8-11<br>13-15  | 23         |              |         |
| 6   |              |  |   | CF-8   |                       |             | 57    |         | 12-14<br>16-17 | 30         |              |         |
| 7   |              |  |   |        |                       |             |       |         |                |            |              |         |
| 8   |              |  |   |        |                       |             |       |         |                |            |              |         |
| 9   |              |  |   |        |                       |             |       |         |                |            |              |         |
| 10  |              |  |   |        |                       |             |       |         |                |            |              |         |
| 11  |              |  |   |        |                       |             |       |         |                |            |              |         |
| 12  |              |  |   |        |                       |             |       |         |                |            |              |         |
| 13  |              |  |   |        |                       |             |       |         |                |            |              |         |
| 14  |              |  |   |        |                       |             |       |         |                |            |              |         |
| 15  |              |  |   |        |                       |             |       |         |                |            |              |         |
| 16  |              |  |   |        |                       |             |       |         |                |            |              |         |
| 17  |              |  |   |        |                       |             |       |         |                |            |              |         |
| 18  |              |  |   |        |                       |             |       |         |                |            |              |         |
| 19  |              |  |   |        |                       |             |       |         |                |            |              |         |
| Notes:<br><br>Equipment: NW/NQ  |              |  |   |        |                       |             |       |         |                |            |              |         |
|   |              |  |   |        |                       |             |       |         |                |            | Page: 1 de 3 |         |

|              |           |               |                               |        |                       |             |       |         |              | <b>BOREHOLE BH-3</b>      |            |                |  |   |    |  |
|--------------|-----------|---------------|-------------------------------|--------|-----------------------|-------------|-------|---------|--------------|---------------------------|------------|----------------|--|---|----|--|
|              |           |               |                               |        |                       |             |       |         |              | Date:                     |            |                |  |   |    |  |
|              |           |               |                               |        |                       |             |       |         |              | Nord (Y)                  |            |                |  |   |    |  |
|              |           |               |                               |        |                       |             |       |         |              | Est (X)                   |            |                |  |   |    |  |
|              |           |               |                               |        |                       |             |       |         |              | Depth of bedrock: 15.80 m |            |                |  |   |    |  |
|              |           |               |                               |        |                       |             |       |         |              | Elevation : 94.1 m (Z)    |            |                |  |   |    |  |
|              |           |               |                               |        |                       |             |       |         |              | End of borehole: 18.39 m  |            |                |  |   |    |  |
| Stratigraphy |           |               |                               | TESTS  |                       |             |       |         |              |                           |            |                |  |   |    |  |
| Depth (feet) | Depth (m) | Elevation (m) | DESCRIPTION OF SOILS AND ROCK | SYMBOL | Waterlevel (m) / DATE | Type/Number | State | CALIBRE | Recovery (%) | Blow/15 cm                | "N" ou RQD | Results        | TENEUR EN EAU ET LIMITES (%)                             |   |    |  |
|              |           |               |                               |        |                       |             |       |         |              |                           |            |                | Wp   | W | WL |  |
|              |           |               |                               |        |                       |             |       |         |              |                           |            |                |  |   |    |  |
|              |           |               |                               |        |                       |             |       |         |              |                           |            |                | Undrained shear strength<br>Dynamic cone penetration<br> |   |    |  |
| 21           |           |               |                               |        |                       | CF-9        |       |         | 49           | 8-11<br>12-14             | 23         |                |  |   |    |  |
| 22           |           |               |                               |        |                       | CF-10       |       |         | 66           | 12-12<br>14-12            | 26         |                |  |   |    |  |
| 23           | 7         |               |                               |        |                       | CF-11       |       |         | 57           | 10-12<br>11-12            | 23         |                |  |   |    |  |
| 24           |           |               |                               |        |                       | CF-12       |       |         |              | 10-13<br>15-14            | 28         |                |  |   |    |  |
| 25           |           |               |                               |        |                       | CF-13       |       |         | 66           | 9-9<br>11-12              | 20         |                |  |   |    |  |
| 26           | 6         |               |                               |        |                       | CF-14       |       |         | 82           | 9-12<br>15-13             | 27         |                |  |   |    |  |
| 27           |           |               |                               |        |                       | CF-15       |       |         | 66           | 10-14<br>12-12            | 26         |                |  |   |    |  |
| 28           |           |               |                               |        |                       | CF-16       | &     |         | 82           | 14-18<br>19-16            | 37         | AG<br>W = 19.4 |  |   |    |  |
| 29           |           |               |                               |        |                       | CF-17       |       |         | 82           | 5-12<br>14-12             | 26         |                |  |   |    |  |
| 30           |           |               |                               |        |                       | CF-18       |       |         | 98           | 17-17<br>18-15            | 35         |                |  |   |    |  |
| 31           |           |               |                               |        |                       | CF-19       |       |         | 49           | 4-8<br>6-8                | 12         |                |  |   |    |  |
| 32           | 10        |               |                               |        |                       | CF-20       | &     |         | 100          | 4-7<br>7-6                | 14         | AG<br>W = 23.1 |  |   |    |  |



## APPENDIX C DETAILS OF THE CALCULATION FOR THE EVALUATION OF THE LIQUEFACTION POTENTIAL OF THE FOUNDATION SOILS USING SIMPLIFIED METHODS

Table 8.1 Details of the calculation of the liquefaction potential based on the *SPT*-method for soil class D and  $M = 6$

| Borehole | SS    | Depth (m) | $N_{60}$ | $(N_1)_{60}$ | $\sigma$ (kPa) | $\sigma'$ (kPa) | $r_d$ | $\alpha$ | $\beta$ | CSR   | FC (%) | $\Delta(N_1)_{60}$ | $(N_1)_{60CS}$ | $m$   | $C_N$ | $CRR_{M=7.5, \sigma'=1atm}$ | $C_\sigma$ | $K_\sigma$ | MSF   | CRR   | FS   |
|----------|-------|-----------|----------|--------------|----------------|-----------------|-------|----------|---------|-------|--------|--------------------|----------------|-------|-------|-----------------------------|------------|------------|-------|-------|------|
| BH-01    | CF-7  | 10.5      | 15       | 10.8         | 209.3          | 200.8           | 0.79  | -0.72    | 0.081   | 0.192 | 99.0   | 5.23               | 16.1           | 0.476 | 0.72  | 0.165                       | 0.12       | 0.92       | 1.482 | 0.226 | 1.17 |
| BH-01    | CF-8  | 10.9      | 13       | 9.2          | 217.9          | 205.2           | 0.78  | -0.76    | 0.085   | 0.193 | 94.0   | 5.23               | 14.4           | 0.492 | 0.71  | 0.151                       | 0.11       | 0.92       | 1.482 | 0.207 | 1.07 |
| BH-03    | CF-7  | 11.8      | 9.2      | 8.4          | 126.0          | 121.5           | 0.89  | -0.36    | 0.041   | 0.216 | 95.7   | 5.23               | 13.6           | 0.500 | 0.91  | 0.145                       | 0.11       | 0.98       | 1.482 | 0.211 | 0.98 |
| BH-03    | CF-8  | 12.4      | 7.1      | 6.3          | 138.0          | 127.6           | 0.87  | -0.41    | 0.046   | 0.222 | 95.7   | 5.23               | 11.5           | 0.523 | 0.89  | 0.129                       | 0.10       | 0.98       | 1.482 | 0.187 | 0.84 |
| BH-01    | CF-9  | 12.6      | 4        | 2.6          | 251.9          | 222.5           | 0.74  | -0.93    | 0.103   | 0.195 | 82.0   | 5.22               | 7.8            | 0.570 | 0.64  | 0.103                       | 0.08       | 0.93       | 1.482 | 0.143 | 0.73 |
| BH-03    | CF-9  | 13.3      | 7.9      | 6.8          | 156.0          | 136.8           | 0.85  | -0.49    | 0.055   | 0.228 | 95.7   | 5.23               | 12.0           | 0.518 | 0.86  | 0.132                       | 0.10       | 0.97       | 1.482 | 0.190 | 0.83 |
| BH-03    | CF-10 | 13.9      | 8.4      | 7.0          | 168.0          | 142.9           | 0.84  | -0.54    | 0.060   | 0.231 | 95.7   | 5.23               | 12.3           | 0.515 | 0.84  | 0.134                       | 0.10       | 0.97       | 1.482 | 0.192 | 0.83 |
| BH-03    | CF-11 | 14.8      | 5.4      | 4.3          | 186.0          | 152.1           | 0.82  | -0.62    | 0.069   | 0.234 | 95.7   | 5.23               | 9.6            | 0.547 | 0.80  | 0.115                       | 0.09       | 0.96       | 1.482 | 0.164 | 0.70 |
| BH-01    | CF-11 | 15.0      | 7        | 4.3          | 300.3          | 247.2           | 0.68  | -1.16    | 0.128   | 0.193 | 74.0   | 5.21               | 9.5            | 0.547 | 0.61  | 0.115                       | 0.09       | 0.92       | 1.482 | 0.156 | 0.81 |
| BH-03    | CF-12 | 15.4      | 5.3      | 4.2          | 198.0          | 158.2           | 0.80  | -0.67    | 0.075   | 0.235 | 95.7   | 5.23               | 9.4            | 0.549 | 0.78  | 0.114                       | 0.09       | 0.96       | 1.482 | 0.162 | 0.69 |
| BH-03    | CF-13 | 16.3      | 4.7      | 3.6          | 216.0          | 167.3           | 0.78  | -0.76    | 0.084   | 0.236 | 95.7   | 5.23               | 8.8            | 0.556 | 0.76  | 0.110                       | 0.09       | 0.96       | 1.482 | 0.155 | 0.66 |
| BH-03    | CF-14 | 16.9      | 7.8      | 5.9          | 228.0          | 173.5           | 0.76  | -0.81    | 0.091   | 0.235 | 95.7   | 5.23               | 11.1           | 0.528 | 0.75  | 0.126                       | 0.10       | 0.95       | 1.482 | 0.177 | 0.75 |
| BH-03    | CF-15 | 17.8      | 10.9     | 8.1          | 246.0          | 182.6           | 0.74  | -0.90    | 0.100   | 0.234 | 95.7   | 5.23               | 13.3           | 0.504 | 0.74  | 0.143                       | 0.10       | 0.94       | 1.482 | 0.198 | 0.85 |
| BH-03    | CF-16 | 18.4      | 7.3      | 5.2          | 258.0          | 188.7           | 0.73  | -0.96    | 0.106   | 0.233 | 42.7   | 5.00               | 10.2           | 0.539 | 0.72  | 0.120                       | 0.09       | 0.94       | 1.482 | 0.167 | 0.72 |
| BH-03    | CF-17 | 19.3      | 5.8      | 4.0          | 276.0          | 197.9           | 0.71  | -1.04    | 0.116   | 0.231 | 42.7   | 5.00               | 9.0            | 0.554 | 0.69  | 0.111                       | 0.09       | 0.94       | 1.482 | 0.155 | 0.67 |
| BH-03    | CF-18 | 21.0      | 12.6     | 8.6          | 310.0          | 215.2           | 0.67  | -1.20    | 0.133   | 0.225 | 42.7   | 5.00               | 13.6           | 0.500 | 0.69  | 0.145                       | 0.11       | 0.92       | 1.482 | 0.198 | 0.88 |
| BH-03    | CF-19 | 21.6      | 17.3     | 12.0         | 322.0          | 221.3           | 0.65  | -1.26    | 0.139   | 0.223 | 42.7   | 5.00               | 17.0           | 0.467 | 0.69  | 0.174                       | 0.12       | 0.91       | 1.482 | 0.234 | 1.05 |

Note: the depth is calculated from the surface of the landside. Hence, since boreholes BH-01 and BH-02 are drilled on the top of the dike as opposed to the others that are performed at the landside, the foundation soils are under a higher vertical pressure for the same “depth”.

Table 8.2 Details of the calculation of the liquefaction potential based on the  $V_s$ -method for soil class D

| Depth<br>(m) | $V_{s1}$ (m/s) | $\sigma_{erd}$ | $r_d$ | $r_{d\_sup}$ | $r_{d\_inf}$ | $\sigma$ (kPa) | $\sigma'$ (kPa) | CSR   | FC (%) | $P_L$   | CRR   | FS   |
|--------------|----------------|----------------|-------|--------------|--------------|----------------|-----------------|-------|--------|---------|-------|------|
| 11.1         | 205.8          | 0.09           | 0.96  | 1.00         | 0.87         | 113.0          | 113.0           | 0.225 | 95.7   | 5.6E-04 | 0.502 | 2.24 |
| 11.9         | 211.2          | 0.10           | 0.95  | 1.00         | 0.85         | 129.1          | 123.1           | 0.232 | 95.7   | 1.6E-04 | 0.566 | 2.44 |
| 12.8         | 199.6          | 0.11           | 0.93  | 1.00         | 0.82         | 147.3          | 132.4           | 0.242 | 95.7   | 7.8E-03 | 0.438 | 1.81 |
| 13.7         | 202.2          | 0.12           | 0.90  | 1.00         | 0.79         | 165.5          | 141.6           | 0.248 | 95.7   | 5.5E-03 | 0.464 | 1.87 |
| 14.5         | 204.0          | 0.13           | 0.88  | 1.00         | 0.75         | 181.0          | 149.5           | 0.250 | 95.7   | 4.0E-03 | 0.482 | 1.93 |
| 15.4         | 197.8          | 0.14           | 0.85  | 0.99         | 0.71         | 199.1          | 158.8           | 0.251 | 95.7   | 1.7E-02 | 0.421 | 1.68 |
| 16.1         | 190.6          | 0.15           | 0.83  | 0.98         | 0.68         | 214.0          | 166.3           | 0.250 | 95.7   | 5.9E-02 | 0.362 | 1.45 |
| 16.6         | 189.7          | 0.15           | 0.81  | 0.97         | 0.66         | 222.7          | 170.8           | 0.248 | 95.7   | 6.5E-02 | 0.355 | 1.43 |
| 17.4         | 199.6          | 0.16           | 0.79  | 0.95         | 0.62         | 238.2          | 178.6           | 0.245 | 95.7   | 9.4E-03 | 0.438 | 1.78 |
| 17.9         | 199.6          | 0.17           | 0.77  | 0.93         | 0.60         | 248.3          | 183.8           | 0.243 | 95.7   | 8.4E-03 | 0.438 | 1.80 |
| 18.5         | 215.7          | 0.17           | 0.75  | 0.91         | 0.58         | 261.0          | 190.3           | 0.240 | 42.7   | 1.7E-04 | 0.581 | 2.43 |
| 18.9         | 216.6          | 0.17           | 0.73  | 0.90         | 0.57         | 269.8          | 194.7           | 0.237 | 42.7   | 1.0E-04 | 0.594 | 2.50 |
| 19.7         | 221.0          | 0.17           | 0.71  | 0.87         | 0.54         | 285.2          | 202.6           | 0.233 | 42.7   | 1.2E-05 | 0.662 | 2.84 |
| 20.1         | 220.1          | 0.17           | 0.70  | 0.86         | 0.53         | 293.3          | 206.7           | 0.231 | 42.7   | 1.5E-05 | 0.648 | 2.80 |
| 20.8         | 234.5          | 0.17           | 0.68  | 0.84         | 0.51         | 306.7          | 213.6           | 0.228 | 42.7   | 4.9E-09 | 0.942 | 4.13 |
| 21.4         | 234.5          | 0.17           | 0.67  | 0.83         | 0.50         | 318.2          | 219.4           | 0.226 | 42.7   | 3.8E-09 | 0.941 | 4.17 |